Département d'Astrophysique, de Géophysique et d'Océanographie
Faculté des Sciences – Université de Liège

The International Liquid Mirror Telescope project : optical quality tests and prospective detection of multiply imaged quasars

François Finet

Astrophysique Extragalactique et Observations Spatiales

Supervisor: Jean Surdej

Dissertation presented for the
acquisition of the grade of
Doctor of Philosophy
in Space Science

Members of the Jury – Pr. S. Habraken (President)
Dr. E. Gosset
Pr. P. Hickson (UBC)
Dr. C. Servais
Pr. J.-P. Swings
Pr. J. Surdej (Supervisor)

”For my part I know nothing with any certainty,
but the sight of the stars makes me dream.”

(Vincent Van Gogh)

Acknowledgements

Here finally comes the apogee of four fascinating and captivating years, filled with so many experiences and questions! This journey would have never been possible without my supervisor, Jean, whom I wish to thank deeply for his help and advice, in both scientific and human matters, for his kindness and patience, for all the opportunities he kept on offering, such as observing runs in Chile, and for these challenging problems he kept on suggesting, always mentioning "new ideas" for my thesis. And most of all, I am very grateful for the ∼200 hours he spent proofreading this thesis, without getting even seemingly upset by my numerous English mistakes!

I would also like to thank Paul for the precious advice he gave for the development of the ILMT, without which the telescope would have never been finished, and for offering me this unique opportunity of an internship at UBC in Vancouver. Discovering the Large Zenith Telescope and installing the UBC-telescope at CTIO were truly fantastic experiences that I shall never forget.

This achievement would not have been possible without my friends, who kept on reminding me that there was a life beside my thesis, especially during the difficult moments.

Thank you Laurent for these long conversations about how important and stimulating research (and life in general) can be, and for always solving my computer problems. Thank you Gilles for hosting us in our trips to Munich!

Thank you to these three unforgettable friends who heard about this thesis every single week-end without ever complaining... Thank you Lionel for saving my life (aka my computer without any backups) so many times, thank you Pierre for these conversations that convinced me one day to study Physics, and for being so patient while listening to all my questioning about the quasar Luminosity Function. And thank you Céline for being there to always remind the three of us that we could use a little more psychology!

These years would not have been the same without all the people in the institute and all these *whist* games during lunch time! For that, and for a lot more, I thank all of you! Olivier, Numero bis (aka Ragga style), Polo, Carlito, Laurent, Arnaud, Denis and finally, thank you Melanie for making this institute a little more attractive, for all the breaks... and for the dance as well! And *Grazie* Davide for teaching me how to speak Italian with animation to computers, to make them work! Thank you Sylvia and Denise for helping me, more than once, to not drown in all these administrative tasks.

Another grateful thought for Arnaud and Innocent for our time together, spent discovering the new students!

And finally, thanks to all those I met next to the coffee machine and a special thank to Dominique (the maintenance guy from the coffee machine) without whom my morning productivity would have been dramatically decreased!

Abstract

The International Liquid Mirror Telescope (ILMT) project is a joint collaboration between different universities and research institutes in Belgium, Canada, India and Poland, for the design, construction and operation of a 4 meter liquid mirror telescope at the Devasthal Observatory (India).

In the framework of the present thesis, we have contributed to the development of the ILMT. We have namely designed and manufactured an innovative instrument capable of measuring the optical quality of the primary mirror that may be affected by the propagation of wavelets on the mercury layer. The instrument is composed of a laser source, emitting a beam whose reflection on the mirror is modulated by slope variations induced by the wavelets. Preliminary tests were carried out showing the validity of the method for on site testing of the mirror.

The ILMT has been designed to perform a photometric variability survey of a narrow strip of sky, making it very suitable for the detection and follow-up of photometrically variable sources such as supernovae and quasars.

In the second part of this thesis, we present an estimate of the number of QSOs to be detected within the ILMT survey, and of the expected number of multiply imaged sources among these caused by the presence of a deflector near the lines-of-sight. We have studied the impact of various parameters on the expected number of detected gravitational lens systems, such as the instrumental resolution of the telescope, the galaxy population type(s) and corresponding lensing model(s), and the cosmological parameters.

The statistical sample of multiply imaged QSOs is intended to be used as a cosmological probe. In order to make a sensitivity comparison between various modelling approaches, we introduce a new formalism to estimate the lensing probabilities, based on the joined probability density of the observed QSOs.

This new formalism allows to calculate three probability densities: that associated with the optical depth distribution, as well as those related to the deflector and the lensed source redshift distributions. For the case of FLRW universes, we compare the sensitivity of these distributions as a function of the cosmological mass density.

Résumé

Le projet du Télescope International à Miroir Liquide (ILMT) résulte d'une collaboration entre différentes universités et instituts de recherche belges, canadiens, indiens et polonais pour la conception, la construction et l'utilisation d'un télescope à miroir liquide de 4 mètres de diamètre à l'Observatoire de Devasthal (Inde).

Au cours de cette thèse, en plus d'une contribution au développement de l'ILMT, nous avons conçu et réalisé un instrument innovant permettant la mesure de la qualité optique du miroir primaire, qui peut être affectée par la propagation d'ondelettes à la surface du mercure. Cet instrument est composé d'une source laser émettant un faisceau dont la réflection sur le miroir est modulée par les variations de pente locale induites par les ondelettes. Des tests préliminaires ont été réalisés, permettant de valider la méthode pour l'évaluation sur site du miroir.

L'ILMT a été conçu en vue de la surveillance de la variabilité photométrique d'une étroite bande de ciel, le rendant de ce fait propice à la détection et au suivi photométrique de sources variables, telles que les supernovae et les quasars.

Dans le seconde partie de cette thèse, nous présentons une analyse prospective de la population de quasars détectés par le télescope, ainsi qu'une estimation du nombre de sources, au sein de cet échantillon, multiplement imagées suite à la présence d'un déflecteur le long de leurs lignes de visée. Nous étudions également l'impact sur le nombre de systèmes de lentille gravitationelle détectés en fonction de différents paramètres, tels que la résolution instrumentale, le(s) type(s) de galaxies déflectrices et le(s) modèle(s) de lentille correspondant(s), ainsi que les paramètres cosmologiques.

L'échantillon statistique de quasars multiplement imagés sera utilisé comme outil d'étude cosmologique. En vue d'effectuer une étude comparative de la sensibiliité de différentes méthodes pour exploiter cet échantillon, nous introduisons un nouveau formalisme pour le calcul de la probabilité d'événement lentille, formalisme basé sur la densité de probabilité jointe de quasars observés.

Ce nouveau formalisme permet le calcul de trois densités de probabilité, à savoir: la distribution de la profondeur optique des sources et les distributions en redshift des déflecteurs et des sources multiplement imagées. Nous comparons la sensibilité de ces distributions en fonction de la densité de masse cosmologique, pour le cas d'univers de type FLRW.

Contents

Part I

The International Liquid Mirror Telescope: optical quality tests

Chapter 1

The 4m International Liquid Mirror Telescope project

The *International Liquid Mirror Telescope* (ILMT) project consists of an effort between institutes[1] from Belgium, Canada, India and Poland to design and construct a 4 meter liquid mirror telescope. The ILMT is composed of a primary liquid mirror, a focal point assembly and a structure to hold the focal point instrument (Fig. 1.1a).

The telescope main characteristics are summarized in Table 1.1.

The ILMT will be located at the observatory of Devasthal (Uttarakhand, India), in the early Himalayan chain at an altitude of 2,450 meters. The geographical coordinates of the observatory are 29.3617°N 79.685°E. The site location is shown in Fig. 1.1b.

The Devasthal site has been tested for astronomical observations by Sagar et al. (2000) and Stalin et al. (2001). The site median seeing is 1.1", and the seeing is better than 1", 35 percent of the time. The monsoon running from June to September precludes observations during this period.

The site will host two other telescopes (Sagar et al. (2012a)) among which a 3.6 meter telescope with spectroscopic capabilities, the *Devasthal Optical Telescope* (DOT) project with which the ILMT is expected to have a strong synergy. The second telescope is a 1.3-m fast (f/4) wide field-of-view optical telescope, already operating on the site, primarily used for wide field photometry.

In this Chapter, after an introduction to the principle of liquid mirror telescopes in section 1.1, we present a technical description of the telescope, its primary mirror assembly in section 1.2, and the focal assembly in section 1.3, including the optical corrector and the CCD camera.

---

[1] The ILMT project consists of a scientific collaboration in observational astrophysics between the Institute of Astrophysics and Geophysics of the Liège University (IAGL), the Royal Observatory of Belgium (ROB), the Aryabatta Research Institute of Observational Science (ARIES, Nainital, India), the Observatory of Poznań (UAM, Poland) and several Canadian universities (British Columbia, Laval, Montréal, Toronto, Victoria and York).

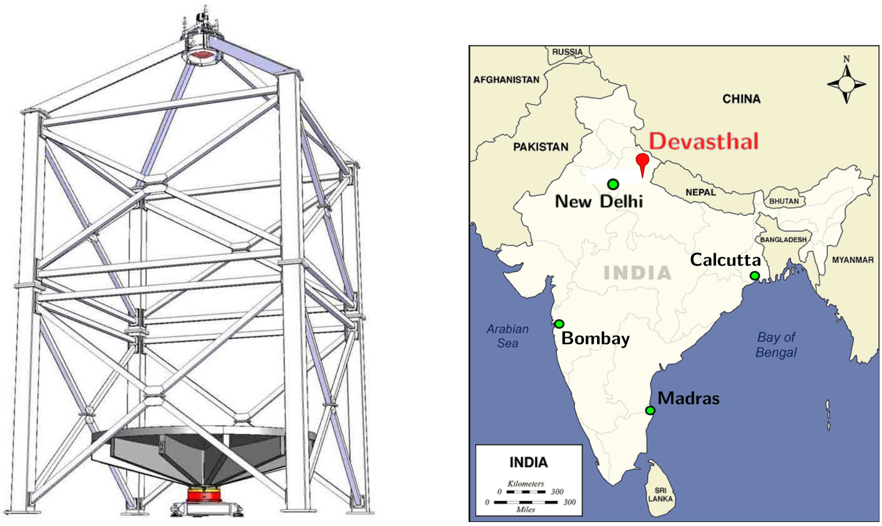

(a) (b)

Figure 1.1: (a) The International Liquid Mirror Telescope scheme. (b) Location of the Devasthal observatory.

Telescope	
Mirror diameter	4 (m)
Focal length	8 (m)
Effective focal length (with the optical corrector)	9.4524 (m)
Field of view	27’ by 27’
CCD	4096 by 4096 (px)
Pixel size	15 ($\mu m/$ px) 0.4 (arcsecond / px)
Filters	g', r', i' (SDSS)
Integration time	102 (s)
Limiting magnitude	$i' \sim 22.5$

Table 1.1: Main characteristics of the ILMT.

1.1 Principle of liquid mirror telescopes

A liquid mirror is obtained by using a rotating dish containing a reflective liquid. Under the combined action of the local gravity and the centrifugal force, as pictured in Fig. 1.2, the liquid surface takes the shape of a paraboloid.

Indeed, a liquid surface at equilibrium sets perpendicularly to the net acceleration it experiences. The centrifugal force scales as $\omega^2 r$ (where ω is the dish

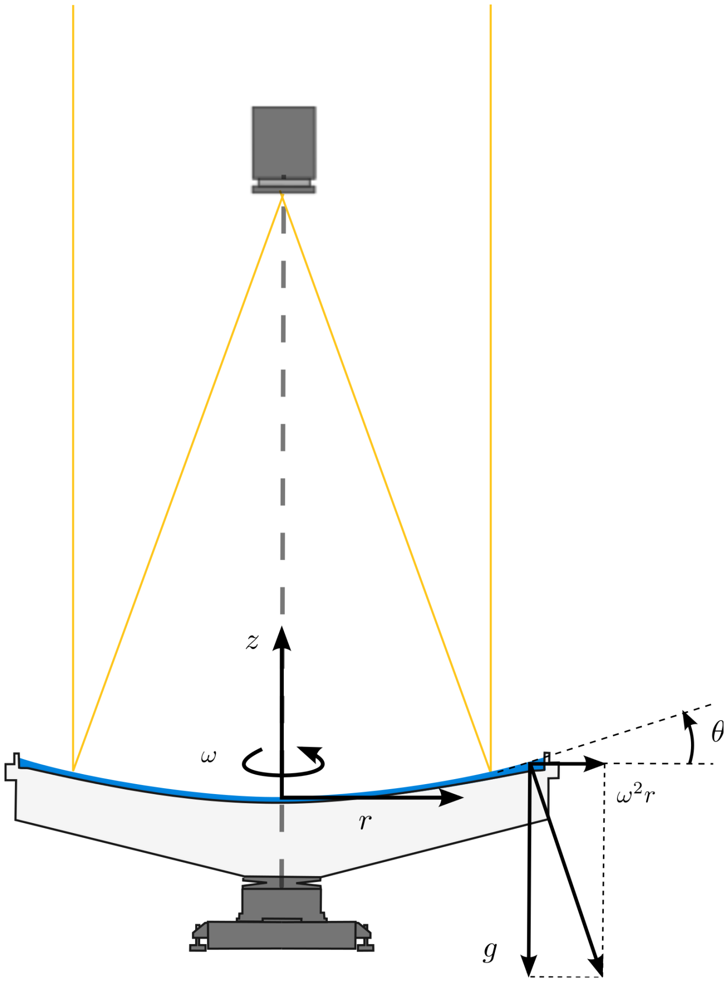

Figure 1.2: Principle of a liquid mirror telescope. The primary mirror is a rotating reflective fluid, taking a parabolic shape under the combined action of the gravity and the centrifugal force. A camera inserted in the focal plane of the paraboloid will image the field-of-view near the Zenith.

angular velocity and r the distance to the central axis) and the gravity is assumed to be constant all over the surface. Defining the angle θ between the liquid surface and the horizontal, as shown in Fig. 1.2, it comes

$$\tan\theta = \frac{dz}{dr} = \frac{\omega^2 r}{g}. \tag{1.1}$$

Integrating Eq. 1.1 and setting the origin of the z axis at the liquid surface central height, we obtain the shape of the liquid surface

$$z = \frac{\omega^2 r^2}{2g}. \tag{1.2}$$

Comparing Eq. 1.2 with the general equation of a parabola with a focal length F

$$z = \frac{r^2}{4F}, \tag{1.3}$$

we see that the rotating liquid surface is a paraboloid having a focal length

$$F = \frac{g}{2\omega^2}. \tag{1.4}$$

A rotating dish containing a reflective liquid thus acts as a parabolic mirror. Its focal length F is determined by the angular velocity through Eq. 1.4.

Parabolic mirrors have the property that all light rays incident parallel to the axis of symmetry of the paraboloid are refelected towards its focal point, as shown in Fig. 1.2. Consequently, inserting a camera or a sensor at the focal point of the paraboloid allows to image the field-of-view at the Zenith of the mirror. A *liquid mirror telescope* is thus obtained by using a reflective liquid as the primary mirror and by inserting a sensor on the focal surface. The angular *field-of-view* (FOV) of the telescope is then determined by the focal length F and the size d of the sensor

$$FOV = \frac{d}{F}. \tag{1.5}$$

The liquid mirror telescope, as previously described, is thus composed of a Zenith point mount. Because the local gravity is used to generate the primary mirror shape, it is not possible to incline it in order to point or track an object, as it is done with classical telescopes. Furthermore, because of the earth rotation, all objects in the telescope FOV are moving at the sidereal rate. It is thus impossible to image the near-Zenith FOV using conventional integration techniques as stars would leave tracks due to their diurnal motion over the detector.

Borra (1982),Borra et al. (1982) and Hickson et al. (1994) showed that it is possible to track electronically the objects crossing the telescope FOV using a CCD imaging technique called *Time Delay Integration* (TDI) or drift-scanning. In the TDI imaging technique, as a source goes through the telescope FOV, the photoelectrons generated on the sensor are drifted in order to stay under the image of the object on the sensor. All the photoelectrons generated are then counted once the source gets out of the FOV.

Using a CCD camera with TDI imaging, the integration time t is fixed by the time necessary for the objects to go through the telescope FOV. Defining the sidereal rate SR of an object at the telescope Zenith, the integration time is

$$t = \frac{FOV}{SR}. \tag{1.6}$$

The interest of such a fixed mount is thus dictated as will its accessible FOV. Thanks to the parabolic primary mirror, the image of an object on the optical axis of the telescope is aberration free. However, off-axis imaging is very quickly deteriorated due to the dominant coma aberration and astigmatism (see Schroeder

(1987) for a full description of aberrations with parabolic reflective mirrors). The coma aberration being very quickly limitating, one must introduce an optical corrector in front of the sensor in order to correct for this aberration.

A great effort has been done to increase the region of the sky accessible with a fixed telescope using this technology by either using optical correctors to correct a field as large as possible (Borra (1993), Hickson and Richardson (1998)) and/or movable secondary systems (Borra et al. (1995), Zaritsky et al. (1996), Hickson (2002)).

The ILMT is a liquid mirror telescope using a 4 meter primary mirror and fixed secondary assembly composed of an optical corrector and a CCD camera working in TDI mode.

In the two next sections, we give a technical description of the ILMT primary mirror and focal-point assembly.

1.2 The primary-mirror assembly

1.2.1 Primary mirror

The primary mirror is a 4 meter rotating dish containing mercury. A picture of the primary mirror is shown in Fig. 1.3.

The dish structure is composed of twelve vertical ribs, covered by a circular plate. The core segments are made of styrofoam, surrounded by carbon fiber sheets. This provides a very light structure to the bowl thanks to its inside foam, yet rigid enough to sustend the load of mercury covering the bowl.

The overall stiffness of the bowl is of critical importance. The dish structure itself must resist to flexure induced by the load of the layer of mercury covering the rotating dish. This flexure should not be larger than one tenth of the mercury layer thickness (Hickson et al. (1993)). Furthermore, any vibration transmitted to the mercury leads to the formation of wavelets on the mercury layer that affect the optical quality (Borra et al. (1992), Borra (1994)). Consequently, the resonance frequency of the mirror should be as high as possible to avoid the transmission of vibrations to the mercury (Hickson et al. (1993)).

In order to reduce the amount of mercury needed, the top surface of the dish is preshaped with the form of the final mercury layer. The reduction of the amount of mercury is important for several reasons. First, it permits to have a lighter structure to be supported by the rotation system and it reduces the load of the bowl structure itself. Secondly, Borra et al. (1992) have shown that reducing the thickness of the mercury layer on the rotating dish increases the damping of the wavelets that could be present on the mercury layer. This operation by which the mirror is preshaped is called the spin-casting. The dish is covered with a layer of Polyurethane (PU), a two-component resine composed of a basis and a hardener. The liquid PU is poured on the mirror while rotating, and the mirror is kept rotating while the PU hardens. The PU thus hardens with the shape that the mercury layer will have.

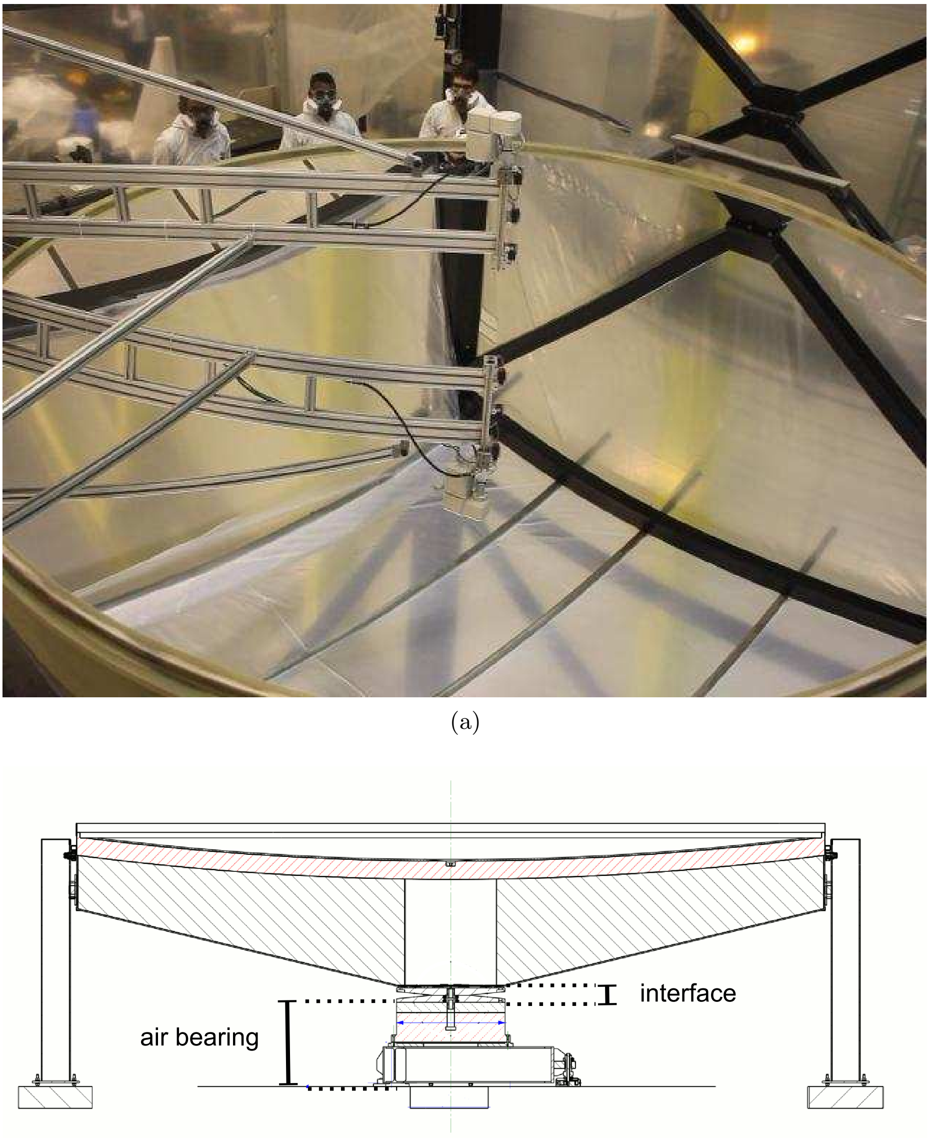

(a)

(b)

Figure 1.3: ILMT primary mirror. (a) Top view of the spinning mirror. (b) Schematic side view of the mirror.

The ILMT mirror is designed to have a focal length of 8 meters. Inverting Eq. 1.4 linking the focal length and the angular velocity, we find

$$\omega = \sqrt{\frac{g}{2F}}, \tag{1.7}$$

and the period of rotation T of the primary mirror is thus

$$T = \frac{2\pi}{\sqrt{\frac{g}{2F}}}. \tag{1.8}$$

Inserting the different numerical values, we find a rotation period $T = 8.02$ seconds.

1.2.2 Air bearing

Any vibration induced by the rotation system to the dish will lead to the formation of wavelets on the mercury surface. To achieve an optical surface quality, it is thus mandatory to avoid any vibration to be transmitted to the mercury. One of the way to achieve this is to use air bearing rotation sytems to avoid transmission of wavelets to the liquid induced by ball-bearing, for instance. Using air bearing systems, Borra et al. (1989, 1992) showed that it is possible to achieve diffraction limited liquid mirrors with a 1.5 m diameter, a Strehl ratio of 0.8 and rms surface deviation of $\sim \lambda/20$. Borra et al. (1993) then demonstrated with a 2.5 meter $f/1.2$ mirror that using this technique can lead to liquid mirrors of astronomical optical quality.

For these reasons, the ILMT rotation system consists of an air-bearing mounted on a three-point mount for the alignment of the axis of rotation. The air bearing used for the ILMT is a *Kugler RT600T* model.

The importance of the angular-velocity stability of the mirror has been emphasized by Borra (1982) who prescribed a rotational period stability better than 10^{-5}, as instabilities in the rotational velocity will also lead to perturbations induced to the liquid mercury. The rotational speed stability of the ILMT air bearing is ensured by a *position controled* feedback loop (Denis (2011)). In this system, the rotor position sensor consists of a 3000 lines per revolution encoder on the rotor, sending pulses to a comparison unit. The encoder pulses are compared to reference pulses generated by a reference clock (a *Synthesized Function Generator* - SRS DS 335). The time difference between the encoder pulses and the reference pulses, defined as the *Following Error* (FE), is measured by the comparison unit. The control loop maintains the FE as small as possible by applying a torque to the rotor, at a frequency of 2 Khz. The stability of the dish rotation period has been measured during tests which have taken place in the AMOS workshop, with a 3mm thickness of mercury on the dish. The relative period variation measured was better than 1.5 10^{-6} (rms) and 7.2 10^{-6} (peak to valley).

The rotor of the air bearing is kept levitating and on axis during its rotation, thanks to a pressurized air system. There are two separate circuits to feed the air bearing:

- an axial thrust circuit: with a nominal working pressure of $\sim$ 6 bar. This circuit supports the vertical load applied to the bearing, i.e. the weight of the rotating dish and the mercury;

- a radial thrust circuit: to guarantee that the rotor stays centered with respect to the stator during its rotation, the nominal working pressure here is ~ 3 bar.

The maximal axial load bearable by the bearing depends on the pressure in the axial thrust circuit. With the nominal pressure of 6 bar, the maximal axial load of the bearing has been measured (Hickson (2008b)) to be

$$W_{max} = 1272(Kg). \tag{1.9}$$

The empty mirror weights $\sim$ 600 Kg and a 3mm thickness of mercury over the whole mirror weights 410 Kg. Consequently, the maximum load to which the bearing is submitted is 1010 Kg which is slightly less than W_{max}.

Content (1992) has emphasized the importance of the overall tilt stiffness of the rotating dish. The overall structure must be sufficiently stiff to resist to the torque created by an off-axis load that would be created due to a global motion of the mercury over the mirror during its startup. An insufficient tilt stiffness would lead to a tilting of the mirror and a spill of its mercury content. It is also important that the rotating structure resists to the torque created by an occasional break of the mercury layer while rotating (Hickson et al. (1993)).

The ability of the dish to resist to a torque m created by an off-axis load is measured through its tilt stiffness K

$$K = \frac{m}{\theta} \qquad \text{(Nm/radian)}, \tag{1.10}$$

where θ is the tilt angle (in radian) induced to the dish by the torque. It is sometimes more practical to define the tilt compliance $G = 1/K$. Based on the hydrostatic stability criterion, Hickson (2008b) has determined the critical tilt stiffness K_{crit} and critical compliance G_{crit} for the ILMT primary mirror

$$\begin{aligned} K_{crit} &= 1.677 \quad (\text{Nm}/\mu\text{radian}) && (1.11)\\ G_{crit} &= 0.596 \quad (\mu\text{radian/Nm}), && (1.12) \end{aligned}$$

with a 50 percent safety factor, the maximal value of the critical compliance is $G_{crit} = 0.4$.

In order to avoid any damage to the rotating table in case of a break of the mercury layer while rotating, the primary mirror dish is not fixed to the air bearing. Two interface plates allow the dish to tilt with respect to the air bearing once an off axis load applies a torque that would be damageable to the air bearing (Fig. 1.3b).

Finally, Girard and Borra (1997) have put in evidence the importance of the alignment of the rotation axis with the vertical. The rotation axis of the mirror should be aligned to better than 0.1 arcsecond (Hickson (2008a)). This is made possible thanks to the three point mount on which the air bearing is mounted, allowing a manual adjustment of the rotation axis.

1.2.3 Mercury handling infrastructure

For different operations, the mercury has to be taken off the mirror. It is thus necessary to have an infrastructure allowing to pump the mercury on and off the mirror and store the 500 Kg of mercury when not used.

Storage of the mercury is done in a stainless steel container located next to the mirror and the mercury is pumped with a commercial peristaltic pump.

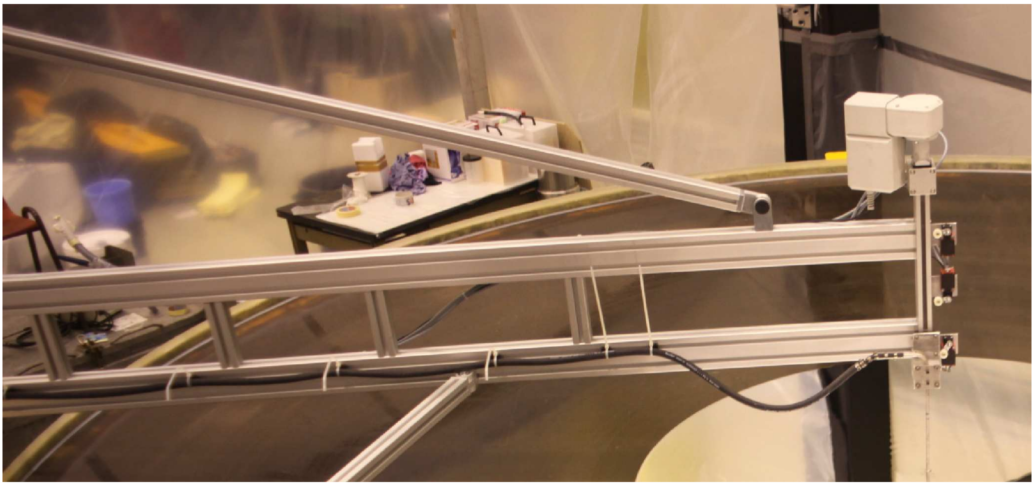

Figure 1.4: The ILMT pumping structure.

Borra et al. (1992) put in evidence the importance of using a thin layer of mercury during operation. This increases the damping of the wavelets on the mercury as well as decreases their amplitude, thus optimising the mirror quality. On the other hand, during start-up, the mirror is spinned manually to communicate enough angular momentum to the mercury. This operation is made easier by using a thicker layer of mercury, making it easier to close the mercury surface over the dish. The pumping infrastructure must thus allow to pump the mercury off the mirror while the primary mirror is rotating, without breaking the mercury layer. This implies the pumping to be performed at the center of the rotating dish, to avoid breaking the symmetry of the system.

In the framework of this PhD thesis, we have designed and assembled the pumping structure shown in Fig. 1.4. It consists of a metallic structure holding the pumping tube. The end of the tube is fixed to a stainless steel tube moveable vertically by a linear translation stage, thus allowing to retract the pumping system out of the mercury, in order to avoid any vibrations to be transmitted to the mercury. The overall structure is attached by hinges on one of the focal assembly tower pilars, permitting to fold the structure on the side in order to avoid additional light obstruction above the mirror.

1.3 The focal-point assembly

The ILMT focal-point assembly is composed of

- a CCD camera with time delay integration imaging capability;
- a slide with medium band-width optical filters;
- an optical corrector;
- several mechanical systems allowing alignment of the whole assembly.

In the next Section, we describe the different components of this assembly.

1.3.1 CCD camera

Imaging with a CCD camera

The CCD camera sensor is composed of a matrix of pixels. In a normal use of the CCD, imaging is done in two different steps: the integration and the readout of the sensor.

During the first phase, the integration, photons arriving on the sensor generate photoelectrons in the pixels. Each pixel acts as a potential well where the photoelectrons are stored during integration. As shown in Fig. 1.5a, the pixels consist of *Metal-Oxyde-Semiconductors* (MOS) junctions. The photons arriving in the semiconductor generate photoelectrons that are attracted towards the Oxyde layer thanks to a positive potential applied to the Metal.

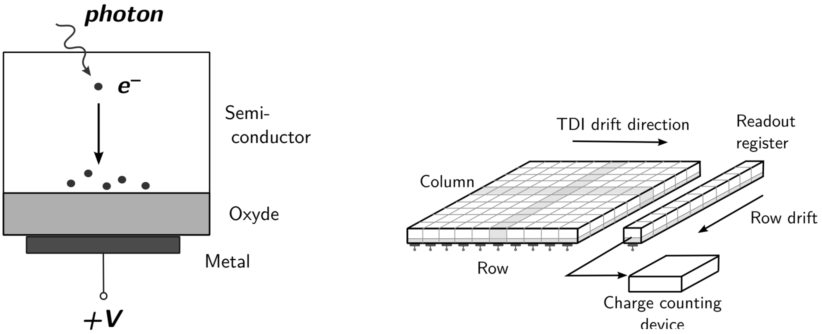

(a) (b)

Figure 1.5: (a) Pixel concept and (b) CCD readout concept.

At the end of the integration starts the readout phase. All photoelectrons generated in the pixels are drifted, row by row, towards the readout register on one side of the CCD. Once a pixel row is transferred to the readout register, the pixels lines are drifted towards a charge detection device that counts the number of photoelectrons generated in each pixel during the integration time, converting it into a voltage.

Time Delay Integration technique

In the case of the ILMT, the camera is working in a particular readout mode called *Time Delay Integration* (TDI) mode.

As the ILMT is a Zenith-pointing telescope, thanks to the earth rotation, all objects in its FOV are moving at the sidereal rate. As an object goes across the FOV of the telescope in the East-West direction, its image goes across the CCD sensor.

In the TDI readout mode, the readout process is slowed down in such a way that the shift rate of the lines towards the readout register, matches the motion rate of the object image on the sensor. Consequently, all the photoelectrons generated by a source stay under the image of the source on the CCD sensor as it goes across it. The tracking of the object in the FOV is thus done electronically.

As soon as an object gets out of the FOV, the pixel line (along the North-South direction) on which the photoelectrons were generated is drifted towards the readout register and the generated photoelectrons are counted. The data flow created by TDI imaging is thus continuous, creating a single long image of the strip of sky to which the telescope has access.

One of the main advantages of the TDI imaging mode is the facility of data reduction. In conventional imaging, the sensitivity irregularities of the sensor must be corrected for by the use of a two dimensional flat field image. In the TDI mode, as the objects go all across the detector along the sensor column, the sensitivity irregularities are averaged over the detector columns. Consequently, the image reduction is done by dividing each line by a one-dimensional flat field. Furthermore, this flat field can be directly estimated from the scientific data, as opposed to conventional imaging where flat field images must be taken before and/or after scientific imaging.

The ILMT CCD camera

The ILMT is equipped with a *Spectral Instrument* camera model SI-1100 mounted with a E2V CCD 231-84-1-E06 chip. The camera is capable of classical and TDI imaging. The general characteristics of the chip are given in Table 1.6.

The camera is equipped with a 4K by 4K sensor, each pixel measuring 15 μm by 15 μm, with a filling factor of 100 %. The main characteristics of the chip are

- the *full well capacity*: the maximum number of photoelectrons that can be stored in a pixel during integration time. The E2V chip has a full well capacity of $\geq 250ke^-$ per pixel,

- the *dark current*: during the integration time, some thermal electrons are created in the pixel potential well, acting as a noise signal. Dark electrons being generated by thermal excitation, this noise is lowered by cooling the CCD,

- the *readout noise*: electrons generated during the readout process,

Number of pixels	4096 x 4112
Filling factor	100 %
Pixel size	15 μm
Flatness	$< 20\mu$m
Illumination	Back illuminated
Pixel charge storage	$\geq$ 250Ke$^-$
Digitization	16 bit
Max readout noise	5e$^-$ (1MHz)
Max readout noise (SI 100 KHz)	2e$^-$ (quotes)
Dark current (e$^-$/pix/s)	0.83 10^{-3} (-100°C)
Dark Current (-100°C SI)	10^{-4} (quotes)

Figure 1.6: Characteristics of the E2V-231 CCD chip.

- the flatness of the sensor: E2V garantees flatness deviations smaller than 20 μm peak to valley,
- the quantum efficiency which is defined as the fraction of incident photons that generate photoelectrons, dependent on the wavelength. The chip quantum efficiency is shown as a function of wavelength in Fig. 1.7. The chip has been coated in order to minimise the light reflection in the corresponding spectral range.

1.3.2 ILMT filters

The ILMT is equipped with median-band optical and near infrared filters. These filters are the g', r', i' filters based on the SDSS photometric system. The transmission of the SDSS spectral bands are shown in Fig. 1.7b.

The choice of the SDSS filter system was made in order to directly compare the data produced by the ILMT with those from other large surveys, such as the SDSS and the CFHT data products also using the SDSS' photometric system. Note that the SDSS data pertain to a slightly different photometric system (u, g, r, i, z bands instead of u', g', r', i', z') due to an alteration of the mounted filters. The conversion between the two photometric systems only necessitates minor corrections to the measured magnitudes.

The telescope will mostly operate in the i' filter with which the time variability survey will be performed. Imaging in g' and r' will be performed in order to ensure a correct photometric calibration of all the detected objects.

The characteristics of the g', r' and i' filters are summarized in Table 1.2. The definition of the SDSS filters may be found in Fukugita et al. (1996). The central wavelength and full width at half maximum values come from the specifications delivered by the *OmegaOptics* company, who manufactured the filters.

For information, the central wavelengths of the SDSS g, r and i filters are also indicated in Table 1.2.

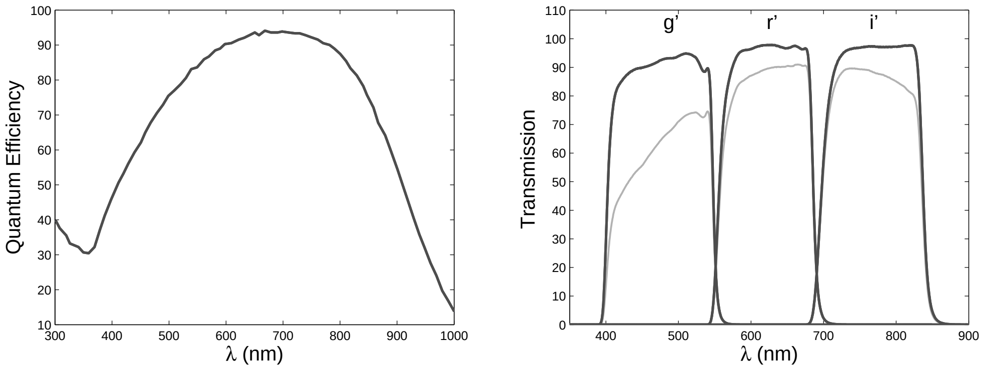

(a) (b)

Figure 1.7: (a)Quantum efficiency, as a function of the wavelength, for the E2V chip equipping the ILMT CCD camera, with a mid-band anti-reflective coating. (b)Transmission of the g', r', i' SDSS filters that will be used with the ILMT. The lighter grey curve is the combined transmission of the filters and the CCD quantum efficiency.

Common characteristics

Flatness	$\lambda/4$ (peak to valley)
Parallelism	$\leq$ 30”
Transmission	$\geq$ 88% (average)
Thickness	5 ± 0.25 (mm)

Individual characteristics

Filter	g’	r’	i’
Central wavelength (*nm*)	475	625	763
Full Width at half maximum (*nm*)	145	150	150
Cut on (±8 nm)	400	550	695
Cut off (±8 nm)	545	695	853
Refractive index	1.53	1.51	1.535

SDSS 2.5m filter characteristics

Filter	g	r	i
Central wavelength (*nm*)	468.6	616.5	748.1

Table 1.2: ILMT and SDSS filter characteristics.

1.3.3 Optical corrector

The ILMT optical quality has been designed such as it will just be limited by the seeing conditions on site.

As mentioned in the previous Chapter, because the primary mirror is parabolic, off-axis imaging is very quickly blurred due to a dominant coma aberration and astigmatism (Schroeder (1987)). The coma aberration being very quickly limitating, one must introduce an optical corrector in front of the sensor in order to correct for this aberration.

Furthermore, there are particular image distortions introduced by TDI imagery. First of all, the star trails in the sky plane are curved. When using the TDI CCD imaging technique, the trajectories of the stars projected on the CCD are also curved whereas the columns of the CCD along which the photoelectrons are shifted are straight. Consequently, the telescope PSF gets spread along the N-S direction over several columns, producing a deformation of the PSF. As an indication, we use the linear relation determined by Gibson and Hickson (1992) of the maximum deviation Δ that a star trail deviates from the center of a column

$$\Delta = (1 - \cos b) \tan l, \tag{1.13}$$

where b is half the detector angular FOV and where l is the telescope latitude. Inserting the values from Table 1.1, in the ILMT field, this leads to a maximum North-South displacement of the star photocenter by $\Delta \sim 0.9$", this North-South elongation being added to the athmospheric seeing effect.

Secondly, the angular velocity of the objects across the FOV is a function of both their declination and the declination of the FOV center. It is thus impossible to match the TDI line shift rate to the sidereal rate over the entire field. By setting the TDI shift rate to match the shift rate for the middle of the field, in the upper and lower edge of the field, the difference between the TDI shift rate and the drift of the objects on the detector due to earth rotation leads to a deformation of the images along the East-West direction. Hickson and Richardson (1998) determined the maximum value of the displacement of the star center due to the speed gradient across the field of view. If the TDI readout rate is set to match the speed of a star whose trail passes through the center of the field, the maximum deviation along the East-West direction Δ_{E-W}, occurs for stars at the North and South edges of the CCD detector. Using the first relationship derived by Hickson and Richardson (1998), we find

$$\begin{aligned} \Delta_{E-W} &= 0.7239\text{"} \qquad (1.14) \\ &= 1.4624 px. \qquad (1.15) \end{aligned}$$

The effect of TDI distortion on astronomical images has been studied by Hickson and Richardson (1998) and Gibson and Hickson (1992) and independently by Vangeyte et al. (2002). If not corrected for, these combined effects lead to a banana-shape PSF as mentioned previously.

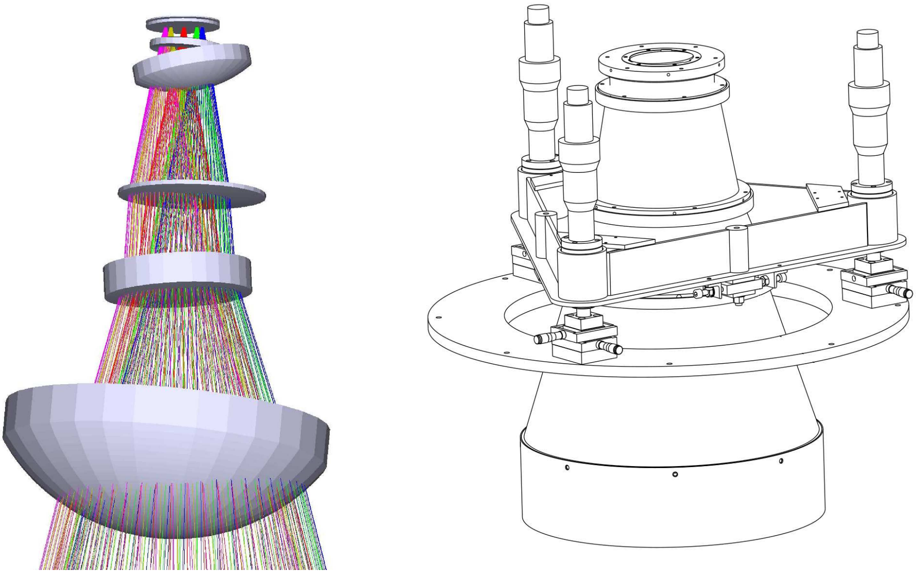

(a) Zeemax model

(b) Corrector structure drawing

Figure 1.8: The ILMT optical corrector.

In order to correct the parabolic off-axis coma distortion and the TDI distortion due to star trail curvature and differential velocity across the field, the ILMT is equipped with an optical corrector whose goal is to correct a field of 27 by 27 arcminutes, to make the ILMT seeing limited. The Zeemax model of the corrector is shown in Fig. 1.8 on the left hand panel and the right hand panel shows the whole corrector assembly with its mount.

This corrector is the first attempt of correcting optically the TDI distortion, leading to a system of tilted lenses as seen on the Zeemax model.

The assembly is equipped with a mechanical mount allowing a tip-tilt alignment of the corrector.

1.4 Science with the ILMT

Thanks to the earth rotation, the ILMT will scan a strip of sky centered at a declination equal to the telescope latitute. The width of this strip is determined by the North-South width of the telescope FOV. The ILMT is located in Devasthal (India) at a latitude of 29.3617°N. The telescope field of view is 27' by 27'. The strip of sky accessible to the telescope is shown in Fig. 1.9, in an all sky projection centered on the galactic center. As seen in the figure, the ILMT strip crosses the galactic plane twice. This gives access to both very crowded low galactic fields and high galactic latitude fields where the detection of fainter and more distant

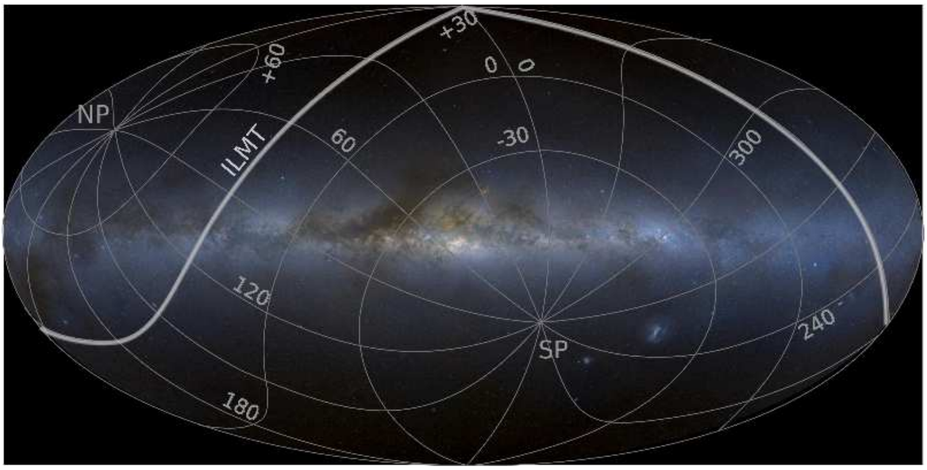

Figure 1.9: All sky image centered on the galactic center in the Hammer-Aitoff projection. The strip of sky accessible by the ILMT is superimposed over the image. Equatorial coordinate isocurves are projected as grey lines on the all sky image, NP and SP being the North and South equatorial pole, respectively.

objects (galaxies, quasars,...) will be possible. The calculation of the solid angle covered by the survey, for both low and high galactic latitude fields, is presented in detail in Chapter 5. The total field covered by the survey is 140 sq.deg., with 70 sq.deg. at a galactic latitude $|b| > 30°$.

The ILMT will image parts of this strip night after night through the broad-band SDSS filters. Because this strip is imaged night after night, we shall use the different images of the same fields

- either by adding them to increase the signal-to-noise ratio and thus simulate a longer integration time, enabling the detection of fainter objects;
- or by subtracting the successive images to detect variable objects and measure their photometric or astrometric variability.

As an example, use of the image subtraction technique described in Alard and Lupton (1998) and Alard (2000) will allow to retrieve relative photometric variability, taking into account the seeing variation from night to night, by desinging a reference image that will be convolved with a kernel to simulate comparable seeing conditions.

The photometric variability study of the strip of sky during the 5 years the telescope is expected to run at first, does really constitute the corner-stone of the ILMT project. Although long-term photometric variability study is commonly used as a tool to study various types of objects such as time-delays between the multiple images of a lensed quasar, supernova remnants or exoplanet transits, the ILMT is really a unique tool that will allow to do photometric variability survey of *all* types of objects.

Thanks to the very low cost of LMTs, such a telescope can be devoted to a unique scientific project. The ILMT main goal is the photometric variability study of all objects passing in the narrow strip of sky. It is thus very suitable for the detection of variable objects as well as their photometric follow up.

The different scientific possibilities offered by the LMT particularities have been addressed by Borra (1995) and Borra (1997). One way to overcome the main limitation of liquid mirrors, i.e. the zenithal pointing, is to use LMTs for statistical cosmological studies. Indeed, thanks to the hypothesis of homogeneity and isotropy at large scales, the direction of pointing does not really matter, as long as the telescope has access to a wide extragalactic field.

Among the different scientific projects achievable with LMTs, let us mention the

- detection and photometric follow up of QSOs, which are variable objects by essence;
- detection of multiply imaged QSOs by gravitational lenses;
- detection and photometric follow up of type Ia Supernovae;
- study of microlensed galactic objects;
- detection of high proper motion objects;
- detection of low surface brightness galaxies by co-addition of the images.

Our two main scientific drivers of the ILMT project are the detection and the photometric follow up of gravitationally lensed QSOs and type Ia Supernovae.

Type Ia Supernovae constitute very useful probes for cosmological tests related to the determination of H_0 and q_0, as these Supernovae have been proposed to be standard distance indicators (see Branch and Tammann (1992) and Krisciunas (2012) for recent reviews on the topic).

As the second part of this thesis adresses the statistical aspect of gravitational lensing in the population of QSOs to be detected with the ILMT, we highlight in the following the different science topics that can be addressed with gravitationally lensed QSOs.

There are several techniques to detect QSOs in surveys (see Weedman (1986) for an introduction). Selection strategies of QSO candidates can be based either on broad or median-band filter colour criteria, photometric variability, or based on the identification of the X-ray or radio counterpart of the objects. QSO candidates can then be confirmed spectroscopically.

In the case of the ILMT project, QSO candidates are selected on the basis of their photometric variability: they will appear as point-like sources in the strip of sky, presenting photometric variability from night to night.

Beside the photometric variability survey in the SDSS i'-band, the ILMT will also image the sky in the g' and r' bands of the SDSS system. Broad or medium band photometry makes possible a confirmation of the QSO candidates on the basis of the candidate colours as well as a photometric redshift estimate (as described in Claeskens et al. (2006b) for the case of the GAIA mission).

On the other hand, the presence of another 3.6 meter telescope with spectroscopic capabilities on the site of the ILMT, the Indo-Belgian *Devasthal Observatory Telescope* (intensively introduced during the 2012 SPIE meeting, see Sagar et al. (2012b), Ninane et al. (2012), Sagar et al. (2012a) for a general description), will also allow a spectroscopic confirmation of the QSO candidates.

The selection of QSOs among selected candidates from their photometric variability has the advantage to provide a very homogeneous QSO sample, free from colour selection biases. Thus this technique will provide a very clean statistical sample of QSOs.

Among these QSOs detected in the survey, some will be detected as being gravitationally lensed. Due to the presence of a foreground massive object near their line-of-sight deflecting the light-rays the QSOs emit, these objects will appear to be multiply imaged. This phenomenon is described intensively in the second part of this thesis. Gravitational lens candidates will be selected for instance as multiple point-like objects, close to each other, all showing some photometric variability. They will have to be confirmed either spectroscopically or on the basis of their colour, in the same way as the QSO candidates.

The detected gravitationally lensed QSOs can be studied either independently or as a statistical sample. The study of each gravitational lens will address various scientific questions such as

- the determination of the time delays between the images, thanks to the photometric variability monitoring of each of the lensed images;
- assuming a mass distribution model for the deflector, knowledge of the time delay between the images allows to determine the local value H_0 of the Hubble constant (Refsdal (1964a,b));
- knowing the deflector mass distribution also permits to invert the lensed images and doing so, to retrieve the real image of the background source benefiting from the magnification of the gravitational lensing event;
- assuming a cosmological model, the astrometry and magnification of the lensed images allow to study the mass distribution of the corresponding deflector;
- moreover, the differential variability between the lensed images due to microlensing will lead to the studies of the structure of the source.

The reader interested in these topics could read the series of papers dedicated to a multi-wavelength study of the gravitationally lensed QSO RXS J1131-1231 by Sluse et al. (2006), Sluse et al. (2007) and Claeskens et al. (2006a). In these papers, multi epoch imaging at multi wavelengths has permitted to reconstruct a multi colour image of the background source as well as its host galaxy, also revealing its structure by microlensing effects. These papers present a very good example of the wide range of science topics rendered possible through the study of a single gravitational lens system.

On the other hand, the sample of gravitational lenses considered as a whole can be used as a statistical tool for cosmological studies. In this context, as mentioned earlier, the ILMT data will be of an excellent quality thanks to its variability selection strategy of QSO candidates.

The statistical aspects of gravitational lensing events were proposed as a statistical tool by Turner and Gott (1984). The idea is to compare an *observable* statistics in a source population with the prediction of a model. The observables suggested by Turner and Gott (1984) are either the fraction of lensing events, the redshift distribution of the lenses, or the distribution of the angular separation of the lensed images.

The probability of a lensing event depends upon the space distribution of the deflectors and their types, the space distribution of the sources and the cosmological model. Consequently, by comparing the observation to the prediction of a model of the different statistics, lensing statistics may be used as a tool to

- constrain the cosmological model parameter Ω_Λ (Cen et al. (1994));
- constrain the density and the evolution of the deflector population (Chae (2010));
- constrain the density and evolution of the source population.

The second part of this thesis presents the expected population of QSOs to be detected with the ILMT (Chapter 5), the expected number of lensing events within this population of sources (Chapter 6) and a comparison study of the different observable statistics as a tool to test the cosmological model (Chapter 7).

Chapter 2

Testing the ILMT mirror surface quality using the CCD triangulation technique

2.1 Method description

2.1.1 Introduction

The quality of the scientific data acquired with the ILMT relies on the sharpness of the telescope PSF. Sharper images allow, on one hand, to achieve a better angular resolution enabling the detection of objects angularly closer to one another, and, on the other hand, it leads to a higher Signal-to-Noise ratio for the same integration time, enabling the detection of fainter objects.

The optical quality of the primary mirror is thus of critical importance for the image sharpness. Liquid mirror surface quality is known to be affected by the possible presence of wavelets, propagating over the mercury layer. The impact of theses wavelets is to diffract light into the wings of the PSF (Hickson and Racine (2007)), reducing the energy contained in the central core of the PSF.

There are different types of wavelets: transitory waves, spiral shaped waves and concentric ones. Fig. 2.1 shows a defocused image of a liquid mirror where the different types of wavelets are clearly visible.

The transitory wavelets (marked as concentric rings on the left side of Fig. 2.1) are induced by any perturbation transmitted to the mirror (a gust of wind, a fly or a debris impacting the mercury layer, ...). These waves propagate through the surface and are damped rapidly with time. They cannot be avoided but their damping is increased by the use of thinner mercury layers (Borra (1994)).

Concentric waves may originate due to vibrations transmitted to the bowl from the bearing. These vibrations will typically have a frequency equal to the eigen frequency of the system bowl+mercury (∼20-30 Hz). They are formed with a pattern of concentric wavelets propagating radially, with a typical amplitude

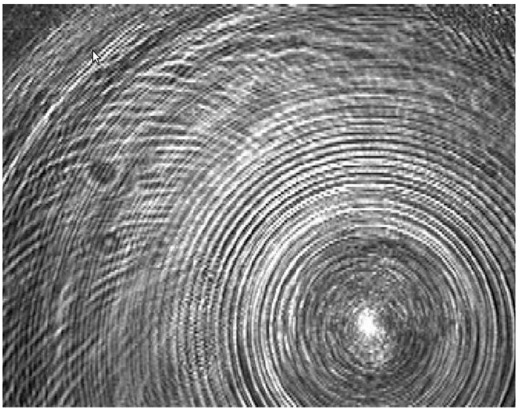

Figure 2.1: Defocused image of a liquid mirror revealing the presence of wavelets on the mercury layer.

and wavelength of $\sim 10^{-6}$ (m) and $\sim 10^{-2}$ (m), respectively[1]. Such wavelets may be avoided thanks to the use of an air bearing system and an increase stiffness of the bowl (in order to increase its eigen frequency). Nevertheless, as their presence reveals a conception and/or a dish stiffness problem, it is important to ensure that they are not present.

Finally, spiral waves are believed to rise because of instability phenomena in the air layer at the interface with the mercury, because of a too high relative velocity between the air and the mercury. Their name is related to their spiral pattern as seen in Fig. 2.1. It is possible to avoid them by covering the rotating mirror with a thin Mylar layer, and thus rotating with the dish. Indeed, the presence of the Mylar captures the air just above the mirror which is thus rotating with the mercury, thus suppressing friction between the air and the mercury.

The typical amplitude and wavelength are of the order of $\sim 10^{-6}$ (m) and $\sim 10^{-2}$ (m), respectively, both increasing with the radius.

Since the different wavelets possibly present on the mercury layer have a different origin, it is important to determine the type of waves present on the dish to be able to avoid them by a appropriate means.

In the framework of this PhD thesis, we have developed a new method to detect and characterise the type of waves possibly present on the mercury layer. This chapter presents a general description of the method and the instruments designed and manufactured to make the measurements. We then present the mathematical modelling necessary to analyse the results and finally present some measurements performed for the ILMT primary mirror.

---

[1] Mulrooney (2000) mentions the presence of concentric waves with a shorter wavelength and a higher frequency ($\sim$ 45 Hz), observed on the NODO. The author has concluded that these waves were due to environmental effects, specific to the telescope location. Consequently, we do not consider these waves in the present work.

2.1.2 General principle

The wave detection principle is represented in Fig. 2.2. A laser beam emitted by a source (on the left hand side) impacts the surface at a given point, with a known incidence angle and is then reflected. The reflected ray position is measured thanks to a detector (on the right hand side of the mirror).

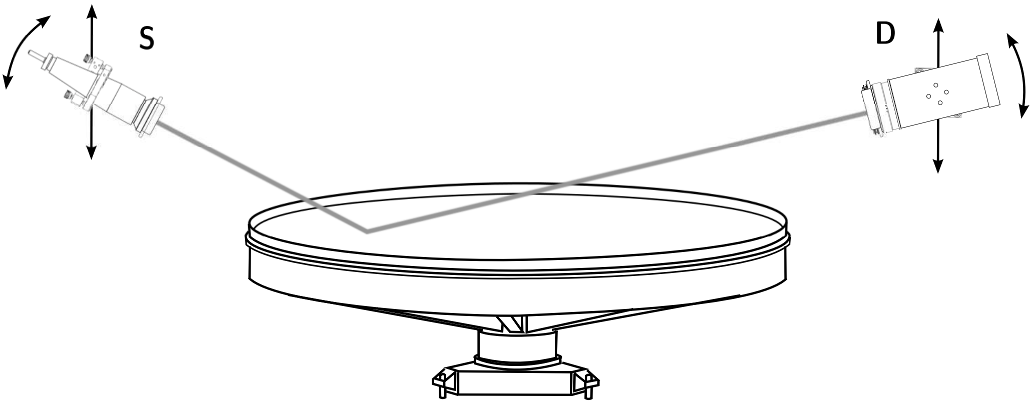

Figure 2.2: Experimental set-up to test the ILMT surface quality using the CCD triangulation technique.

The presence of wavelets at the impact point, modifies the local slope of the mercury layer, which leads to a change in the reflected ray trajectory. By measuring the modification induced to the reflected beam, it is possible to retrieve the wave information at the impact point on the mirror surface.

By changing the height and the angle of the emitted beam, the ray can impact the surface at different radii, allowing to study the wavelet characteristics as a function of the radius. As the mirror is spinning, impacting at a given radius does actually allow to probe a small ring of the mirror.

Both the laser source and the detector are fixed on opposite pillars of the ILMT structure supporting the upper end of the telescope. They are both fixed on a mount enabling a vertical translation and a rotation in a fixed meridian.

In order to differentiate the different types of wavelets, the laser beam section is a horizontal line. Wavelets propagating with different angles relatively to the line-section will induce a different deformation of the line.

During this thesis, we have designed and manufactured the laser source and detector. We describe them in the next sections.

2.1.3 Emitter description

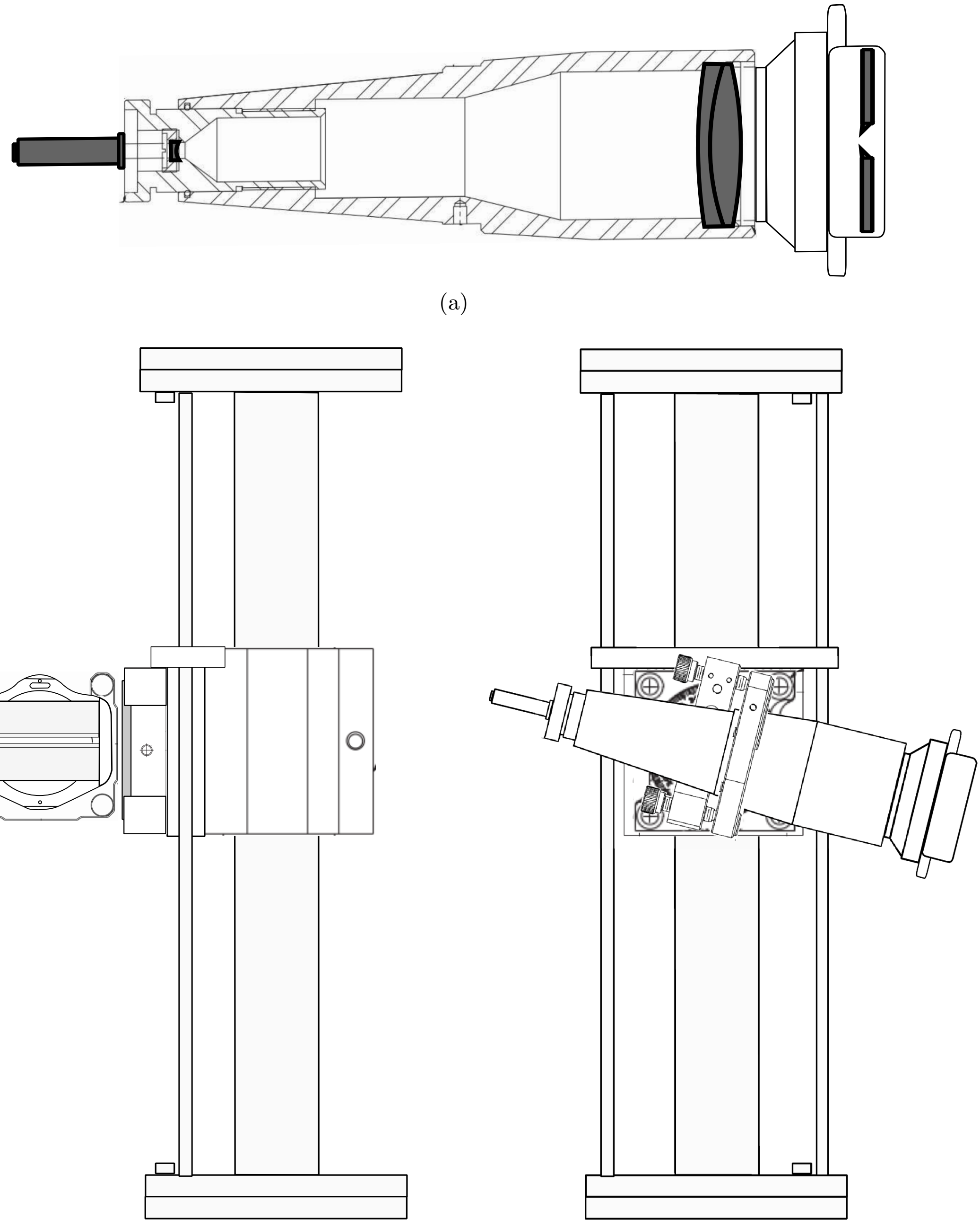
(a)

(b)

Figure 2.3: Conceptual drawing of the emitting system. (a) Internal view of the laser source itself where the important optical elements are shown in dark grey. (b) Front and side views of the laser source and of its mount.

The concept of the laser source and its mount is shown in Fig. 2.3. Fig. 2.3a shows the interior of the laser source where the optical elements are indicated in dark grey. The laser source is composed of a laser pen emitting at 360 nm, a beam expander and two blades spaced by 2 mm. The section of the collimated beam emitted by the laser is expanded while going through the lenses of the beam expander, out of which, the beam is almost collimated. Part of the beam section is then blocked by the two blades. Out of the laser source comes an almost collimated beam, which section is a rectangle with a width of 5 cm and a height of 2 mm.

Due to the intrinsic divergence of the rays, the out-coming beam is slightly divergent. We neglect the beam divergence in the meridional plane of the laser source and the situation in the sagittal plane is shown in Fig. 2.4, where π_e represents the laser source output plane (defined by the two blades).

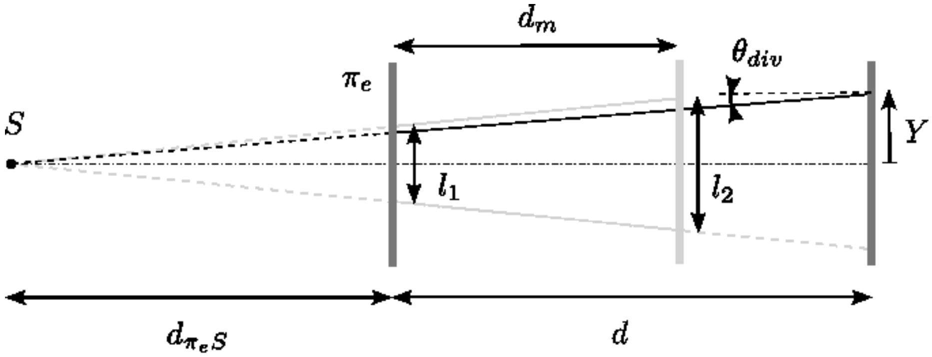

Figure 2.4: Beam divergence in the laser source sagittal plane.

In the sagittal plane, the light rays seem to be emitted by a point-like source S located at a distance $d_{\pi_e S}$ from π_e. To determine the distance of the equivalent source (and thus characterise the beam divergence), we have measured the width of the beam at the output of the laser source ($l_1 = 0.047$ m) and at a distance $d_m = 6.1$ m ($l_2 = 0.068$ m).

A simple geometrical consideration leads to the conclusion that the rays emitted by the laser source could be modelled as coming from a point-like source at a distance $d_{\pi_e}S^2$

$$d_{\pi_e S} = \frac{d_m l_1}{(l_2 - l_1)} = 13.6 \text{ (m)}. \tag{2.1}$$

Furthermore, a ray impacting at a distance d from π_e, and at a distance Y from the optical axis, makes an angle θ_{div} with respect to the optical axis related to $d_{\pi_e S}$

$$\theta_{div}(Y, d) = \arctan\left(\frac{Y}{d_{\pi_e S} + d}\right). \tag{2.2}$$

---

[2] Due to the very large value of $d_{\pi_e S}$ compared to the beam width and for clarity, the scales in Fig. 2.4 are arbitrary.

This relation will be used to calculate the incidence angle of the rays on the mirror surface.

Let us now look at the mount of the laser source. Fig. 2.3b shows the front and side views of the laser source on its mount (on the left and right hand side, respectively). The laser beam section defined by the two blades is clearly visible on the front view.

To allow the laser beam to impact at different radii on the mirror, the laser source is mounted on a vertical translation stage, combined with a rotation stage allowing the laser source to be rotated in a meridian plane.

Finally, to provide a fine adjustment, the beam-expander holder is mounted with three alignment screws (cf. the side view).

2.1.4 Detector description

The concept of the detector is shown in Fig. 2.5a. It is composed of a CMOS detector, a single lens, two linear polarisers, and the housing. The different parts are darkened in the figure.

The CMOS chip is a commercial USB 2.0 CMOS detector manufactured by *The Imaging Source*, with 744 by 480 pixels of 6 by 6 μm. The highest frame rate achievable with the detector composed of 744x480 pixels is 60 Hz[3].

The detector entrance lens is a 75 mm diameter lens with a focal ratio of f/2. Note that, as the incoming laser beam is almost collimated, the CMOS chip is designed to be out of focus: focal length of the lens is 150 mm whereas the distance between the lens and the chip is 159.5 mm. In front of the lens, the two linear polarisers are used to control the flux arriving on the chip, in order to avoid its saturation.

The calibration process and the determination of the characteristics of the detector are presented in Appendix A.

As in the case of the laser source, the detector is mounted on a translation stage coupled with a rotation stage (see Fig. 2.5b). This enables the detector to intercept the reflected rays at different impact radii.

Fig. 2.6 displays a typical frame detected by the CMOS sensor. In this particular case, the laser beam impacted at a distance $r \sim 1.5$ m from the primary mirror rotation axis. During acquisition, the detector thus acquires 60 frames per second similar to that of Fig. 2.6.

In each frame column we detect the photocenter of the signal of the laser beam image. This is done by resampling the vector of the pixel measured flux in the column, and convolving it with a Gaussian kernel having a FWHM equal to that of the flux signal in the column. The photocenter position is determined by the maximum of the convolution.

---

[3] At the time of the purchase, this was the fastest USB detector manufactured by the company. A year later, they sell comparable detectors capable to make data acquisition at 150 Hz. The use of such a camera would result in an improvement of the instrument.

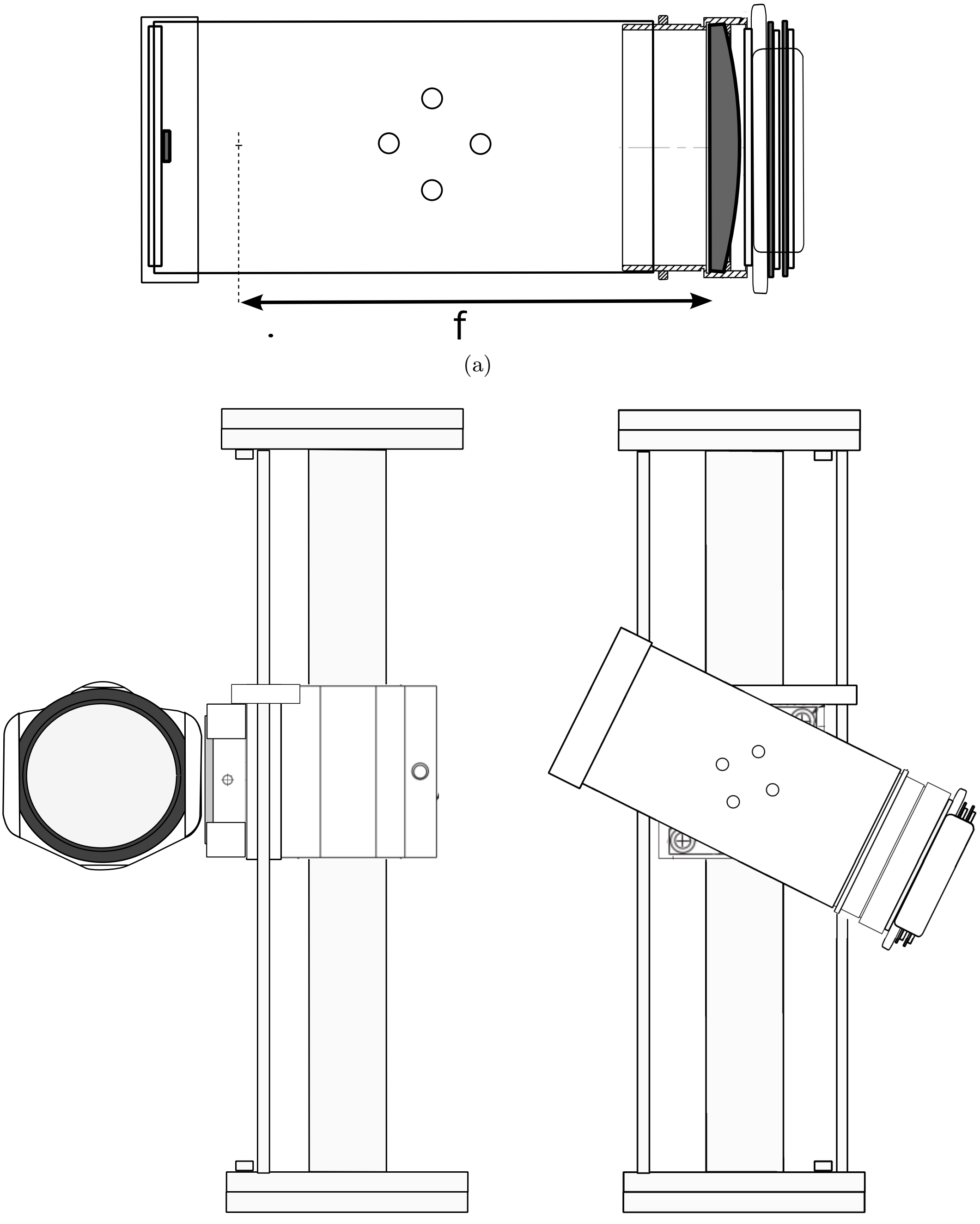

(a)

(b)

Figure 2.5: Conceptual drawing of the detector. (a) Internal view of the detector itself where the CMOS, the lens and the linear polarisers are shown in darker grey. (b) Front and side views of the detector and its holding structure.

Figure 2.6: Typical frame detected by the CMOS sensor. In this case, the laser beam impacts at a distance $r \sim 1.5$ m from the primary mirror rotation axis.

Consequently, in each frame, we detect the laser beam image height as a function of the pixel column index. For each pixel column, we have thus access to the time dependence of the photocenter height.

2.2 Laser ray path equation

Let us now derive the equation governing the path of the rays reflected on the mercury surface. We will proceed by determining the impact point on the mirror, then the reflection angles of the ray and finally, the impact position on the detector lens. We then calculate the intersection of the reflected rays with the detector lens plane, in a reference frame containing the lens plane and centred on the detector optical axis.

2.2.1 Impact point on the mirror surface

In a reference frame centred at the vertex of the parabola, where the z axis coincides with the rotation axis of the mirror (as shown in Fig. 2.7), the paraboloidal surface is defined by

$$z_{paraboloid} = a\left(x^2 + y^2\right), \quad \text{with} \quad a = \frac{1}{4F}, \tag{2.3}$$

where F is the focal distance of the paraboloid.

All emitted rays are contained in a single plane (the laser source sagittal plane). We consider the optical axis of the laser source to be contained in the plane $y = 0$, and we define the angle α between the z axis and the laser source optical axis (as

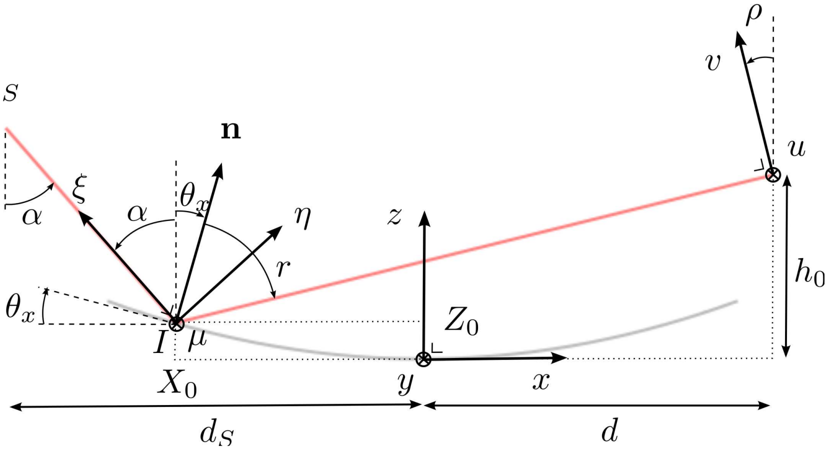

Figure 2.7: Drawing of the laser ray path with the different reference frames.

shown in Fig. 2.7), and $X0$ the x coordinate of the intersection between the laser source optical axis and the mirror surface.

Let us now consider a second orthonormal reference frame (η, μ, ξ), as shown in Fig. 2.7. Its origin is located at the impact point of the optical axis (i.e. the point with coordinates $\left(X_0, 0, aX_0^2\right)$), and the ξ axis is aligned towards the laser source. Coordinates in this reference frame are defined by the change of variables

$$\begin{aligned} \begin{pmatrix} x \\ y \\ z \end{pmatrix} &= \begin{pmatrix} \cos\alpha & 0 & -\sin\alpha \\ 0 & 0 & 0 \\ \sin\alpha & 0 & \cos\alpha \end{pmatrix} \begin{pmatrix} \eta \\ \mu \\ \xi \end{pmatrix} + \begin{pmatrix} X_0 \\ 0 \\ a * X_0^2 \end{pmatrix}, && (2.4) \\ &= \mathcal{R}(\alpha) \begin{pmatrix} \eta \\ \mu \\ \xi \end{pmatrix} + \mathcal{T}, && (2.5) \end{aligned}$$

where we have defined the rotation matrix $\mathcal{R}(\alpha)$ and the translation matrix $\mathcal{T}$.

The equation of the paraboloid in the new reference frame is obtained by inserting the change of variables in the paraboloid equation, and by isolating ξ. This leads to

$$\xi_{1,2} = \frac{\left(2X_0 \sin\alpha + \eta \sin 2\alpha + \dfrac{\cos\alpha}{a}\right)}{2\sin^2\alpha} \pm \frac{\sqrt{R}}{2\sin^2\alpha}, \tag{2.6}$$

with

$$\begin{aligned} R &= \left(2X_0 \sin\alpha + \eta \sin 2\alpha + \frac{\cos\alpha}{a}\right)^2 \\ &\quad -4\sin^2\alpha \left(\eta^2 \cos^2\alpha + 2X_0 \eta \cos\alpha - \eta \frac{\sin\alpha}{a} + \mu^2\right). \end{aligned}$$

In this reference frame the plane defined by the ξ and μ axes corresponds to the laser source sagittal plane. Consequently, the impact points of the laser rays on the mirror are given by Eq. 2.6 where we set $\eta = 0$. This leads to

$$\xi\left(\mu\right) = \frac{\left(2X_0\sin\alpha + \frac{\cos\alpha}{a}\right)}{2\sin^2\alpha} - \frac{\sqrt{\left(2X_0\sin\alpha + \frac{\cos\alpha}{a}\right)^2 - 4\sin^2\alpha\,\mu^2}}{2\sin^2\alpha}. \tag{2.7}$$

Expressing $\xi\left(\mu\right)$ in terms of the (x, y, z) reference frame coordinates thanks to Eq. 2.5, we find the coordinates of the laser impact points $\left(X\left(Y\right), Y, Z\left(Y\right)\right)$ in the reference frame centred on the mirror vertex

$$\begin{aligned} X\left(Y\right) &= X_0 + \frac{1}{2\sin\alpha}\left(\left(-2X_0\sin\alpha + \frac{\cos\alpha}{a}\right)\right. \\ &\left.-\sqrt{\left(-2X_0\sin\alpha + \frac{\cos\alpha}{a}\right)^2 - 4\sin^2\alpha\,Y^2}\right), \qquad (2.8) \\ Y &= Y, \qquad (2.9) \\ Z\left(Y\right) &= aX_0^2 + \frac{\cos\alpha}{2\sin^2\alpha}\left(\left(-2X_0\sin\alpha + \frac{\cos\alpha}{a}\right)\right. \\ &\left.-\sqrt{\left(-2X_0\sin\alpha + \frac{\cos\alpha}{a}\right)^2 - 4\sin^2\alpha\,Y^2}\right). \qquad (2.10) \end{aligned}$$

We have chosen as the affine parameter of the intersection curve, the coordinate Y of the impact point, as measured along the y axis.

2.2.2 Reflected laser rays

Let us now find the incidence angle of the ray impacting at a point labelled by means of its Y coordinate. The projection in the (x, z) plane of any incident laser ray makes an angle α with the vertical (cf. Fig. 2.8a).

In the laser source sagittal plane, using Eq. 2.2, the ray with an impact parameter Y makes an angle $\theta_{div}\left(Y\right)$ with the optical axis given by

$$\theta_{div}\left(Y\right) = \arctan\left(\frac{Y}{d_{\pi_e S} + \frac{d_s + X(Y)}{\sin\alpha}}\right), \tag{2.11}$$

where d_s is the distance from the laser source to the rotation axis of the mirror and $\left(d_s + X\left(Y\right)\right)/\sin\alpha$ represents the distance from the laser source output plane π_e to the impact point, as measured along the laser source optical axis. The projection of the incident ray on the (y, z) plane makes an angle $\delta_y\left(Y\right)$ with the vertical axis (cf. Fig. 2.8b), which is given by the projection of θ_{div} on (y, z), i.e.

$$\delta_y\left(Y\right) = \arctan\left(\frac{\tan\theta_{div}}{\cos\alpha}\right). \tag{2.12}$$

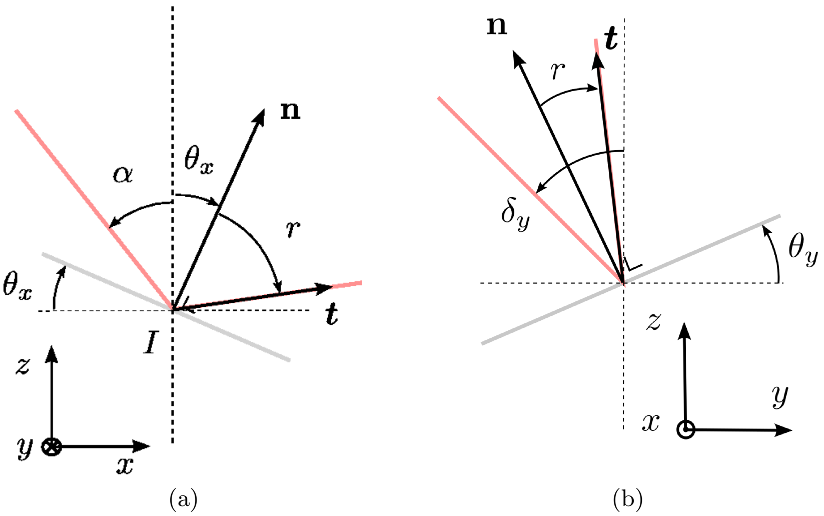

(a) (b)

Figure 2.8: Incidence angle and reflection vector at the impact point, projected on (a) the (x, z) and (b) the (y, z) planes.

Eq. 2.11 and Eq. 2.12 may be linearised with respect to Y, leading to linear expressions

$$\theta_{div}(Y) = \frac{Y}{d_{\pi_e S} + \frac{d_s + X(Y)}{\sin\alpha}}, \tag{2.13}$$

$$\delta_y(Y) = \frac{Y}{\cos(\alpha)\, d_{\pi_e S} + cot(\alpha)(d_s + X_0)}. \tag{2.14}$$

Let us now define the slopes θ_x and θ_y at the impact point on the paraboloid

$$\tan\theta_x = \frac{d}{dx}(z(x, y))\Big|_{x=X(Y), y=Y} \tag{2.15}$$

$$\tan\theta_y = \frac{d}{dy}(z(x, y))\Big|_{x=X(Y), y=Y} \quad , \tag{2.16}$$

where $z(x, y)$ is defined by means of Eq. 2.3. From Fig. 2.8a and Fig. 2.8b, as we know the expressions of δ_y, θ_x and θ_y, the application of the reflection law allows to find the unitary director vector $\boldsymbol{t}$ of a reflected ray parametrised by Y. We find

$$\boldsymbol{t} = \frac{(\tan(\alpha - 2\theta_x), -\tan(2\theta_y - \delta_y), 1)}{\sqrt{\tan(\alpha - 2\theta_x)^2 + \tan(2\theta_y - \delta_y)^2 + 1}}, \tag{2.17}$$

where θ_x and θ_y are evaluated at the impact point $(X(Y), Y, Z(Y))$.

In the matrix formalism, the equation of a reflected ray parametrised by Y is thus given by

$$\begin{pmatrix} x \\ y \\ z \end{pmatrix} = \begin{pmatrix} X(Y) \\ Y \\ Z(Y) \end{pmatrix} + k\,\boldsymbol{t}, \tag{2.18}$$

where k is the affine parameter of the ray impacting at the point with the coordinates (X, Y, Z).

2.2.3 Laser ray impact in the lens plane

We define the detector lens position such as its optical axis coincides with the reflected ray impacting at $(X_0, 0, Z_0)$ (cf. Fig. 2.7). Let us assume that the detector is located at a distance d from the paraboloid axis of rotation.

Inserting the impact coordinates $(X_0, 0, Z_0)$ in the reflected ray equation, and fixing $x = d$, we find the height h_0 of the reflected ray impact

$$h_0 = Z_0 + (d - X_0)\,\cot(\alpha - 2\theta_{X_0}). \tag{2.19}$$

We consider the detector lens to be centred on this position. Furthermore, the lens plane has to be perpendicular to the reflected ray that impacted the surface of the mirror at X_0. Consequently, from Fig. 2.7, simple geometrical arguments lead to an inclination angle ρ of the detector equal to

$$\rho = \arctan\left(\frac{h_0 - aX_0^2}{d - X_0}\right). \tag{2.20}$$

Let us now find the impact coordinates of a ray in the lens plane. As we know the height of the lens center (Eq. 2.19) and the inclination of the lens plane (Eq. 2.20), we can determine the plane equation of the detector first lens, which is given by

$$x = d - \tan\rho\,(z - h_0). \tag{2.21}$$

Combining the definition of the detector lens plane in Eq. 2.21 with the first relation of Eq. 2.18 of the reflected ray trajectories, and isolating the ray affine parameter k, leads to

$$k = \frac{1}{t1}\left(d - X(Y) - \tan(\rho)\,(z - h_0)\right), \tag{2.22}$$

where t_1 is the first component of the normalised directing vector $\boldsymbol{t} = (t_1, t_2, t_3)$ of the reflected ray, given by Eq. 2.17.

Inserting Eq. 2.22 into the two last relations of Eq. 2.18, we find the impact point coordinates on the lens plane

$$\begin{cases} y = Y + \dfrac{t2}{t1}\left(d - X(Y) - \tan(\rho)\,(z - h_0)\right), \\ \\ z = Z(Y) + \dfrac{t3}{t1}\left(d - X(Y) - \tan(\rho)\,(z - h_0)\right). \end{cases} \tag{2.23}$$

We now introduce the new variables (u, v) defined as

$$\begin{aligned} u &= y, \\ v &= \frac{z - h_0}{\cos(\rho)}. \end{aligned}$$

(u, v) are the coordinates of the impact points as measured in the lens plane (see Fig. 2.7). The reference frame is centred on the intersection of the optical axis (the ray impact on the mirror in the $y = 0$ plane) with the lens plane. u and v are the coordinates as measured in the detector sagittal and meridional planes, respectively. Introducing (u, v) and the expressions of t_1, t_2 and t_3 in Eq. 2.23, we find

$$u = Y - \tan(2\theta_y - \delta_y) \frac{(d - X) + (h_0 - Z)\tan(\rho)}{\tan(\alpha - 2\theta_x) + \tan(\rho)}, \tag{2.24}$$

$$v = \frac{(d - X)\cos(\alpha - 2\theta_x) + (Z(Y) - h_0)\sin(\alpha - 2\theta_x)}{\sin(\rho + \alpha - 2\theta_x)}. \tag{2.25}$$

The former expression of (u, v) can be linearised by neglecting in Eq. 2.10 the Y^2 term in the square root, and by using the linearised expression of δ_y (Eq. 2.14) in order to obtain a linear expression of $\tan(2\theta_y - \delta_y)$, relatively to Y, i.e.

$$\tan(2\theta_y - \delta_y) = P\,Y, \tag{2.26}$$

with

$$P = 4a - \frac{1}{\cos(\alpha)\, d_{\pi_e S} + \cot(\alpha)\,(d_s + X_0)}. \tag{2.27}$$

Furthermore introducing the expression of h_0, we find the linear expression for (u, v)

$$\begin{cases} u = S\,Y, \\ v = 0, \end{cases} \tag{2.28}$$

where we have defined

$$S = 1 - P\left(\frac{(d - X) - (Z_0 - h_0)\tan(\rho)}{\tan(\alpha - 2\theta_x) + \tan(\rho)}\right). \tag{2.29}$$

In this linearised form, the reflected beam impacts the lens plane on a horizontal line, passing through the lens center. In the sagittal plane, as the relation between the impact coordinate on the mirror Y and the one on the lens (u) is linear, this means that the coordinates measured on the lens plane are a simple scaling of the ones measured on the mirror. For information, in our case, the scaling factor S for an impact radius of 1.5 m of the mirror is $S \sim 1.05$. Thanks to this linear relation, in the sagittal plane, light rays impacting the lens appear to emanate from a single point source. For an impact radius of 1.5 m, the distance is of the order $d_S \sim 100m^4$.

---

[4] The determination of d_S is presented in Appendix A.

2.2.4 Wavelet effect

In the remainder, we assume that the effects of the wavelets only consist in a slope variation at the impact point on the mirror, i.e. we assume that the modification of the impact point position due to the presence of the wavelets is negligible because of the small amplitude of the wavelets ($A \sim 10^{-6}$ m). So the wavelet induces a local slope variation

$$\theta_x \mapsto \theta_x + \Delta\theta_x, \tag{2.30}$$

$$\theta_y \mapsto \theta_y + \Delta\theta_y. \tag{2.31}$$

Inserting these expressions in the non-linearised set of equations 2.28 for (u, v), one finds

$$u = Y - \tan(2\theta_y + 2\Delta\theta_y - \delta_y)\frac{(d - X) + (h_0 - Z)\tan(\rho)}{\tan(\alpha - 2\theta_x - 2\Delta\theta_x) + \tan(\rho)}, \tag{2.32}$$

$$v = \frac{(d - X)\cos(\alpha - 2\theta_x - 2\Delta\theta_x) + (Z(Y) - h_0)\sin(\alpha - 2\theta_x - 2\Delta\theta_x)}{\sin(\rho + \alpha - 2\theta_x - 2\Delta\theta_x)}. \tag{2.33}$$

This expression can be linearised relatively to the slope perturbations $\Delta\theta_x$ and $\Delta\theta_y$. Furthermore, assuming the same linearisation as for the unperturbed case (and after some algebra), we find

$$\begin{aligned} u &= SY - 2\Delta\theta_y \frac{(d - X_0) + (h_0 - Z_0)\tan(\rho)}{\tan(\alpha - 2\theta_{x_0}) + \tan(\rho)} \\ &\quad -2\Delta\theta_x PY \frac{(d - X_0)\cos^2(\rho) + (Z_0 - h_0)\cos(\rho)\sin(\rho)}{\sin^2(\rho + \alpha - 2\theta_{x_0})}, \end{aligned} \tag{2.34}$$

$$v = 2\Delta\theta_x \frac{(d - X_0)\cos(\rho) - (Z_0 - h_0)\sin(\rho)}{\sin^2(\rho + \alpha - 2\theta_{x_0})}. \tag{2.35}$$

These relations lead to the impact coordinates of the laser rays on the lens (expressed in the lens plane coordinate system), as a function of the slope modification $\Delta\theta_x$ and $\Delta\theta_y$ induced by the wavelets at the impact point.

One very interesting result is that the v coordinate (i.e. the height as measured on the lens plane) is a linear function of the slope variation $\Delta\theta_x$ along the x direction. Furthermore, the coefficient of proportionality is entirely determined by the geometrical characteristics of the ray impacting the $y = 0$ plane (i.e. the equation of the optical axes of the laser source and detector).

Let us now assume that a wavelet is propagating at the impact line of the laser beam. Locally, we model the wave as a plane sinusoidal wave propagating on a plane. If we assume that the wave front, characterised by the wave number k and a frequency ω, is propagating along a direction forming an angle β with the x direction, then its equation is

$$z = A\sin(k(x\cos\beta + y\sin\beta) - \omega t). \tag{2.36}$$

Consequently, the equation of the Hg surface is, locally,

$$z = a\left(x^2 + y^2\right) + A \sin\left(k\left(x\cos\beta + y\sin\beta\right) - \omega t\right), \tag{2.37}$$

and the local slope variation in the x direction $\Delta\theta_x$ due to the wavelets is given by

$$\begin{aligned}\tan\left(\theta_X + \Delta\theta_x\right) &= \left.\frac{dz\left(x,y\right)}{dx}\right|_{x=X,y=Y}, & (2.38)\\ &= 2AX + Ak\cos\beta\sin\left(k\left(X\cos\beta + Y\sin\beta\right) - \omega t\right), & (2.39)\\ &\simeq \tan\theta_X + \frac{1}{\cos^2\theta_X}\Delta\theta_X. & (2.40)\end{aligned}$$

Similarly, we find the expression of $\Delta\theta_y$. We thus obtain for the slope variation

$$\begin{aligned}\Delta\theta_x &= \cos^2\theta_X Ak\cos\beta\cos\left(k\left(X\cos\beta + Y\sin\beta\right) - \omega t\right), & (2.41)\\ \Delta\theta_y &= \cos^2\theta_Y Ak\sin\beta\cos\left(k\left(X\cos\beta + Y\sin\beta\right) - \omega t\right). & (2.42)\end{aligned}$$

A wavelet propagating along the impact line of the laser beam on the mirror thus creates a slope modulation $\Delta\theta_x$ that oscillates with time. Consequently, through Eq. 2.35, this leads to an oscillation of the impact coordinate v on the lens.

By measuring the amplitude of the vertical oscillation on the lens, we may derive the value of $Ak\cos\beta$.

Furthermore, we have seen that the average impact line on the detector lens plane (i.e. that of the unperturbed case) is a simple scaling of the intersection line on the mirror. When the wavelets propagate along the impact line on the mirror, the same oscillation is imposed to every point of the line, with a phase difference that varies linearly (in our linear approximation) with the impact parameter Y. Consequently, on the lens plane, the phase of the signal varies proportionally to $SYk\sin\beta$.

For a concentric wavelet, $\beta = 0$ and all points on the line oscillate in phase. The impact of a concentric wavelet is thus an horizontal oscillation of the whole impact line on the detector. For a spiral wave, $\beta \neq 0$ and the different points of the impact line oscillate with a phase difference.

2.3 Measurements

Series of measurements were conducted on the primary mirror of the ILMT, using the instruments and method previously described. These tests were performed in the workshop of the AMOS company.

Prior to the tests, we have determined sets of laser source heights and emitting angles α (as well as the corresponding detector positions and angle ρ) allowing the beam to impact at various mirror radii, ranging from 0.2 to 1.6 m.

For each impact radius, we have recorded several 60 fps videos (of frames similar to that in Fig. 2.6), each one composed of 600 frames (~ 10 seconds). To characterise potential lower frequency signals in the reflected beam oscillations, a couple of longer videos (1800 frames) were acquired as well.

For each video frame, we then detected the beam line photocenter as a function of the pixel column coordinate x_d. These measured coordinates were then mapped to the corresponding impact positions on the detector lens. This mapping was done, as mentioned previously, using the CMOS-to-lens mapping relation derived in Appendix A.

The (u, v) coordinates obtained for each frame were then re-sampled in a regular grid with respect to the u coordinate.

Fig. 2.9 shows the time dependence of the v coordinate (i.e. the oscillation amplitude) for each value of u (i.e. the distance to the optical axis, as measured in the lens sagittal plane). The black/grey/white map indicates the amplitude of the oscillation expressed in meters. This map is part of a 30 second video acquired for an impact radius of 1.5 m.

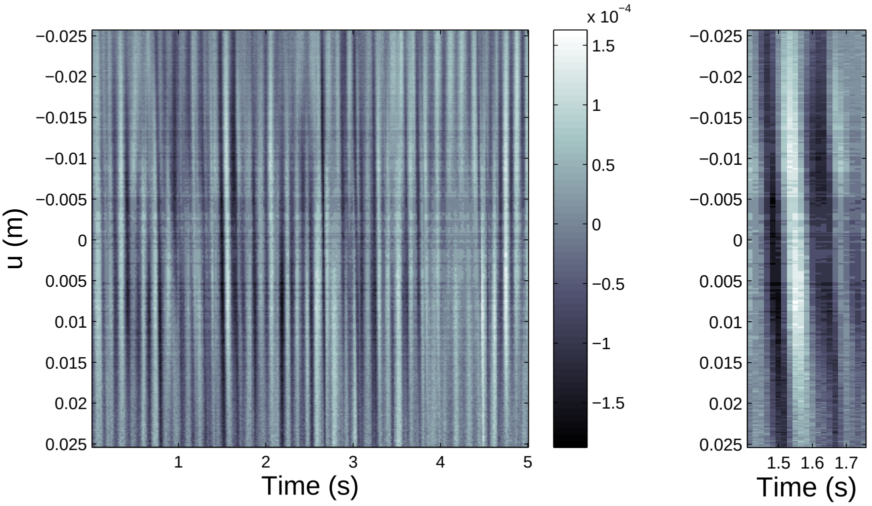

Figure 2.9: Time behaviour of the impact height v in the lens plane for each value of u. The black/grey/white scale expresses the v coordinates in meter.

We have seen that the impact of a concentric wavelet (with a wave-front being parallel to the impact line of the laser on the mirror) is an overall oscillation of the line impacting the lens. In other words, the oscillations for all values of u are co-phased. Consequently, in Fig. 2.9, a concentric wave would lead to oscillations marked as exactly vertical lines, i.e. lines of constant height, and thus of constant grey level. A close visual inspection of the figure shows that this is not the case. All the lines defined by a same grey level are slightly inclined with respect to the vertical direction in the figure. To see this inclination more clearly, on the right hand side of the figure, we have reproduced part of the data with an enlarged time scale, on which we can clearly see the slight inclination of the lines. A close visual inspection of all videos leads to the same conclusion. Consequently, this tends to show the absence of concentric wavelets on the mirror.

All wave-fronts thus propagate along the impact line on the mirror with an angle β. Furthermore, there is a seemingly periodic signal in the oscillation.

To further analyse the wavelets present and isolate their apparent frequency, we used the Fourier transform of the photocenter time oscillation in meridian planes. A periodic wave propagating (with an angle) across the impact line of the laser beam on the mirror, will induce a periodic oscillation of the impact points on the lens plane. Each point with a coordinate u on the lens will have the same signal, but with a different phase. Consequently, if we calculate the Fourier transform of the height oscillation as a function of time, for each coordinate u, the absolute value of all these Fourier transforms will have a peak at the apparent frequency of the propagating wavelet (although its complex component will differ).

To try to increase the Signal-to-Noise ratio of these peaks, we decided to analyse average values of the Fourier transform modulus along the impact line on the lens.

The resulting average Fourier transform modulus is shown as a function of the frequency, in Fig. 2.10a.

We see the presence of several peaks at a frequency close to ~ 8 Hz, which are the signature of the seemingly periodic oscillation observed in Fig. 2.9.

As mentioned earlier, the test procedures were carried out in the workshop of the private company AMOS. Because of health concern issues for the workers in the workshop, these tests could not be carried out freely in the company and had to be performed under severe time constraints.

Furthermore, to avoid the contamination of the workshop by mercury vapours, the telescope tower was surrounded by a plastic cover, aimed to contain the mercury vapours around the mirror. Although working with specific gas masks while being around the mirror, the mercury vapours had to be extracted from this plastic tent, in order to guarantee a mercury vapour concentration lower than a critical value.

The mercury vapour extraction was done with an industrial fan, attached to the telescope tower, close to the mirror. This fan was noticed to induce perturbations on the mirror mercury layer, as will be shown in the following. Nevertheless, stopping the fan for a too long period led to an increase of the mercury vapours, quickly getting above the security threshold of the mask.

Consequently, very few measurements were carried out without the fan.

Fig. 2.10 shows the spectra acquired at a same impact radius, with an increasing ventilation (v= 0, 1 and 2 in figure a, b and c, respectively). We clearly see that the ventilation results in a dramatic drop of the Signal-to-Noise ratio of the observed peaks, and leads to the appearance of numerous secondary peaks.

This tends to indicate that the fan induces wavelets on the mercury. Nevertheless, part of this parasite signal may be due to vibrations transmitted to the

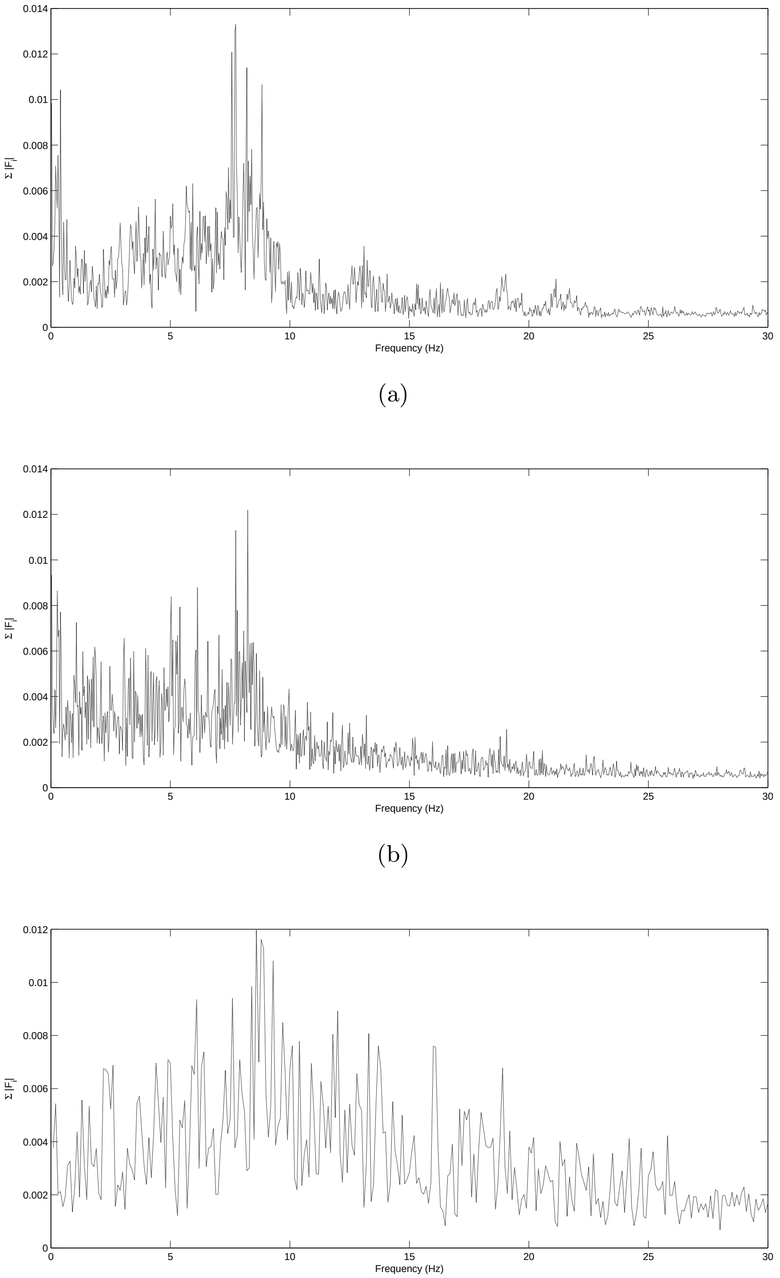

(a)

(b)

(c)

Figure 2.10: Average modulus of the Fourier of the height v as a function of time. The different spectra correspond to cases with (a) no fan, (b) low fan level and (c) a higher fan level.

detector directly by means of the telescope tower (as the fan was attached to it).

Fig. 2.10c corresponds to the spectrum for a 10 second video. This shorter recording results in a loss of Fourier frequencies probed, and the peak corresponding to the spiral waves is almost not detectable anymore. About 95 % of the recorded videos during the test sessions are of this third type, thus highly reducing the usefulness of the measurements.

Nevertheless, the fact that the frequency where the peaks are located in Fig. 2.10a still presents an excess in Fig. 2.10b and c, indicates that the spiral pattern responsible for this signature is still present.

A first conclusion of these tests is that the on-site facility and testing will require to minimize at maximum environmental induced vibrations.

Another interesting point is the position of the peaks at $\sim$ 8 Hz. Indeed, spiral waves are quasi-stationary waves in the rotating reference frame attached to the mercury. If λ is the wavelength of the spiral wave and β the angle between its wave-fronts and the laser beam impact line on the mirror, then the apparent wave length along the impact line is

$$\lambda_{ap} = \lambda \sin{(\beta)} \, .$$

For a given radius r of impact of the laser on the mercury, the propagation speed of the wave is given by the azimuthal speed of the mercury

$$v = r\omega_{mirror},$$

where $\omega_{mirror} = 0.78$ (rad s^{-1}) is the angular rotation speed of the mirror. Consequently, the apparent frequency of the wave on the detector is

$$\nu_{ap} = \frac{v}{\lambda_{ap}} = \frac{\sin{(\beta)}\, r\omega_{mirror}}{\lambda}.$$

Due to the spiral wavelet characteristics, we expect a rather high frequency signature ($\gtrsim$ 20 Hz), but the observed frequency is about $\sim$ 8 Hz. This is thus an argument in favour of the fact that the signal is undersampled.

The highest frequency being imaged by the detector is its Nyquist frequency $\nu_{Nyq} = 30$Hz. Consequently, the limiting criterion on the accessible wavelengths is given by ensuring that the apparent frequency ν_{ap} is lower than the Nyquist frequency ν_{Nyq}. This gives

$$\lambda \geq \frac{\sin\beta r \, \omega_{mirror}}{\nu_{Nyq}}.$$

For an apparent frequency higher (or a shorter apparent wavelength) the signal will be under-sampled. Fig. 2.11 shows the accessible wavelength regime as a function of the β angle, for different impact points.

Thus, as the apparent frequency of the spiral wavelet is low, on-site testing of the mirror will necessitate the acquisition of longer videos, in order to better probe the low frequency regime of the line oscillations.

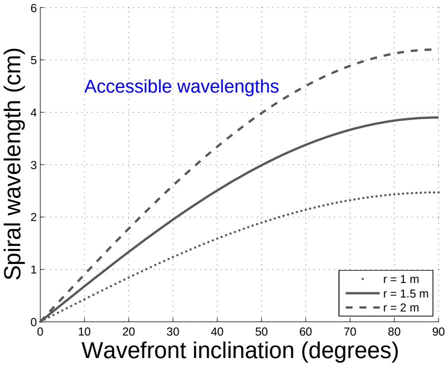

Figure 2.11: Accessible wavelength as a function of the β angle, for different impact points. In the accessible part, the wavelets are sufficiently well sampled by the camera.

Another possible improvement would be the use of the new camera generation of the *Imaging source* company, capable of imaging at 150 fps.

Although the results of these first tests are quite limited because of the rather hostile environment existing during the measurements, we may however conclude that these first tests allowed the detection of the spiral wavelets and the differentiation between the wavelet types.

Furthermore, we have seen that the transmission of vibration to the mirror from the environment generates vibration on the mercury. As these will affect the optical quality of the primary mirror, it will be mandatory to avoid all vibration sources on the ILMT site.

Furthermore, we have proven that the instrument is now ready for on site testing and optimisation of the ILMT primary mirror and that we will benefit from the conclusions of these first tests to improve the sensitivity of the instrument, by the acquisition of longer videos to better sample the lower frequency range and/or by the use of a CMOS detector capable of higher frequency imaging.

Part II

ILMT observations of multiply imaged quasars

Chapter 3

Gravitational lensing theory

The ILMT has been designed to perform a photometric variability survey of a narrow strip of sky, making it very suitable for the detection and follow-up of photometrically variable sources such as supernovae and quasars.

In the second part of this thesis, we present an estimate of the number of QSOs to be detected within the ILMT survey, and of the expected number of multiply imaged sources among these caused by the presence of a deflector near their lines-of-sight.

In Chapters 3 and 4, we introduce the different tools necessary to the study of the gravitational lensing phenomenon and its statistical aspects. We then estimate the population of QSOs to be detected with the ILMT and apply these different tools to the simulated catalogue, in Chapter 5 and 6, respectively. We study the impact of various parameters on the expected number of detected gravitational lens systems, such as the instrumental resolution of the telescope, the galaxy population type(s) and corresponding lensing model(s), and the cosmological parameters.

The statistical sample of multiply imaged QSOs detected with the ILMT is intended to be used as a cosmological probe. In order to make a sensitivity comparison between various modelling approaches, in Chapter 7, we introduce a new formalism to estimate the lensing probabilities, allowing us to compare the sensitivity, as a function of the cosmological mass density, of the average optical depth over the detected QSOs, and those of the deflector and the lensed source redshift distributions.

3.1 Basic theory of gravitational lensing

Deflection angle

General Relativity predicts that a light ray undergoes deflection in a gravitational field.

Let us consider a light ray propagating along a straight line, encountering the most simple mass distribution imaginable: a point-like mass. The situation is depicted in Fig. 3.1. Due to the presence of the point-like object with a mass M, the light ray is deflected by an angle

$$\boldsymbol{\alpha} = -\frac{4GM}{c^2}\frac{\boldsymbol{b}}{b^2}, \tag{3.1}$$

where G represents the Cavendish gravitational constant, c is the light velocity and $\boldsymbol{b}$ the impact parameter vector of the light ray in the plane containing the point-like mass, perpendicular to the incoming light ray.

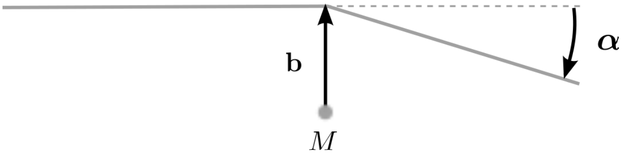

Figure 3.1: Light ray deflection due to a point-like object with a mass M.

Following the approach of Kochanek et al. (2005), let us now consider a light ray passing through a three-dimensional mass distribution with volume density ρ. The field equations of General Relativity can be linearised if the gravitational field is weak. The deflection angle of an ensemble of mass points is then the sum of the deflections due to the individual mass components.

The light ray's spatial trajectory is described by $(b_1(\lambda), b_2(\lambda), r_3(\lambda))$, where λ is the ray affine parameter. The coordinates are chosen such that, far from the mass distribution, the incoming light ray propagates along r_3.

The light ray is deflected by the mass distribution. If the size of the mass distribution is negligible compared to the considered light ray path length, we can use the *geometrically-thin lens* approximation. This implies that we consider all the mass contained in the plane passing through the center of the mass distribution, perpendicular to the direction r_3. Furthermore, the deflection of the ray is supposed to take place when the ray hits the deflector plane.

If we define the impact parameter vector $\boldsymbol{b}(\lambda) = (b_1(\lambda), b_2(\lambda))$ of the light ray with respect to the center of the mass distribution, the geometrically-thin lens approximation implies $\boldsymbol{b}(\lambda) \simeq \boldsymbol{b}$, i.e. the impact parameter is independent of the affine parameter λ.

The deflection angle $\boldsymbol{\alpha}$ due to the mass distribution is obtained by adding the contribution of all the mass elements in the distribution. Thus, the total deflection angle $\boldsymbol{\alpha}(\boldsymbol{b})$ as a function of the impact parameter is

$$\boldsymbol{\alpha}(\boldsymbol{b}) = -\frac{4G}{c^2}\int d\boldsymbol{b'}\int dr'_3 \rho\left(b'_1, b'_2, r'_3\right)\frac{\boldsymbol{b}-\boldsymbol{b'}}{|\boldsymbol{b}-\boldsymbol{b'}|^2}.$$

$\boldsymbol{b}$ is a two dimensional vector. Since the impact parameter is independent of r_3, we can perform the integration of the mass density ρ over r_3. We define the *surface mass density* $\Sigma(\boldsymbol{b})$ as

$$\Sigma(\boldsymbol{b}) = \int dr'_3 \rho\left(b_1, b_2, r'_3\right).$$

$\Sigma(\boldsymbol{b})$ is thus the mass density projected onto the plane perpendicular to the incoming light ray. The expression of the deflection angle produced by the total mass distribution becomes

$$\boldsymbol{\alpha}(\boldsymbol{b}) = -\frac{4G}{c^2}\int d\boldsymbol{b'}\Sigma\left(\boldsymbol{b'}\right)\frac{\boldsymbol{b}-\boldsymbol{b'}}{\left|\boldsymbol{b}-\boldsymbol{b'}\right|^2}. \tag{3.2}$$

Eq. 3.2 thus permits to calculate the deflection angle induced by any known mass distribution.

Deflection potential

The deflection angle may be expressed as deriving from a potential ψ. Using the identity $\bigtriangledown \ln|\boldsymbol{b}| = \boldsymbol{b}/|\boldsymbol{b}|^2$ valid for any two-dimensional vector, Eq. (3.2) may be writen as

$$\boldsymbol{\alpha}(\boldsymbol{b}) = -\bigtriangledown\psi, \tag{3.3}$$

where

$$\psi = \frac{4G}{c^2}\int d\boldsymbol{b'}\Sigma\left(\boldsymbol{b'}\right)\ln\left|\boldsymbol{b}-\boldsymbol{b'}\right| \tag{3.4}$$

is called the *deflection potential.*

Furthermore, using the identity[1] $\bigtriangledown^2 \ln|\boldsymbol{b}| = 2\pi\delta_D(\boldsymbol{b})$ and the definition of the deflection potential from Eq. 3.4, one can show that ψ satisfies the Poisson equation

$$\bigtriangledown^2\psi = \frac{8\pi G}{c^2}\Sigma(\mathbf{b}). \tag{3.5}$$

Lens equation

Let us now consider an observer (O), a source (S) and a mass distribution acting as a deflector (D), as shown in Fig. 3.2. Light rays emitted from the background source are deflected by an angle $\boldsymbol{\alpha}$ due to the presence of the foreground deflector. Consequently, from the point-of-view of the observer, the position of the image (I) is displaced by the angle $\boldsymbol{\theta}-\boldsymbol{\theta}_s$ with respect to S.

From Fig. 3.2, it is straightforward to derive the relationship between the angular position $\boldsymbol{\theta}_s$ of the source and that of the image $\boldsymbol{\theta}$, measured relatively to

---

[1] This identity can be demonstrated by considering the integral

$$I = \int_{|\boldsymbol{b}|\le R} \bigtriangledown^2 \ln|\boldsymbol{b}|\, d\boldsymbol{b},$$

with $R \geq 0$ and by using the Green theorem in 2 dimensions to show that

$$\begin{aligned} I &\to 0 &&, \text{if } |\boldsymbol{b}| < R \quad \text{and} R \to 0 \\ I &\to 2\pi &&, \text{if } |\boldsymbol{b}| = R \quad \text{and} R \to 0. \end{aligned}$$

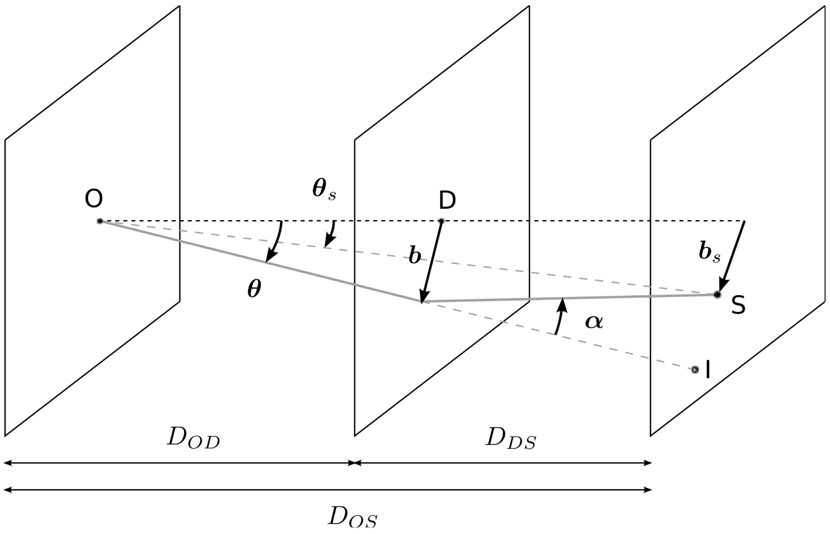

Figure 3.2: Illustration of the gravitational lensing phenomenon.

the deflector center D. We find

$$\boldsymbol{\theta}_s = \boldsymbol{\theta} + \frac{D_{DS}}{D_{OS}} \boldsymbol{\alpha} \left(D_{OD} \boldsymbol{\theta} \right), \tag{3.6}$$

where D_{OD}, D_{DS} and D_{OS} are the different angular distances between O, D and S. Eq. 3.6 expresses the angular position of the source as a function of the angular position of the lensed image(s) as seen by the observer; it is the *lens equation* in terms of angular coordinates.

Multiplying Eq. 3.6 by D_{OS} and introducing the impact parameter vector $\boldsymbol{b} = \boldsymbol{\theta} D_{OD}$ and the source position relatively to the optical axis $\boldsymbol{b}_s = \boldsymbol{\theta}_s D_{OS}$, the lens equation can be expressed in terms of physical distances defined in the source and in the deflector plane

$$\boldsymbol{b}_s = \frac{D_{OS}}{D_{OD}} \boldsymbol{b} + D_{DS} \boldsymbol{\alpha} \left(\boldsymbol{b} \right). \tag{3.7}$$

If the deflection angle $\boldsymbol{\alpha}(\boldsymbol{b})$ induced by a given mass distribution is known, the inversion of Eq. 3.6 or Eq. 3.7 allows to calculate the position of the lensed image(s) formed due to the presence of the deflector near the line-of-sight of the background source.

Adimensional formalism

In the lens Eq. 3.7, we can introduce the normalized variables $\boldsymbol{x}$ and $\boldsymbol{y}$

$$\boldsymbol{x} = \frac{\boldsymbol{b}}{b_0} \tag{3.8}$$

$$\boldsymbol{y} = \frac{\boldsymbol{b}_s}{b_0} \frac{D_{OD}}{D_{OS}}, \tag{3.9}$$

where b_0 is a scaling factor corresponding to the Einstein radius $b_0 = \theta_E D_{OD}$. In this formalism, $\boldsymbol{x} = (x_1, x_2)$ is a two dimensional vector giving the position of the lensed image in the deflector plane, normalized to the Einstein radius or, equivalently, the angular position of the image, expressed in units of the Einstein angular radius θ_E. $\boldsymbol{y} = (x_1, x_2)$ is a vector giving the position of the source, projected on the deflector plane, normalized to the Einstein radius.

Injecting the new variables $\boldsymbol{x}$ and $\boldsymbol{y}$ in Eq. 3.7, we obtain the expression of the dimensionless gravitational lens equation

$$\boldsymbol{y} = \boldsymbol{x} + \hat{\boldsymbol{\alpha}}\left(\boldsymbol{x}\right), \tag{3.10}$$

with the adimensional angle of deflection $\hat{\boldsymbol{\alpha}}$ given by

$$\hat{\boldsymbol{\alpha}} = \boldsymbol{\alpha}\left(b_0 \boldsymbol{x}\right) \frac{D_{OD} D_{DS}}{b_0 D_{OS}}. \tag{3.11}$$

$\hat{\boldsymbol{\alpha}}$ now derives from the adimensional deflection potential $\hat{\psi}\left(\boldsymbol{x}\right)$, i.e.

$$\hat{\boldsymbol{\alpha}} = -\bigtriangledown_{\boldsymbol{x}} \hat{\psi}\left(\boldsymbol{x}\right), \tag{3.12}$$

with $\hat{\psi}\left(\boldsymbol{x}\right)$ being linked to the deflection potential ψ introduced in Eq. 3.4 by

$$\hat{\psi}\left(\boldsymbol{x}\right) = \frac{D_{OD} D_{DS}}{D_{OS} b_0^2} \psi\left(\boldsymbol{x}\right). \tag{3.13}$$

The Poisson equation linking the adimensional deflection potential to the surface mass density is

$$\begin{aligned} \bigtriangledown^2 \hat{\psi} &= 2\kappa, \qquad (3.14) \\ \text{where} \quad \kappa &= \frac{\Sigma\left(b_0 \boldsymbol{x}\right)}{\Sigma_{crit}} \\ \text{and} \quad \Sigma_{crit} &= \frac{c^2 D_{OS}}{4\pi G D_{DS} D_{OD}}. \end{aligned}$$

In the following, unless mentioned otherwise, we exclusively use the adimensional formalism and we omit the ˆ sign on the variables.

To summarise, considering a deflector with a surface mass density κ, we may determine the deflection potential through Eq. 3.14, and the deflection angle using Eq. 3.12. Once the expression of the deflection angle is known, we can determine the position of the observed images of the background source for a given source position by inverting the lens Eq. 3.10.

Amplification, caustics and critical curves

A beam of light emitted within a given solid angle around the source position is distorted through the lensing event and appears distorted around the image position because of the differential deflection. If the images are resolved, this distortion may be observed. When the image is unresolved, because the specific intensity of the source is preserved (Etherington (1933)), the ratio between the solid angles covering the lensed images and the source leads to an apparent amplification A of the images, given by the ratio of the solid angles.

The lens Eq. 3.10 defines a univocal change of variables $\mathbf{x} \mapsto \mathbf{y}$. The amplification $A(\boldsymbol{x})$ of the images is given by the inverse of the determinant of the Jacobian matrix $\mathcal{A}$, called for this reason the **amplification matrix**

$$A(\boldsymbol{x}) = (\det \mathcal{A})^{-1} . \tag{3.15}$$

The amplification matrix $\mathcal{A}$ is given by

$$\mathcal{A} = \begin{pmatrix} \frac{\partial y_1}{\partial x_1} & \frac{\partial y_1}{\partial x_2} \\ \frac{\partial y_2}{\partial x_1} & \frac{\partial y_2}{\partial x_2} \end{pmatrix} = \begin{pmatrix} 1 - \frac{\partial^2 \psi}{\partial^2 x_1} & -\frac{\partial^2 \psi}{\partial x_1 \partial x_2} \\ -\frac{\partial^2 \psi}{\partial x_1 \partial x_2} & 1 - \frac{\partial^2 \psi}{\partial^2 x_2} \end{pmatrix} . \tag{3.16}$$

In its proper reference frame, the amplification matrix is diagonal with its elements being the eigenvalues. We can define the convergence K as the isotropic part of the eigenvalues and the shear γ as their anisotropic part. Consequently, in its proper reference frame, the amplification matrix becomes

$$\mathcal{A} = \begin{pmatrix} K - \gamma & 0 \\ 0 & K + \gamma \end{pmatrix} . \tag{3.17}$$

K is associated with the change in size and γ with the deformation of the light beam through the mapping $\boldsymbol{x} \mapsto \boldsymbol{y}$.

Using the conservation of the trace and the determinant of the matrix through its representation in different reference systems, and using the Poisson equation (3.14), comparison between Eq. 3.16 and Eq. 3.17 leads to

$$\begin{aligned} K &= \frac{\mathrm{tr}\mathcal{A}}{2} = 1 - \kappa \\ \gamma &= \pm\sqrt{\left(\frac{\mathrm{tr}\mathcal{A}}{2}\right)^2 - \det \mathcal{A}} \\ A(\boldsymbol{x}) &= (\det \mathcal{A})^{-1} = \frac{1}{(1-\kappa(\boldsymbol{x}))^2 - (\gamma(\boldsymbol{x}))^2} . \end{aligned}$$

The **critical curves** are defined as the region where the determinant of the amplification matrix is null. Through Eq. 3.15, we see that the critical curves correspond to regions in the image plane with infinite amplification. The image of the critical curve in the source plane is called the source **caustic**. A source on a caustic will give rise to infinitely amplified images formed on the critical curves. The caustic defined in the source plane defines the regions within which a source is multiply imaged as seen by a fixed observer. One way to understand this is the following.

Let us consider a source (S) emitting light rays which are deflected by a lens (D) before reaching an observer (O), as shown in Fig. 3.3.

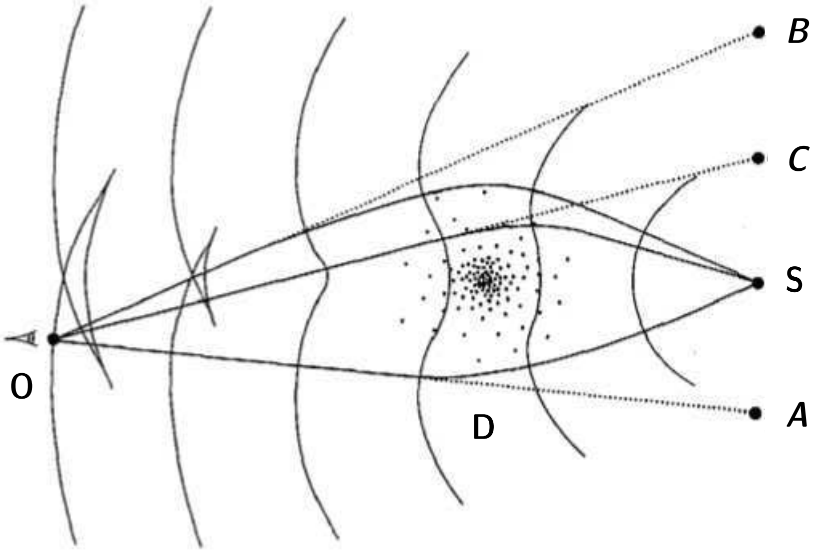

Figure 3.3: Principle of the formation of multiple images inside a caustic (Refsdal and Surdej (1994)).

Considering the wave-front of the emitted light (i.e. the surface perpendicular to all the rays), the presence of the deflector curves the wave-front which eventually may fold on itself in some areas. If the observer is located in one of these regions, several wave-fronts may arrive to him from different directions. Consequently, because several rays are arriving from different directions, he sees multiple images of the source at the positions A, B and C.

The surface defining the volume in which multiple wave-fronts arrive to the observer is called the caustic envelope. If the source is slightly displaced laterally, the envelope moves as well and, eventually, the observer may get out of the volume defined by the caustic envelope.

In the source plane, the curve delimiting the points where a source forms an envelope containing the observer, is called the source caustic. The shape of this caustic curve in the source plane is identical to that of the intersection of the observer plane with the caustic envelope. In the following, when the concept of caustic is used, we refer to the curve defined in the source plane.

3.2 Properties of simple deflectors

In the previous section, we have introduced the equations and concepts necessary to study the gravitational lens phenomenon. In this section, we introduce and study the peculiarities of three different mass models commonly used to represent galaxy mass distributions. Namely, we study the Singular Isothermal Sphere (SIS) model in Section 3.2.1, the Singular Isothermal Ellipsoid (SIE) in Section 3.2.2 and finally the SIS model plus external shear in Section 3.2.3.

For each model, we have developed *Matlab* libraries that enable to

- find the position and the number of lensed images formed as a function of the source position;
- calculate the amplification of a lensed image;
- calculate the shape of the caustics and critical curves.

All the figures in this section were constructed using these libraries.

3.2.1 Singular Isothermal Sphere (SIS) lens model

Spiral galaxies present a flat rotation curve, i.e. the one-dimensional line-of-sight velocity of stars in the galaxy is observed to be constant as a function of the distance to the galaxy's center. Such a flat rotation curve cannot be explained by the distribution of visible matter alone. In order to account for the observed rotation curves, astrophysicists assume the presence of a mass halo composed of dark matter and containing more than 90 percent of the galaxy's mass.

The *Singular Isothermal Sphere* (SIS) mass distribution model was introduced to reproduce the mass distribution in the halo of spiral galaxies and reproduces pretty well the mass ditribution in elliptical galaxies. It aims at reproducing the observed flat rotation curves.

We thus show hereafter how to describe a mass distribution in which a test particle's azimuthal speed v would keep a constant value whatever the radius of its orbit. The speed of the particle (a star for instance) has to be such that the centrifugal acceleration compensates the gravity force g, we thus need

$$\frac{v^2}{r} = g = - \bigtriangledown \phi, \tag{3.18}$$

where ϕ is the gravitational potential.

The mass density ρ can be found solving the Poisson equation

$$\triangle \phi = \bigtriangledown \cdot (\bigtriangledown \phi) = 4\pi G \rho. \tag{3.19}$$

Introducing Eq. 3.18 in Eq. 3.19, we obtain for the density

$$\rho = \frac{v^2}{4\pi G} \frac{1}{r^2}. \tag{3.20}$$

We may show that this density profile corresponds to an isothermal gas in autogravitating equilibrium. Indeed, the equation governing the behaviour of an autogravitating gas at hydrostatic equilibrium is

$$- \bigtriangledown p + \boldsymbol{g} \rho = 0, \tag{3.21}$$

where p, $\boldsymbol{g}$ and ρ are the pressure, the gravity and the volume density fields, respectively. Inserting the obtained density of Eq. 3.20 in Eq. 3.21, we obtain

$$p = \frac{v^4}{8\pi G r^2} = \frac{v^2}{2}\rho. \qquad (3.22)$$

We see that an auto-gravitating gas following the density relation given in Eq. 3.20 shows a pressure law alike the density one.

Now, if we consider a perfect gas which particles are in Brownian motions, we have the state equation of a perfect gas

$$p = \rho\frac{kT}{m}, \qquad (3.23)$$

where T is the temperature, k is the Boltzmann constant and m the mass of the individual particles constituting the gas. From statistical physics, we know that the one-dimensional velocity dispersion σ of the velocity distribution in the gas, is linked to the temperature via the relationship

$$\sigma^2 = \frac{kT}{m}. \qquad (3.24)$$

Thus, combining Eq. 3.23 and Eq. 3.24, we obtain a relation linking the one-dimensional velocity dispersion to the pressure in the case of a perfect gas in Brownian motions

$$p = \sigma^2\rho. \qquad (3.25)$$

If this gas is isothermal then the velocity dispersion is constant all through the gas cloud and we retrieve a pressure following the density law as in Eq. 3.22. Thus, a gas having a density profile alike that given in Eq. 3.20 behaves as an isothermal perfect gas in auto-gravitating equilibrium and we can assimilate the stars of the galaxy to particles in brownian motions.

By comparing these equations, we further obtain

$$\sigma^2 = \frac{v^2}{2}, \qquad (3.26)$$

that we may insert in Eq. 3.20 in order to obtain the density of the SIS as a function of the observed line-of-sight velocity dispersion σ

$$\rho_{SIS} = \frac{\sigma^2}{2\pi G}\frac{1}{r^2}. \qquad (3.27)$$

The SIS surface mass density Σ_{SIS} is obtained by projecting ρ_{SIS} on a plane passing through the lens center

$$\Sigma_{SIS}\left(b, \phi\right) = \frac{\sigma^2}{2Gb}. \qquad (3.28)$$

Deflection potential and deflection angles

Let us consider an SIS mass distribution acting as a deflector on the light emitted by a background source.

The dimensionless deflection potential ψ_{SIS} is obtained using the expression of Σ_{SIS} given in the previous section and solving the dimensionless Poisson equation for the deflection potential

$$\begin{aligned} \bigtriangledown^2 \psi_{SIS} &= 2\kappa_{SIS}, & (3.29)\\ \text{with} \quad \kappa_{SIS} &= \frac{\Sigma_{SIS}}{\Sigma_{crit}}, & (3.30)\\ &= 2\pi \left(\frac{\sigma}{c}\right)^2 \frac{D_{OD} D_{DS}}{D_{OS}} \frac{1}{b}. & (3.31) \end{aligned}$$

Expressing the Laplacian operator in cylindrical coordinates and taking into account the spherical symmetry of the deflector, leads to

$$\begin{aligned} \frac{1}{b}\partial_b \left(b \partial_b \psi_{SIS}\right) &= 4\pi \left(\frac{\sigma}{c}\right)^2 \frac{D_{OD} D_{DS}}{D_{OS}} \frac{1}{b}, \\ \Rightarrow \psi_{SIS} &= 4\pi \left(\frac{\sigma}{c}\right)^2 \frac{D_{OD} D_{DS}}{D_{OS}} b + A \ln b + B, \end{aligned}$$

where A and B are integration constants. As we are only interested in the gradient of the deflection potential (fixing the deflection angle), we may set $B = 0$. The term in $\ln b$ corresponds to the addition of a plane with a constant surface mass density between the observer and the source, we thus set $A = 0$. The deflection potential ψ_{SIS} of a SIS deflector thus becomes

$$\psi_{SIS} = 4\pi \left(\frac{\sigma}{c}\right)^2 \frac{D_{OD} D_{DS}}{D_{OS}} b. \qquad (3.32)$$

The deflection angles are calculated by inserting the deflection potential from (3.32) in (3.12)

$$\begin{aligned} \boldsymbol{\alpha} &= - \bigtriangledown \psi_{SIS}, \\ &= -\frac{4\pi\sigma^2}{c^2} \frac{\mathbf{b}}{b}. & (3.33) \end{aligned}$$

Using Eq. 3.11 defining the adimensional deflection angle, we find

$$\begin{aligned} \hat{\boldsymbol{\alpha}} &= -\frac{\boldsymbol{x}}{x} & (3.34)\\ \text{and} \quad b_0 &= \frac{4\pi\sigma^2}{c^2} \frac{D_{DS} D_{OD}}{D_{OS}}, & (3.35) \end{aligned}$$

where b_0 is the scale factor of the lens system.

The lens equation and image positions

The 2-D dimensionless lens equation is obtained by inserting the expression of the deflection angle in the lens Eq. 3.10

$$\begin{aligned} y_1 &= \left(1 - \frac{1}{\sqrt{x_1^2 + x_2^2}}\right) x_1, \\ y_2 &= \left(1 - \frac{1}{\sqrt{x_1^2 + x_2^2}}\right) x_2, \end{aligned} \tag{3.36}$$

where (y_1, y_2) and (x_1, x_2) represent the cartesian coordinates of $\boldsymbol{y}$ and $\boldsymbol{x}$, respectively.

When the source, the deflector and the observer are perfectly aligned ($\boldsymbol{y} = \boldsymbol{0}$), we notice from Eq. 3.36 that all positions along the unitary circle in the deflector plane (normalized to b_0) are solutions. In other words, the background source is imaged as a ring called the Einstein ring. In dimensional units, the radius R_E of this circle in the deflector plane, called the Einstein radius, is thus equal to the normalisation factor b_0. We define the Einstein angular radius θ_E as

$$R_E = b_0 = D_{OD}\,\theta_E, \tag{3.37}$$

where D_{OD} is the angular distance between the observer and the deflector.

Eq. 3.36 may be put in a scalar form by defining $y = \sqrt{y_1^2 + y_2^2}$ and $x = \sqrt{x_1^2 + x_2^2}$ and by adding the square of the two above equations. The scalar equation can then be solved analytically and leads to

$$\begin{cases} x = y \pm 1 & ,\text{if} \quad y < 1 \\ x = y + 1 & ,\text{if} \quad y \geq 1. \end{cases}$$

Fig. 3.4a and Fig. 3.4b display different source positions and the corresponding lensed image positions, repectively.

When the source is located outside the solid angle defined by the Einstein circle ($y > 1$, cf. the white marker), there is only a single image of the background source.

When the source is located within the solid angle defined by the Einstein circle ($y \leq 1$), there is formation of a second lensed image, which converges towards the Einstein circle as the source gets closer to perfect alignment with respect to the deflector. The two lensed images are located along the line passing through the source and the center of the deflector, on each side of the deflector's center . The angular separation between the images is always equal to the Einstein angular diameter.

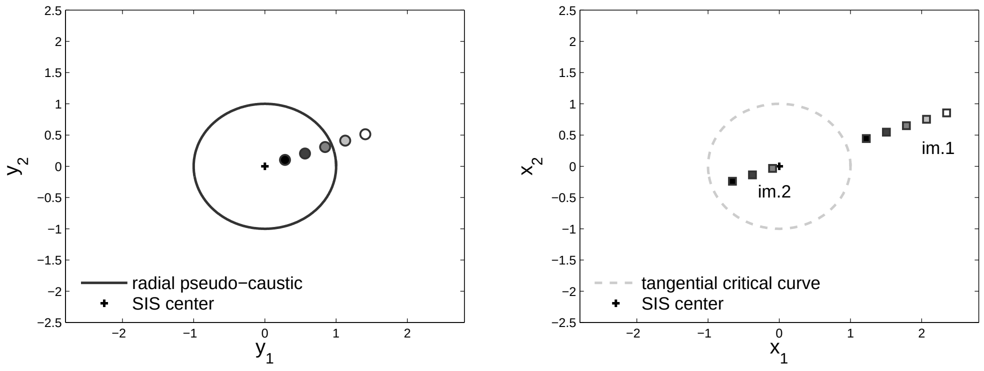

(a) Source positions and the radial pseudo-caustic

(b) Lensed image positions and the tangential critical curve

(c) Source plane amplification

(d) Image plane amplification

Figure 3.4: SIS deflector for different positions of (a) the source and (b) the resulting lensed images. Amplification maps in the source (c) and the deflector (d) plane, respectively. The source amplification is the sum of the moduli of the amplifications of all the lensed images produced for a source located at that position.

Critical curves and caustics

The amplification in the image plane is given by

$$A^{-1}(x) = \frac{x-1}{x}. \tag{3.38}$$

The tangential critical curve is the circle $x_t = 1$ and the radial critical curve does not exist and is degenerated into a single point located at $\boldsymbol{x} = \mathbf{0}$.

The radial pseudo-caustic, image of the point $\boldsymbol{x} = \mathbf{0}$, is the unitary circle in the source plane projected on the normalized deflector plane. As seen in the previous sub-section, there is formation of multiple lensed images whenever the source is inside the unitary circle.

The total amplification in the source plane is obtained by adding the moduli of the amplifications of the two lensed images

$$\begin{cases} A\left(y\right) = \dfrac{2}{y} & \text{, if} \quad y \leq 1 \\ A\left(y\right) = \dfrac{1+y}{y} & \text{, if} \quad y > 1 \end{cases}$$

We directly notice that even when there is no formation of multiple images ($y > 1$), the background source is amplified due the presence of the deflector near its line-of-sight .

Fig. 3.4c and Fig. 3.4d illustrate the amplification of the lensed images in the source and the image plane, respectively. The closer the position of an image to the critical curve, the more amplified is the lensed image. In Fig. 3.4c the total amplification increases as the source gets closer to a perfect alignment with respect to the deflector because the lensed images get closer to the critical curves, as we can see in Fig. 3.4a and Fig. 3.4b.

3.2.2 Singular Isothermal Ellipsoid (SIE) lens model

The SIS deflector model represents very well the radial density dependence in the spiral galaxy's halos and elliptical galaxies. Nevertheless, the galaxy mass distributions tend to be slightly more ellipsoidal than spherical. In order to take into account the internal ellipticity of the galaxy mass distribution, we introduce a new deflector model : the *Singular Isothermal Ellipsoid* (SIE) (Kormann et al. (1994)).

Furthermore, we have seen that an SIS deflector produces at maximum two lensed images. An SIS deflector does thus not permit to reproduce observed gravitational lens configurations with 3 or 4 lensed images. We will see that the introduction of the internal ellipticity in the SIE deflector model makes possible to reproduce such image configurations.

Surface mass density

The SIE surface mass density is obtained by introducing an elliptical symmetry to the SIS surface mass density Σ_{SIS}, i.e. replacing b by $b\sqrt{\cos^2\phi + f^2\sin^2\phi}$ in Eq. 3.28. The SIE surface mass density Σ_{SIE} is thus given, in polar coordinates (b, ϕ), by

$$\Sigma_{SIE}\left(b, \phi\right) = \frac{\sqrt{f}\sigma^2}{2Gb\sqrt{\cos^2\phi + f^2\sin^2\phi}}, \tag{3.39}$$

where σ is the line-of-sight central velocity dispersion, and where f is the ellipse axis ratio. Note that the normalisation by the factor $\sqrt{f}$ ensures that the mass located inside an iso-density contour is identical to that for the case of the SIS lens model. This mass profile corresponds to the projection in the lens plane of an ellipsoid mass distribution with a radial dependence proportional to r^{-2}.

Deflection potential and deflection angles

The dimensionless deflection potential ψ_{SIE} is obtained by using the expression of Σ_{SIE} in Eq. 3.39 and by solving the dimensionless Poisson equation for the deflection potential

$$\begin{aligned} \nabla^2 \psi_{SIE} &= 2\kappa_{SIE} && (3.40) \\ \kappa_{SIE} &= \frac{\Sigma_{SIE}}{\Sigma_{crit}} = \frac{c^2 D_{OS} \Sigma_{SIE}}{4\pi G D_{DS} D_{OD}}. && (3.41) \end{aligned}$$

The dimensionless deflection potential is given in polar coordinates by (Kormann et al. (1994))

$$\psi_{SIE} = \frac{\sqrt{f}\, b}{f'} \left[\sin\phi \arcsin\left(f' \sin\phi\right) + \cos\phi\, \mathrm{arcsh}\left(\frac{\mathrm{f}'}{\mathrm{f}} \cos\phi\right)\right],$$

with $f' = \sqrt{1 - f^2}$.

The deflection angle is calculated through the deflection potential using the relation

$$\boldsymbol{\alpha} = - \nabla \psi_{SIE}.$$

Along the deflector main axes, the deflection angles are given by (Kormann et al. (1994), Claeskens (1999), Eq. 2.72)

$$\begin{aligned} \alpha_1 &= -\frac{4\pi\sigma^2}{c^2} \frac{\sqrt{f}}{f'} \mathrm{arcsh}\left(\frac{\mathrm{f}'}{\mathrm{f}} \cos\phi\right), \\ \alpha_2 &= -\frac{4\pi\sigma^2}{c^2} \frac{\sqrt{f}}{f'} \arcsin\left(f' \sin\phi\right), \\ \text{with} \quad b_0 &= \frac{4\pi\sigma^2}{c^2} \frac{D_{OD} D_{DS}}{D_{OS}}, && (3.42) \end{aligned}$$

where b_0 is the lens system scale factor. Using Eq. 3.11, the dimensionless deflection angles are given by

$$\begin{aligned} \hat{\alpha}_1 &= -\frac{\sqrt{f}}{f'} \mathrm{arcsh}\left(\frac{\mathrm{f}'}{\mathrm{f}} \cos\phi\right), \\ \hat{\alpha}_2 &= -\frac{\sqrt{f}}{f'} \arcsin\left(f' \sin\phi\right). && (3.43) \end{aligned}$$

Lens equation

Inserting the expression 3.43 of the deflection angle for an SIE deflector in the lens equation 3.10 and introducing the polar coordinates (x, ϕ) in the deflector plane (normalized to b_0), the two-dimensional lens equation becomes

$$\begin{aligned} y_1 &= x\cos\phi - \frac{\sqrt{f}}{f'} \mathrm{arcsh}\left(\frac{\mathrm{f}'}{\mathrm{f}} \cos\phi\right), && (3.44) \\ y_2 &= x\sin\phi - \frac{\sqrt{f}}{f'} \arcsin\left(f' \sin\phi\right). && (3.45) \end{aligned}$$

In this case, the lens equation cannot be inverted analytically. Nevertheless, (3.44)× cos ϕ + (3.45)× sin ϕ and (3.44)× sin ϕ − (3.45)× cos ϕ lead respectively to the equations

$$\begin{aligned} x\left(\phi\right) &= \left[y_1 + \frac{\sqrt{f}}{f'}\mathrm{arcsh}\left(\frac{\mathrm{f}'}{\mathrm{f}}\cos\phi\right)\right]\cos\phi + \left[y_2 + \frac{\sqrt{f}}{f'}\arcsin\left(f'\sin\phi\right)\right]\sin\phi, \\ 0 &= \left[y_1 + \frac{\sqrt{f}}{f'}\mathrm{arcsh}\left(\frac{\mathrm{f}'}{\mathrm{f}}\cos\phi\right)\right]\sin\phi - \left[y_2 + \frac{\sqrt{f}}{f'}\arcsin\left(f'\sin\phi\right)\right]\cos\phi. \end{aligned}$$

The latter equation is only a function of the angular coordinates of the lensed images. Consequently, we can solve it numerically and insert the image angular coordinates in the former relation to determine their radial coordinates.

Amplification, critical curves and caustics

The amplification in the image plane $A\left(\boldsymbol{x}\right)$ can be derived calculating the determinant of the Jacobian matrix of the change of variables defined by Eq. 3.44 and Eq. 3.45 and leads to

$$A^{-1}\left(\boldsymbol{x}\right) = 1 - \frac{\sqrt{f}}{x\sqrt{\cos^2\phi + f^2\sin^2\phi}}. \tag{3.46}$$

The amplification in the image plane is shown in Fig. 3.5a for an SIE deflector with $f = 0.4$. In Fig. 3.5b we have calculated the amplification in the source plane $A\left(\boldsymbol{y}\right)$ for the same deflector. For every position of the source, we invert the lens equation to find the positions of the lensed images and add the absolute values of the amplifications of the lensed images.

As the deflector is singular, there is no radial critical curve. The tangential critical curve equation is obtained, in polar coordinates, by nulling the expression of $A^{-1}\left(\boldsymbol{x}\right)$ in Eq. 3.46. This leads to

$$x_t\left(\phi\right) = \frac{\sqrt{f}}{\sqrt{\cos^2\phi + f^2\sin^2\phi}}. \tag{3.47}$$

The tangential critical curve due to an SIE deflector with $f = 0.4$ is shown in Fig. 3.5c. Comparing the shape of the critical curve with the amplification map in the image plane in Fig. 3.5a, we clearly see that the region of high amplification of the images is situated along the tangential critical curve.

The equation of the radial pseudo-caustic is obtained by inserting $x = 0$ in the lens equations 3.44 and 3.45, which leads to

$$\begin{cases} y_{r,1}\left(\phi\right) = -\dfrac{\sqrt{f}}{f'}\mathrm{arcsh}\left(\frac{\mathrm{f}'}{\mathrm{f}}\cos\phi\right), \\ y_{r,2}\left(\phi\right) = -\dfrac{\sqrt{f}}{f'}\arcsin\left(f'\sin\phi\right). \end{cases}$$

(a) Amplification in the image plane (b) Amplification in the source plane

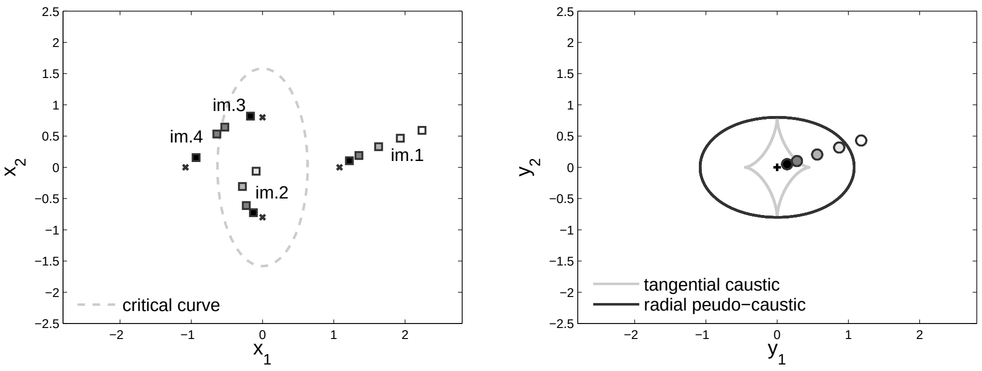

(c) Image positions and critical curve (d) Source positions and (pseudo-)caustics

Figure 3.5: Amplification maps in the deflector (a) and source (b) planes for an SIE deflector with $f = 0.4$. Various source positions (d) and the corresponding lensed image positions (c).

The equation of the tangential caustic is obtained by inserting Eq. 3.47 of the tangential critical curve in the lens equation. This gives

$$\left\{ \begin{aligned} y_{t,1}(\phi) &= \frac{\sqrt{f}\cos\phi}{\sqrt{\cos^2\phi + f^2\sin^2\phi}} - \frac{\sqrt{f}}{f'}\mathrm{arcsh}\left(\frac{\mathrm{f}'}{\mathrm{f}}\cos\phi\right), \\ y_{t,2}(\phi) &= \frac{\sqrt{f}\sin\phi}{\sqrt{\cos^2\phi + f^2\sin^2\phi}} - \frac{\sqrt{f}}{f'}\arcsin\left(f'\sin\phi\right). \end{aligned} \right. \tag{3.48}$$

The radial and tangential (pseudo-)caustics due to an SIE deflector with axis ratio $f = 0.4$ are shown in Fig. 3.5d. The radial pseudo-caustic has an elliptical shape whereas the tangential caustic shows a characteristic diamond shape. Comparing the caustics to the amplification map in the source plane, we directly see that the tangential caustic curve defines an area of high amplification, especially near the *cusps* (the corner of the diamonds), and the caustic curve is itself by definition characterised by an infinite amplification.

The tangential critical curves for different values of the axis ratio f are shown in Fig. 3.6a. As f converges to 1, the SIE converges to the SIS mass distribution and the critical curve converges toward the SIS critical curve, i.e. the unitary circle.

The radial and tangential (pseudo-)caustics are shown in Fig. 3.6b for different values of f. For f converging to 1, the radial pseudo-caustic converges to that of the SIS model, the unitary circle. The tangential caustic is no longer degenerated to the singularity at $\boldsymbol{y} = \mathbf{0}$: we notice the diamond shaped tangential caustic. For values of $f < 0.392$, the tangential caustic crosses the radial one, giving rise to the existence of so-called *naked cusps*.

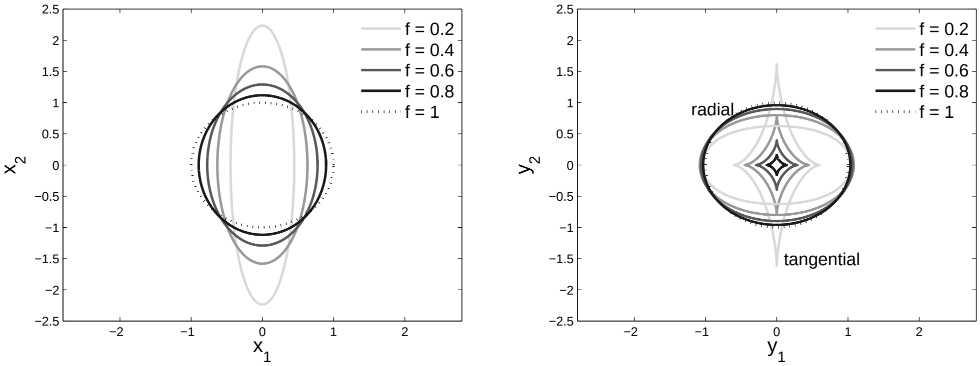

(a) Image plane

(b) Source plane

Figure 3.6: Tangential critical curves (a) and tangential and radial (pseudo-) caustics (b) for different values of the f parameter.

Number and position of lensed images

The position of the lensed images are found by solving numerically the lens equations 3.44 and 3.45 for the case of the SIE deflector.

Fig. 3.5d and Fig. 3.5c show different positions of the source and the corresponding lensed images, respectively. When the source is located outside both caustics (white markers), a single image is being formed. As soon as the source crosses the radial pseudo-caustic curve, there is formation of a second image close to the line-of-sight of the deflector ($\boldsymbol{x} \simeq \mathbf{0}$). Observing the amplification in the deflector plane in Fig. 3.5a, we see that this image is deamplified; from Eq. 3.46, we confirm that the image is infinitely deamplified.

As the source gets closer to the deflector line-of-sight (darker markers), the second image goes away from the center and gets more amplified.

When the source crosses the tangential caustic, there is formation of 2 new lensed images appearing along the tangential critical curve. As seen in Fig. 3.5a, the amplification of these images is infinite on the critical curve and they get fainter as they move away from it. The positions of the lensed images in the case of perfect alignment are marked with crosses in Fig. 3.5c.

When the source is perfectly aligned with the deflector and the observer, there is no longer formation of an Einstein ring as in the SIS case. Because of the introduction of the deflector internal ellipticity, the ring breaks in 4 lensed images, located by pair along the main axes of the deflector, on each side of the deflector center.

We have seen that for very elliptical deflectors (f close to 0), the diamond-shaped tangential caustic goes through the radial pseudo-caustic and there is the appearance of *naked cusps*. In such cases, there exist configurations with the formation of 3 lensed images when the source is located inside the tangential caustic and outside the radial one. These configurations where the source is located close to the cusp lead to a very high amplification of the background source.

The main effect of introducing an ellipticity in the deflector, is to break the degeneracy of the tangential caustic, making it possible to produce lens configurations with 3 or 4 images.

3.2.3 SIS with external shear

In Section 3.2.2, we have seen that breaking the spherical symmetry of the SIS deflector through the introduction of an internal ellipticity in the mass distribution allows to take into account gravitational lensing configurations with more than 2 images.

The spherical symmetry of the SIS deflector can also be broken by adding an external perturbation to the gravitational potential. Physically, this may correspond to a perturbation due to the presence of a nearby massive object. The effect of the companion is modelled by adding a constant external shear to the SIS potential.

Deflection angle

For any mass distribution, the vectorial deflection angle $\boldsymbol{\alpha}$ can be expressed in a matricial form as follows

$$\begin{aligned}\boldsymbol{\alpha} &= \begin{pmatrix} a_1\,(x_1, x_2) & 0 \\ 0 & a_2\,(x_1, x_2) \end{pmatrix} \begin{pmatrix} x_1 \\ x_2 \end{pmatrix}, \\ &= \left(\begin{pmatrix} \dfrac{a_1 + a_2}{2} & 0 \\ 0 & \dfrac{a_1 + a_2}{2} \end{pmatrix} + \begin{pmatrix} \dfrac{a_1 - a_2}{2} & 0 \\ 0 & -\dfrac{a_1 - a_2}{2} \end{pmatrix} \right) \begin{pmatrix} x_1 \\ x_2 \end{pmatrix}, \end{aligned} \tag{3.49}$$

where the deflection angle has been separated in its isotropic and anisotropic parts in the second equation. The easiest non trivial way to introduce anisotropy in the mass distribution is to set constant $\gamma = (a_1 - a_2)/2$ in the deflector plane.

The SIS model plus external shear introduces an anisotropic term to the deflection angle of the SIS mass distribution. The deflection angle is thus given by

$$\begin{aligned}
\boldsymbol{\alpha} &= \boldsymbol{\alpha}_{SIS} + \gamma \begin{pmatrix} 1 & 0 \\ 0 & -1 \end{pmatrix} \begin{pmatrix} x_1 \\ x_2 \end{pmatrix}, \\
&= \begin{pmatrix} -\dfrac{1}{\sqrt{x_1^2 + x_2^2}} + \gamma & 0 \\ 0 & -\dfrac{1}{\sqrt{x_1^2 + x_2^2}} - \gamma \end{pmatrix} \begin{pmatrix} x_1 \\ x_2 \end{pmatrix}, \\
&= \begin{pmatrix} \cos\phi \left(r\gamma - 1 \right) \\ -\sin\phi \left(r\gamma + 1 \right) \end{pmatrix}, \qquad (3.50)
\end{aligned}$$

where r and ϕ are the polar coordinates in the deflector plane, normalized to b_0.

The **lens equation** 3.10 thus becomes

$$\begin{pmatrix} y_1 \\ y_2 \end{pmatrix} = \begin{pmatrix} \cos\phi \left(r \left(\gamma + 1 \right) - 1 \right) \\ \sin\phi \left(r \left(1 - \gamma \right) - 1 \right) \end{pmatrix}, \qquad (3.51)$$

$$= \begin{pmatrix} x_1 - \dfrac{x_1}{\sqrt{x_1^2 + x_2^2}} + x_1\gamma \\ x_2 - \dfrac{x_2}{\sqrt{x_1^2 + x_2^2}} - x_2\gamma \end{pmatrix}. \qquad (3.52)$$

There is no simple analytical solution to this lens equation. It must thus be solved numerically. By isolating $\cos\phi$ and $\sin\phi$ in Eq. 3.51 and by adding their squares, we obtain a relationship that is no longer function of the angular coordinate ϕ. This relationship can be expressed as a fourth-order polynomial in the radial coordinate r

$$c_4 r^4 + c_3 r^3 + c_2 r^2 + c_1 r^1 + c_0 = 0, \qquad (3.53)$$

with

$$\begin{aligned}
c_4 &= \left(1 + \gamma\right)^2 \left(1 - \gamma\right)^2, \\
c_3 &= -4 \left(1 - \gamma^2\right), \\
c_2 &= \left(1 - y_2^2\right) \left(1 + \gamma\right)^2 + \left(1 - y_1^2\right) \left(1 - \gamma\right)^2 + 4 \left(1 - \gamma^2\right), \\
c_1 &= 2 \left(y_2^2 - 1\right) \left(1 + \gamma\right) + 2 \left(y_1^2 - 1\right) \left(1 - \gamma\right), \\
c_0 &= 1 - \left(y_1^2 + y_2^2\right).
\end{aligned}$$

Solving the lens equation of an SIS plus shear deflector can thus be solved numerically by finding the roots of Eq. 3.53 in order to determine the radial coordinates and inserting them in relation 3.51 to retrieve the angular coordinates of the lensed images.

Amplification, critical curves and caustics

The amplification is given in polar coordinates in the image plane by

$$A^{-1} = 1 - \gamma^2 - \frac{1 + \gamma \cos(2\phi)}{r}. \tag{3.54}$$

Fig. 3.7a and Fig. 3.7b illustrate the amplification in the image plane normalised to b_0 and in the source plane projected on the normalized image plane, respectively, for a SIS deflector with an external shear $\gamma = 0.4$.

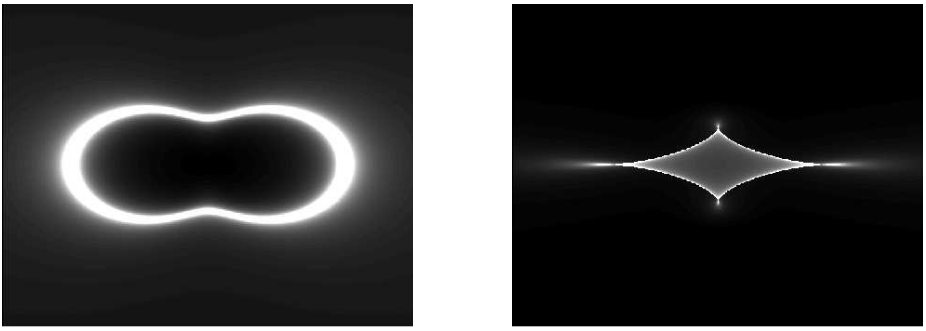

(a) Amplification in the image plane (b) Amplification in the source plane

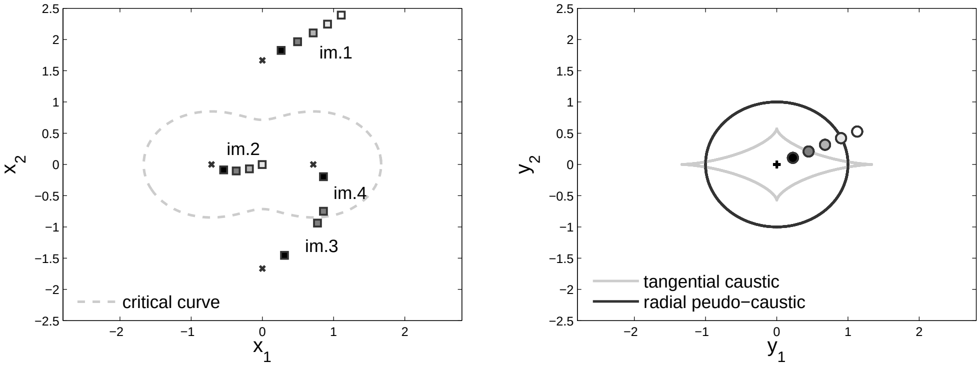

(c) Image position and tangential critical curve (d) Source position and caustic curves

Figure 3.7: Amplification maps in the deflector (a) and source (b) planes. Different source positions (d) and corresponding lensed image positions (c) for a SIS deflector with an external shear $\gamma = 0.4$.

The **tangential critical curve** equation is found by solving $A^{-1} = 0$ in Eq. 3.54, which leads to

$$r_t(\phi) = \frac{1 + \gamma \cos 2\phi}{1 - \gamma^2} \quad , \gamma \neq \pm 1, \tag{3.55}$$

with $\phi \in [0, 2\pi[$ representing the polar angle. The bottom panel of Fig. 3.8 shows the tangential critical curves for different values of the external shear γ. The **radial critical curve** is degenerated to the point $r = 0$ because the deflector is singular.

The tangential critical curve is shown in Fig. 3.7c for the same deflector as before ($\gamma = 0.4$): we notice once again the good correspondence between the shape of the tangential critical curve and the area of high amplification in the deflector plane.

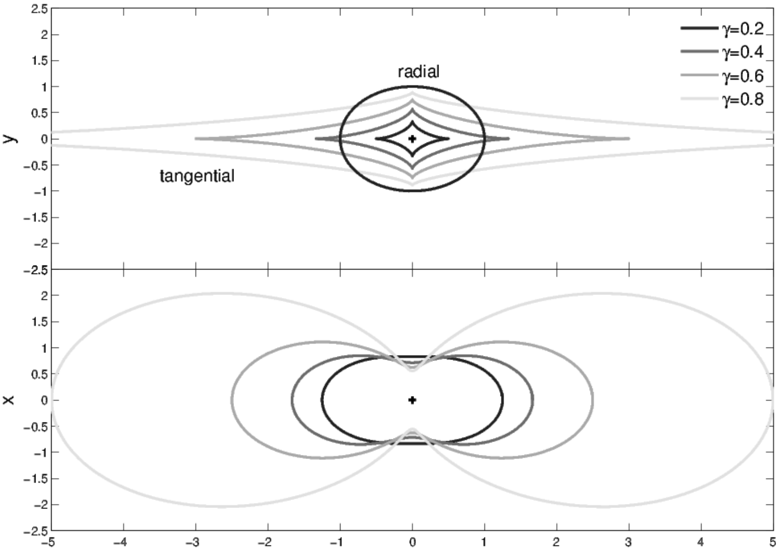

Figure 3.8: Caustics and critical curves for the SIS case with $\gamma = 0.2, 0.4, 0.6$ and 0.8. The radial critical curve is degenerated to the origin point in the deflector plane and the radial pseudo-caustic is independent of the shear value.

The **tangential caustic** is obtained by inserting the equation of the tangential critical curve in the lens equation, this gives

$$\left\{ \begin{array}{lcl} y_1 & = & \cos\phi \dfrac{\gamma\left(\cos\left(2\phi\right)+1\right)}{1-\gamma}, \\ \\ y_2 & = & -\sin\phi \dfrac{\gamma\left(1-\cos\left(2\phi\right)\right)}{1+\gamma}. \end{array} \right. \tag{3.56}$$

The radial pseudo-caustic curve, found by considering the image at $r = 0$ in the lens equation, is the unitary circle $y_r = 1$.

The tangential and radial (pseudo-)caustics are shown in Fig. 3.7d, for $\gamma = 0.4$. We see the correspondence between the tangential caustic and the area of high amplification in the source plane.

Source caustics for different values of γ are shown in the top panel of Fig. 3.8. It is interesting to notice that there is no dependence of the radial pseudo-caustic as a function of the shear: this pseudo-caustic is always identical to that for the SIS case.

When increasing the external shear, the diamond-shaped tangential caustic gets more elongated, and crosses the radial pseudo-caustic, giving rise to naked cusps, similarly to the SIE case.

Number and position of the lensed images

Fig. 3.7d and Fig. 3.7c show different source positions and the corresponding lensed images, respectively.

When the source is located outside both caustics (white marker) there is only one image of the background source. As in the SIE case, crossing the radial pseudo-caustic leads to the formation of a second image near the center of the deflector, infinitely deamplified. Furthermore, crossing the tangential caustic leads to the formation of two highly amplified images, emerging from the tangential critical curve.

From Fig. 3.8, we see that there is also formation of naked cusps when the deflector differs sufficiently from the spherical case, i.e. for values of the external shear close to 1.

Consequently, the SIS plus external shear model also enables to represent lensing configurations with 3 and 4 lensed images.

SIE versus SIS plus shear

Although the SIE and SIS plus external shear models are both capable to produce lensing events with 3 or 4 images, these two models are fundamentally different. To emphasize this difference, in this sub-section, we demonstrate that, even for a very small asymmetry (i.e. $f \sim 1$ and $\gamma \sim 0$), the 2 models behave differently. We show this by demonstrating that the SIS deflector model plus constant external shear cannot be interpreted as a first order development of the SIE model.

Let us consider a Singular Isothermal Ellipsoid (SIE) which deflection angles are given by Eq. 3.43 and let us develop the expression (3.43) for small deflector ellipticities. The hypothesis of small ellipticities ($e \ll 1$) implies $f \sim 1$ and $f' \ll 1$.

In Eq. (3.43), the arcsin and arcsh may be developed as

$$\begin{aligned}\operatorname{arcsh}\left(\frac{\mathrm{f}'}{\mathrm{f}}\cos\phi\right) &\simeq \left[\operatorname{arcsh}\left(\frac{\mathrm{f}'}{\mathrm{f}}\cos\phi\right)\right]_{\frac{f'}{f}=0} + \left(\frac{f'}{f}\cos\phi\right)\left[\frac{1}{\sqrt{1+\left(\frac{f'}{f}\cos\phi\right)^2}}\right]_{\frac{f'}{f}=0}, \\ &\simeq \frac{f'}{f}\cos\phi \quad \text{and}\end{aligned}$$

$$\begin{aligned}\arcsin\left(f'\sin\phi\right) &\simeq \left[\arcsin\left(f'\sin\phi\right)\right]_{f'=0} + \left(f'\sin\phi\right)\left[\frac{1}{\sqrt{1-(f'\sin\phi)^2}}\right]_{f'=0}, \\ &\simeq f'\sin\phi.\end{aligned}$$

Inserting these relations in Eq. 3.43, it comes

$$\begin{aligned}\alpha_1 &\simeq -\frac{\cos\phi}{\sqrt{f}}, \\ \alpha_2 &\simeq -\sqrt{f}\sin\phi. \end{aligned} \tag{3.57}$$

Developing the square roots to the first order, we get

$$\begin{aligned}\frac{1}{\sqrt{f}} &\simeq \frac{3-f}{2} + \bigcirc\left((f-1)^2\right), \\ \sqrt{f} &\simeq \frac{1+f}{2} + \bigcirc\left((f-1)^2\right).\end{aligned}$$

Inserting these relations in Eq. 3.57, we obtain

$$\begin{aligned}\alpha_1 &\simeq -\frac{3-f}{2}\cos\phi, \\ \alpha_2 &\simeq -\frac{1+f}{2}\sin\phi \quad \text{, for } f\sim 1. \end{aligned} \tag{3.58}$$

In the ellipsoid eigen reference frame, the lens equation in a matrix format may be writen as

$$\begin{aligned}\begin{pmatrix} y_1 \\ y_2 \end{pmatrix} &= \begin{pmatrix} x_1 \\ x_2 \end{pmatrix} - \begin{pmatrix} a_1 & \\ & a_2 \end{pmatrix}\begin{pmatrix} x_1 \\ x_2 \end{pmatrix}, \\ &= \begin{pmatrix} x_1 \\ x_2 \end{pmatrix} - \begin{pmatrix} \frac{a_1+a_2}{2} & \\ & \frac{a_1+a_2}{2} \end{pmatrix}_{iso}\begin{pmatrix} x_1 \\ x_2 \end{pmatrix} - \begin{pmatrix} \frac{a_1-a_2}{2} & \\ & -\frac{a_1-a_2}{2} \end{pmatrix}_{an}\begin{pmatrix} x_1 \\ x_2 \end{pmatrix},\end{aligned}$$

where $a_1 = -\alpha_1/x_1$ and $a_2 = -\alpha_2/x_2$. In the second equality, we have developed the deviation angle matrix in its isotropic and anisotropic parts. Inserting the expressions (3.58) in the lens equation, we obtain

$$\begin{pmatrix} y_1 \\ y_2 \end{pmatrix}_{SIE} = \begin{pmatrix} x_1 \\ x_2 \end{pmatrix} - \begin{pmatrix} \frac{1}{b} & \\ & \frac{1}{b} \end{pmatrix}_{iso} \begin{pmatrix} x_1 \\ x_2 \end{pmatrix} - \frac{1-f}{2} \begin{pmatrix} \frac{1}{b} & \\ & -\frac{1}{b} \end{pmatrix}_{an} \begin{pmatrix} x_1 \\ x_2 \end{pmatrix}, \tag{3.59}$$

with $b = \sqrt{x_1^2 + x_2^2}$. The isotropic contribution of the lens corresponds to that of the contribution of a SIS. If we compare Eq. 3.59 with the equation obtained in the case of an SIS deflector plus constant shear, i.e. (cf. Eq. 3.49)

$$\begin{pmatrix} y_1 \\ y_2 \end{pmatrix}_{SIS} = \begin{pmatrix} x_1 \\ x_2 \end{pmatrix} - \begin{pmatrix} \frac{1}{b} & \\ & \frac{1}{b} \end{pmatrix}_{SIS} \begin{pmatrix} x_1 \\ x_2 \end{pmatrix} - \gamma \begin{pmatrix} 1 & \\ & -1 \end{pmatrix}_{an} \begin{pmatrix} x_1 \\ x_2 \end{pmatrix},$$

we see that, in the anisotropic contribution of the SIE deflector (developed for small ellipticities), there appears a b^{-1} factor. Consequently, the SIS model plus a constant external shear cannot be interpreted as the first order development of an SIE model.

Chapter 4

Gravitational lensing probabilities

Let us consider the population of QSOs detected in a survey, N_{QSO} representing the number of detected sources. We would like to determine the number of gravitationally lensed sources expected among this population.

Let us define τ, the probability that a given QSO is detected as a gravitational lensing event with multiple lensed images, due to the presence of a foreground deflector near its line-of-sight. The expected number of gravitational lenses N_{GL} among the detected sources is given by the relation

$$N_{GL} =< \tau > N_{QSO}, \tag{4.1}$$

where $< \tau >$ is the mean value of τ evaluated over all the sources.

In this chapter, we derive the expression of τ and we introduce the different tools necessary for its estimation.

4.1 Geometrical cross section

Let us consider a fixed source S, an observer O and, at a given distance in between, a plane perpendicular to the line-of-sight, containing a potential deflector D (see Fig. 4.1).

When the deflector is located along the line-of-sight to the source, multiple images of the background source are produced or an Einstein ring, depending on the symmetry of the deflector. If the deflector is slightly moved away from the source line-of-sight, the lensed images move relatively to each other. If the deflector is moved further away from the source line-of-sight, at some distance, the multiple images of the background source disappear, either by merging together or by being gradually de-amplified.

We can thus define an area in the deflector plane where the presence of a deflector leads to the formation of multiple images. This area is defined as the **geometrical cross section** associated with the lens event.

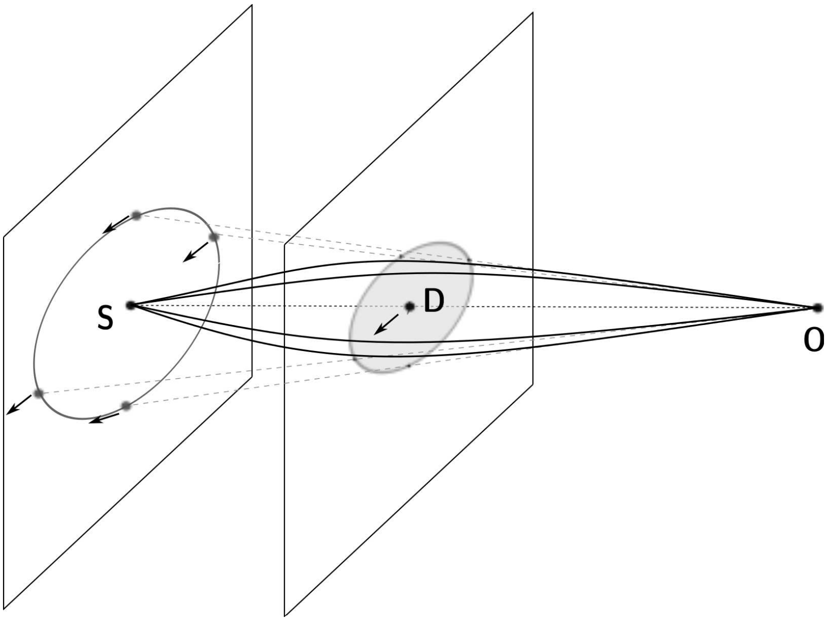

Figure 4.1: Illustration of the geometrical cross section.

We have so far considered a fixed source and we have defined the cross section by moving the deflector with respect to the line-of-sight.

Let us now consider that the deflector position is fixed. If the source is perfectly aligned along the line-of-sight towards the deflector, we would see multiple lensed images or an Einstein ring. We have seen that the mass distribution of the deflector defines curves in the source plane called caustics inside which a source will be seen as being multiply imaged by the observer.

If we project the source plane on the deflector plane, it is straightforward that an angular displacement of the source in one direction is equivalent to the same angular displacement of the deflector in the opposite direction. The area in the deflector plane intercepted by the solid angle defined by the caustics is thus the geometrical cross section.

Using the dimensionless formalism introduced in Section 3.1, the geometrical cross section $\boldsymbol{\Sigma}_{geom}^{dim}$ can thus be calculated as follows

$$\begin{aligned} \boldsymbol{\Sigma}_{geom}^{dim} &= b_0^2\,(z) \int_{S_y} d\boldsymbol{y}, \\ &= b_0^2\,\Sigma_{geom}, \end{aligned} \tag{4.2}$$

where

- $\boldsymbol{y} = (y_1, y_2)$ are the angular coordinates of the source position projected on the deflector plane, normalised by the angular Einstein radius θ_E;

- S_y is the area inside the caustic curves, projected on the deflector plane, normalised to θ_E;
- b_0 is the scale factor of the lens system, i.e. the Einstein radius in the deflector plane.

The dimensional geometrical cross section $\mathbf{\Sigma}^{dim}_{geom}$ is a function, through its dependence on b_0, of the redshifts of both the source and the deflector, the universe model and the deflector mass distribution. It is possible to isolate the effect of the geometrical configuration of the lens system (i.e. the different distances between the observer, the deflector and the source). In Eq. 4.2, we have defined the dimensionless geometrical cross section Σ_{geom} as

$$\Sigma_{geom} = \int_{S_y} d\boldsymbol{y} \tag{4.3}$$

which is calculated in the projected source plane, normalised to the Einstein radius. Σ_{geom} is no longer dependent on the geometrical configuration of the lens system: it is a measure of the intrinsic ability of the mass distribution to produce multiple images of the source.

The lensing cross section is thus calculated by integrating the source area projected in the deflector plane, centred on the deflector, in which a source must be located in order to lead to the formation of multiple lensed images.

Let us now examine the cross sections for the different deflector mass distribution models introduced in Chapter 3: the SIS, the SIE and SIS plus external shear.

SIS deflector

Let us consider a deflector whose mass distribution follows the *Singular Isothermal Sphere* (SIS) law introduced in Section 3.2.1.

We have seen that the tangential caustic is degenerated to the origin and that the radial pseudo-caustic is the unitary circle. The source area S_y (projected on the deflector plane, normalised to θ_E) is thus the unitary circle. Consequently, the dimensionless cross section is $\Sigma_{geom} = \pi$.

In the case of the SIS deflector, the scale factor is given by Eq. 3.35.

The expression of the dimensional geometrical cross section given by Eq. 4.2, particularized to the SIS deflector, thus becomes

$$\Sigma_{geom,SIS} = \frac{16\pi^3}{c^4}\sigma^4 \left(\frac{D_{DS}D_{OD}}{D_{OS}}\right)^2, \tag{4.4}$$

where σ is the central line-of-sight velocity dispersion, and where D_{DS}, D_{OS} and D_{OD} are the different angular distances between the observer, the deflector and the source. We see that the geometrical cross section is a function of the line-of-sight central velocity dispersion up to the fourth power, and it is a function of the distances between the observer, the deflector and the source.

SIE deflector

It is possible to define different geometrical cross sections depending on how we define the *lensing event*. In Eq. 4.2, we have defined the lensing event as the formation of multiple lensed images from the point-of-view of the observer. S_y was thus defined as the area in which the source must be located to lead to the formation of multiple images. The obtained Σ_{geom} is thus the cross section associated with the formation of multiple images.

We have seen that introducing an ellipticity to the deflector mass distribution can lead to gravitational lensing systems with more than 2 images. We might in fact be interested in the formation of multiple images *with some given characteristics.*

Let us consider a deflector with a *Singular Isothermal Ellipsoid* mass profile, as defined in Section 3.2.2. With such a deflector, the tangential caustic is no longer degenerated as in the SIS case; it has a diamond shape. Depending on the position of the source relatively to the tangential and radial (pseudo-)caustic curve, such a deflector may lead to the formation of 2, 3 or 4 lensed images of the background source. With an SIE deflector, we may now define a cross section linked to a lensing event *with a given number of lensed images*; we can thus define a cross section leading to the formation of 2, 3 or 4 lensed images or simply of multiple images independently of the number. In Eq. 4.2, we would then define S_y as the area in which a source must be located to lead to the formation of the considered number of images.

Fig. 4.2 shows the dependence of different geometrical cross sections as a function of the axis ratio f of the deflector. As the scale factor b_0 is the same as in the SIS case, we have only represented the dimensionless cross sections. The value of $\Sigma_{geom,SIS}$ is shown as the dotted line. The right panel of the figure shows the dependence of the caustic as a function of f.

When f equals 1, the deflector is a SIS. The tangential caustic is degenerated to a single point. All sources inside the caustic (except on the optical axis) lead to the formation of two lensed images. Consequently, $\Sigma_{geom,2} = \Sigma_{geom,tot} = \Sigma_{geom,SIS}$.

As f decreases, the tangential caustic increases in size and the radial pseudo-caustic flattens. A source located inside the radial pseudo-caustic only leads to the formation of 2 images whereas a source inside both caustics will be imaged 4 times. As the area inside the tangential caustic increases, $\Sigma_{geom,4}$ increases. $\Sigma_{geom,2}$ decreases because of both the increase in size of the tangential caustic and the decrease of the area inside the radial pseudo-caustic due to its flattening. $\Sigma_{geom,tot}$ decreases because the total area leading to multiple images decreases due to the flattening of the radial pseudo-caustic.

For $f \lesssim 0.392$, the tangential caustic goes through the radial one leading to

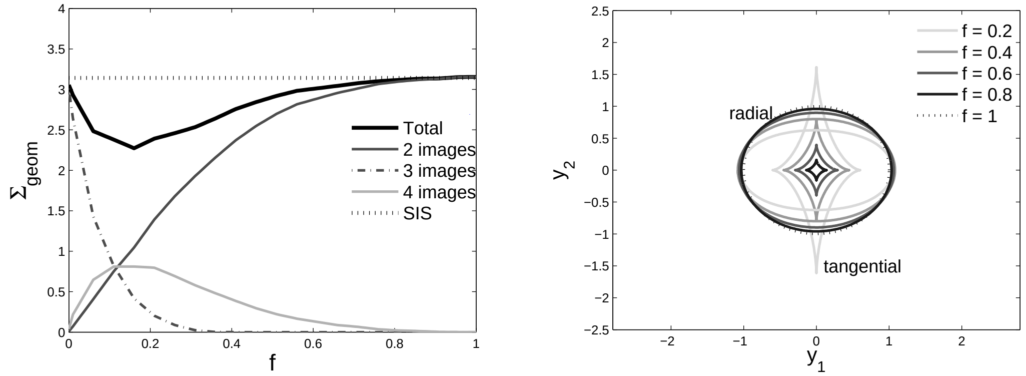

(a) SIE deflector (b) Caustic dependence as a function of f

Figure 4.2: (a)Dependence of the dimensionless geometrical cross section as a function of the axis ratio f of an SIE deflector. As a reference point, the value of the SIS dimensionless cross section is shown as a dotted black line. (b) Dependence of the caustics as a function of the axis ratio f of the deflector.

the presence of naked cusps. A source inside the tangential caustic curve only is seen into 3 images; consequently, $\Sigma_{geom,3}$ increases as f decreases. The flattening of the radial pseudo-caustic continues, leading to a decrease of both $\Sigma_{geom,2}$ and $\Sigma_{geom,4}$.

The decrease of $\Sigma_{geom,tot}$ due to the flattening of the radial pseudo-caustic is compensated by the increasing size of the tangential caustic. For the limit of f converging to 0, the tangential caustic converges to a diamond shaped surface with an area equal to π.

SIS plus external shear

Let us now examine the case of an SIS deflector with the presence of an external shear. In this case as well, we can have configurations with 2, 3 or 4 lensed images. The dependence of the dimensionless geometrical cross sections as a function of the external shear γ is shown in Fig. 4.3a. Fig. 4.3b illustrates the behaviour of the caustics with γ.

As in the case of the SIE deflector, when the shear γ is null, we retrieve the results of the SIS deflector. When γ increases, $\Sigma_{geom,4}$ increases due to the increased size of the tangential caustic (cfr Eq. 3.48).

For the critical value $\gamma = 1/3$, there appear naked cusps and $\Sigma_{geom,3}$ increases and becomes dominant at the limit for γ converging to 1.

Nevertheless, there are a few fundamental differences with the SIE model:

- there is no change of the radial pseudo-caustic with the value of the shear γ. Because of this, $\Sigma_{geom,tot}$ never gets below the SIS case and increases when the cusp crosses the radial pseudo-caustic.

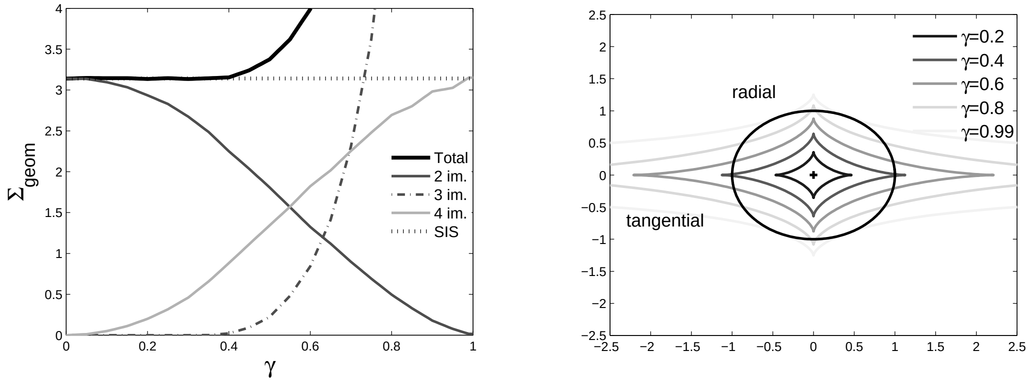

(a) SIS plus external shear

(b) SIS plus external shear

Figure 4.3: (a)Dependence of the dimensionless geometrical cross section as a function of the shear γ of an SIS deflector with external shear. As a reference point, the value of the SIS dimensionless cross section is shown with a dotted black line. (b) Radial and tangential caustics for different values of γ.

- the radial pseudo-caustic is fully located inside the tangential caustic for $\gamma = 1$. Consequently, the whole area becomes a region leading to the formation of 4 lensed images and $\Sigma_{geom,4}$ converges to π (instead of 0 in the SIE case).
- The area inside the tangential caustic diverges for $\gamma \to 1$ (contrary to the SIE case where it converges to π), leading to a divergence of $\Sigma_{geom,tot}$.

4.2 Geometrical lensing volume and gravitational lensing probabilities

For a source at a fixed distance, we may define a geometrical cross section in every plane perpendicular to the source line-of-sight, located in between the source and the observer. The envelope of all the cross sections defines the **lensing geometrical volume** associated with the event. By definition, the geometrical volume is the volume in which the presence of a deflector leads to the formation of multiple lensed images from the observer point-of-view.

The probability of a source to be gravitationally lensed with the formation of multiple images can be estimated through the probability of having a deflector located within the lensing geometrical volume. For a small density of deflectors, this is equivalent to calculating the optical depth associated with the source.

For information, the dependence of the geometrical lensing volume as a function of the source redshift is shown in Fig. 4.4a, for a deflector with $\sigma = 161$ km/s and $f = 0.697$ (corresponding to typical values for an early type galaxy in the local universe), modelled as an SIE or an SIS deflector. In both cases, as

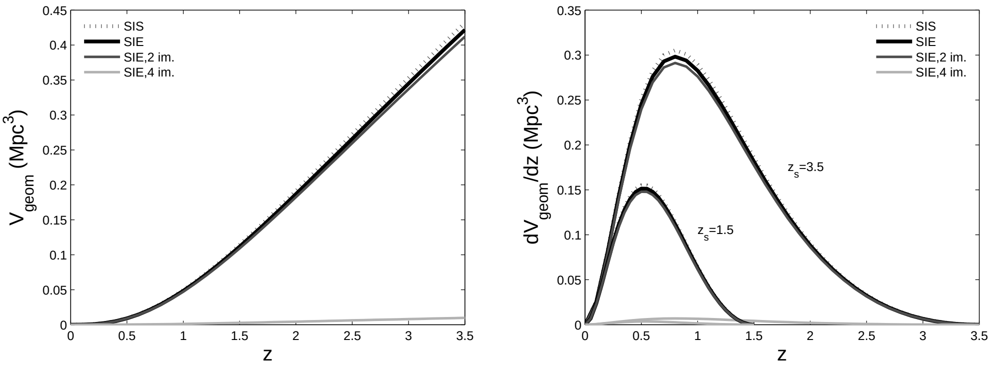

(a)

(b)

Figure 4.4: (a) Dependence of the geometrical lensing volume as a function of the source redshift for an SIS and an SIE deflector with $\sigma = 161$ km/s and $f = 0.697$. (b) Contribution of the differential geometrical lensing volume as a function of the deflector redshift for two different source redshifts. The values of σ and f correspond to typical values for an early type galaxy in the local universe. The volume is expressed in the comoving reference frame, assuming a flat FLRW universe with $H_0 = 70$ km s^{-1}Mpc^{-1} and $\Omega_m = 0.3$.

the source redshift increases, its lensing volume increases as well. In the case of the SIE deflector, we have reproduced the geometrical volume associated with the formation of a given number of lensed images. Fig. 4.4b shows the contribution of the different deflector redshift to the lensing volume, for two different source redshifts.

Let us consider an observer and a QSO source at a redshift z_s. In the case where the deflector population is composed of all similar individuals, the probability of a lensing event τ_{geom} is given by integrating the density of deflectors over the geometrical lensing volume V_{geom}, i.e.

$$\tau_{geom} = C_{sel} \int\int\int_{V_{geom}} n d\boldsymbol{V}, \tag{4.5}$$

where n is the density of deflectors at redshift z per unit of proper volume.

We have introduced a correction factor C_{sel} to account for a non favourable selection effect to the inclusion of gravitationally lensed events in a sample of luminous QSOs. This correction factor was introduced by Surdej et al. (1993) to take into account that part of the lensing events which have been discarded through the process of the source population selection. If we consider a survey for detection of QSOs for instance:

- the QSO candidates can be selected on the basis of their colours. The presence of a redder foreground galaxy can lead to the exclusion of part of the GL systems in the colour selection process.

- On the other hand, QSOs are expected to be point-like sources. Multiple merged images with the deflector may lead to an object with an apparent ellipticity that can be discarded on the basis of the point-like selection criterion.

Let us introduce in Eq. 4.5 a new reference frame b_1, b_2, b_3 with b_3 aligned along the line-of-sight to the source and b_1 and b_2 are coordinates in a plane perpendicular to the line-of-sight. It comes

$$\tau_{geom} = \int\int\int_{V_{geom}} n_d\left(b_1, b_2, b_3\right) db_1 db_2 db_3. \tag{4.6}$$

Expressing b_3 as a function of the deflector redshift z

$$\tau_{geom}\left(z_s\right) = \int_0^{z_s} \left\{\int\int_{S_{GL}} db_1 db_2 n_d\left(z\right) \frac{cdt}{dz}\right\} dz, \tag{4.7}$$

where S_{GL} is the area in the deflector plane in which the presence of a deflector leads to the formation of multiple images and where *cdt* is the infinitesimal light distance element along the line-of-sight at redshift z. In a flat FLRW universe model, we have (Peebles (1993))

$$\frac{cdt}{dz} = \frac{c}{H_0\left(1+z\right)} \frac{1}{\sqrt{\left(1+z\right)^3 \Omega_{m,0} + \Omega_{\Lambda,0}}}, \tag{4.8}$$

where H_0 is the value of the Hubble constant in the local universe, $\Omega_{m,0}$ [1] is the local universe value of the cosmological density parameter, and $\Omega_{\Lambda,0}$ [2] is the dimensionless Cosmological constant.

The density of deflectors is independent of b_1 and b_2 under the assumption of an isotropic universe and can be taken out of the integration of b_1 and b_2. The remaining integral in the plane perpendicular to the line-of-sight towards the source, over the area S_{GL} in which the presence of a deflector leads to the formation of multiple images, is by definition the geometrical cross section Σ^{dim}_{geom}

$$\Sigma^{dim}_{geom} = \int\int_{S_{GL}} db_1 db_2 = b_0^2 \int\int_{\Omega_{GL}} d\boldsymbol{y}. \tag{4.9}$$

Inserting Σ^{dim}_{geom} in Eq. 4.7 leads to

$$\tau_{geom}\left(z_s\right) = \int_0^{z_s} \Sigma^{dim}_{geom}\left(z\right) n\left(z\right) \frac{cdt}{dz} dz. \tag{4.10}$$

---

[1] $\Omega_{m,0}$ is the ratio between the energy density in the local universe ρ_0 and the critical density $\rho_{crit} = \frac{3H_0^2}{8\pi G}$.

[2] $\Omega_{\Lambda,0} = \Lambda c^2/3H_0^2$, where Λ is the cosmological constant.

In order to perform this integration, we need an expression for the density of deflectors $n\,(z)$. The expression of the density of deflectors will be different depending on the population of deflectors we consider.

4.3 Effective cross section

Amplification phenomenon in GL

The gravitational lensing phenomenon may lead to an amplification of the flux from the background source. Indeed, when a foreground deflector deviates the light rays emitted from a background source towards the observer, the solid angle of the lensed image(s) can be different in size and in shape with respect to that of the non-lensed source. If a lensed image is not resolved, thanks to this change in solid angle and because the specific intensity of the source is preserved, this image will appear *(de-)amplified* with respect to the hypothetical non-lensed source. The amplification factor is given by the ratio of the solid angles of the lensed image and the unlensed source. Schneider (1984) has shown that at least one of the images is always amplified.

If multiple images are formed but detected as a single point-like source (because of a too small angular separation), the amplification of flux received from the background source is the sum of the moduli of the individual image amplifications.

These amplification phenomena can have different effects, among which the possible inclusion of intrinsically fainter sources in a flux limited sample. This is typical in the flux limited case of QSOs, because these objects are unresolved by nature. Thanks to the increase of their geometrical lensing volume, their lensing optical depth increases with their distance. Consequently, in this case, the selection bias in flux limited samples is favourable towards the inclusion of gravitationally lensed sources. There is thus a bias in the calculation of a source optical depth, due to the amplification.

Amplification bias effect

How can we properly take into account the impact of the amplification bias in gravitational lensing statistics? Let us first have an idea of the context in which we want to know the impact of the amplification phenomenon.

Our goal is to estimate the number of gravitational lens systems N_{GL} that will be detected in the population of N_{QSO} within the ILMT survey. In order to determine N_{GL}, we must estimate the mean lensing probability $\langle\tau\rangle$ through the population of QSOs and we will then use the relation

$$N_{GL} = \langle\tau\rangle\, N_{QSO}. \tag{4.11}$$

Defining the distribution $n\,(m, z)$ as a function of their apparent magnitude and redshift of the detected sources (per solid angle), $\langle\tau\rangle$ may be calculated via the

$$\langle \tau \rangle = \frac{1}{N_S} \int \int n\left(m, z_s\right) \tau\left(m, z_s\right) dm dz_s, \tag{4.12}$$

where N_S is the number of sources observed per solid angle unit and $\tau\left(m, z_s\right)$ is the lensing probability of a source with redshift z_s and *observed* apparent magnitude m. τ is thus to be understood as the probability that a source with an apparent magnitude m and redshift z_s, is lensed with formation of multiple images.

The number of gravitational lens systems $dN_L\left(m, z_s\right)$ per solid angle, with a source in the redshift range $[z_s, z_s + dz_s]$ and an apparent magnitude (after the lensing event) in the range $[m, m + dm]$, is thus given by

$$dN_L\left(m, z_s\right) = n\left(m, z_s\right) \tau\left(m, z_s\right) dm dz_s. \tag{4.13}$$

We have seen that gravitational lensing can affect the apparent magnitude of an unresolved source due to the amplification phenomenon.

Let us suppose that all lensing events with a source at redshift z_s have a same amplification $\langle A \rangle$. In Eq. 4.13, as we multiply $\tau\left(m, z\right)$ by the number of *observed* sources with apparent magnitude between m and $m + dm$, $\tau\left(m, z\right)$ must take into account that, due to the amplification, we are referring to a source population whose magnitude is m after the amplification of the lensing event. If there was no amplification due to the lensing event, these sources would have a magnitude of $m + 2.5 \log \langle A \rangle$.

To ensure that $\tau\left(m, z\right)$ accounts for the amplification, we can decompose it as

$$\tau\left(m, z\right) = B\left(m, z, \langle A \rangle\right) \; \tau_{geom}\left(z\right), \tag{4.14}$$

where $\tau_{geom}\left(z\right)$ is the geometrical lensing probability introduced in Section 4.2, taking into account the increase of the geometrical lensing volume with the increasing source redshift, and with

$$B\left(m, z, \langle A \rangle\right) = \frac{n\left(m + 2.5 log \langle A \rangle, z\right)}{n\left(m, z\right)} \tag{4.15}$$

being the amplification bias. The effect of the amplification is thus taken into account by introducing a correction factor to τ_{geom}.

In real lensing events however, the amplification A of the background source is different depending on the deflector position in the lensing volume. In order to take the variation of this amplification into account, when calculating $\tau\left(m, z_s\right)$, the correction factor in Eq. 4.14 is used as a weighing factor while integrating over the geometrical lensing volume. $\tau\left(m, z_s\right)$ is thus calculated through, similarly to Eq. 4.7

$$\tau\left(m, z_s\right) = \int_0^{z_s} \left\{ \int \int_{S_{GL}} B\left(m, z_s, A\left(b_1/b_0, b_2/b_0\right)\right) db_1 db_2 \, n_d\left(z\right) \frac{cdt}{dz} \right\} dz,$$

where $n_d(z)$ is the density of deflectors in the proper volume. Introducing the dimensionless formalism leads to

$$\tau(m,z_s)=\int_0^{z_s}\left\{b_0^2\int\int_{S_y}\frac{n\left(m+2.5logA_{tot}\left(\boldsymbol{y}\right),z_s\right)}{n\left(m,z_s\right)}d\boldsymbol{y}\,n_d\left(z\right)\frac{cdt}{dz}\right\}dz. \quad (4.16)$$

As for the geometrical cross section, we can define the dimensional Σ_{eff}^{dim} and dimensionless Σ_{eff} *effective* cross sections

$$\begin{aligned}\Sigma_{eff}^{dim} &= b_0^2\int\int_{S_y}\frac{n\left(m+2.5logA_{tot}\left(\boldsymbol{y}\right),z_s\right)}{n\left(m,z_s\right)}d\boldsymbol{y},\\ &= b_0^2\Sigma_{eff},\end{aligned} \quad (4.17)$$

that know accounts for the bias introduced by the amplification. The effective optical depth of a lensing event becomes

$$\tau(m,z_s)=\int_0^{z_s}b_0^2\,\Sigma_{eff}\,n_d\left(z\right)\frac{cdt}{dz}\,dz \quad (4.18)$$

Although the definition of Σ_{eff} in Eq. 4.17 is the proper way to take into account the impact of the amplification bias on the lensing cross section, the effective cross section is commonly calculated as

$$\Sigma_{eff}=b_0^2\int\int_{S_{GL}}\frac{N\left(m+2.5logA\left(\boldsymbol{y}\right)\right)}{N\left(m\right)}d\boldsymbol{y} \quad (4.19)$$

where $N(m)$ is the DNCF of the observed sources as a function of their observed apparent magnitude

$$N\left(m\right)=\int_{z_{min}}^{z_{max}}n\left(m,z'\right)dz'. \quad (4.20)$$

where z_{min} and z_{max} define the redshift range of the sources.

The definition of Eq. 4.19 is actually used for historical reasons because the amplification bias was initially introduced considering a mean amplification $\langle A\rangle$. After its introduction, this definition has been adapted (apparently not accounting for the mean amplification assumption) by using the DNCF ratio as a weighing factor over the entire lensing volume.

Calculating the expression of Σ_{eff} via Eq. 4.19 implies the assumption

$$\frac{N\left(m+2.5logA\right)}{N\left(m\right)}=\frac{n\left(m+2.5logA,z_s\right)}{n\left(m,z_s\right)} \quad (4.21)$$

for all values of A and z_s. In other words, it assumes that the slope of $n(m,z_s)$ as a function of m is independent of the redshift.

To check the reliability of this assumption, we have compared the dependence of the ratio of $n\left(m, z_s\right)$ between different magnitudes, as a function of the redshift. The observational data used comes from the quasar catalogue of the SDSS-DR7.

Fig. 4.5a shows the distribution of the QSOs from the SDSS-DR7 in the $\left(m, z_s\right)$ plane. Due to the selection strategy of the SDSS, this constitutes a fairly complete source sample for $m < 19.1$ and $z_s < 2$. We thus use this homogeneous sample to check the slope dependence of $n\left(m, z_s\right)$ (as a function of m) with the redshift.

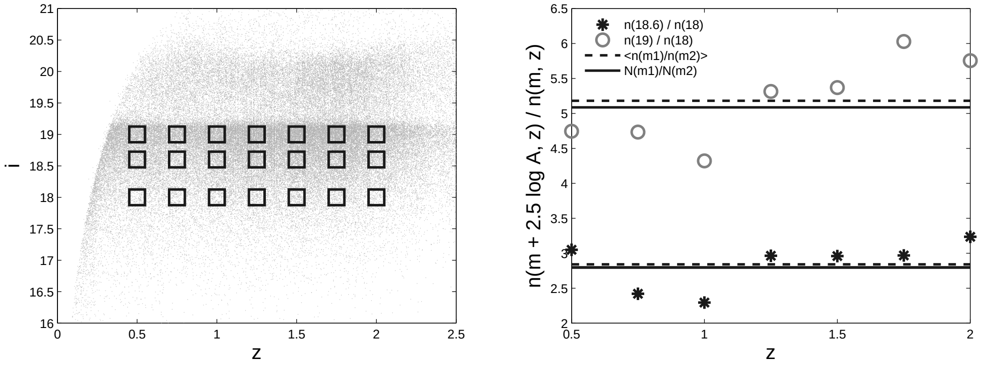

(a)

(b)

Figure 4.5: (a) Distribution of the apparent magnitude i of the QSOs detected in the SDSS-DR7 catalogue of quasars. (b) Ratios between the number of quasars in different magnitude intervals as a function of various redshift values. The dashed lines show the average values of the different ratios, whereas the continuous lines represent the ratios of the DNCF, evaluated at the considered apparent magnitudes, and restricted to the same redshift range.

For different redshift positions ranging from 0.5 to 2, we calculate the mean value of $n\left(m, z_s\right)$ in areas around the magnitudes $i = 18$, 18.6 and 19. The areas in the $\left(m, z_s\right)$ plane over which the mean value of $n\left(m, z_s\right)$ is calculated are shown in Fig. 4.5a. We then compare the dependence of the ratios $n\left(19, z_s\right)/n\left(18.6, z_s\right)$ and $n\left(19, z_s\right)/n\left(18, z_s\right)$ as a function of the QSO redshift. The results are shown in Fig. 4.5b. There is no clear trend for a redshift dependence of these ratios. Although this sample of sources does not span over a sufficiently wide range of magnitude and redshift to ensure that Eq. 4.21 holds over the entire population of QSOs to be detected with the ILMT, we assume that this relation is verified.

We thus follow the definition of Σ_{eff} in Eq. 4.19 and we define the *amplification bias* B as the ratio

$$B = \frac{N\left(m + 2.5logA\left(\boldsymbol{y}\right)\right)}{N\left(m\right)}. \tag{4.22}$$

4.4 Instrumental resolution effect

Let us consider two point-like objects on the sky separated by an angle $\Delta\theta$, imaged by an instrument. Because of the finite size of the instrument PSF, we can define a critical value $\Delta\theta_{crit}$ under which the objects are detected as a single point-like object. $\Delta\theta_{crit}$ is a function of the flux ratio between the two objects.

Let us now consider a gravitational lens system such that the angular separation between the multiple lensed images is too small, these images will be detected as a single point-like object, i.e. a single image. If two such lensed images were the only ones produced by the gravitational lens, then this will not be detected as a lens event; if there were more than two lensed images, then this would be detected as a lensing event with a number of lensed images smaller than the number really produced.

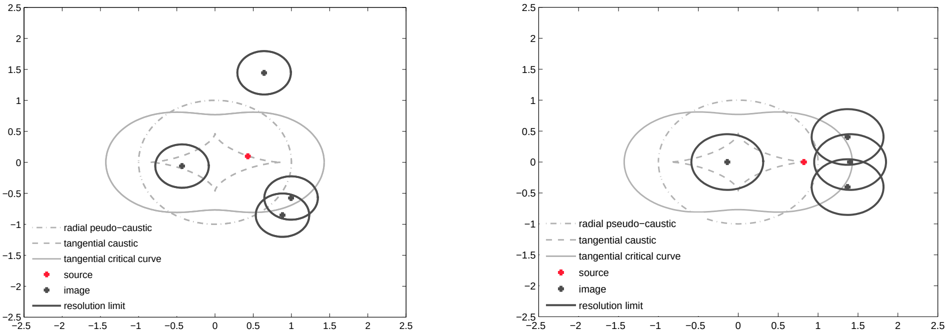

(a) 2 merged lensed images, resolution is $0.35\theta_E$ (b) 3 merged lensed images,resolution is $0.45\theta_E$

Figure 4.6: Two different lensed image configurations. The deflector is an SIS with external shear $\gamma = 0.3$.

As an example, Fig. 4.6a shows a lens system projected in the lens plane normalised to b_0 of an SIS deflector plus external shear $\gamma = 0.3$. The position of the source inside both caustics leads to the formation of 4 images.

We define the parameter R as the critical distance measured in the deflector plane normalised to b_0 corresponding to the angle $\Delta\theta_{crit}$, we thus have

$$R = \frac{\Delta\theta_{crit}}{\theta_E}. \tag{4.23}$$

R is the projection of the instrumental resolution on the deflector plane, normalised to b_0. The circles around the images represent the projection of the instrumental resolution on the normalised deflector plane: the radius of such a circle is R.

In Fig. 4.6a, as the distance between the two lensed images in the bottom right part of the figure is smaller than R, these two images will be detected as a single point-like object. Consequently, when calculating the effective cross sections, this source position will no longer contribute to $\Sigma_{eff,4}$ but will instead contribute to $\Sigma_{eff,3}$.

Deciding on whether a source position leading to the formation of multiple images should be contributing to one effective cross section or another is not always straightforward, as in the configuration depicted on Fig. 4.6b. In this case, the source position leads to the formation of 4 lensed images, with three of them being detected as a single object. But in this case, the object is detected as having an internal ellipticity. We choose that such image configurations contribute to $\Sigma_{eff,3}$ although there are only 2 images detected. The reason for this is that for such a configuration, there will be the detection of a lensing event which will eventually be thoroughly analysed, leading to the conclusion that the non-point like object is composed of multiple images unresolved because of the limited instrumental resolution.

When calculating the effective lensing cross section through equation 4.19, the finite instrumental resolution is taken into account by changing the definition of S_y. It was previously defined as the region of the source plane projected on the deflector plane (normalised to b_0) where a source would lead to the formation of multiple images of the background source, or leading to the formation of a given number of images. We now define S_y as the region where a given number of images is formed and *detected as resolved*.

The dimensional cross section depends on both the instrumental resolution (fixed by $\Delta\theta_{crit}$) and the Einstein angular radius θ_E (through the dependency on $b_0 = D_{OD}\theta_E$). As θ_E is a function of the angular distances between the observer, the deflector and the source, Σ_{eff}^{dim} depends on

- the redshifts of the source z_s and the deflector z_d;
- the universe model parameters;
- the apparent magnitude of the source (through the calculation of the amplification bias effect).

On the other hand, the dimensionless effective cross section Σ_{eff} is only depending on

- the source apparent magnitude,
- the projection R of the instrumental resolution in the deflector plane normalised to θ_E.

We thus see that Σ_{eff} is no longer a function of the universe model and the geometrical configuration of the lens system.

4.5 Lensing probability for simple deflectors

The lensing optical depth expression in Eq. 4.18 was derived assuming that all deflectors are identical. A real population of deflectors, however, is composed of galaxies that may differ in size and shape. Furthermore, the cross section depends on the mass distribution of the deflectors.

In Chapter 3, we have introduced two different mass distributions commonly used in the lensing theory to represent the total mass profiles of galaxies, namely the SIS and SIE profiles. Let us now derive an expression for the lensing optical depth of a source, when modelling the deflectors as SIS or SIE models.

4.5.1 SIS deflectors

Let us consider a population of deflectors composed of spherically symmetric galaxies modelled as SIS, the different individuals possibly differing from one another by their mass. Because their mass dependence, the galaxies have different efficiencies to produce a gravitational lensing event. Therefore, we have to take into account the mass distribution of the deflector population. As the observable linked to the mass distribution of galaxies, we consider their central velocity dispersion σ along the line-of-sight.

We thus need an expression for the density of deflectors $n\left(z,\sigma\right)$ (expressed in terms of proper volume) at a given redshift and for a given σ. This can be expressed as a function of the *Velocity Dispersion Function* (VDF) $\Phi_\sigma\left(\sigma\right)$ of the deflector population. By definition, $\Phi_\sigma\left(\sigma\right)d\sigma$ gives the number of galaxies per unit of comoving volume, with a central velocity dispersion between σ and $\sigma + d\sigma$.

Consequently, the density of deflectors with a central velocity dispersion between σ and $\sigma + d\sigma$ per unit of proper volume at redshift z is given by

$$n\left(z,\sigma\right)d\sigma = \left(1+z\right)^3\,\Phi_\sigma\left(\sigma\right)d\sigma. \tag{4.24}$$

Eq. 4.18 considers a deflector population of identical individuals, with a central velocity in the range $[\sigma, \sigma + d\sigma[$. The probability for a source to be gravitationally lensed with the formation of multiple lensed images by the population of deflectors with a line-of-sight central velocity dispersion in the range σ and $\sigma{+}d\sigma$ is obtained by inserting Eq. 4.24 in Eq. 4.18.

When calculating the probability of a background source to be gravitationally lensed by the deflector population, we have to add the contribution of all the different types of individuals, we thus have to integrate Eq. 4.18 over σ.

Consequently, when considering a population of spherical deflectors with a given mass distribution, the probability τ that a background source with redshift z_s and magnitude m undergoes a gravitational lensing event due to the presence of a deflector near its line-of-sight is given by

$$\tau = C_{sel}\int_0^{z_s} b_0^2 dz \int_{\sigma_{min}}^{\sigma_{max}} \left(1+z\right)^3\Phi\left(\sigma\right)\frac{cdt}{dz}\Sigma_{eff}\left(m\right)d\sigma. \tag{4.25}$$

We thus need an expression for the VDF of the deflector population.

Deflector population VDF

The deflector population is the combination of early and late type galaxies. Although late type galaxies are more abundant in the universe, we will see that early type galaxies are much more efficient deflectors. Consequently, most of the contribution to the lensing probability of a distant source is due to the population of early type galaxies. In this subsection, we present the measured local universe VDF for both galaxy type populations.

Treu et al. (2006) studied the properties of the elliptical galaxy population of lenses detected in the SLACS survey, in combination with the velocity dispersion measurements of the galaxies available in the SDSS data.

They have compared the measured stellar velocity dispersion σ measured in the SDSS with the velocity dispersion σ_{SIE} obtained by fitting the lens events with an SIE lens model.

The authors conclude that

- after correction for evolution of the stellar populations, the SLACS[3] lenses are on the fundamental plane of early type galaxies in the local universe. SLACS lenses thus represent a fair sample of high velocity dispersion ($\sigma \gtrsim 240$ km s^{-1}) early type galaxies. In conclusion, taking into account the selection process (in favour of very massive and luminous early type galaxies), the galaxies are indistinguishable from normal early type galaxies in the local universe;

- the ratio between σ and σ_{SIE} is found to be $f_{SIE} = 1.01 \pm 0.017$ with an rms scatter of 0.065. Lenses are extremely close to isothermal ellipsoids with $\rho \propto r^{-\gamma'}$, with $\gamma' = 2.01^{+0.02}_{-0.03} \pm 0.05$ and an intrinsic rms scatter of 0.12.

Treu et al. (2006) have proved that we can use statistical properties measured from the local universe population in order to characterise the lens galaxy population. Furthermore, this lens population is very well modelled by an SIE profile. In the present work, we thus assume that the statistical properties of the local universe elliptical population properly characterise the population of deflecting early type galaxy lenses (i.e. deflectors).

Basing their work on the SDSS data, Sheth et al. (2003) and Choi et al. (2007) found that the velocity dispersion function of early type galaxies in the local universe is well fitted by a modified Schechter function ϕ of the form

$$\phi\left(\sigma\right) d\sigma = \phi_{*} \left(\frac{\sigma}{\sigma_{*}}\right)^{\alpha} \exp\left(-\left(\frac{\sigma}{\sigma_{*}}\right)^{\beta}\right) \frac{\beta}{\Gamma\left(\alpha/\beta\right)} \frac{d\sigma}{\sigma}. \tag{4.26}$$

---

[3] The Sloan Lens ACS Survey.

Evolution processes of the galaxy population might be taken into account by introducing a redshift dependence on the number density ϕ_*, on the velocity dispersion σ_* and the exponents α and β.

Choi et al. (2007) have determined the VDF of early type galaxies in the local universe, using the SDSS DR5 data (the NYU-VAGC) with a completeness down to $\sigma \approx 70$ km/s using volume limited samples. The best fit parameters obtained are given in Table 4.1. Unless mentioned otherwise, we will use the VDF shape determined by Sheth et al. (2003) throughout this work.

ϕ_* $(h^3 Mpc^{-3})$	σ_* $(km\, s^{-1})$	α	β
	Early type (Choi et al. (2007))		
8.0×10^{-3}	161 ± 5	2.32 ± 0.1	2.67 ± 0.07
	Late type (Chae (2010))		
66.0×10^{-3}	91.5	0.69	2.10

Table 4.1: VDF parameters for early and late type galaxies, derived in the local universe.

On the other hand, Chae (2010) have determined the VDF for late type galaxies, fitting the data with the modified Schechter function Eq. 4.26. The best fit parameters are given in Table 4.1.

Use of the VDF instead of the LF

The density of deflectors can be expressed as a function of the *Luminosity Function* (LF) $\Phi_L(L)$ of the deflector population, fixing the number of galaxies per unit of comoving volume with a given luminosity. The density of deflectors with a luminosity between L and $L + dL$ per unit of proper volume at redshift z is then given by

$$n(z, L)\, dzdL = (1+z)^3\ \Phi_L(L)\, dLdz. \tag{4.27}$$

The probability for a lensing event given by Eq. 4.25 could be calculated using the luminosity function of the galaxy population ϕ_L instead of the VDF, and by integrating over all luminosities L, instead of integrating over the velocity dispersion σ. The early type galaxy luminosity function was shown to be well modelled by the Schechter LF (Schechter (1976))

$$\phi_L(L)\, dL = \phi_L^* \left(\frac{L}{L_*}\right)^{\alpha_L} \exp\left(-\frac{L}{L_*}\right) \frac{dL}{L_*}. \tag{4.28}$$

We would still need to express the galaxy density as a function of the central velocity dispersion because the effective cross section is a function of the σ and not of the luminosity[4].

The VDF would then be inferred from the LF using the observed power-law relation between the galaxy luminosity and velocity dispersion (the Faber-Jackson and the Tully-Fischer law for early and late type galaxies, respectively)

$$\frac{L}{L_*} = \left(\frac{\sigma}{\sigma_*}\right)^{\beta}. \tag{4.29}$$

Note that equations (4.28) and (4.29) along with relation (4.26) imply

$$\alpha_L = \alpha/\beta - 1 \quad \text{and} \quad \phi_L^* = \phi_*/\Gamma\left(\alpha/\beta\right). \tag{4.30}$$

Although the LF in combination with Eq. 4.29 have been used commonly for lensing statistic study, Chae (2010) has shown the use of the LF should be avoided. The author argues that the relations $L = L\left(\sigma\right)$ and $\sigma = \sigma\left(L\right)$ give different values for the power slope β, because the scatter in the luminosity-velocity dispersion correlation acts differently in the fits (Sheth et al. (2003)). To convert the luminosity function into the VDF, one should take into account the scatter in the $L - \sigma$ correlation. To link $\phi\left(\sigma\right)$ to $\phi_L\left(L\right)$, one should use the relation

$$\phi_\sigma\left(\sigma\right) = \int dL\, \phi\left(L\right) p\left(\sigma|L\right), \tag{4.31}$$

where $p\left(\sigma|L\right)$ is the probability of having a line-of-sight velocity dispersion σ for a galaxy with a luminosity L.

Expression of τ for the SIS deflector population

Let us now use the VDF Eq. 4.28 to express the lensing optical depth τ_{SIS} of a source when modelling the deflectors with an SIS profile.

For an SIS deflector, the link between the dimensional cross section Σ_{eff}^{dim} and the dimensionless cross section Σ_{eff} is

$$\Sigma_{eff}^{dim} = b_0^2 \Sigma_{eff} \quad \text{,with} \quad b_0 = 4\pi \left(\frac{\sigma}{c}\right)^2 \frac{D_{OD} D_{DS}}{D_{OS}}. \tag{4.32}$$

If we define $\Sigma_{eff}^{dim}\left(\sigma_*, m\right)$ as the value of the cross section for σ_*, it comes

$$\Sigma_{eff}^{dim}\left(\sigma\right) = \left(\frac{\sigma}{\sigma_*}\right)^4 \Sigma_{eff}^{dim}\left(\sigma_*, m\right). \tag{4.33}$$

Introducing $\Sigma_{eff}^{dim}\left(\sigma_*, m\right)$ in Eq. 4.25 and using the modified Schechter expression in Eq. 4.26 for the VDF, the lensing probability τ_{SIS} of a source, is given

---

[4] We could do the integration over the luminosity but then we would need to express the effective cross section as a function of the luminosity. In order to do this, we could use the Tully-Fischer relationship, still neglecting the dispersion in this relationship.

by

$$\begin{aligned} \tau_{SIS} &= C_{sel}\int_0^{z_s}\left\{(1+z)^3\frac{cdt}{dz}\phi_*\frac{\beta}{\Gamma(\alpha/\beta)}\Sigma_{eff}^{dim}(\sigma_*,m)\right. \\ &\left.\int_{\sigma_{min}}^{\sigma_{max}}\left(\frac{\sigma}{\sigma_*}\right)^{\alpha+4}\exp\left(-\left(\frac{\sigma}{\sigma_*}\right)^{\beta}\right)\frac{d\sigma}{\sigma}\right\}dz. \end{aligned} \tag{4.34}$$

Introducing the new variable $u = \left(\frac{\sigma}{\sigma_\star}\right)^\beta$, it comes:

$$\begin{aligned} du &= \beta\left(\frac{\sigma}{\sigma_*}\right)^{\beta-1}\frac{d\sigma}{\sigma_*}, \\ &= \beta\left(\frac{\sigma}{\sigma_*}\right)^{\beta}\frac{d\sigma}{\sigma}, \\ \Rightarrow \frac{d\sigma}{\sigma} &= \frac{1}{\beta}\frac{du}{u}. \end{aligned} \tag{4.35}$$

The integral over σ in Eq. 4.34 can be expressed as

$$\begin{aligned} I_\sigma &= \int_{\sigma_{min}}^{\sigma_{max}}\left(\frac{\sigma}{\sigma_*}\right)^{\alpha+4}\exp\left(-\left(\frac{\sigma}{\sigma_*}\right)^{\beta}\right)\frac{d\sigma}{\sigma}, \\ &= \frac{1}{\beta}\int_{u_{min}}^{u_{max}} u^{\frac{\alpha+4}{\beta}}\exp(-u)\frac{du}{u}, \\ &= \frac{1}{\beta}\Gamma((\alpha+4)/\beta),. \end{aligned} \tag{4.36}$$

where $u_{min} = (\sigma_{min}/\sigma_*)^\beta$ and $u_{max} = (\sigma_{max}/\sigma_*)^\beta$ and where the last expression is obtained by defining $\sigma_{min} = 0$ and $\sigma_{max} \to \infty$, and by using the definition of the gamma function

$$\Gamma(x) = \int_0^{+\infty} t^{x-1}\exp^{-t} dt. \tag{4.37}$$

Introducing the expression of I_σ into Eq. 4.34, we obtain

$$\tau_{SIS} = C_{sel}\int_0^{z_s}\left\{(1+z)^3\frac{cdt}{dz}\phi_*\Sigma_{eff}^{dim}(\sigma_*,m)\frac{\Gamma((\alpha+4)/\beta)}{\Gamma(\alpha/\beta)}\right\}dz.$$

If we furthermore assume that there is no evolution of the deflector population with redshift, then α, β and ϕ_* can be taken out of the integral sign, which leads to

$$\tau_{SIS}(m,z_s) = C_{sel}\phi_*\frac{\Gamma((\alpha+4)/\beta)}{\Gamma(\alpha/\beta)}\int_0^{z_s}\left\{(1+z)^3\frac{cdt}{dz}\Sigma_{eff}^{dim}(\sigma_*,m)\right\}dz. \tag{4.38}$$

This relation allows to calculate the lensing optical depth associated with a source with a redshift z_s and an apparent magnitude m. We will use this expression to calculate the mean lensing probability in the expected population of QSOs to be detected with the ILMT.

4.5.2 SIE deflectors

Let us now consider a population of deflectors with an internal ellipticity described by the SIE mass profile. Individuals may thus differ by both their mass and by their internal ellipticity. The internal ellipticity of the deflector mass distribution is thus modelled by the ellipticity of the mass distribution itself.

The observable chosen to be representative of the mass distribution ellipticity is the axis ratio f of the isodensity ellipses of the projected mass distribution. As in the case of the SIS, the observable representing the mass of the deflector is the central velocity dispersion σ along the line-of-sight.

The density of deflectors per unit of proper volume with a central velocity dispersion between σ and $\sigma + d\sigma$ and an axis ratio in the range f and $f + df$, at redshift z is given by

$$n\left(z, \sigma, f\right) d\sigma df = \left(1+z\right)^3 \; \Phi_{\sigma, f}\left(\sigma, f\right) d\sigma df, \tag{4.39}$$

where $\Phi_{\sigma,f}$ is the density of deflectors with a line-of-sight velocity dispersion σ and mass distribution axis ratio f.

The probability of a source to be lensed by a deflector with σ and f in the range $\sigma + d\sigma$ and $f + df$, respectively, is obtained by inserting Eq. 4.39 in Eq. 4.18. To take into account the axis ratio f dependence in the mass distribution of the deflector galaxy population, we integrate relation (4.18) over f and σ.

The probability τ_{SIE} that a source with a given redshift and apparent magnitude m undergoes a gravitational lensing event due to the presence of a deflector near its line-of-sight, is thus given by

$$\tau\left(m, z_s\right) = C_{sel} \int_0^{z_s} \mathrm{d}z \int_{\sigma_{min}}^{\sigma_{max}} \mathrm{d}\sigma \int_0^1 \mathrm{d}f \left\{ \left(1+z\right)^3 \frac{cdt}{dz} \; \Phi_{\sigma,f} \; \Sigma_{eff}^{dim}\left(\sigma, f, m\right) \right\}. \tag{4.40}$$

$\Phi_{\sigma,f}$ is linked to the VDF of the deflecting galaxy population by means of the relation

$$\Phi_{\sigma,f} \, \mathrm{d}\sigma \, \mathrm{d}f = \Phi_\sigma \, \mathrm{p}\left(f|\sigma\right) \mathrm{d}\sigma \, \mathrm{d}f, \tag{4.41}$$

where $\mathrm{p}\left(f|\sigma\right)$ is the probability of having an axis ratio f, given a galaxy with velocity dispersion σ.

If we assume that the distribution of the central velocity dispersion σ and the distribution of the axis ratio f in the population of the deflecting galaxies are independent[5], then τ_{SIE} may be written as

$$\tau_{SIE} = C_{sel} \int_0^{z_s} \mathrm{d}z \int_{\sigma_{min}}^{\sigma_{max}} \mathrm{d}\sigma \int_0^1 \mathrm{d}f \left\{ \left(1+z\right)^3 \frac{cdt}{dz} \; \Phi_\sigma \; \mathrm{p}\left(f\right) \; \Sigma_{eff}^{dim}\left(\sigma, f, m\right) \right\}, \tag{4.42}$$

---

[5] By definition of the conditional probability

$$\mathrm{p}\left(f|\sigma\right) = \frac{\mathrm{p}\left(f \cap \sigma\right)}{\mathrm{p}\left(\sigma\right)}$$

where $\mathrm{p}\left(f \cap \sigma\right) = \mathrm{p}\left(f\right) \mathrm{p}\left(\sigma\right)$ if the distributions of f and σ are independent.

where p (f) is the density of probability of having an axis ratio f. As for the case of an SIS deflector population, we use the VDF from Eq. 4.26.

Nevertheless, beside the expression of the VDF, we also need the probability density function of the axis ratio in the deflector population.

The probability density p (f) associated with the axis ratio f can be obtained by normalising the axis ratio function Φ_f of the axis ratio distribution for the early type galaxy population observed in the nearby universe.

Axis ratio distribution of the deflector population

Koopmans et al. (2006) used data from a sub-sample of the SLACS (Bolton et al. (2008)) survey (15 lenses), combining constraints from HST images with stellar velocity dispersions from the SDSS database in order to study the correlation between isophotal-ellipticity and the mass distribution ellipticity found when modelling the gravitational lenses. They conclude that

- the misalignment between the stellar component and the SIE lens model is found to be null in the lens population ($\langle \Delta\theta \rangle = 0^\circ \pm 3^\circ$, with an rms spread of 10°);

- no external shear was necessary to better fit the lenses in addition to the ellipticity of the deflectors ($\langle \gamma_{ext} \rangle \lesssim 0.035$);

- the elliptical isophotal and isodensity contours (from the fitted SIE) seem to trace each other very well. The ratio of the ellipticity of the stellar light ($q_\star$) and the SIE ellipticity q_{SIE} is $\langle q_{SIE}/q_\star \rangle = 0.99$ with an rms of 0.11. Hence, mass traces light also in the ellipticity. $\langle q_{SIE} \rangle = 0.78 \pm 0.03$ (rms 0.12), which is in very good agreement with nearby E/S0 galaxies which peaks between 0.7 and 0.8. Thus, they also conclude that ellipticities of the SLACS lens galaxies are similar to those of nearby early type galaxies;

- below $z \sim 1$, massive early type galaxies show a very homogeneous inner mass density profile ($\rho_{tot} \propto r^{-\gamma'}$, with an average value of $\langle \gamma' \rangle = 2.01^{+0.02}_{-0.03}$, with an intrinsic spread $\sigma_{\gamma'} = 0.12$, i.e. less than 6%). There is no evidence of γ' evolution with redshift below $z = 1$.

The work of Koopmans et al. (2006) tends to prove that the direction of the mass ellipticity and the direction of the isophote ellipticity are the same.

Sluse et al. (2012) gave an independent confirmation of the link between the ellipticity in the mass distribution and the isophote ellipticity.

Furthermore, we have seen in Section 4.5.1 that there are strong arguments in favour of using local universe measurements of early type galaxies to characterise the deflector population associated with the lensing events.

Consequently, the probability density p (f) associated with the axis ratio f can be obtained by normalizing the axis ratio function Φ_f from the isophotes of nearby galaxies.

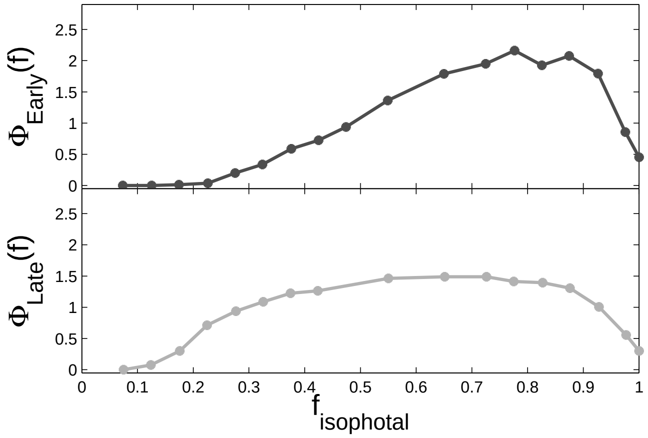

Figure 4.7: Axis ratio distribution for early and late type galaxies, based on SDSS local universe data analyzed by Choi et al. (2007)

.

Choi et al. (2007) have determined the distribution of isophote axis ratios of early type and late type galaxies (in the local universe), based on the analysis of a cleaned sample of the SDSS DR5 called the NYU-VAGC (*New-York University Value-Added Galaxy Catalog*). The determined distribution Φ_{Early} and Φ_{Late} are shown as a function of the axis ratio f in Fig. 4.7.

Expression of τ_{SIE}

Let us now introduce the VDF expression of Eq. 4.26 in Eq. 4.42. The scaling factor b_0 of an SIE deflector being the same as for the SIS case, the link between the SIE cross section and the dimensionless SIE cross section is also given by Eq. 4.32. Consequently, expression of $\Sigma_{eff}^{dim}(\sigma_*)$ in Eq. 4.33 is still valid.

Inserting Eq. 4.33 in Eq. 4.42 and considering a VDF for the early type galaxies with the shape of the modified Schechter function in Eq. 4.26, the optical depth τ_{SIE} of a lensing event for a given source, when considering a population of SIE deflectors becomes

$$\begin{aligned}\tau_{SIE} &= C_{sel}\int_0^1 \mathrm{d}f \int_0^{z_s} dz \left\{ (1+z)^3 \frac{cdt}{dz}\phi_* \frac{\beta}{\Gamma(\alpha/\beta)} \mathrm{p}(f)\, \Sigma_{eff}^{dim}(\sigma_*, f, m) \right. \\ &\left. \left(\int_{\sigma_{min}}^{\sigma_{max}} \left(\frac{\sigma}{\sigma_*}\right)^{\alpha+4} \exp\left(-\left(\frac{\sigma}{\sigma_*}\right)^{\beta}\right) \frac{d\sigma}{\sigma} \right) \right\} dz.\end{aligned}$$

As for the SIS case, performing the integration over σ when considering $\sigma_{min} = 0$ and $\sigma_{max} \to \infty$, and using the definition of the Γ function (see Eq. 4.37), the probability τ_{SIE} for a source to be lensed is given by

$$\tau_{SIE} = C_{sel} \int_0^{z_s} dz \int_0^1 \mathrm{d}f \left\{ (1+z)^3 \phi_* \frac{\Gamma\left(\left(\alpha+4\right)/\beta\right)}{\Gamma\left(\alpha/\beta\right)} \frac{cdt}{dz} \mathrm{p}\left(f\right) \Sigma_{eff}^{dim}\left(\sigma_*, f, m\right) \right\}.$$

Furthermore, assuming that the deflector VDF does not evolve with redshift, we obtain

$$\begin{aligned} \tau_{SIE}\left(m, z_s\right) = C_{sel}\phi_* \frac{\Gamma\left(\left(\alpha+4\right)/\beta\right)}{\Gamma\left(\alpha/\beta\right)} & \\ \int_0^{z_s} dz \int_0^1 \mathrm{d}f \left\{ (1+z)^3 \frac{cdt}{dz} \mathrm{p}\left(f\right) \Sigma_{eff}^{dim}\left(\sigma_*, f, m\right) \right\} & \end{aligned} \tag{4.43}$$

$\tau_{SIE}\left(m, z_s\right)$ allows to calculate the lensing optical depth for a source with redshift z_s and apparent magnitude m, for a population of deflectors modelled with SIE profiles. As noticed earlier, an SIE deflector allows to produce more than 2 lensed images of a background source. Consequently, we can define cross sections associated with the number of lensed images formed. In Eq. 4.43, depending on the cross section used, we can thus calculate the probability of a source to be lensed with the formation of 2, 3 or 4 lensed images.

4.6 Numerical considerations about the calculation of the gravitational lensing optical depth and the cross sections

In Sections 4.5.1 and 4.5.2, we have derived in Eq. 4.38 and Eq. 4.43 the expressions of the lensing optical depth τ_{SIS} and τ_{SIE} for a source with apparent magnitude m and redshift z_s in presence of a deflector population of SIS and SIE, respectively. These expressions of the lensing optical depth take into account the bias introduced by the amplification phenomenon, as well as the effect of the finite instrumental resolution.

In the framework of this thesis, we have implemented Matlab libraries allowing to calculate τ_{SIS} and τ_{SIE}.

In both cases, the calculation of the optical depth is done through the calculation of an integral along the source line-of-sight (the redshift of the deflector) of an integrand where the effective cross section Σ_{eff}^{dim} appears as a weighing factor.

Σ_{eff}^{dim} is itself defined as an integral that has to be calculated numerically. Because of calculation time considerations, we cannot afford to re-calculate the cross section integral for every redshift step.

We have seen that when decomposing Σ_{eff}^{dim} as

$$\Sigma_{eff}^{dim} = b_0^2\, \Sigma_{eff} = b_0^2 \int_{S_y(R)} \frac{N\left(m + 2.5\log A_{tot}\right)}{N\left(m\right)} d\boldsymbol{y}, \tag{4.44}$$

the dimensionless cross section is no longer directly a function of the redshifts of the source and the universe model, the impact of these being all included in the parameter R. Σ_{eff}^{dim} is thus a function of the :

- the source and deflector redshifts z_s and z_d;
- the universe model parameters;
- the magnitude of the source m;
- the deflector parameters (σ_*, and f for the SIE deflectors);
- the differential number counts of the sources as a function of their magnitude for the calculation of the amplification bias;
- the instrumental angular resolution (through the dependence of S_y on $R = FWHM/\theta_E$)

and the dimensionless cross section is a function of

- the magnitude of the source m;
- the axis ratio f for the SIE deflectors;
- the differential number counts of the sources as a function of their magnitude for the calculation of the amplification bias;
- R the projection of the instrumental resolution on the normalised deflector plane.

To perform the integration of the lensing optical depth, we have thus generated a database of Σ_{eff} in which we pick up the needed values when integrating over the deflector redshift. We have generated a database ranging over all possible values of f, the apparent magnitude m and the parameter R.

The dimensionless cross sections are calculated performing Monte-Carlo integration. The numerical integration process is explained in the next section.

The Monte-Carlo calculation of the cross section

The calculation of the dimensionless effective cross section is performed by doing a plain pseudo-random Monte Carlo integration of the following relationship

$$\Sigma_{eff} = \int_{S_{MC}} S\left(\boldsymbol{y}\right) \frac{N\left(m + 2.5 \log A_{tot}\right)}{N\left(m\right)} d\boldsymbol{y} = \int_{S_{MC}} f_{\Sigma}\left(\boldsymbol{y}\right) d\boldsymbol{y}$$

where

- S_{MC} is the area in the source plane projected on the normalised deflector plane including the entire area over which contribution to the cross section is non-zero: it is called the Monte-Carlo integration surface, all the evaluation points of the function during MC integration are generated in this area;

- $S(\boldsymbol{y})$ is a selection function that equals one if the point $\boldsymbol{y}$ has a non-zero contribution to the cross section, and equals 0 otherwise. This function takes into account whether the considered source position leads to the formation of multiple images and whether these images can be detected considering the finite instrumental resolution;
- A_{tot} is the total amplification of the source at the position $\boldsymbol{y}$, i.e. the sum of the moduli of the multiple lensed image amplifications;
- $f_\Sigma(\boldsymbol{y})$ is a function giving the contribution of the point $\boldsymbol{y}$ to the effective cross section
$$f_\Sigma(\boldsymbol{y}) = S(\boldsymbol{y}) \frac{N(m + 2.5 \log A_{tot})}{N(m)}.$$

Through the Monte-Carlo integration the effective dimensionless cross section value is thus calculated as

$$\Sigma_{eff} \simeq \frac{S_{MC}}{N_{iter}} \sum_{iter} f_\Sigma(\boldsymbol{y}_{iter}),$$

where $\boldsymbol{y}_{iter}$ are the Monte-Carlo test points generated in the source plane, and where N_{iter} is the number of Monte-Carlo evaluation points.

For each iteration, we generate a random position $\boldsymbol{y}_{iter}$ in the source plane (projected on the deflector plane, normalised to b_0) and determine whether this position is inside the caustics. If it is inside the caustics, we invert the lens equation to find the position of the images formed. If there is more than one image formed and detected by the instrument, we calculate the total amplification of the source $A_{tot}(\boldsymbol{y}_{iter})$ and calculate the amplification bias.

All the operations at each iteration make use of the libraries mentioned in Chapter 3. Each dimensionless cross section in the database was calculated with 10^6 iterations.

Thanks to these libraries and the database, we now have the tools to calculate the lensing optical depths τ_{SIS} and τ_{SIE} for a population of sources.

In the next chapter, we will explain how we simulate the QSO sources to be detected with the ILMT, for which we calculate τ_{SIS} and τ_{SIE} in Chapter 6.

Chapter 5

Simulating the ILMT QSO catalogue

In Chapter 4, we have derived relationships to calculate the probability τ that a QSO source with a known redshift and apparent magnitude undergoes a gravitational lensing event due to the foreground deflector population. We want to use this relationship to estimate the number of gravitationally lensed QSOs to be detected with the ILMT. This is achieved by simulating the QSO population that is to be detected in the ILMT survey and by calculating the lensing event probability associated with each simulated source. Afterwards, using the average lensing probability $\langle\tau\rangle$ through the source population, the number N_{GL} of expected gravitational lens systems is merely given by the relation

$$N_{GL} = \langle\tau\rangle\ N_{QSO},$$

where N_{QSO} is the total number of detected QSOs.

The aim of this chapter is to estimate the population of QSOs that is to be detected in the ILMT survey.

We first determine the survey angular coverage in which QSO detection is possible and the accessible cosmological volume defined by this solid angle. We then determine the luminosity function of QSOs based upon recent and independent surveys, fixing the density of QSOs as a function of their luminosity and redshift. The final catalogue is constructed by simulating the QSO population in the cosmological volume and keeping only sources whose apparent magnitude is brighter than the survey limiting magnitude.

5.1 Survey angular coverage and accessible volume

Because of the ILMT zenithal pointing mount, at any time, the ILMT *field of view* (FOV) is centred at a declination δ_{ILMT} equal to the observatory latitude.

The ILMT is located at the Devasthal observatory which latitude is 29.3617°N (see Sagar et al. (2000) for a full description of the site), with a field-of-view of

$27'$ by $27'$ centred on the zenith.

Thanks to the Earth rotation, the angular area $\Omega_{ILMT,tot}$ accessible by the ILMT is a strip of sky, centered at the constant declination δ_{ILMT}. The width of the strip is defined by the FOV North-South width $\Delta_{ILMT} = 27'$.

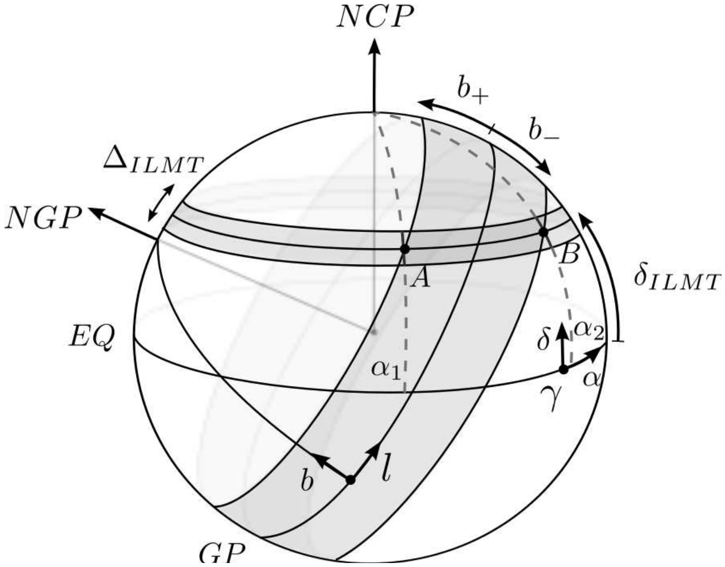

Figure 5.1: Projection on the unitary celestial sphere of the ILMT strip of sky and the strip characterised by a low galactic latitude. QSO detection will only be possible in the ILMT strip with a galactic latitude larger than $|b| \gtrsim 30°$.

Let us represent the celestial sphere as depicted in Fig. 5.1, on which we have projected the *Equatorial Plane* (EQ), the direction of the *North Celestial Pole* (NCP), defined by the Earth rotation axis direction and the vernal point γ. The ILMT sky coverage is represented as a shade strip centered on δ_{ILMT}.

Assuming a unitary celestial sphere radius and expressing the right ascension α and the declination δ in radians, the solid angle $\Omega_{ILMT,tot}$ accessible by the ILMT is given by

$$\begin{aligned}\Omega_{ILMT,tot} &= \int_0^{2\pi}\int_{\delta_-}^{\delta_+} \cos(\delta)\,\mathrm{d}\delta\,\mathrm{d}\alpha \\ &= 2\pi\,[\sin(\delta)]_{\delta_-}^{\delta_+} \\ &= 141.2 \quad \text{(sq.deg.)},\end{aligned}$$

where $\delta_\pm = \delta_{ILMT} \pm \Delta_{ILMT}/2$ represent the declinations of the accessible strip borders. The ILMT will thus cover 141.2 square degrees of the sky.

The ILMT strip crosses the galactic plane twice as shown in Fig. 5.1 where we have projected the *Galactic Plane* (GP) and the *North Galactic Pole* (NGP) on the celestial sphere.

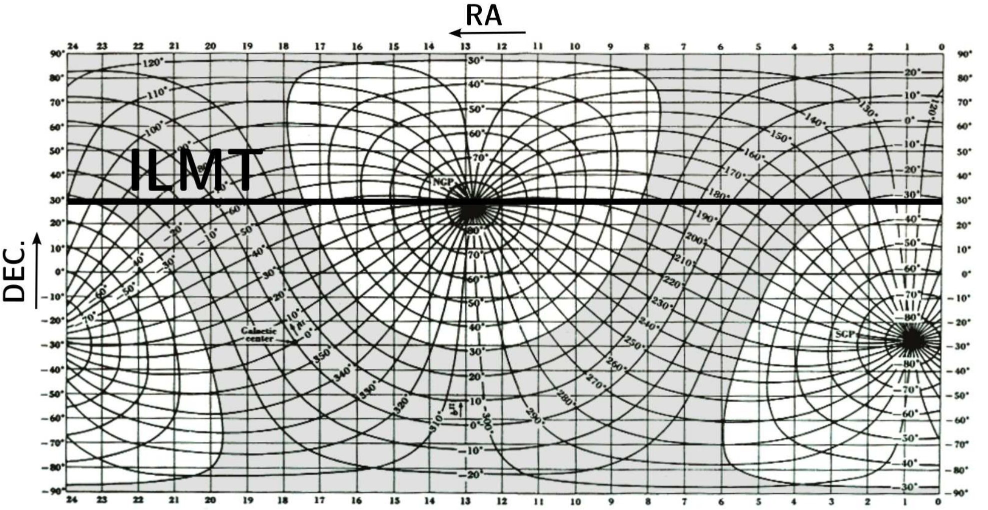

Figure 5.2: Projection of the galactic coordinates in the Right Ascencion - Declination plane. The ILMT strip is marqued as a black line. The low galactic latitude fields ($|b| < 30°$) are shaded.

Low galactic latitude fields are very crowded fields due to the presence of foreground milky way stars, making very difficult to detect fainter extra-galactic objects. Consequently, the detection of QSOs will only be possible in areas at high galactic latitude b (typically $|b| \gtrsim 30°$). Fig. 5.2 shows the projection of the galactic coordinates in the Right Ascencion - Declination plane, where the fields with a galactic latitude lower that $|b| < 30°$ have been shaded. The strip accessible with the ILMT is shown as a black line.

To evaluate the area Ω_{ILMT} where QSO detection is possible, we must thus subtract the part of the ILMT strip at low galactic latitude, i.e. with a galactic latitude $b_- < b < b_+$, with $b_\pm = \pm b_{crit}$.

We approximate the angular area corresponding to each intersection of the ILMT and galactic strips by the part of the ILMT strip between right ascension α_1 and α_2, where the center of the strip crosses the curves of constant galactic latitude b_+ and b_-, respectively.

In order to find the expression of α_1 and α_2, we use the transformation law between galactic coordinates (l, b) and equatorial coordinates (α, δ) given in Lane (1979); Duffet-Smith (1988). The galactic latitude is related to the equatorial coordinates as follows

$$\sin b = \cos\delta \cos\delta_{NGP} \cos(\alpha - \alpha_{NGP}) + \sin(\delta) \sin(\delta_{NGP}), \tag{5.1}$$

where $(\alpha_{NGP}, \delta_{NGP})$ [1] represent the north galactic pole equatorial coordinates. Inverting Eq. 5.1, we find the expression of α_1 and α_2

$$\alpha_{1,2} = \alpha_{NGP} + \arccos\left[\frac{\sin b_\pm - \sin\delta_{ILMT}\sin\delta_{NGP}}{\cos\delta_{ILMT}\cos\delta_{NGP}}\right].$$

Inserting the values, we find that QSO detection is possible for right ascencions in the range 8h12' - 17h26' and 23h28' - 2h10'. The position of these fields at high galactic latitude can easily be seen in Fig. 5.2.

The ILMT angular coverage at high galactic latitude Ω_{ILMT} is thus given by

$$\begin{aligned}\Omega_{ILMT} &= \Omega_{ILMT,tot} - 2\int_{\alpha_1}^{\alpha_2}\int_{\delta_-}^{\delta_+}\cos\delta\,\mathrm{d}\delta\,\mathrm{d}\alpha \\ &= \Omega_{ILMT,tot} - 2\,(\alpha_2 - \alpha_1)\,(\sin\delta_+ - \sin\delta_-)\,.\end{aligned}$$

The accessible extra-galactic FOV is given in Table 5.1 for different values of the critical galactic latitude b_{crit}. The high galactic latitude condition excludes about half of the accessible sky, leaving between 70 and 85 deg^2. For information, the total and high galactic sky when considering a range $\Delta_{ILMT} = 30'$ is also indicated in the table.

FW	total	$\|b\| > 30$	$\|b\| > 27.5$	$\|b\| > 25$
27'	141.2	70.2	78.1	85
30'	156.8	77.9	86.7	94.4

Table 5.1: Total and high galactic latitude FOV accessible with the ILMT for different values of the critical galactic latitude b_{crit} and the Field North-South width (FW).

The solid angle Ω_{ILMT} defines a volume within which QSOs may be detected. In a flat static universe, the volume element at distance D and of width dD defined by this solid angle would simply be

$$dV = \Omega_{ILMT} D^2 dD. \tag{5.2}$$

When considering a flat expanding FLRW universe, the latter relation is valid as long as comoving distances are used. Furthermore, the comoving volume element is more usefully expressed as a function of the redshift z which is directly accessible through observation.

The infinitesimal comoving volume element dV_c over the solid angle Ω_{ILMT} defined in the redshift range $[z, z + dz]$ as shown in Fig. 5.3 is

$$dV_c = \Omega_{ILMT}\, D_C^2\, \frac{dD_C}{dz}\, dz, \tag{5.3}$$

---

[1] In conventional units, $\alpha_{NGP} = 12^h 49^m$ and $\delta_{NGP} = +27°24'$.

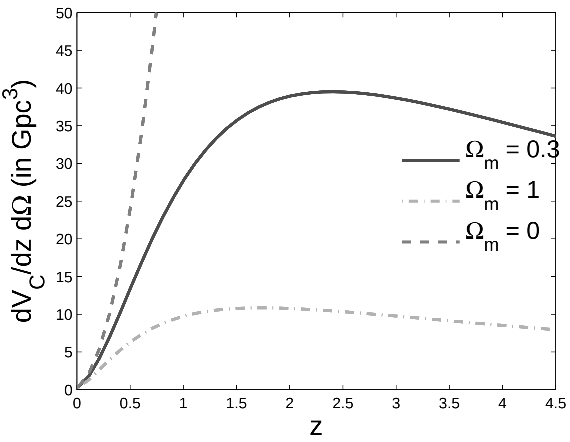

Figure 5.3: Variation of the comoving volume per unit of solid angle as a function of the redshfit z in a flat FLRW expanding universe, for three different values of $\Omega_m = 0, 0.3$ and 1.

where $\frac{dD_C}{dz}$ is the variation of the comoving distance as a function of the redshfit and can be expressed as

$$\begin{aligned} \frac{dD_C}{dz} &= \frac{c}{H_0}\frac{1}{E(z)}, \qquad (5.4) \\ \text{with} \quad E(z) &= \sqrt{\Omega_M (1+z)^3 + \Omega_\Lambda} \end{aligned}$$

and where Ω_M and Ω_Λ are the local values of the dimensionless density parameters (Peebles (1993); Hogg (2000)). The line-of-sight comoving distance $D_c(z)$ of an object with redshift z is obtained by integrating Eq. 5.4 over the redshift.

The volume defined by the ILMT survey coverage at high galactic latitude up to a redshift z is obtained by integrating Eq. 5.3

$$V_{ILMT}(z) = \Omega_{ILMT} \int_0^z \frac{c}{H_0} \frac{D_c^2(z')}{E(z')} \mathrm{d}z' \qquad (5.5)$$

This integration as well as all cosmological distance determinations are performed numerically using the cosmological *Matlab* library developed by E. Ofek[2].

5.2 QSO Luminosity Function

We now know the expression of the cosmological volume accessible to the ILMT observations in which QSOs are detectable. In order to simulate the QSO population to be detected, we need to know how the population of QSOs is distributed in this volume, i.e. the QSO population density all through the accessible volume.

---

[2] http://www.astro.caltech.edu/~eran/matlab.html

This information is contained in the QSO *Luminosity Function* (LF) giving the density of QSOs per comoving volume unit, per interval of the QSO luminosity. The LF can also be expressed as a function of the absolute magnitude of the QSO. Before describing the QSO LF, in the next section, we remind the definition the absolute magnitude and the K-correction.

5.2.1 Absolute magnitude and K-correction

Let us consider a QSO with a bolometric luminosity L (i.e. the total energy emitted per time interval over all wavelengths). An astronomer observing this source can measure its flux F which, in the UV/optical/infrared is commonly measured along a logarithmic scale called the magnitude. The apparent magnitude of the source is

$$m = -2.5 \log_{10} \left(\frac{L}{4\pi D_l^2} \right) - C^{st}, \tag{5.6}$$

where D_l is the luminosity distance and C^{st} the magnitude of a reference source to set the zero point.

In order to compare the intrinsic brightness of objects at different distances, we define the *absolute magnitude* M as the apparent magnitude of an object located at a reference luminosity distance of 10 parsec,

$$\begin{aligned} M &= -2.5 \log_{10} \left(\frac{L}{4\pi 10^2} \right) - C_{st} & (5.7) \\ &= m - 5 \log_{10} \left(\frac{D_L}{10pc} \right) & (5.8) \\ &= m - DM. & (5.9) \end{aligned}$$

The apparent magnitude m and the absolute magnitude are linked through the term DM which is a function of the distance of the object, called the *distance modulus.*

Astronomical observations are usually performed through a filter with a given band width at a given wavelength. It is thus convenient to define the fluxes, luminosities and the magnitudes relatively to the observed spectral window. For observations performed at a wavelength λ, we thus define the luminosity at this wavelength L_λ and the corresponding magnitudes m_λ and M_λ calculated through (5.6) and (5.9), respectively.

The monochromatic absolute magnitude M_λ does not provide any longer a good comparison between the intrinsic brightnesses of sources located at different distances.

Indeed, because of the universe expansion, a photon emitted by a source at a wavelength λ_e is redshifted and is observed at a wavelength λ_o

$$\lambda_o = \lambda_e \left(1 + z\right), \tag{5.10}$$

where z is the redshift of the object. Thus, when observing at a wavelength λ objects at different distances (and thus with different redshifts), we are probing different parts of the restframe spectra of the objects.

Furthermore, photons observed in the interval $d\lambda_o$ were emitted in the interval

$$d\lambda_e = \frac{d\lambda_o}{(1+z)}. \tag{5.11}$$

The effective bandwidth defined by a filter in the object restframe thus contracts as $(1+z)$ as the object redshift increases.

To account for these effects, when calculating the absolute magnitude of an object we must introduce a correction term K, the *K-correction*, accounting for the change of the restframe spectral window

$$M = m - DM - K. \tag{5.12}$$

The absolute magnitude calculated through this equation allows a direct comparison of the intrinsinc brightnesses of objects located at different distances.

Oke and Sandage (1968) and Kim et al. (1996) define the K-correction as

$$K(z) = 2.5\log_{10}(1+z) + 2.5\log_{10}\left(\frac{\int F(\lambda)\, S(\lambda)\, d\lambda}{\int F(\lambda/(1+z))\, S(\lambda)\, d\lambda}\right), \tag{5.13}$$

where $F(\lambda)$ is the source spectral energy distribution as measured in its comoving restframe and $S(\lambda)$ is the filter transmission. The first term accounts for the contraction of the bandwidth with redshift whereas the second term accounts for the difference of flux density at the emission wavelength.

As seen in Eq. 5.13, the K-correction depends on the spectral energy distribution of the source. As we are interested in QSOs, let us consider a typical QSO spectrum as shown in Fig. 5.4, in its restframe. This synthetic QSO spectrum has been constructed by Vanden Berk et al. (2001) who have combined QSO spectra from the SDSS survey.

For wavelengths redder than the Ly_α emission line, the QSO spectrum results from the superposition of a continuum spectrum described as a power-law distribution F_{cont} that shows a wavelength dependence according to

$$F_{cont}(\lambda) \propto \lambda^{-(2+\alpha_\nu)}, \tag{5.14}$$

plus a contribution due to emission lines. The power-law contribution is due to emission from the central regions of the QSO.

It is practical to separate the contribution to the K-correction due to the continuum part of the spectrum K_{cont} and due to the emission lines K_{em} (Richards et al. (2006),Ross et al. (2012)), i.e.

$$K = K_{cont} + K_{em}. \tag{5.15}$$

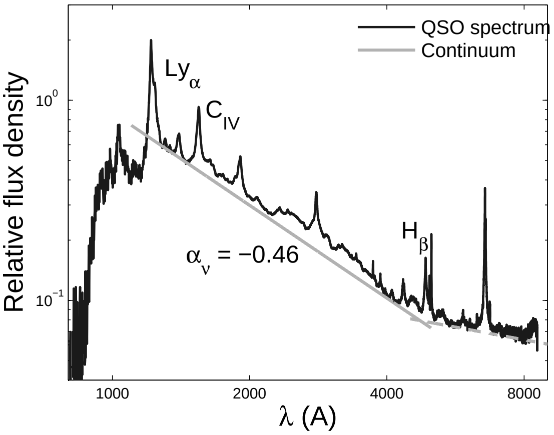

Figure 5.4: Composite spectrum of a QSO based upon observed SDSS spectra, from Vanden Berk et al. (2001).

When comparing all QSOs in their restframe at redshift $z = 0$, the continuum contribution K_{cont} is calculated by inserting the power-law form of the continuum (5.14) into the K-correction definition (5.13). This leads to

$$K_{cont} = -2.5\,(1 + \alpha_\nu)\log_{10}(1 + z)\,. \tag{5.16}$$

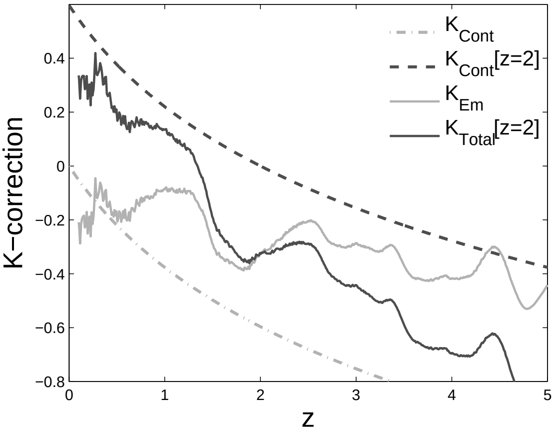

Figure 5.5: K-correction for the SDSS i band: contribution of the continuum, the emission lines and the total. The zero point of the K-correction is at z = 2 for the continuum. The K-correction is part of the on-line material of Ross et al. (2012).

K_{em} is estimated after subtracting the continuum contribution from a QSO-synthetic spectrum and by calculating the K-correction associated with the remaining spectral energy distribution (SED) of the QSO.

Ross et al. (2012) have determined the K-correction as a function of redshift for the SDSS i-band. The synthetic QSO spectrum used by the authors is composed of an underlying continuum with $\alpha_\nu = -0.5$ and an emission line template. The total K-correction and the individual contributions due to the continuum and the emission are shown in Fig. 5.5.

K_{em} is actually the contribution from the emission lines to the apparent magnitude. It can thus be used to retrieve the contribution of the emission lines to the apparent magnitude of an object

$$m_{cont} = m_{obs} - K_{em}. \tag{5.17}$$

m_{cont} is the apparent magnitude of the central engine of the QSO by its own.

The absolute magnitude derived through

$$M = m_{cont} - DM - K_{cont} \tag{5.18}$$

is thus a measure of the energy output of the central engine of the AGN, the *continuum absolute magnitude* (Richards et al. (2006)).

Finally, instead of K-correcting the continuum absolute magnitude to a common restframe at $z = 0$, we may K-correct to a redshift equal to the mean redshift of the QSO population considered. As the population of QSOs seems to peak somewhere around redshift $z \sim 2$, it is convenient to chose this redshift for the reference frame. This is done by retrieving the contribution of $K_{cont}\,(z = 2)$ at the redshift $z = 2$. We can define the absolute continuum magnitude $M_{[z=2]}$, with a zero point of the continuum K-correction at $z = 2$

$$M_{[z=2]} = m_{obs} - DM - K_{em} - K_{cont,[z=2]}, \tag{5.19}$$

where

$$K_{cont,[z=2]} = -2.5\,(1 + \alpha_\nu)\log(1 + z) + 2.5\,(1 + \alpha_\nu)\log(1 + 2)\,.$$

K-correcting closer to the median redshift value of the QSO population has the advantage that we need to extrapolate less the QSO spectra. Furthermore, in the particular case of the SDSS i-band, the effective wavelength of the filter projected on the restframe of the QSO at redshift $z = 2$ is ~ 2250 A°; around this wavelength, QSO spectra are relatively free of strong emission lines as can be seen in Fig. 5.4.

As the ILMT will mainly image through the SDSS-i' filter, we are interested in the QSO optical LF expressed in terms of the absolute magnitude $M_{i'}$ in the i'-band. Because the SDSS i and i' bands are very similar to each other and because most of the literature publications are expressed in the i band, we have performed the simulation of the QSO population in the SDSS i magnitudes, instead of i'.

Consequently, in what follows, except whenever mentioned otherwise, we use the absolute continuum magnitude in the SDSS i band, K-corrected with the zero point of the continuum K-correction at $z = 2$. We subsequently omit the $[z = 2]$ subscript in our notations.

5.2.2 LF and evolution

The QSO LF has been shown to be well represented by a double power law form (see Johnston (2011) for a review on the topic). When expressed as a function of the absolute magnitude M

$$\Phi\left(M\right) = \frac{\Phi_*}{10^{0.4(\alpha+1)(M-M_*)} + 10^{0.4(\beta+1)(M-M_*)}}, \tag{5.20}$$

where Φ_* is the characteristic density, M_* the characteristic absolute magnitude, and α and β the bright and faint end slope, respectively. The typical shape of the QSO LF with this expression is shown in Fig. 5.6. Adopting a semi-logarithmic scale, the LF presents a break at the absolute magnitude M_*, the two parameters α and β fixing the slope of the LF for objects brighter and fainter than M_*, respectively. The LF characteristic density Φ_* represents the double of the LF value at the characteristic absolute magnitude.

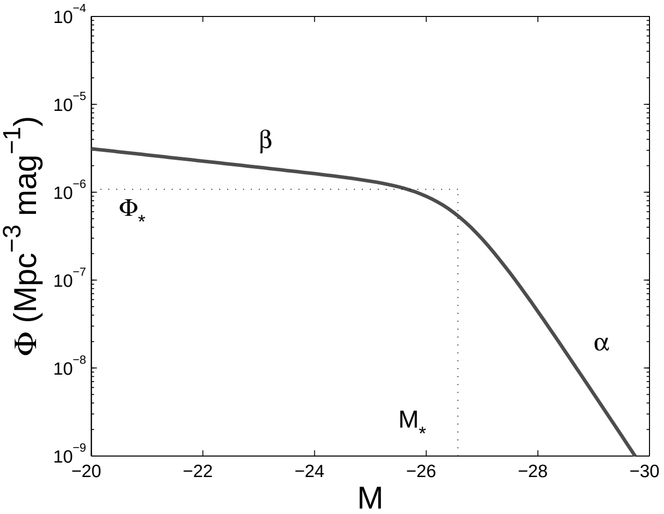

Figure 5.6: Typical double power law LF of QSOs. The LF shown corresponds to the LF in Ross et al. (2012) at a redshift $z = 2$.

The space density of QSOs evolves strongly with redshift and luminosity and the determination of the QSO LF and its redshift dependence have been the subject of many studies (see Table 5.2 for instance, for an overview of the recent determination of the QSO LF evolution in the UV, the optical and the near infrared).

The redshift dependence of the QSO population space density is modelled by introducing a redshift dependence of the LF parameters Φ_*, M_*, α and β. Different families of evolution models exist depending on the choice of the redshift dependence of these parameters. We differentiate

- *Pure Luminosity Evolution* (PLE) models where only the characteristic absolute magnitude M_* evolves with redshift. In this model, the LF redshift dependence is due to an evolution of the luminosity of the QSOs with time, their comoving density remaining constant.
- *Pure Density Evolution* (PDE) models where only Φ_* shows a redshift dependence, reflecting a change in the number density of QSOs with time, the luminosity of the individual objects remaining unchanged.
- Evolution models where both the characteristic luminosity and density vary with redshift. In this case, the LF behaviour is the consequence of both a density evolution of the QSOs and a modification of their individual luminosity. In this category, different models exist depending on whether the LE and DE are independent or correlated.

Finally, some authors also introduce a modification in the slope parameters α and β with redshift.

The optical QSO LF and its redshift dependence have been studied over a wide range of redshifts and magnitudes through numerous surveys. An overview of these LF determinations in the optical, near infrared and UV domains are shown in Table 5.2.

For each of them, the limiting apparent magnitude of object detection and the completeness limitation due to different observational biases (such as colour selection biases,...) limit the range of redshift and absolute magnitude over which the QSO LF can be determined.

Author	z range	magnitude	N_{QSO}	Survey coverage (deg^2)	Survey	Acronym (when cited)
Croom et al. (2004)	$0.4 < z < 2.1$	$b_J < 20.85$	23338	2	2QZ	
		$b_J < 18.25$	322	6	6QZ	
Croom et al. (2009)	$0.4 < z < 2.6$	$b_J < 20.85$	10637	191.9	2SLAQ	
Palanque-Delabrouille et al. (2012)	$0.7 < z < 4$	$g < 22.5$	1877		SDSS-III & MMT	MMT
Richards et al. (2006)	$0.3 < z < 2.2$	$i < 19.1$	15343	1622	SDSS-DR3	DR3-DR7
	$3 < z < 5$	$i < 20.8$				
Ross et al. (2012)	$0.3 < z < 2.2$					
	$2.2 < z < 3.5$	$i \lesssim 21.8$	22301	2236	SDSS-III:BOSS	BOSS-DR9
Fontanot et al. (2007)	$3.5 < z < 5.2$					F07
Ikeda et al. (2011)	$z \sim 4$	$22 < i' < 24$	31		COSMOS	
Ikeda et al. (2012)	$z \sim 5$	$22 < i' < 24$	14		COSMOS	
Masters et al. (2012)	$z \sim 3.2$	$I_{AB} < 24$	155		COSMOS	
	$z \sim 4$					
Glikman et al. (2011)	$z \sim 4$	$R < 24$		3.75		

Table 5.2: Overview of QSO luminosity function determinations obtained from different recent surveys in the optical, near infra-red and UV domains.

5.2.3 The LF for the ILMT QSOs

In order to simulate the ILMT QSO population, we need the QSO LF in the i-band and its redshift behaviour to be determined over the $M_i - z$ plane area defined by the limiting magnitude of the survey $i \sim 22.5$. Fig. 5.7 shows the accessible area in the $M_i - z$ plane for the ILMT survey. The lower dark curve corresponds to a source with an apparent magnitude equals to the limiting magnitude of the survey whereas the upper curve corresponds to a source with an apparent magnitude $i = 16.5$. The latter magnitude cut is imposed because it is not likely that we shall be able to detect a QSO brighter than 16.5 with the ILMT, due to saturation of the CCD detector.

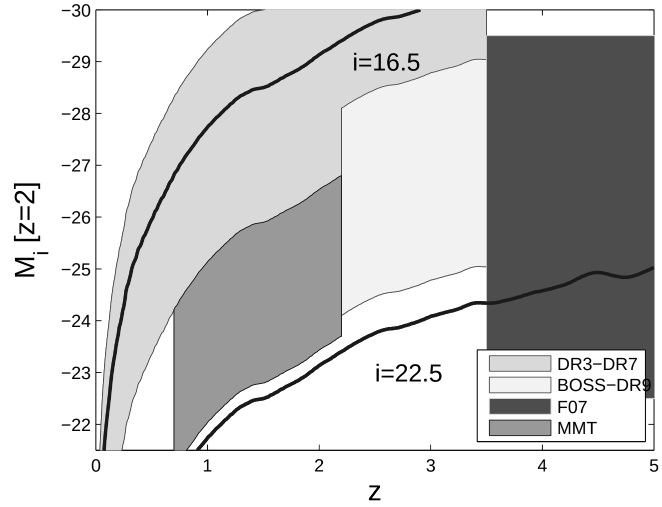

Figure 5.7: Accessible area in the $M_i - z$ with the ILMT survey defined by the limiting magnitude $i \sim 22.5$ for the case of a flat FLRW universe with $\Omega_m = 0.3$ and $H_0 = 70$ km s^{-1} Mpc^{-1}. The figure displays also the footprint of the surveys used to determine the luminosity function of the ILMT QSOs. The two black curves correspond to sources with an apparent magnitude $i = 16.5$ and $i = 22.5$.

We want the largest possible redshift range, and we are especially interested in distant bright sources as these are the most likely to be gravitationally lensed. The higher redshift for which the LF has been determined being $z \sim 5$, we limit the redshift range to this maximum value.

We thus want to simulate the QSO population in the redshift range $0 < z < 5$, brighter than the apparent magnitude $i \sim 22.5$. None of the LF determinations in Table 5.2 spans over a sufficiently wide redshift and apparent magnitude ranges. We thus have to combine different LF determined by different authors in different redshift ranges.

In the redshift range $0.3 < z < 3.5$, we use the LF determined by Ross et al. (2012). The authors combine the QSO population from different surveys in order to construct a uniform sample spanning over a redshift and magnitude range as wide as possible. The footprint of the different combined surveys are shown in Fig. 5.7, in order to place them in the context of the ILMT survey. Ross et al. (2012) combines QSOs from

- the SDSS-III(DR9): BOSS survey from which they derive a uniform sample of 22301 QSOs with $i \leq 21.8$ and redshift in the range $2.2 < z < 3.5$;
- the SDSS-DR7 survey: this survey being mostly complete for $i \leq 19.1$ and $0.3 < z < 2.2$. This survey also spans over the redshift range $3 < z < 5$ and down to $i \leq 20.8$. Richards et al. (2006) already determined the QSO LF of this QSO sample, Ross et al. (2012) thus extending their work;
- the SDSS-III & MMT survey. Ross et al. (2012) use a sub-sample resulting from the combination of the two surveys described in Palanque-Delabrouille et al. (2012), in order to cover the fainter sources in the redshift range $0.7 < z < 2.2$, not accessible by the two previous surveys.

The footprint of the different sub-samples of the surveys used by Ross et al. (2012) are shown in Fig. 5.7.

For the more distant sources in the redshift range $3.5 < z < 5.2$, we use the LF dependence determined by Fontanot et al. (2007) who combined the known QSOs in the SDSS-DR3 in this redshift range with distant faint QSOs detected in the GOODS survey. Although this work has been made for a fairly small number of QSOs, it has the advantage of giving an evolution model for the LF whereas other authors only determine the LF for discrete redshift values (Ikeda et al. (2011), Ikeda et al. (2012), Masters et al. (2012), Glikman et al. (2011)).

Ross et al. (2012) and Fontanot et al. (2007) have both used the double power law model from Eq. 5.20 for their determination of the LF. Nevertheless, they use different evolution models. In order to combine the LFs derived by the others, we use Eq. 5.20 and the dependence of the LF parameters derived by Ross et al. (2012) and Fontanot et al. (2007) in their own redshift range.

Ross et al. (2012) test different evolution models on their data to reproduce the dependence of the LF as a function of redshift but unfortunately, they were not able to describe the redshift behaviour over the whole redshift range with a single model. Consequently, they use two different models in the redshift range $0.3 < z < 2.2$ and $2.2 < z < 3.5$.

In the lower redshift interval, their data are well described by a PLE model with the characteristic absolute magnitude M_i^* evolving as

$$M_i^*(z) = M_i^*(z=0) - 2.5\left(k_1 z + k_2 z^2\right). \tag{5.21}$$

In the higher redshift range ($2.2 < z < 3.5$), the authors adopt a *Luminosity Evolution - Density Evolution* (LEDE) model where both the characteristic absolute magnitude and density evolve with redshift, but with no correlation between the two parameter behaviour. The LEDE evolution model is defined by

$$\log\left(\Phi_*\left(z\right)\right) \; = \; \log\left(\Phi_*\left(z=2.2\right)\right)+c_1\left(z-2.2\right). \tag{5.22}$$

$$M_i^*\left(z\right) \; = \; M_i^*\left(z=2.2\right)+c_2\left(z-2.2\right). \tag{5.23}$$

Both evolution models consider a constant value for the slope parameters α and β over the corresponding redshift range. The best values for the fit parameters of the PLE and LEDE models in the different redshift ranges are given in Table 5.3.

$0 < z < 2.2$, PLE (Ross et al. (2012))

$M_i^*\left(0\right)$	k_1	k_2	α	β	$\log\left(\phi_0^*\right)$
-22.85	1.241	-0.249	-3.37	-1.16	-5.96

$2.2 < z < 3.5$, LEDE (Ross et al. (2012))

$M_i^*\left(z=2.2\right)$	c_1	c_2	α	β	$\log\left(\phi_0^*\right)$
-26.70	-0.576	-0.774	-3.71	-1.46	-6.06

$3.5 < z < 5.2$, PDE (Fontanot et al. (2007))

M_{1450}^*	-	α	β	Φ_* (Mpc^{-3})	k_z
-26.31	-	-3.31	-1.45	$1.67.10^{-6}$	-1.27

Table 5.3: Luminosity function parameters taken for the different redshift ranges. k_1, k_2 are the characteristic absolute magnitude evolution parameters of the PLE (Eq. 5.21), c_1 and c_2 are the evolution parameters of the LEDE model in Eq. 5.22 and Eq. 5.23 and k_z, the PDE parameter from Eq. 5.24.

The redshift dependence of the LF parameters adopted by Ross et al. (2012) are shown in Fig. 5.8.

Although the transition between the models (PLE and LEDE) at $z = 2.2$ works out pretty smoothly for the characteristic magnitude M_i, there is a break at the transition of the characteristic density and also for both slope parameters.

First of all, the presence of discontinuities is not surprising as the authors fit the two redshift ranges separately with no constraint on the continuity of the parameters.

The authors fit their data in two small redshift intervals ($0.3 < z < 2.2$ and $1 < z < 2.2$) and conclude that the PLE models represent the data better when restraining the data to $z > 1$. In this work, we take the fit parameters corresponding to the largest redshift interval ($1 < z < 2.2$) in an attempt to

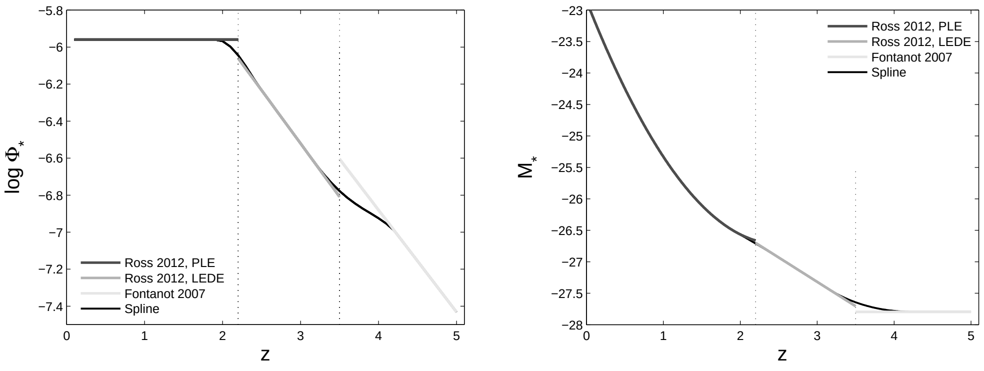

(a) Φ_* (b) M_*

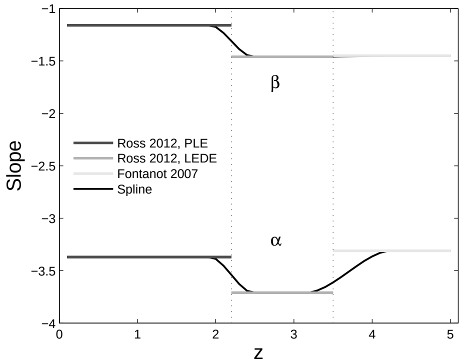

(c) α and β

Figure 5.8: Redshift dependence of the parameters Φ_* and M_* and α and β of the QSO LF. The characteristic absolute magnitude is expressed for the SDSS i band luminosity. For redshifts below 2.2, we use the dependence introduced by Ross et al. (2012) with a PLE model and its LEDE in the redshift range $2.2 < z < 3.5$. We use the estimation of Fontanot et al. (2007) for redshifts larger than 3.5. Cubic spline interpolation guarantees continuity at the junction redshifts 2.2 and 3.5.

reproduce the QSO population at low redshifts as well. The discrepancies between the two models at $z = 2.2$ (i.e. the break at $z = 2.2$ of the $\log \Phi_*$ in Fig. 5.8a and in α and β in Fig. 5.8c) are smaller when taking the fit parameters for the smaller redshift range ($1 < z < 2.2$).

We thus associate these discrepancies to the inclusion of the lower redshift QSO sample ($0.3 < z < 0.7$). This is probably the sign of an evolution model that does not reproduce well all the physics at lower redshifts.

In the redshift range $3.5 < z < 5$, Fontanot et al. (2007) use a PDE evolution model with the characteristic density evolving as

$$\Phi_* = \Phi_{*,z=2} \exp\left(k_z\left((1+z)-3\right)\right). \tag{5.24}$$

The parameter values for the best fit are given in Table 5.3 and the redshift dependence of the parameters is shown in Fig. 5.8. In the model we chose, the authors only fit the characteristic absolute magnitude and the characteristic density evolution parameter k_z in Eq. 5.24. The slope parameter and the characteristic density parameter were taken from Croom et al. (2004), who have fitted a LF on data in the redshift range $0.4 < z < 2.1$. Fontanot et al. (2007) fixed these parameters to match the value found by Croom et al. (2004) at redshift $z = 2.1$.

Fontanot et al. (2007) express the QSO LFs in terms of the monochromatic absolute AB magnitudes M_{1450} at 1450 A° (Oke and Gunn (1983)). Following Richards et al. (2006), assuming that a QSO spectrum can be described as a power-law with spectral index α_ν (i.e., $F(\nu) \propto \nu^{\alpha_\nu}$), the monochromatic magnitude at 1450 A° is linked to $M_{i,[z=2]}$ through the relation

$$M_{1450} \;=\; M_{i,[z=2]} + 2.5\left(1+\alpha_\nu\right)\log_{10}\left(1+2\right) + 2.5\alpha_\nu \log\left(\frac{1450A^\circ}{7471A^\circ}\right).$$

In Fig. 5.8, at the transition redshift $z = 3.5$, there is a clear break in the characteristic density and the bright end slope parameter. In order to ensure a continuous and smooth LF, and a smooth redshift distribution of the simulated QSO population, we have interpolated the parameter behaviour around redshifts $z = 2.2$ and $z = 3.5$ with cubic spline curves. The interpolated curves are shown as continuous black lines in Fig. 5.8.

The final LF used to simulate the QSO population is thus obtained by inserting the redshift dependence of Φ_*, M_i^*, α and β in Fig. 5.8, into the double power law LF expression given by Eq. 5.20. The final LF used is shown in Fig. 5.9. The left panel shows the dependence of the LF as a function of the absolute magnitude, for different redshifts. The right panel shows the dependence of the LF as a function of the redshift, for different absolute magnitudes. In the latter, we have plotted with thin black lines the LF obtained without the spline interpolation of the redshift dependence of the parameters in Fig. 5.8.

Although the LF transitions at redshifts $z = 2.2$ and $z = 3.5$ are more or less consistent for absolute magnitudes near the characteristic absolute magnitude ($M_i^*(z = 2.2) \sim -26.7$ and $M_i^*(z = 3.5) \sim -27.5$), the transition of the LF is not physical for absolute magnitudes very far from M_i^* because of the difference in the slope parameter values.

The overall aspect of the LF redshift dependence is not physical. Nevertheless, our goal is to reproduce reasonably well the QSO population observed over all the redshift and magnitude ranges or sub-samples of the population and not to study the phenomenological implication of the LF shape on the QSO evolution or cosmological evolutionary scenarii. In this spirit, this piecewise continuous LF is

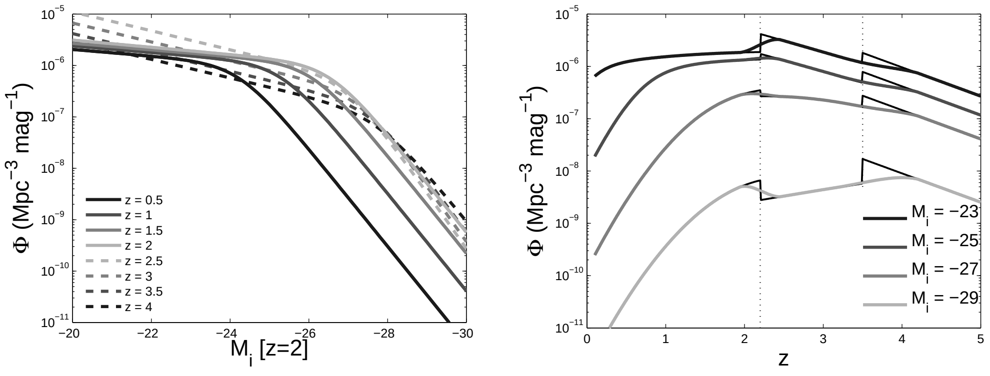

(a) as a function of M_i

(b) as a function of z

Figure 5.9: Final QSO LF in the i band as a function of $M_i[z = 2]$ and z.

expected to better represent the observed population over the entire $M_i - z$ space than simply extrapolating a LF model determined over a restricted $M_i - z$ plane area.

In the next sections, after explaining how we simulate the QSO population to be detected within the ILMT survey, we check the reliability of both the generation method and the LF by reproducing the number counts observed in other surveys.

5.3 ILMT catalogue generation

In the previous sections, we have derived the volume accessible through the ILMT survey as well as the space density of QSOs in this volume, as a function of the absolute magnitude and redshift. We have thus all what is needed to simulate the expected population of QSOs in the volume and generate the catalogue of QSOs to be detected with the ILMT.

We first divide space in redshift shells with $\Delta z = 0.2$ for redshifts ranging from $z_{min} = 0.01$ to $z_{max} = 5$. For each redshift interval, we calculate the volume ΔV of the shell in the comoving reference frame defined by the ILMT field of view Ω_{ILMT}. This volume is calculated through the difference of the comoving volumes at redshifts $z + \Delta z$ and z, i.e.

$$\Delta V = V_C\left(z + \Delta z\right) - V_C\left(z\right), \tag{5.25}$$

where V_C is calculated numerically by integrating Eq. 5.5.

For each redshift shell, we consider the absolute SDSS i band magnitude M_i intervals $\Delta M = 0.25$ ranging from $M_{min} = -30$ to $M_{max} = -22.5$. The absolute magnitude range corresponds to the SDSS DR3 limits (see Richards et al. (2006), Fig. 17).

For each redshift interval Δz and absolute magnitude interval ΔM, we evaluate the number N_{QSO} of QSOs in the shell within that absolute magnitude and redshift ranges

$$N_{QSO} = \Delta V \, \Delta M \, \Phi \left(M + \Delta M/2, z + \Delta z/2 \right), \tag{5.26}$$

where $\Phi \left(M, z \right)$ is the QSO LF described in Section 5.2.3.

We then generate the number of expected QSOs with redshifts and absolute magnitudes randomly chosen in the redshift and absolute magnitude bins, respectively. For each generated source, we calculate the apparent magnitude m in the i band through (see Eq. 5.19)

$$m = M + DM + K_{cont,[z=2]} \left(z \right) + K_{em} \left(z \right), \tag{5.27}$$

where the K-correction is taken from the online material in Ross et al. (2012), as described in Section 5.2.1. We only keep the sources that have an apparent magnitude brighter than the critical magnitude of the ILMT survey $i \sim 22.5$.

5.4 Checking the catalogue generation

In order to check the reliability of the QSO LF determined by combining different LFs over different redshift intervals and in order to check the QSO population generation algorithm, we reproduce the QSO number counts as a function of the apparent magnitude, for existing surveys in different redshift ranges. In Fig. 5.10a, we first reproduce the *Cumulative Number Counts Function* (CNCF) of QSOs as a function of the apparent magnitude i that was observed in the SDSS-DR9 BOSS survey and is given as on-line material by Ross et al. (2012). For clarity, the error bars of the BOSS data are not shown in the figure: for magnitudes fainter than 19.5, they are samller than the maker size. The QSO population of the survey is restricted to the redshift range $2.2 < z < 3.5$ and to apparent magnitudes brighter than $i = 21.8$. We thus impose the same restriction to the simulated catalogue.

The simulated CNCF was calculated as follows. We have generated 10 catalogs of QSOs that would be detected in a survey spanning over 500 deg^2. For each of the generated catalogue, we calculated the CNCF per square degree, as a function of the apparent magnitude. For each apparent magnitude, we calculated the mean value and the standard deviation of the CNCF.

From Fig. 5.10 we see that the simulated CNCF in this redshift range is in very good agreement with the BOSS observations.

In the right panel of Fig. 5.10, we reproduce the CNCF of the sub-sample of the BOSS & MMT QSO catalogue (Palanque-Delabrouille et al. (2012)) used by Ross et al. (2012) to determine their LF. The QSOs of this sub-sample are restricted to the redshift range $1 < z < 2.2$. Because this catalogue has been constructed by imposing an absolute magnitude cut in the g-band (see Palanque-Delabrouille et al. (2012) for details), it is difficult to determine the corresponding magnitude in

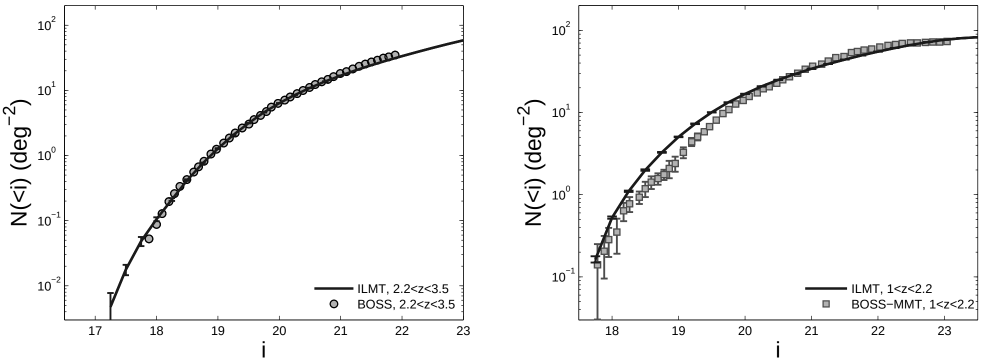

(a)

(b)

Figure 5.10: Cumulative number counts function of QSOs as a function of the apparent magnitude in the SDSS i band. (a) QSOs restricted to the redshift range $2.2 < z < 3.5$. The observational data come from the BOSS DR9 survey (Ross et al. (2012)), after correction for selection effect incompleteness. (b) redshift range restricted to $1 < z < 2.2$. The observational data come from the BOSS & MMT sample presented in Palanque-Delabrouille et al. (2012).

the i-band precisely as it varies with redshift. We restrict the simulated catalogue to the same redshift interval and keep sources with $M_{i,[z=2]} < -22.5 - 0.569$. This limit corresponds to the QSO definition of Richards et al. (2006) (i.e. $M_{i,[z=0]} < -22.5$). We then calculate the CNCF for sources with apparent magnitude in the same range.

The agreement between the simulated and observed CNCF are pretty good for sources fainter than $i \sim 20$. The data is marginally consistent for sources brighter than $i \sim 20$, where the simulated catalogue apparently overestimates the number of sources. The possible reasons for these differences are:

- the difficulty to define the QSO absolute magnitude cut in the i-band (since the original catalogue cut was done in the g-band absolute magnitudes),
- the BOSS-MMT data show a strange shape in this magnitude interval which could be the sign of its incompleteness or due to cosmic variance.

In Fig. 5.11, to test the reliability of the QSO LF in the redshift range $0.3 < z < 2.2$, we now compare the QSO *Differential Number Counts Function* (DNCF) as a function of magnitude obtained for the simulated population of QSOs in this redshift range with observational data from different surveys. For clarity, we plot the error bars for the simulated catalogue only. In the observational data, for magnitudes fainter than 18.5, the error bars are smaller than the size of the markers.

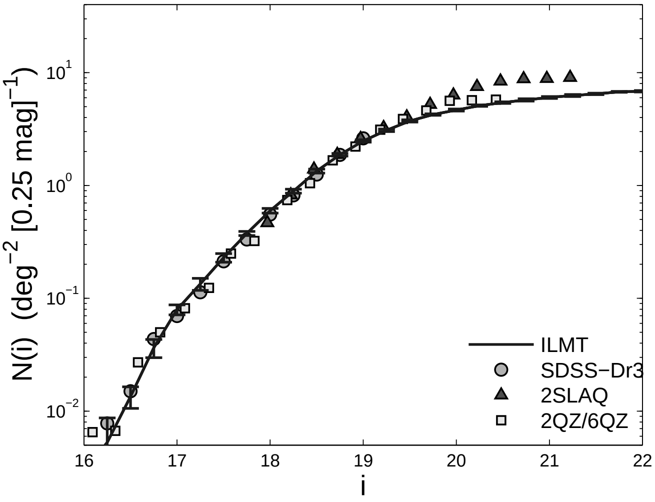

Figure 5.11: Comparison of the Differential Number Counts Function between the simulated QSO population restricted to the redshift range $0.3 < z < 2.2$, and observational data from 3 surveys: the SDSS-DR3, the 2SLAQ and the 2QZ/6QZ.

First of all the DNCF of the SDSS-DR3 in the i-band from Richards et al. (2006) is shown with grey disks. The sample has been limited to sources brighter than the apparent magnitude $i \sim 19.1$ because the SDSS-DR3 is incomplete over this magnitude. The SDSS-DR3 from Richards et al. (2006) was used by Ross et al. (2012) for the determination of the LF in this redshift range, in combination with the SDSS-MMT data from Palanque-Delabrouille et al. (2012) shown in Fig. 5.10. The simulated catalogue reproduces very well the observed population of bright sources in this redshift range.

For fainter sources in the same redshift interval, we use the DNCF observed in the 2dF-SDSS LRG QSO survey (2SLAQ) by Croom et al. (2009) and the one from the combined 2QZ/6QZ surveys from Croom et al. (2004). The 2SLAQ has been observed in the SDSS g-band and the conversion to the SDSS i-band is done by using the average $g - i$ colour difference for QSOs in this redshift range in the SDSS-DR3 ($g - i \sim 0.255$, Richards et al. (2006)) and assuming that the DNCF in the i and g bands has the same shape. The 2SLAQ is limited to objects with an absolute g band magnitude brighter than $M_{g,z=0} < -22.5$, with a K-continuum zero point at redshift $z = 0$. The 2QZ/6QZ data were acquired in the b_J magnitude system. The b_J magnitudes were converted to i magnitudes assuming $b_J \sim g$ and $g - i \sim 0.255$.

The simulated catalogue is restricted to the same interval and absolute magnitude cut of $M_{i,z=0} < -22.5$.

The simulated catalogue is in good agreement with both DNCF for sources brighter than $i \sim 19.5$. For the fainter sources, the simulated catalogue is marginally consistent with the 2QZ data, although slightly underestimating the QSO population at these faint magnitudes. However, we underestimate the 2SLAQ data by 20-30 percent for such faint sources.

The discrepancies between the 2QZ and 2SLAQ DNCF were already observed by Croom et al. (2009) with apparently no clear explanation. Croom et al. (2009) associate these differences to a combination of different effects like a slight incompleteness of the 2QZ, an overestimate of the incompleteness of the 2SLAQ in this magnitude/redshift range.

Concerning our work, first of all, discrepancies between simulation and these observations may appear due to the difficulty of defining the absolute magnitude cut in the i-band (corresponding to the one in the g-band). We have also assumed that the DNCF in the i-band has the same shape as in the g and b_J bands.

We apparently underestimate the population of QSOs for $19.5 < i < 21.5$ and in the redshift range $0.3 < z < 2.2$. This trend is not observed in the CNCF of Palanque-Delabrouille et al. (2012) on the right panel of Fig. 5.10 that is limited to $1 < z < 2.2$. This would mean that we are underestimating faint sources in the redshift range $0.3 < z < 1$. This is however incompatible because this redshift region does not contribute much to these faint source populations, but contributes rather to sources with bright apparent magnitudes. Nevertheless, if we do consider that we underestimate the QSO population in the redshift range $0.3 < z < 2.2$ with apparent magnitudes in the range $19.5 < i < 21.5$, what are the implications for our results? These sources do not have a very high amplification bias (because they are close or fainter than the break in the DNCF) and are not the most distant in the sample. Consequently this source population is not the one contributing the most to the lensing probability of the overall population. However, because the QSO population peaks at a redshift $z \sim 2$ and that faint sources are more numerous than bright ones, this population does contribute considerably to the number of QSOs detected with the ILMT survey. This would thus lead to an underestimate of the number of detected QSOs but would have a small impact on the number of detected muultiply imaged quasars.

5.5 Properties of the simulated catalogue

In the previous section, we have shown that using the composite LF and the catalogue generation algorithm described in sections 5.2.3 and 5.3, we reproduce reasonably well different observational data spanning over various redshift and magnitude ranges. We now use the same procedure to simulate the QSO population to be detected with the ILMT, spanning over a redshift range from 0.01 to 5. In our simulation, we follow Richards et al. (2006) and define QSOs as objects with $M_{i,[z=0]} < -22.5$. All results are obtained assuming $i \sim i'$.

The limiting magnitude after a single scan of the region of the sky is $i \sim 22.5$. Co-addition of images will lead to an increase of the signal-to-noise ratio and thus enable to detect fainter sources. The catalogue of QSOs detected will depend on how faint an object can be detected with the ILMT, knowing that QSOs will be detected based upon variability criteria.

Another unknown is the critical galactic latitude under which QSO detection will not be possible. Table 5.4 gives the expected numbers of QSOs for different configurations (i.e. $i_{crit} = 20, 22.5$ or 23 and $b_{crit} = 30°$, $27.5°$ or $25°$).

	$b_{crit} = 30°$	$b_{crit} = 27.5°$	$b_{crit} = 25°$
$i_{crit} = 22$	7738	8609	9370
$i_{crit} = 22.5$	9072	10109	11016
$i_{crit} = 23$	11032	12293	13396

Table 5.4: Expected numbers of QSOs in the ILMT survey for different detection limiting magnitudes i_{crit} and critical galactic latitude values b_{crit}. For all calculations, we defined a QSO as being an AGN brighter than $M_{i,z=0} < -22.5$ (Richards et al. (2006)) and we assume $i \sim i'$.

The final QSO population for which we calculate the lensing probability has been selected adopting the parameters $i_{crit} = 22.5$ and $\Omega_{ILMT} = 70$ deg^2 (corresponding to $b_{crit} = 30°$).

The DNCF, redshift distributions and CNCF of the QSO population per square degree brighter than $i_{crit} = 22.5$ are shown in Fig. 5.12.

The DNCF and CNCF are estimated by simulating onne hundred catalogues spanning over 70 sq.deg. and calculating the DNCF and the CNCF for each catalogue. Then for every magnitude bin, we calculate the value and standard deviation of the counts in each catalogue.

The importance of the DNCF for the estimation of the amplification bias has been emphasized in Chapter 4. The DNCF is fitted using a power law of the form

$$N(i) \propto 10^{P_4(i)}, \tag{5.28}$$

where $P_4(i)$ is a fourth order polynomial in i for sources brighter than $i = 20.5$. For the fainter sources, we extrapolate the slope of the DNCF in the range $20.5 < i < 22.5$. The resulting fit is shown in Fig. 5.12a as a light grey line.

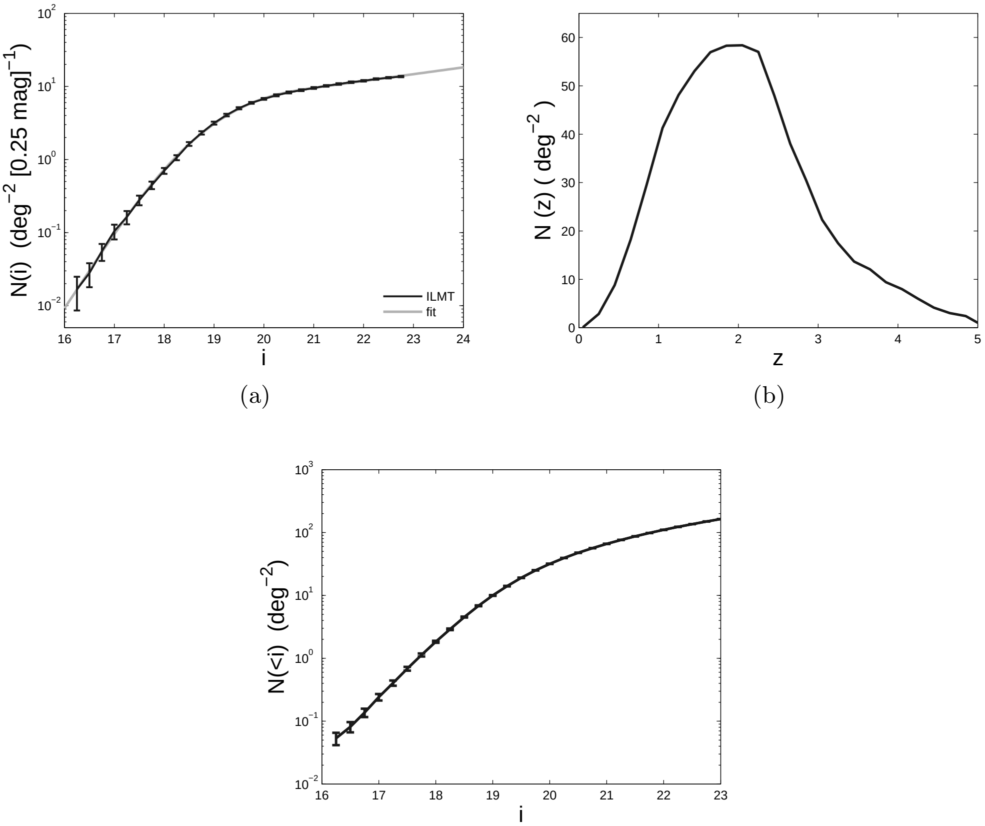

(a) (b)

(c)

Figure 5.12: (a) DNCF, (b) redshift distribution and (c) CNCF of the simulated QSO population to be detected with the ILMT.

Chapter 6

Lensing statistics for the ILMT QSO population

In Chapter 5, we have estimated the population of QSOs to be detected with the ILMT. In this Chapter, we estimate the number of sources N_{GL} in this sample that will be multiply imaged due to the presence of a deflector near their lines-of-sight. N_{GL} is estimated through the relation

$$N_{GL} = \langle\tau\rangle \; N_{QSO}, \tag{6.1}$$

where N_{QSO} is the total number of QSOs to be detected with the ILMT and where $\langle\tau\rangle$ ($\ll 1$) is the averaged value of the lensing probability τ over the source population. $\langle\tau\rangle$ is the mathematical esperance of the lensing probability and it is estimated by calculating the lensing probability τ associated with each source and by taking the average value.

In Chapter 4 we have derived the expressions τ_{SIS} (Eq. 4.38) and τ_{SIE} (Eq. 4.43) for the lensing probability of a source with known redshift and apparent magnitude, when considering a population of deflectors modelled with an SIS or an SIE mass distribution, respectively.

The calculation of τ_{SIS} and τ_{SIE} necessitates the knowledge of the lensing cross section Σ^{dim}_{SIS} and Σ^{dim}_{SIE} associated with the population of deflectors. The cross section calculation has to be done for each distance configuration of the deflector and the source (i.e. each set of distances D_{OD} and D_{OS}). The calculation of the cross sections necessitates much calculation time because, in most cases, there is no simple analytical expression and they have to be calculated numerically through Monte-Carlo integration.

The dimensional lensing cross sections Σ^{dim}_{SIS} and Σ^{dim}_{SIE} may be expressed as a function of the dimensionless lensing cross sections Σ_{SIS} and Σ_{SIE} that are no longer a direct function of the geometrical configuration of the lens system (i.e. the set of distances D_{OD} and D_{OS}). Although the dimensionless cross section still necessitates to be calculated numerically, we have seen in Chapter 3 that we can generated a database for the dimensionless cross section that we use to calculate the dimensional cross sections and the lensing probability for each source.

The lensing probability τ associated with a single source as well as the dimensional Σ^{dim} and dimensionless cross section Σ are the fundamental tools in the estimation of the number of multiply imaged QSOs to be detected with the ILMT.

In this Chapter, we calculate the expected number of multiply imaged QSOs in the ILMT survey and we analyse the impact of different factors on this expectation. Namely, we look at the impact of the instrumental resolution in Section 6.2, the type of deflector population (early or late type galaxy population) in Section 6.3 and the cosmological model parameters in Section 6.4. The impact of the different factors is studied through their effect on the mean probability, the probability associated with each source and/or the influence on the cross sections.

6.1 Perfect instrument and early type galaxy deflectors

Let us first consider a perfect instrument (i.e. all the lensed images are detected, independently on their angular separation).

We only consider early type galaxies as forming the deflector population. The statistical properties of the deflector population are described through their VDF presented in Table 4.1 and the axis ratio distribution in Fig. 4.7.

Before applying the probability calculation to the entire simulated catalogue from Chapter 5, let us consider the influence of the characteristics of a single source on its lensing probability, namely the source redshift and its apparent magnitude.

6.1.1 Geometrical lensing probability

Let us consider the impact of the source redshift on the lensing probability. We have derived in Chapter 4 an expression for the dimensional geometrical cross section of an SIS deflector with a known line-of-sight velocity dispersion (Eq. 4.4). Furthermore, for an SIE deflector, we have calculated numerically the dimensionless geometrical cross section (as a function of the deflector ellipticity) and we know the relation between the dimensionless and the dimensional cross section (Eq. 4.2).

We can thus insert the geometrical cross sections in the expressions of the lensing optical depth τ_{SIS} and τ_{SIE} when modelling the deflectors as SIS (Eq. 4.38) and SIE (Eq. 4.43), respectively.

Fig. 6.1 shows the dependence of the geometrical optical depth as a function of the source redshift, when modelling the deflector population as SIS or SIE deflectors. As the SIE population of deflectors is able to reproduce lensing events with the formation of 2, 3 or 4 images, we have represented the geometrical probability associated with the formation of each possible number of lensed images, as well as the total lensing probability. The calculations were done assuming a flat FLRW universe with $H_0 = 70$ km s^{-1} Mpc^{-1} and $\Omega_m = 0.3$. In the following, unless mentioned otherwise, all calculations were done assuming such a universe model.

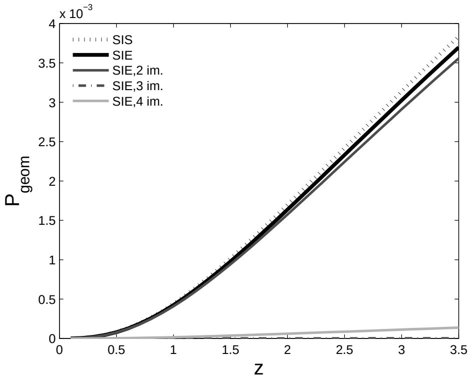

Figure 6.1: Dependence of the geometrical lensing probability as a function of the source redshift for a population of deflectors modelled with an SIS or an SIE mass profile.

The geometrical lensing optical depth corresponds to the probability that a source with a known redshift z_s undergoes a gravitational lensing event, if we do *not* know the source apparent magnitude. It is thus only dependent on the geometrical lensing volume of the source.

The first observation is that all the lensing probabilities increase with the source redshift. This is a direct consequence of the increase of the geometrical lensing volume with the source redshift (cf. Chapter 4). This volume is a function of the line-of-sight velocity σ distribution of the deflectors (and of the axis ratio f distribution for an SIE). τ_{geom} is an averaged value over all σ (and all f) of the deflector population.

When considering the SIE population with a perfect instrument, the fraction of events with a given number of lensed images is independent on the source redshift. The lensing probability of lensing events with more than two images is less than 4% of the total geometrical probability.

Finally, we see that when modelling the deflectors with an SIS, we overestimate the geometrical lensing probability with respect to the SIE ($\tau_{SIE}/\tau_{SIS} \sim 0.96$). We will come back to this point in Section 6.2.

6.1.2 Amplification bias effect

We have seen in Chapter 4 that the gravitational lensing phenomenon can lead to an amplification of the lensed images of a background source. One of the possible implication of this bias is the inclusion of intrinsically fainter sources in a flux limited sample, thanks to the lensing amplification. To take into account the bias introduced by the amplification, we introduced a correction factor in the calculation of the dimensionless cross section, namely, the amplification bias B

$$B = \frac{N\left(m + 2.5\log(A_{tot}\left(\mathbf{y}\right))\right.}{N\left(m\right)}, \tag{6.2}$$

where $N\left(m\right)$ represents the differential number counts of QSOs as a function of their apparent magnitude m. Because QSOs with a fainter apparent magnitude are more numerous than brighter ones, the amplification bias increases the value of the cross section, and thus increases the total lensing probability of a source.

Let us analyse the impact of the amplification bias on the dimensionless lensing cross section. In this Section and in the following one, we consider the QSO DNCF fitted on the simulated QSO population to be detected with the ILMT (see Section 5.5).

Fig. 6.2 shows the dependence of Σ_{eff} as a function of the object apparent magnitude m for an SIS or an SIE deflector, considering a perfect instrument. In the case of the SIE deflector, we have represented the total lensing cross section as well as the cross sections associated with the formation of 2, 3 or 4 lensed images, for a deflector with $f = 0.3$. Although such elliptic deflectors are not very common in the early type galaxy population, we have considered this value because, thanks to the presence of a naked cusp, Σ_3 is different from 0.

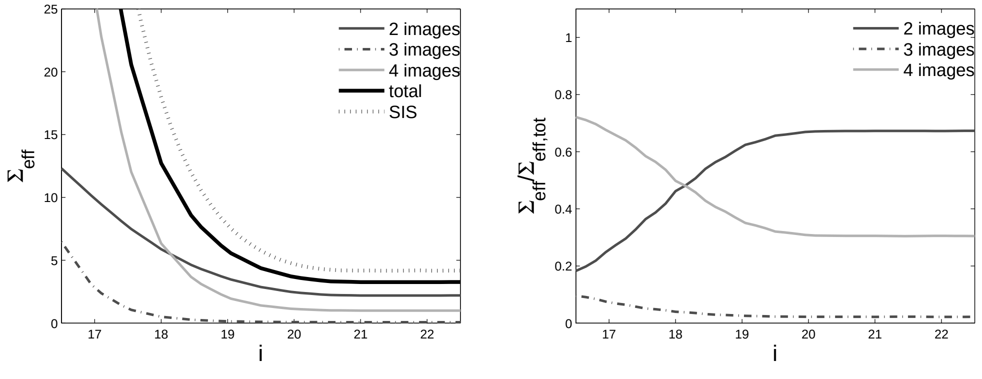

(a) (b)

Figure 6.2: (a) Dependence as a function of the source apparent magnitude, of the dimensionless effective lensing cross section Σ_{eff} for an early type galaxy modelled as an SIS or an SIE deflector (with $f = 0.3$). (b) Dependence of Σ_{eff} for a given number of images, relatively to $\Sigma_{eff,tot}$, for the case of the SIE deflector ($f = 0.3$).

A first observation is that the amplification bias leads to an increase of the dimensionless cross section for the brighter sources (and thus an increase in their lensing probability). Secondly, if we look at the lower value of the total cross section for the SIE and SIS (i.e. for the fainter sources), we see that the cross sections are larger than the geometrical dimensionless cross section ($\Sigma_{SIS,geom} =$

π, the surface of the unitary circle). For the fainter magnitudes, there is no more dependence of the cross section as a function of the source apparent magnitude. This is due to the fact that the QSO DNCF has been extrapolated linearly (in a logarithmic scale, see Fig. 5.12a) for magnitudes fainter than $i = 20.5$.

The SIS cross section is once again larger than that for the SIE model when considering all the lensed image configurations, independently on their number.

The increase of the cross section with the object brightness is not uniform for Σ_2, Σ_3 and Σ_4.

Fig. 6.2b shows the dependence as a function of the source magnitude, of Σ_2, Σ_3 and Σ_4 relatively to the total cross section for the SIE deflector. We clearly see that the amplification bias acts in favour of configurations with 3 and 4 lensed images, thus reducing the fraction of 2-image events.

Let us now look at Fig. 6.3a illustrating the dependence, as a function of the source apparent magnitude, of the ratio $\Sigma_{eff}/\Sigma_{geom}$. This ratio is a measure of the effect of the amplification bias, averaged over the whole cross section.

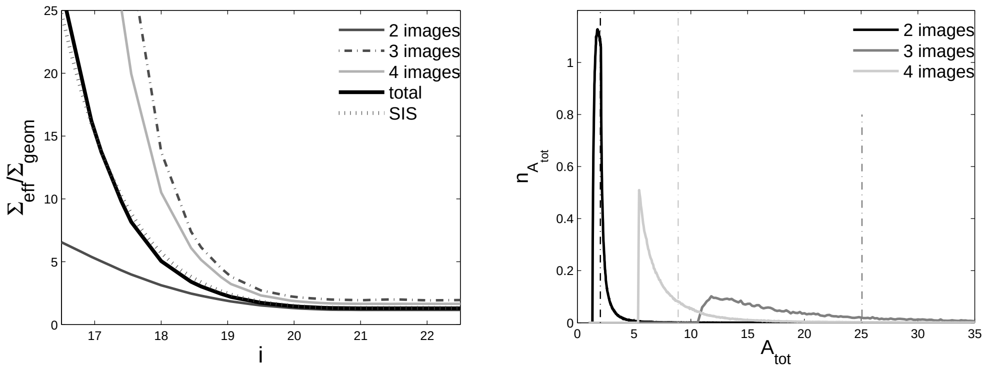

(a) (b)

Figure 6.3: (a)Dependence of $\Sigma_{eff}/\Sigma_{geom}$ as a function of the QSO apparent magnitude for an SIS and an SIE deflector (with $f = 0.3$). (b) Total amplification probability density associated with the configurations leading to the formation of 2, 3 and 4 lensed images for an SIE deflector with $f = 0.3$.

We see that the amplification bias act the most in favour of the configurations with 3 and 4 lensed images.

On the other hand, when comparing the mean amplification bias effect on the total lensing cross section of the SIE and that of the SIS, we see that the amplification increases similarly the two cross sections for the bright sources. We conclude from this common trend that the average amplifications induced by an SIS and an SIE deflector are the same.

To understand why the amplification bias leads to an excess of lensing configurations with 3 and 4 images, we have calculated the probability density $n_{A_{tot}}$ for having a total amplification A_{tot}, depending on the number of lensed images.

$n_{A_{tot}}$ was calculated as follows, using the different libraries developed during this thesis. For the considered SIE deflector ($f = 0.3$), we have randomly generated $5\ 10^6$ source positions. For each source position, we have inverted the lens equation to determine the lensed image positions and their amplifications. The total amplification associated with each source position is the sum of the moduli of the lensed image amplifications. We have then constructed a histogram (as a function of A_{tot}) of all the configurations leading to a given number of lensed images. This histogram is then normalised by the number of source positions leading to the considered number of lensed images.

The results are shown in Fig. 6.3b, illustrating the amplification probability density for configurations leading to 2, 3 and 4 lensed images, for an SIE deflector with $f = 0.3$. The mean value of the total amplification associated with each probability density is indicated with dashed lines. We see that the mean amplification of the source position with more than 2 images is higher. This can be understood as follows. We have seen in Chapter 3 that source positions near the tangential caustic lead to the most amplified lensed images (see the amplification map in Fig. 3.5b, for instance) because the images formed near the tangential critical curve are very amplified. In this case ($f = 0.3$) most of the three image configurations are due to a source located inside the naked cusps, thus a source very close to the tangential caustic and with highly amplified images. 4 image configurations are due to sources inside both the (pseudo-)caustics and thus highly amplified tangential images are also present. On the other hand, most of the 2 image configurations occur when the source is inside the radial pseudo-caustic but outside the tangential one. Consequently, the highly amplified images near the tangential caustic are not present and the total amplification is lower [1].

6.1.3 Probability distribution

In the two previous sections, we have analysed the impact of a source redshift and that of its apparent magnitude on the lensing optical depth. An increase of the source redshift leads to an increase of its lensing volume and its lensing optical depth. On the other hand, sources with a brighter apparent magnitude see their lensing probability increased thanks to the bias induced in a flux limited sample by the amplification phenomenon.

Let us now analyse the distribution of the lensing probability in the simulated catalogue of QSOs to be detected with the ILMT, and how the effects induced by the source redshift and the amplification bias affect this distribution.

We have calculated the lensing probability for all the sources in the simulated ILMT QSO samples presented in Chapter 5. Fig. 6.4 shows the lensing probability for each source as a function of its redshift (a) and its absolute magnitude (b).

---

[1] We do not consider the configurations where the point-like source is located exactly on the tangential caustic, as the probability of such a configuration is null for a point-like source.

We here show the probability of forming 2 lensed images with the population of deflectors modelled by an SIE mass distribution.

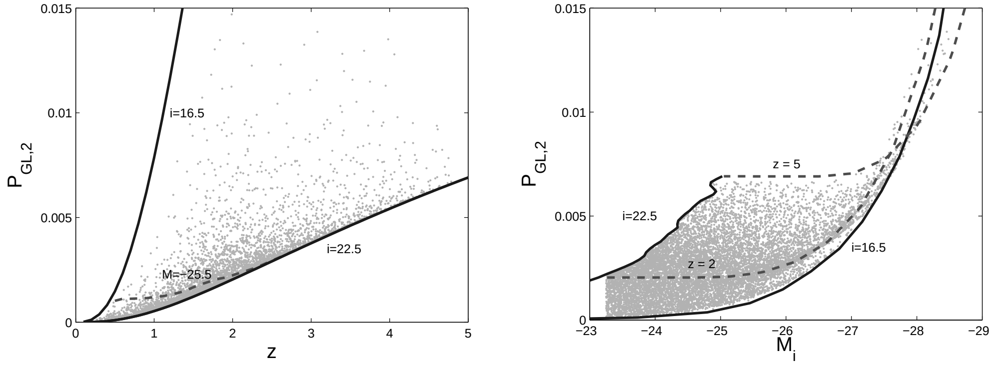

(a) (b)

Figure 6.4: Probability distribution of forming 2 lensed images for the early type galaxies modelled as SIE deflectors, as a function of (a) the source redshift and (b) their absolute magnitude.

Let us first analyse Fig. 6.4a illustrating the distribution of the source probability as a function of their redshift.

First of all, we see that sources with a high lensing probability are pretty rare. All QSOs are located in an area delimited by the two black curves. These curves represent the dependence of the lensing optical depth as a function of the source redshift, for sources with a constant apparent magnitude ($i = 16.5$ and 22.5, respectively). These apparent magnitude cuts correspond to the cuts applied to the simulated catalogue: 22.5 is the limiting magnitude of the ILMT survey and the cut at $i = 16.5$ is applied because sources brighter than this limit are very unlikely to be detected with the ILMT. If we look at the redshift dependence of the lensing probability, for a source with constant apparent magnitude (black curves), we see the same redshift dependence as in Fig. 6.1 showing the geometrical lensing cross section as a function of the redshift. Indeed, as the apparent magnitude is constant along these curves, the amplification bias remains constant; the curve dependence is thus entirely determined by the increase of the lensing geometrical volume.

If we consider all sources with a given redshift (a vertical line in Fig. 6.4a), the lensing probability increases as the sources becomes brighter. This is due to the increase of the amplification bias as the source gets brighter.

Let us now look at the lensing probability dependence as a function of the redshift for a source with a constant absolute magnitude (the dashed curve). As the source redshift increases, its geometrical lensing volume increases but its apparent magnitude decreases. As the overall probability increases with redshift, this means that, for the 2 image lensing probability, the probability distribution is mostly determined by the redshift of the source. This is linked to the fact that 2-image configurations tend to be low amplification events, and thus not highly biased by the amplification phenomenon.

Let us now analyse Fig. 6.4b showing the lensing probability of the sources as a function of their absolute magnitude. The two dashed curves show the probability dependence for sources with a constant redshift, as a function of their absolute magnitude. In both cases ($z = 2$ and $z = 5$), the probability remains constant at first and starts to increase after a given magnitude. This trend is the same as the dependence of the lensing cross section with the source apparent magnitude shown in Fig. 6.3. When the apparent magnitude of a source is fainter than $i \sim 20.5$, a change in its apparent magnitude does not change the amplification bias (as the slope of the DNCF remains constant for the fainter sources); thus the lensing optical depth remains constant with the absolute magnitude. For these faint sources, the higher the redshift, the higher the probability.

For an apparent magnitude brighter than 20.5, an increase in brightness leads to a higher amplification bias and thus increases the lensing probability. For sources intrinsically very bright, we see that the amplification bias effect overcomes that of the redshift and the sources at lower redshift ($z = 2$) have a higher lensing probability than the one further away ($z = 5$).

6.2 Finite angular-resolution effect

In the previous section, we have considered a perfect instrument, i.e. an instrument capable of detecting all the lensed images, independently of their angular separations and their relative fluxes.

In the case of the ILMT, the telescope PSF core has a finite width avoiding to distinguish two separate point-like sources once their angular separation is too small. This finite width is due first of all to the wave nature of light, and secondly to the atmospheric seeing. We have also seen that, if not corrected for, aberrations due to the TDI imaging mode leads to a deformation of the PSF. As the telescope is meant to be seeing limited, the main limitation to the PSF core width is the seeing.

Furthermore, the presence of wavelets over the mercury layer of the primary mirror tends to diffract light in the wings of the PSF, reducing the amount of energy in the PSF central core (Hickson and Racine (2007)).

In this section we study the impact of the ILMT finite angular resolution on its ability to detect the multiply imaged QSOs.

6.2.1 Impact on the dimensionless cross section

The critical angular separation under which multiple point-like sources are undistinguishable from a single one is also a function of their flux ratio(s). The smaller angular distance at which sources are distinguishable occurs for sources that have the same flux. As the difference in flux between the point-like sources increases, they have to be more distant angularly from each other in order to be resolved.

When calculating the dimensionless lensing cross section, thanks to the amplification bias, the regions leading to a very high amplification of the lensed images contribute the most to the cross section. These regions are located along the tangential caustic (cf. the amplification map in Fig. 3.5b). When the source is just located inside the tangential caustic, the two closest images are the highly amplified images located near the tangential critical curve (i.e. the two images appearing when the source crosses the diamond-shaped tangential caustic). These two images are about equally amplified. Consequently, what determines the detectability of these images is the critical angular separation (above which point-like sources are distinguishable) for sources with a *same amplification*. As these configurations (where the closest images are the brightest, and with a very similar amplification) are the ones contributing the most to the lensing cross section, the most important parameter to characterise the impact of the instrument resolution on the cross section is thus the angular resolution for images with the same flux. Consideration of the instrument dynamic limitation will have very little impact on the cross sections.

We have introduced in Chapter 4 the projection R of the instrumental resolution on the deflector plane, normalised to the Einstein radius. R should be a function of the relative amplification of the lensed images. But, thanks to the fact that, in the regions contributing the most to the cross section, the closest very bright images have a very similar amplification, we assume that R is independent on the relative image amplification.

Let us analyse the impact of the R parameter (the instrumental resolution, normalised to the Einstein angular radius) on the calculation of the dimensionless lensing cross sections. Fig. 6.5a shows the dependence of the dimensionless effective cross section Σ_{eff} as a function of R, for an SIS and an SIE mass distribution, with an axis ratio $f = 0.3$, for a source with an apparent magnitude $i = 18.5$.

For the SIS deflector (the black dotted curve), Σ_{eff} remains constant up to $R = 2$ where it drops to 0. We have seen in Chapter 3 that an SIS deflector leads to the formation of two lensed images with the same angular separation, twice the Einstein angular radius. As R is normalised to θ_E, we thus detect all lensed images for values of R smaller than 2, and none when $R > 2$.

For the SIE deflector, the total cross section (plain black curve) remains fairly constant up to $R \sim 1.3$ and then decreases up to $R \sim 2.2$ where its becomes null. In this case, the angular separation between the lensed images is not constant. Consequently, Σ_{eff} starts decreasing for larger values of R. An SIE deflector is also able to produce lensed images with angular separations greater than the Einstein angular diameter which explains why Σ_{eff} gets null for a value of R slightly above that of the SIS case.

Let us now look at how the total SIE cross section is distributed with respect to the number of lensed images. For R values between 0 and ~ 1.2, an increase of R leads to an increase of the fraction of lens events with the formation of 3

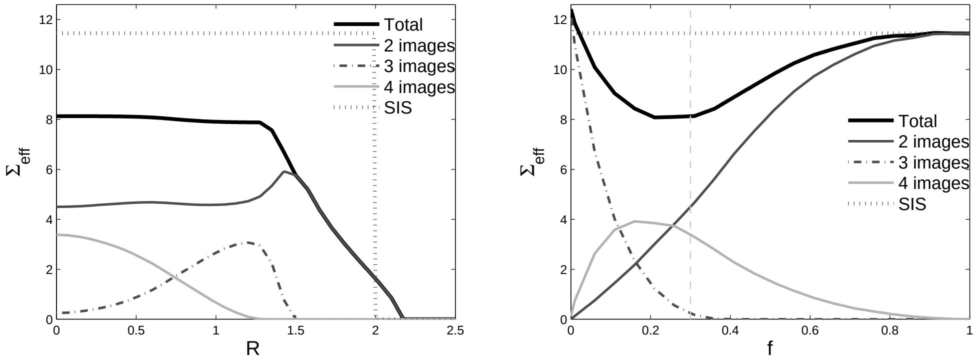

(a)

(b)

Figure 6.5: (a)Dependence of the dimensionless effective cross section Σ_{eff} as a function of R, for an SIS or an SIE with an axis ratio $f = 0.3$, for a source with an apparent magnitude $i = 18.5$.

images, and a decrease of the 4-image configurations. This corresponds mostly to the instrument becoming unable to distinguish the two images near the tangential critical curve. Then for larger values of R, the merging of two inner images leads to an increase of the fraction of 2-image configurations, that eventually, represents all of the detected lens systems.

If we compare Σ_{eff} for the SIS and SIE deflector (with $f = 0.3$), we see that the SIS cross section overestimates the lensing event probability by $\sim 50\%$ with respect to the SIE deflector. To understand this, let us look at Fig. 6.5b showing the dependence of Σ_{eff} for an SIE deflector as a function of its axis ratio f. We have considered $R = 0$ (i.e. a perfect instrument) and a source apparent magnitude $i = 18.5$. For comparison, the value of the SIS cross section is shown as a black dotted line.

For $f \sim 1$, the SIE deflector is almost spherical and Σ_{eff} is equal to that of the SIS deflector. As the SIE deflector becomes more elliptical, its overall cross section diminishes. This is due to the flattening of the radial pseudo-caustic with the increasing deflector ellipticity, noticed in Chapter 3. For $f = 0.3$, we retrieve the same cross section values as in Fig. 6.5a for the case of a perfect instrument. For a given axis-ratio f, the decrease of the cross section of the SIE deflector is thus due to the flattening of the SIE radial pseudo-caustic.

The effective cross section Σ_{eff} for an SIE deflector with a given axis ratio is thus not a practical quantity to compare the efficiency of the SIS and SIE lens populations to produce multiple images of the background QSOs. We thus introduce a new quantity: the SIE cross section averaged over the deflector-population ellipticity distribution. In Eq. 4.43 giving a convenient expression for τ_{SIE}, we can perform the integration over f. This leads to

$$\begin{aligned}
\tau_{SIE} &= C_{sel}\phi_* \frac{\Gamma\left(\left(\alpha+4\right)/\beta\right)}{\Gamma\left(\alpha/\beta\right)} \\
&\quad \int_0^{z_s} dz \int_0^1 \mathrm{d}f \left\{ \left(1+z\right)^3 \frac{cdt}{dz} \mathrm{p}\left(f\right) \Sigma_{eff}^{dim}\left(\sigma_*, f, m\right) \right\}, \\
&= C_{sel}\phi_* \frac{\Gamma\left(\left(\alpha+4\right)/\beta\right)}{\Gamma\left(\alpha/\beta\right)} \\
&\quad \int_0^{z_s} dz \left\{ \left(1+z\right)^3 \frac{cdt}{dz} \int_0^1 \mathrm{d}f \left\{ \mathrm{p}\left(f\right) \Sigma_{eff}^{dim}\left(\sigma_*, f, m\right) \right\} \right\}, \\
&= C_{sel}\phi_* \frac{\Gamma\left(\left(\alpha+4\right)/\beta\right)}{\Gamma\left(\alpha/\beta\right)} \int_0^{z_s} dz \left\{ \left(1+z\right)^3 \frac{cdt}{dz} \Sigma_{<f>}^{dim}\left(\sigma_\star, m\right) \right\},
\end{aligned}$$

where we have introduced

$$\Sigma_{<f>}^{dim} = \int_0^1 \mathrm{d}f \left\{ \mathrm{p}\left(f\right) \Sigma_{eff}^{dim}\left(\sigma_*, f, m\right) \right\}. \tag{6.3}$$

$\Sigma_{<f>}^{dim}$ is the lensing cross section averaged over the axis ratio distribution of the deflector population. We then define dimensionless lensing cross section $\Sigma_{<f>}$ averaged over the axis ratio distribution of the deflector population by means of the relation

$$\Sigma_{<f>}^{dim} = \pi b_0^2 \Sigma_{<f>}. \tag{6.4}$$

Fig. 6.6 shows the dependence of $\Sigma_{<f>}$ as a function of the instrumental resolution R, normalised to the Einstein angular radius, for a source with an apparent magnitude $i = 18$. For comparison, the dimensionless SIS cross section is shown as a black dotted line. The overall behaviour of $\Sigma_{<f>}$ is the same as when considering Σ_{eff} for one particular value of the axis ratio f. Nevertheless, we are now able to compare the overall efficiency of the population of deflectors when modelled with an SIE or an SIS mass distribution.

For $R < 1.5$, the cross section for the SIS case overestimates that of the SIE by less than 10%. It is the overestimate of the cross section, due to the SIE flattening of the radial pseudo-caustic for very elliptical deflectors, that induces the overestimation of the lensing optical depth with the SIS model, observed in Fig. 6.1 and Fig. 6.2a.

If we look at the fraction of events with a given number of lensed images induced by the deflectors, when modelled with an SIE mass profile, we see that the instrumental resolution increases the fraction of events with 3 images with respect to the 4 images ones. Furthermore, the finite resolution tends to increase the fraction of 2 image events relatively to the ones with more than 2 images.

The value of R, the projection of the instrumental resolution on the normalised deflector plane, will of course depend on the position of the deflector plane with respect to the source and the observer. The different redshifts between the observer and the source are thus impacted differently by the instrumental resolution.

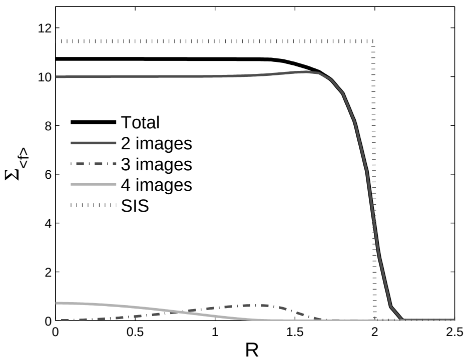

(a)

Figure 6.6: $\Sigma_{<f>}$ as a function of the instrumental resolution R, normalised to the Einstein angular radius, for a source with apparent magnitude $i = 18$.

Let us calculate the contribution of each possible deflector redshift to the overall lensing probability by differentiating the expression of τ_{SIE} (Eq. 4.43) and τ_{SIS} (Eq. 4.38) with respect to the deflector redshift. This gives

$$\frac{d\tau_{SIS}}{dz} = C_{sel}\phi_* \frac{\Gamma\left(\left(\alpha+4\right)/\beta\right)}{\Gamma\left(\alpha/\beta\right)} \left(1+z\right)^3 \frac{cdt}{dz} \Sigma_{eff}^{dim}\left(\sigma_*, m, z, z_s\right), \tag{6.5}$$

$$\frac{d\tau_{SIE}}{dz} = C_{sel}\phi_* \frac{\Gamma\left(\left(\alpha+4\right)/\beta\right)}{\Gamma\left(\alpha/\beta\right)} \left(1+z\right)^3 \frac{cdt}{dz} \Sigma_{<f>}^{dim}\left(\sigma_*, m, z, z_s\right). \tag{6.6}$$

Fig. 6.7 shows the dependence of $d\tau_{SIS}/dz$ and $d\tau_{SIE}/dz$ (defined in Eq. 6.5 and Eq. 6.6) as a function of the deflector redshift, for the case of a source with a redshift $z_s = 2.5$ and an apparent magnitude $i = 18$. The plain curves show the SIE case whereas the SIS case is represented as dashed-dotted lines.

Let us first consider the case of a perfect instrument (the black curves). The redshift range contributing the most to the lensing optical depth is 0.5 to 1, with a maximum for the distribution at $z \sim 0.7$.

If we now consider that only the lensing events with an image angular separation larger than 0.5" are detected (grey curves), we see that the contribution to the lensing optical depth vanishes for deflector redshifts larger than $z \sim 1.2$. If we consider the critical angular separation to be 1", the contribution of redshifts larger than $z \sim 0.5$ vanishes.

Thus, the effect of the finite angular resolution of the telescope is to reject all the lens systems with a high redshift deflector. This can be understood as follows. The Einstein angular radius θ_E as defined in Eq. 3.37 scales as D_{DS}/D_{OS} (where D_{DS} and D_{OS} are the angular distances between the deflector and the source, and between the observer and the source, respectively). As θ_E is a measure of the typical angular separation between the lensed images, for a fixed source redshift,

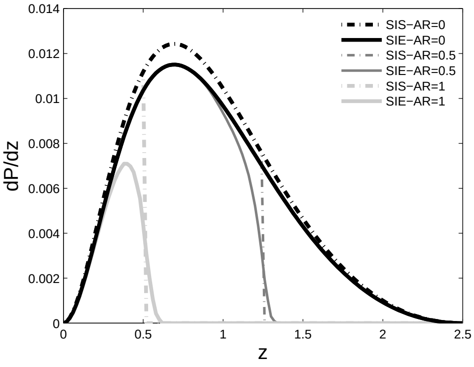

(a)

Figure 6.7: Illustration of $d\tau_{SIS}/dz$ and $d\tau_{SIE}/dz$ as a function of the deflector redshift, for the case of a source with a redshift $z_s = 2.5$ and an apparent magnitude $i = 18$. We have considered 3 different telescope resolutions, namely $AR = 0, 0.5$ and 1".

distant deflectors tend to form lensed images closer to one another. These are thus the first ones not to be detected once the instrumental resolution deteriorates.

6.2.2 Impact on the mean lensing probabilities

Now that we have analysed the impact of the instrumental finite resolution, let us see how it influences the mean lensing optical depth over the whole QSO population.

For the simulated QSO population to be detected with the ILMT, we have calculated the average value of the lensing probability, as a function of the telescope *angular resolution* (AR). Results are shown in Fig. 6.8. Results are shown for the cases where the deflector population is modelled as SIS and SIE mass distributions.

The angular resolution AR is to be understood as the largest angular separation below which multiple point-like sources cannot be resolved. For a PSF with a good Strehl ratio and well sampled, we can use PSF fitting techniques to disentangle point-like sources very close to each other. Typically, for a well sampled and good Strehl ratio, we can hope to detect point-like sources separated by half the PSF FWHM (for point-like sources with comparable flux).

In the case of the ILMT, the best case scenario would be that the telescope is seeing limited. The average site seeing is 1.1" and is better than 1" 35% of the time. The *critical* AR would then be in the range 0.5" - 0.6".

In Chapter 5, we have seen that, assuming that the ILMT will detect all the QSOs brighter than $i \sim 22.5$ in fields with a galactic latitude $|b| > 30°$, the telescope should detect ~ 9072 QSOs.

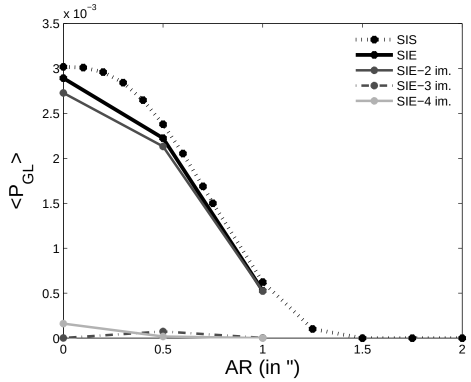

(a)

Figure 6.8: Dependence of the mean lensing probability as a function of the telescope critical resolution for the population of early type galaxies modelled as SIS and SIE deflectors.

Among these QSOs, the ILMT is expected to detect 22 (23 with the SIS model) multiply imaged sources, out of the 28 (29 for the SIS model) multiply imaged QSOs formed in the ILMT sample. Among these gravitational lens systems, only 3 are expected to have more than 2 images. Only 1 gravitational lens system with more than 2 images is ought to be detected with the ILMT for $AR = 0.5$”. Assuming $AR = 1$”, the expectation goes down to 5-6 multiply imaged QSOs (also assuming that, all of the QSOs are still detected).

As seen in Fig. 6.8, the critical resolution range between 0.5 and 1” is where the curve is the steepest. The critical resolution achieved with the ILMT will hopefully be within this range. As a small change in AR in this range induces a big difference on the mean lensing probability, the sharpness of the ILMT is clearly of a critical importance and many efforts will have to be deployed to achieve an angular resolution as good as possible.

6.3 Impact of late type galaxies

So far, we have only considered the population of early type galaxies as possible deflectors. In this section, we study the impact of the late type galaxy population.

Using the VDF parameters for the late type galaxies derived by Chae (2010) (presented in Table 4.1), and the axis ratio distribution determined by Choi et al. (2007), we have calculated the mean lensing optical depth through the ILMT catalogue, as well as its behaviour as a function of the telescope angular resolution AR. Results are shown in Fig. 6.9.

When considering a perfect instrument ($AR = 0$), the average lensing optical depth due to the late type galaxies is about three times less than that due to the

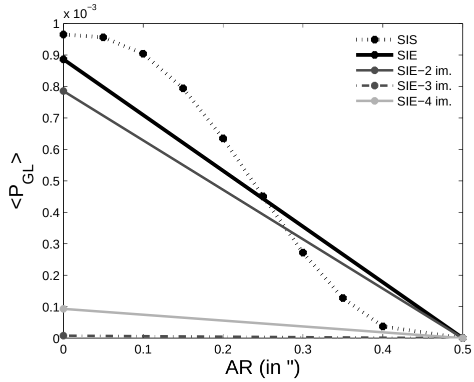

(a)

Figure 6.9: Dependence of the mean lensing probability as a function of the telescope critical resolution for the population of late type galaxies modelled as SIS and SIE deflectors.

early type galaxy population. This can be understood from Eq. 4.38 and Eq. 4.4. We see that the lensing optical depth τ of a source scales as

$$\tau \propto \Phi_* \sigma_*^4 \frac{\Gamma\left((\alpha+4)/\beta\right)}{\Gamma\left(\alpha/\beta\right)}, \tag{6.7}$$

where Φ_* is the characteristic density of the deflector population, σ^* its typical line-of-sight velocity dispersion, and where α and β are the slope parameters of the VDF. From Table 4.1, we see that although late type galaxies are ~ 8 times more numerous, their σ^* is about twice as small as that for early type galaxies. Early type galaxies are thus more efficient deflectors than the late type ones. Inserting the parameter values for both populations, we find $\tau_{early}/\tau_{late} \sim 3.19$.

Furthermore, as the Einstein angular radius of a lens system scales as $\theta_E \propto \sigma^2$, late type galaxies tend to form multiple images with smaller angular separations. This explains why the average lensing probability diminishes very quickly as a function of AR.

For $AR = 0.5$", which is the best case scenario for the ILMT, we expect less than one multiply imaged QSO due to the late type galaxy population. Consequently, we neglect their effect in our estimations.

6.4 Impact of the universe model

The ILMT will detect a population of QSOs with a given redshift distribution and number counts as a function of their apparent magnitude. As the redshifts and the apparent magnitudes consit of observables, they are independent on the assumed universe model.

On the other hand, QSOs are defined on the basis of their absolute magnitudes: they are point-like objects with an absolute (continuum) magnitude M brighter than -22.5. The calculation of the absolute magnitude of an object necessitates the assumption of a universe model.

To calculate the dependence of the average lensing probability over a sample of sources as a function of the universe model parameters, we must thus clearly define the sample we are using.

We calculate the mean lensing probability over a unique sample of sources. We thus simulate the population of sources (with their redshift and apparent magnitude) that are defined as QSOs in a flat FLRW with $H_0 = 70$ km s^{-1} Mpc^{-1} and $\Omega_m = 0.3$. We have then calculated the dependence of the average lensing probability over this sample as a function of Ω_m.

The Ω_m parameter will first have an impact on the distance and volume calculations. The impact of the value of Ω_m on the comoving distances is given by Eq. 5.4 that we integrate to calculate the comoving distances. Because the comoving distances are used to calculate the scale factor b_0 of the lens systems, they affect the dimensional lensing cross section and the lensing volume associated with a source.

Furthermore, because the volume calculation is modified when changing the value of Ω_m, there is also an impact on the density of deflectors in the lensing volumes. The density of deflectors is calculated through the VDF.

The VDF Φ_σ of early type galaxies has been determined in the local universe by Choi et al. (2007) for a flat universe model with $U = (H_0, \Omega_m,) = (70, 0.3)$. Let us derive the relationship between Φ_σ and the VDF $\Phi_{\sigma,2}$ that would have been derived assuming another set of cosmological parameters $U_2 = (H_{0,2}, \Omega_{m,2})$.

In the nearby Euclidean universe, the volume element dv over a square degree in the reshift range $[z, z + dz]$ scales as (Weedman (1986))

$$dv = 8.2\,10^{12}\; H_0^{-3}\, z^2\, dz \quad \left(Mpc^3 deg^{-2}\right). \tag{6.8}$$

Assuming a universe defined by U_2, if dv_2 is the corresponding volume element over a square degree in the redshift range $[z, z + dz]$, then it comes

$$\frac{dv}{dv_2} = \frac{H_{0,2}^3}{H_0^3}.$$

The measured central velocity dispersion for galaxies is independent on the universe model parameters, consequently, when deriving the VDF $\Phi_{\sigma,2}$, the only difference is the change in volume between the two different models. Consequently, we find

$$\Phi_{\sigma,2} = \Phi_\sigma \frac{dv}{dv_2} = \Phi_\sigma \left(\frac{H_{0,2}}{H_0}\right)^3 . \tag{6.9}$$

Thus, thanks to the fact that the VDF has been measured in the local universe and thanks to the assumption of non-evolution of the VDF, the deflector density is not a function of Ω_m.

We have calculated the mean lensing probability for the QSO sample defined by the catalogue of QSOs presented in Chapter 5, when considering $\Omega_m = 0.3$. The dependence of the average lensing optical depth as a function of Ω_m is shown in Fig. 6.10.

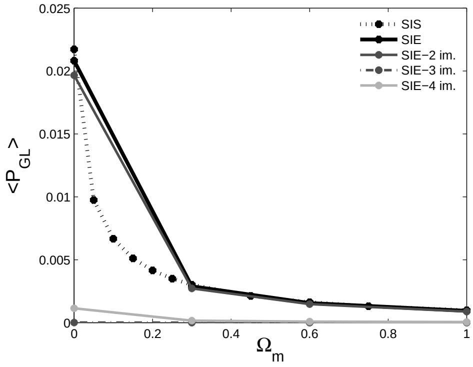

(a)

Figure 6.10: Dependence of the mean lensing probability as a function of Ω_m for early type galaxies modelled as SIS or SIE deflectors.

Results are shown when modelling the deflector population as SIS and SIE. Because of calculation time considerations, we have calculated more points with the SIS model (thanks to the structure of the dimensionless cross section database; probability calculation with the SIS model takes about 10 times less than for the SIE case).

The mean lensing probability for a same source sample decreases as the fraction of matter in the universe increases. An empty flat universe has a lensing probability about 10 times that of a universe full of matter ($\Omega = 1$).

As there is a strong dependence of the mean lensing probability with Ω_m, the fraction of lensing events in a source sample was proposed by Turner and Gott (1984) as a a statistical tool to constrain cosmological parameters. As the dependence of $\langle P_{GL} \rangle$ in Fig. 6.10 as a function of Ω_m is steeper for small values of Ω_m, the fraction of multiply imaged sources in a QSO sample will be an efficient tool to determine a lower limit on Ω_m.

There are different ways to use a statistical sample of sources containing multiply imaged sources. In the next Chapter, we present different methods and compare their sensitivity to a variation of Ω_m.

Chapter 7

Exploiting a sample of gravitational lens systems

In the previous chapters, we have determined the number of QSOs to be detected with the ILMT as well as an expectation for the number of multiply imaged sources among them. We now introduce and compare the different statistical tools that may be used to analyse the clean statistical sample formed by the ILMT sources.

7.1 Lensing statistics as a cosmological probe

Statistics of gravitational lenses have been considered as a cosmological tool since the work of Turner and Gott (1984) who laid down the theoretical basis of strong lensing statistics.

Since then, strong lensing statistics have been used to constrain values of the cosmological parameters and test dark enery models (Keeton (1998), Chae et al. (2002), Keeton (2002), Ofek et al. (2003), Mitchell et al. (2005), Dobke et al. (2009), Cao et al. (2012)).

As the lensing optical depth depends on the deflector population properties, strong lensing statistics have also been used to study the number density of the deflecting galaxy population, their velocity dispersion function and their evolution (Keeton et al. (1998), Keeton (1998), Ofek et al. (2003), Matsumoto and Futamase (2008), Chae (2010)). It has also proven to be a useful tool for the study of the structure of the deflecting galaxies, their distribution of dark matter and their environment (Keeton et al. (1998), Keeton and Kochanek (1998), Faure et al. (2011), Thomas et al. (2011)).

In the different strong lensing statistical studies, there are two commonly used *observables* in the sample of gravitational lens systems: the fraction of lensed events and the redshift distribution of the deflectors.

Let us consider a catalogue of sources, among which multiply imaged sources are present. A first possibility is to use the fraction of lensing events as the *observable statistic* of the catalogue. The idea is to let the parameters of the cosmological model vary in order to reproduce the fraction of observed lensing events in the source population. The catalogue is then exploited by using a maximum likelihood technique: we determine the values of the cosmological parameters that are the most likely, i.e. that allow to reproduce at best the fraction of observed lensing events.

A second observable statistic introduced by Turner and Gott (1984) is the redshift distribution of the deflectors in the sample of multiply imaged sources. To exploit this observable statistic, we introduce a new quantity $\left(d\tau/dz_d\right)/\tau$. $\left(\left(d\tau/dz_d\right)/\tau\right)dz_d$ represents the probability that, when observing a multiply imaged source, the deflector leading to the formation of the multiple images has a redshift in the range $[z_d, z_d + dz_d]$. It is the relative contribution of the redshift range $[z_d, z_d + dz_d]$ to the lensing optical depth of the source.

Let us consider a source at redshift z_s potentially deflected by a foreground galaxy modelled as an SIS. We have determined in Eq. 4.38 the expression of τ_{SIS}, assuming a non-evolving deflector population, uniformly distributed in the comoving reference frame. The derivative of Eq. 4.38 with respect to z_d leads to

$$\begin{aligned}\frac{d\tau_{SIS}}{dz_d} &= C_{sel}\phi_*\frac{\Gamma\left(\left(\alpha+4\right)/\beta\right)}{\Gamma\left(\alpha/\beta\right)}\left(1+z\right)^3\frac{cdt}{dz}\Sigma_{eff}^{dim}\left(\sigma_*,m\right)\\ &= C_{sel}\phi_*\frac{\Gamma\left(\left(\alpha+4\right)/\beta\right)}{\Gamma\left(\alpha/\beta\right)}\left(1+z\right)^3\frac{cdt}{dz}\left(4\pi\left(\frac{\sigma_*}{c}\right)^2\frac{D_{OD}D_{DS}}{D_{OS}}\right)^2\Sigma_{eff}\left(m\right).\end{aligned} \tag{7.1}$$

Dividing Eq. 7.1 by the expression of τ_{SIS} in Eq. 4.38 leads to

$$\begin{aligned}\frac{1}{\tau_{SIS}}\frac{d\tau_{SIS}}{dz_d} &= \frac{C_{sel}\phi_*\frac{\Gamma((\alpha+4)/\beta)}{\Gamma(\alpha/\beta)}\left(1+z\right)^3\frac{cdt}{dz}\Sigma_{eff}^{dim}\left(\sigma_*,m\right)}{C_{sel}\phi_*\frac{\Gamma((\alpha+4)/\beta)}{\Gamma(\alpha/\beta)}\int_0^{z_s}\left\{\left(1+z\right)^3\frac{cdt}{dz}\Sigma_{eff}^{dim}\left(\sigma_*,m\right)\right\}dz},\\ &= \frac{\left(1+z\right)^3\frac{cdt}{dz}\left(\frac{D_{OD}D_{DS}}{D_{OS}}\right)^2\Sigma_{eff}}{\int_0^{z_s}\left\{\left(1+z\right)^3\frac{cdt}{dz}\left(\frac{D_{OD}D_{DS}}{D_{OS}}\right)^2\Sigma_{eff}\right\}dz}.\end{aligned} \tag{7.2}$$

This quantity depends on the geometrical configuration of the lens system (i.e. the different distances D_{OD}, D_{DS} and D_{OS}), the universe model and the effective cross section. If we express the amplification bias in terms of the source differential number counts as a function of the apparent magnitude and if the instrumental resolution is considered independent of the redshift, then the only dependency of $\left(d\tau/dz\right)/\tau$ to the source distribution is through its DNCF. In other words, $\left(d\tau/dz\right)/\tau$ is a function of three observables (z_s, z_d and the DNCF) and the universe model parameters.

Fig. 7.1 shows the relative contribution to the lensing optical depth, as a function of the deflector redshift. We show the dependence of $\left(d\tau/dz\right)/\tau$ for two different source redshifts ($z = 2$ and $z = 4$) and for 3 different values of the cosmological parameter Ω_m.

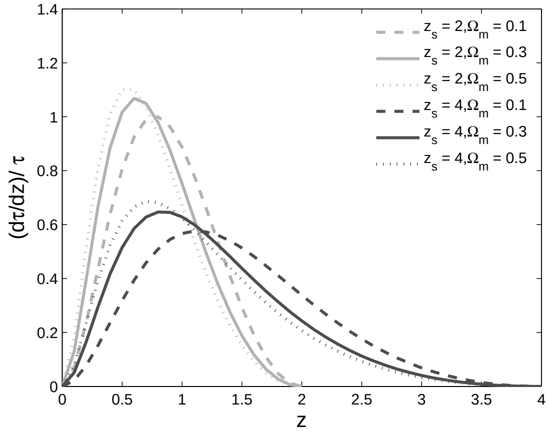

Figure 7.1: The $(d\tau/dz)/\tau$ dependence as a function of the deflector redshift for a population of SIS deflectors. We consider 2 different source redshifts and 3 different flat universes with $\Omega_m = 0.1$,$\Omega_m = 0.3$ and $\Omega_m = 0.5$.

When using the quantity $(d\tau/dz)/\tau$ as a cosmological probe, the idea is to maximise the likelihood of a set of universe parameters by maximising the likelihood of the deflector redshifts for the detected lenses.

Other observable statistics have been proposed as well such as the angular separation distribution between the lensed images (Turner and Gott (1984)). As most of the work in strong lensing statistics uses the fraction of lens events or the deflector redshift distribution, we will concentrate on their study and compare their sensitivity to the cosmological model parameters in order to determine the most efficient way to exploit the information contained in the catalogues.

Both statistics use a maximum likelihood method, where the likelihood for each object is added. When considering the fraction of lens events in a sample, we add the likelihood of the lensed sources to effectively be lensed and that of the others of not being lensed. When considering the deflector redshift distribution, we add the likelihood of each deflector to be located at its observed redshift.

We have developed a new formalism for gravitational lensing statistics, allowing to calculate the fraction of lensing events and the distribution of deflector the redshifts, but now taking into account the entire population at once and the average distributions over the population of detected sources.

This new formalism also enables to calculate a new quantity which we propose to use as a cosmological tool : the redshift distribution of the sources among the lensing events. We test as well the sensitivity of this distribution as a function of the universe model parameters.

7.2 QSO joined probability density $d_{obs}\left(M,z\right)$

We now introduce a new concept that we will use to calculate the different distributions: the QSO joined probability density $d_{obs}\left(M,z\right)$.

Let us consider a QSO survey that detects a population of N_{QSO} sources. Each QSO is characterised by its absolute magnitude M and its redshift z.

If we want to estimate the expected number N_{GL} of gravitationally lensed sources with formation of multiple images to be detected in the source population (as it has been done in Chapter 6), we may use the relationship

$$N_{GL} = \langle\tau\rangle\, N_{QSO},$$

where τ is the optical depth associated with a single source and $\langle\tau\rangle$ the mean value of the optical depth over the whole catalogue.

For a given source and assuming a universe model, τ is a function of the source redshift z and apparent magnitude m (necessary to calculate the amplification bias). As the source apparent magnitude is calculated from the absolute magnitude M_i and redshift z_i, it is possible to derive an expression for the lensing probability $\tau\left(M,z\right)$ as a function of M and z. Let us assume known such an expression for $\tau\left(M,z\right)^1$.

So far, in the previous chapters, the mean value of the lensing probability for all the quasars was evaluated through

$$\langle\tau\rangle = \sum_{i=1}^{N_{QSO}} \frac{1}{N_{QSO}} \tau\left(M_i, z_i\right), \tag{7.3}$$

where M_i and z_i are the absolute magnitude and the redshift of the i^{th} QSO in the detected population.

Now let us suppose that we do a two-dimensional histogram of the sources by sampling the absolute magnitude M and the redshift z using the borders of the interval values M_k and z_j defined as

$$\begin{aligned} M_k &= M_{min} + k\Delta M \quad &&\text{, with} \quad k = 0, 1, ..., k_{max}, \\ z_j &= z_{min} + j\Delta z \quad &&\text{, with} \quad j = 0, 1, ..., j_{max}. \end{aligned}$$

Introducing the M_k and z_j in Eq. 7.3, $\langle\tau\rangle$ can be expressed as

$$\langle\tau\rangle = \sum_{j=0}^{j_{max}} \sum_{k=0}^{k_{max}} \frac{N_{jk}}{N_{QSO}}\, \tau\left(M_k, z_j\right), \tag{7.4}$$

---

[1] $\tau\left(M,z\right)$ is obtained using the developed Matlab libraries described in Chapter 4. We make use of a function returning the apparent magnitude as a function of M and z as an argument to the function $\tau\left(m,z\right)$ calculating the lensing optical depth as a function of the apparent magnitude m. Thus

$$\tau\left(M,z\right) = \tau\left(m\left(M,z\right), z\right)$$

where N_{jk} represents the number of QSOs observed in the survey interval

$$\begin{aligned} M &\in [M_k - \Delta M/2, M_k + \Delta M/2[\,, \\ z &\in [z_j - \Delta z/2, z_j + \Delta z/2[\,. \end{aligned} \tag{7.5}$$

Let us now consider the limit to the continuous case, i.e. we consider $\Delta M \to 0$ and $\Delta z \to 0$ in expression 7.4 which leads to

$$\langle \tau \rangle = \int_{M_{min}}^{M_{max}} \int_{z_{min}}^{z_{max}} \left\{ d_{obs}\left(M, z\right) \tau\left(M, z\right) \right\} dz dM. \tag{7.6}$$

M_{min} and M_{max} are the minimum and maximum absolute magnitudes of the observed population of QSOs. z_{min} and z_{max} define the range of redshifts for the detected sources, and we define

$$d_{obs}\left(M, z\right) = \lim_{N_{QSO} \to \infty} \lim_{\substack{\Delta M \to 0 \\ \Delta z \to 0}} \frac{N_{jk}}{N_{QSO}}.$$

If we consider the absolute magnitude M and the redshift z of the sources as random variables (the *random event* being to pick a QSO in the population detected by the survey), then $d_{obs}\left(M, z\right)$ is the joined probability density associated with the random variables M and z. In other words,

$$d_{obs}\left(M, z\right) dM dz$$

represents the probability that observing a source in the survey, this source has an absolute magnitude and a redshift in the range $[M, M + dM[$ and $[z, z + dz[$, respectively.

The *QSO joined probability density* $d_{obs}\left(M, z\right)$ in the (M, z) space is the cornerstone of our new formalism. Before showing how we can express the fraction of multiply imaged sources and the average redshift distribution of the deflectors as a function of $d_{obs}\left(M, z\right)$, we explain in the next subsection how the QSO joined probability density is linked to the observations.

Determining d_{obs} from observations

We may define the joined *Cumulative Distribution Function* (CDF) $D_{obs}\left(M, z\right)$ of the observed QSOs

$$D_{obs}\left(M, z\right) = \int_{M_{min}}^{M} \int_{0}^{z} d_{obs}\left(M', z'\right) dz' dM'. \tag{7.7}$$

$D_{obs}\left(M, z\right)$ represents the probability that a source, randomly chosen in the population observed in the survey, has an absolute magnitude smaller than M and a redshift lower than z. Furthermore, for the two continuous random variables M and z, we have

$$d_{obs}\left(M, z\right) = \frac{\partial^2 D_{obs}\left(M, z\right)}{\partial M \partial z}. \tag{7.8}$$

When considering a survey, the Cumulative Distribution Function $D_{obs}\left(M, z\right)$ can be directly determined from the observations (after choosing a cosmological model in order to calculate the absolute magnitudes). Indeed, $D_{obs}\left(M, z\right)$ corresponds to a cumulative histogram of the population of detected sources as a function of their absolute magnitude and redshift, normalised by the total number of detected sources. By fitting this histogram in the (M, z) plane, we directly determine $D_{obs}\left(M, z\right)$ and thus, through Eq. 7.8 we determine the joined probability density d_{obs} associated with the random variables M and z.

We can thus consider d_{obs} to be directly accessible from the observations.

Estimating d_{obs} for simulation purposes

The joined probability density $d_{obs}\left(M, z\right)$ of the observable population is a difficult distribution to simulate. It will depend on the intrinsic source distribution through space as a function of their absolute magnitude, as well as the universe model. Furthermore, it will be highly dependent on the selection effects due to the survey characteristics and detection strategies; colour selection of QSOs for instance will lead to a bias at redshifts where QSO colours become similar to those of certain types of stars.

For the purpose of this chapter, we will use a simplified model for $d_{obs}\left(M, z\right)$: we consider as the only selection effect the flux of the source that must be higher than a critical value. This represents a *perfect* flux limited sample. This would thus represent the $d_{obs}\left(M, z\right)$ distribution of a perfect flux limited survey. Although such survey characteristics are very hardly achievable, the simulated d_{obs} is sufficient to show the main trends of the dependence of the different distributions on the universe models.

We estimate $d_{obs}\left(M, z\right)$ through

$$d_{obs}\left(M, z\right) = S\left(M, z\right)\, \Phi_{QSO}\left(M, z\right) \frac{dV_C}{dz} \frac{1}{N_{QSO}}, \tag{7.9}$$

where

- $S\left(M, z\right)$ is a function accounting for the survey selection effect (in this case only flux limited). This function equals 1 if the apparent magnitude of a QSO having an absolute magnitude M and redshift z is brighter than the limiting apparent magnitude of the survey;
- $\Phi_{QSO}\left(M, z\right)$ is the QSO luminosity function;

- $\frac{dV_C}{dz}$ is the variation of the comoving volume accessible by the survey at redshift z. It is calculated, in a flat FLRW universe, by means of the relation

  $$\frac{dV_C}{dz} = D_C^2\left(z\right)\frac{dD_C}{dz}\Omega_{Survey},$$

  where D_C is the line-of-sight comoving distance, dD_C/dz its variation with redshift, and Ω_{Survey} the survey solid angle;

- N_{QSO} is the number of sources detected in the survey. This is a normalisation factor to ensure that d_{obs} has a unitary norm, necessary to consider it as a probability density.

7.3 Calculating distributions with $d_{obs}\left(M, z\right)$

7.3.1 Lensing optical depth distribution

Let us consider M and z as two random variables following a probability law described by the joined probability density $d_{obs}\left(M, z\right)$. Because a randomly chosen source, characterised by the value of the random variables M and z, has an associated lensing optical depth τ, we can consider $\tau\left(M, z\right)$ as a function of these two random variables. The calculation of the average lensing optical depth $\langle\tau\rangle$ over the sources of the catalogue can thus be done by calculating the mathematical expectation $E\left[\tau\right]$ of τ, seen as a function of the two random variables, i.e.

$$\langle\tau\rangle = \int_{M_{min}}^{M_{max}}\int_{z_{min}}^{z_{max}}\left\{d_{obs}\left(M, z\right)\tau\left(M, z\right)\right\}dzdM. \tag{7.10}$$

$\langle\tau\rangle$ is thus the mathematical expectation of τ through the population of detected QSOs. Furthermore, the calculation of the variance σ_τ^2 for τ over the catalogue can be done through the calculation of

$$\begin{aligned}\sigma_\tau^2 &= \left\langle\left(\tau - \langle\tau\rangle\right)^2\right\rangle \\ &= \int_{M_{min}}^{M_{max}}\int_{z_{min}}^{z_{max}}\left\{d_{obs}\left(M, z\right)\left(\tau\left(M, z\right) - \langle\tau\rangle\right)^2\right\}dzdM. \end{aligned}\tag{7.11}$$

So far, we have considered $\tau\left(M, z\right)$ as a function of the random variables M and z and we have calculated the expectation of the mean value of this function as well as the expectation of the variance of the function for the randomly chosen sources.

On the other hand, we may consider τ as being itself a random variable associated with the randomly chosen sources. Consequently, we can define a probability density w_τ associated with this variable within the detectable population of sources. $w_\tau d\tau$ thus represents the probability that a randomly chosen QSO (within the population of detectable QSOs in the survey) has a lensing optical depth in the range $\left[\tau, \tau + d\tau\right]$.

We have no explicit expression for ω_τ. Nevertheless, in order to have an idea of how the probability density is distributed as a function of τ, we have estimated ω_τ by doing a histogram, as a function of the lensing optical depth, for the ILMT QSOs simulated in Chapter 5, for which we have calculated the optical depth in Chapter 6. The resulting estimation of ω_τ for a flat FLRW universe with $\Omega_m = 0.3$ is shown in Fig. 7.2.

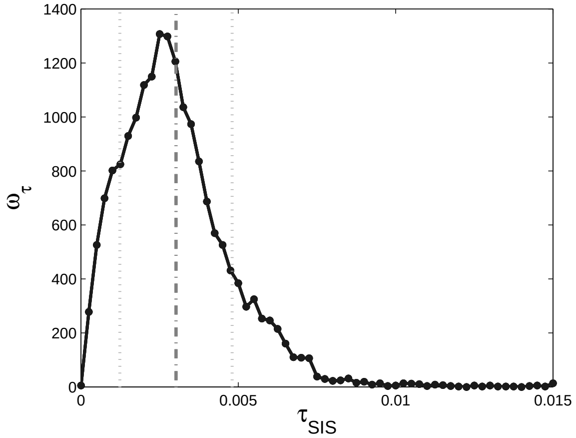

Figure 7.2: Probability density ω_τ as a function of the lensing optical depth τ_{SIS} for the ILMT QSOs. ω_τ is estimated through the histogram of the ILMT QSO catalogue.

We may use w_τ to calculate the expectations $E\left[\tau\right]$ and $E\left[\left(\tau - \langle\tau\rangle\right)^2\right]$ of the random variable τ through

$$\begin{aligned}
E\left[\tau\right] &= \int_0^1 w_\tau \tau d\tau \\
&= \langle\tau\rangle = m_1 \\
E\left[\left(\tau^2 - \langle\tau\rangle^2\right)\right] &= \int_0^1 w_\tau \left(\tau - \langle\tau\rangle\right)^2 d\tau \\
&= \sigma_\tau^2 = \mu_2, \qquad (7.12)
\end{aligned}$$

where $\langle\tau\rangle$ and σ_τ^2 are thus the values given by Eq. 7.10 and Eq. 7.11, respectively. We recognise through these relationships the definitions of the first moment m_1 of the random variable τ and its second centred moment μ_2 (i.e. its standard deviation). Indeed, the centred moment μ_k of order k $(> 0)$is defined as

$$\mu_k = \int w_\tau\left(\tau\right)\left(\tau - \langle\tau\rangle\right)^k d\tau. \qquad (7.13)$$

In Fig. 7.2, the value of m_1 is shown as a grey dashed-dotted line, and the values of τ_{SIS} within a distance of one μ_2 are marked with vertical dotted lines.

Consequently, when using the observed number of detected gravitational lenses within a catalogue of sources, we are actually calculating the first moment of the optical depth probability density w_τ. Since the observed number of lenses has been proposed as a tool to probe the universe, the reliability of this approach thus depends on the sensitivity of the w_τ distribution to the cosmological parameters.

We propose to test the sensitivity of this distribution to the universe models through the sensitivity of the two first moments of the distribution, namely its mean $\langle\tau\rangle$ and variance σ_τ^2. These dependence to the universe will be analysed in Section 7.4.

As the distribution w_τ is not easy to calculate, we estimate these two parameters by considering τ as a function of the two random variables M and z. We thus use Eq. 7.10 and Eq. 7.11 to calculate $\langle\tau\rangle$ and σ_τ^2, respectively.

7.3.2 Redshift distribution of the lens deflectors

In Section 7.3.1, we have derived the expression of the mean lensing probability in a sample of sources, as a function of the QSO joined probability density $d_{obs}\left(M, z\right)$. In this section, we derive the expression of the redshift distribution of the deflectors for the detected lensing events. We calculate the expected redshift distribution of the deflectors that are effectively forming multiple images of the background sources.

Let us first define $P\left(GLE\right)$ the probability of having a gravitational lens event in the source population and $P\left(z_d = Z\right)$ the probability of having a foreground galaxy at a redshift z_d in the range $[Z, Z + dZ[$ (independently of the fact that this deflector leads to the formation of multiple images of a background source).

We can now define the conditional probability $P\left(\left(z_d = Z\right)|GLE\right)$ of having a deflector with a redshift z_d in the range $[Z, Z + dZ]$, knowing that there is a lensing event produced by this deflector. By definition of a conditional probability

$$P\left(\left(z_d = Z\right)|GLE\right) = \frac{P\left(\left(z_d = Z\right) \cap GLE\right)}{P\left(GLE\right)}. \tag{7.14}$$

$P\left(\left(z_d = Z\right)|GLE\right)$ is linked to the probability density $w_{z_d}\left(Z\right)$ such that

$$P\left(\left(z_d = Z\right)|GLE\right) = w_{z_d}\left(Z\right) dZ. \tag{7.15}$$

$w_{z_d}\left(Z\right)$ is thus the probability density of having a deflector with a redshift $z_d = Z$, knowing that this deflector is near the line-of-sight of a background source and leads to the formation of multiple images of this source.

In other words, the deflectors of the multiply imaged sources in our sample are distributed as a function of the redshift according to the distribution $w_{z_d}\left(Z\right)$. Thus, when observing the redshift of a deflector in a lens system chosen randomly in our sample, we may consider the deflector redshift as a random variable and the probability of the variable to take a value z_d in the range $[Z, Z + dZ]$ is given by $w_{z_d}\left(Z\right) dZ$.

Let us now express Eq. 7.15 in terms of the probability density $d_{obs}(M,z)$. As in Section 7.3.1, the probability of having a lensing event in the source sample $P(GLE)$ is given by

$$\begin{aligned} P(GLE) &= \int_{z_{min}}^{z_{max}} \int_{M_{min}}^{M_{max}} \left\{ d_{obs}(M,z)\,\tau(M,z) \right\} dM dz \\ &= \langle \tau \rangle . \end{aligned} \tag{7.16}$$

For a single source, at redshift z_s, the probability of being multiply imaged by a deflector with a redshift in the range $[Z, Z+dZ]$ is given by $(d\tau/dz_d)\,dZ$. The probability through the whole detected population, of having a deflector with a redshift z_d in the range $[Z, Z+dZ]$ is thus given by the average value of $(d\tau/dz_d)\,dZ$ over the source population, i.e.

$$P((z_d = Z) \cap GLE) = \int_{z_{min}}^{z_{max}} \int_{M_{min}}^{M_{max}} \left\{ d_{obs}(M,z)\,(d\tau/dz_d)\,dZ \right\} dM dz. \tag{7.17}$$

Inserting Eq. 7.16 and Eq. 7.17 in Eq. 7.15 and using Eq. 7.14, we find

$$\omega_{z_d}(Z) = \frac{1}{\langle \tau \rangle} \int_{Z}^{z_{max}} \int_{M_{min}}^{M_{max}} \left\{ d_{obs}(M,z)\,\frac{d\tau(M,z)}{dz} \right\} dM dz. \tag{7.18}$$

Since we have an explicit expression for $d_{obs}(M,z)$ and of $d\tau(M,Z)/dz$ (see Eq. 7.1), we can use Eq. 7.18 to calculate the probability distribution $\omega_{z_d}(Z)$ as a function of the redshift deflector z_d.

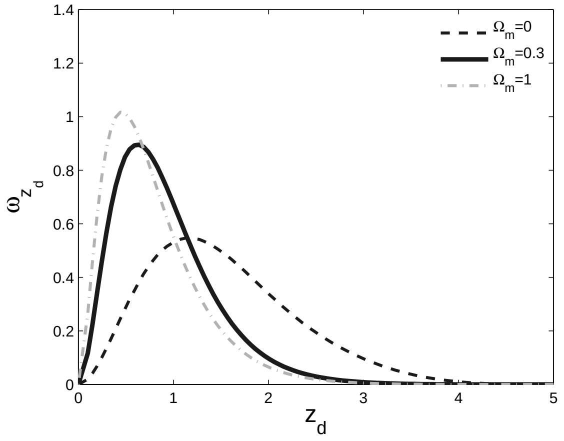

Figure 7.3: ω_{z_d} as a function of z_d for different universe models.

Fig. 7.3 shows the evolution of ω_{z_d} as a function of z_d for different universe models, when considering the population of early type galaxies modelled as SIS deflectors and a perfect instrument.

7.3.3 Redshift distribution of the lensed sources

Use of the QSO joined probability density d_{obs} gives access to a new distribution: the redshift distribution of the sources that are effectively multiply imaged.

Let us define the probability $P\left(z_s = Z\right)$ of having a source with a redshift z_s in the range $[Z, Z + dZ]$, independently of the fact that this source is detected as being multiply imaged.

We may define the conditional probability $P\left(\left(z_s = Z\right)|GLE\right)$ of having a source with a redshift z_s in the range $[Z, Z + dZ]$, knowing that this source is multiply imaged. $P\left(\left(z_s = Z\right)|GLE\right)$ is defined as

$$P\left(\left(z_s = Z\right)|GLE\right) = \frac{P\left(\left(z_s = Z\right) \cap GLE\right)}{P\left(GLE\right)}. \tag{7.19}$$

$P\left(GLE\right)$ is given by Eq. 7.10. $P\left(\left(z_s = Z\right)|GLE\right)$ is linked to the probability density $w_{z_s}\left(Z\right)$, which is the probability density of having a source with a redshift $z_s = Z$ knowing that this source is multiply lensed. $w_{z_s}\left(Z\right)$ and $P\left(\left(z_s = Z\right)|GLE\right)$ are linked through the relation

$$P\left(\left(z_s = Z\right)|GLE\right) = w_{z_s}\left(Z\right) dZ. \tag{7.20}$$

For a single source with an absolute magnitude M and a redshift z_s, the probability of having a redshift z_s in the range $[Z, Z + dZ[$ and being multiply imaged is given by $\delta\left(z_s - Z\right) \tau\left(M, z_s\right) dZ$. This can be averaged over the whole population of the detected QSOs to find $P\left(\left(z_s = Z\right) \cap GLE\right)$. Thus, proceeding similarly as in Section 7.3.2, we find

$$P\left(\left(z_s = Z\right)|GLE\right) = \frac{\int_{z_{min}}^{z_{max}} \int_{M_{min}}^{M_{max}} \left\{d_{obs}\left(M, z\right) \delta\left(z - Z\right) \tau\left(M, z\right)\right\} dM dz}{\int_{z_{min}}^{z_{max}} \int_{M_{min}}^{M_{max}} \left\{d_{obs}\left(M, z\right) \tau\left(M, z\right)\right\} dM dz} dZ. \tag{7.21}$$

The redshift distribution $\omega_{z_s}\left(Z\right)$ of the sources that are detected as multiple images is thus given by

$$\omega_{z_s}\left(Z\right) = \frac{1}{\langle\tau\rangle} \int_{M_{min}}^{M_{max}} \left\{d_{obs}\left(M, Z\right) \tau\left(M, Z\right)\right\} dM. \tag{7.22}$$

As we know the explicit expressions of $\langle\tau\rangle$ (Eq. 7.10), $d_{obs}\left(M, Z\right)$ (Eq. 7.9) and $\tau\left(M, Z\right)$, we are able to calculate the value of the distribution $\omega_{z_s}\left(Z\right)$ as a function of the source redshift. The dependence of ω_{z_s} as a function of the redshift is shown in Fig. 7.4, for different values of Ω_m. For comparison, we have represented as a dotted black line the normalised redshift distribution of all the detected QSOs in the ILMT survey.

Compared to the redshift distribution of all the sources, ω_{z_s} is shifted towards higher redshifts. As expected, the lensed sources tend to be very distant sources as they are characterised by a higher geometrical lensing volume.

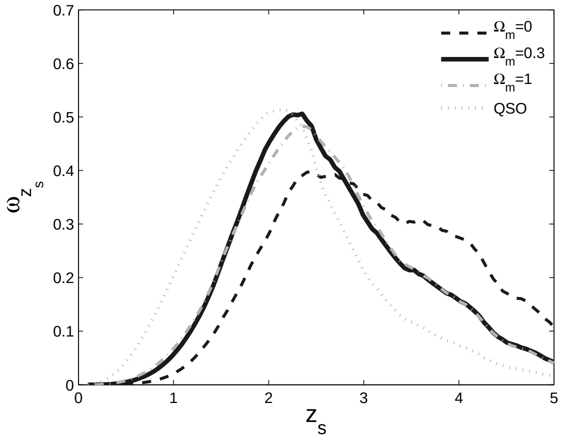

Figure 7.4: ω_{z_s} as a function of z_s for different universe models. For comparison, the redshift distribution of all the QSOs is shown as the dotted light-grey curve.

A second observation, is that for redshifts higher than $z \sim 2$, although ω_{z_s} decreases as a function of the redshift in all cases, the distribution is not smooth. For instance, there seems to be an excess of the density of quasars with a redshift in the range 3.36 - 4.32. This is an effect caused by the emission lines in the spectra of the QSOs. In the range 3.36 - 4.32 for instance, the CIV line enters the SDSS-i filter[2]. Thus thanks to this strong emission line, the sources in this redshift range will appear brighter. Because their apparent magnitude is decreased thanks to the emission line, the effect of the amplification bias is increased. Consequently, there is an increase of ω_{z_s} in this redshift range compared to the situation corresponding to a pure continuum spectrum.

Inspection of Fig. 7.4 leads to the conclusion that the source redshift distribution among multiply imaged quasars is not very sensitive to Ω_m.

7.4 Sensitivity comparison to Ω_m

In the previous section, we have described three probability densities, namely

- ω_τ: the probability density of the optical depth associated with the multiply imaged sources;

---

[2] The SDSS i filter spans over the wavelength range 675 to 825 nm. As the CIV line is located at 154.9 nm, it enters the i filter at a redshift

$$z_{in} = \frac{675}{154.9} - 1 = 3.36$$

- ω_{z_d}: the normalised redshift distribution of the deflectors forming the multiply imaged sources;

- ω_{z_s}: the normalised redshift distribution of the sources that are detected as multiply imaged.

These three distributions determine the behaviour of an observable in a sample of sources containing multiply imaged QSOs (the fraction of multiply imaged sources, the deflector and multiply imaged source redshift distribution, respectively).

We would like to compare the sensitivity of these distributions to the cosmological parameter Ω_m. Although we do have an explicit formulation allowing us to calculate ω_{z_d} and ω_{z_s} (Eq. 7.18 and Eq. 7.22, respectively), we do not have such an expression for ω_τ. Consequently, we cannot calculate the direct dependence of ω_τ as a function of Ω_m.

To compare the behaviour of the three probability densities, we will thus compare the mean value of their distribution and their standard deviation. For ω_τ, these are calculated using Eq. 7.10 and Eq. 7.11. For the other distributions, we calculate the probability density as a function of the redshift through Eq. 7.18 and Eq. 7.22, and then calculate the mean value and standard deviation.

We have already explained in Chapter 6 how the universe model parameters affect the calculation of the lensing optical depth τ (and $d\tau/dz$ is affected in the same way). In the next section, we explain how the choice of a universe model impacts on the QSO joined probability density $d_{obs}(M, z)$.

7.4.1 Modification of the simulated d_{obs} with the universe model

In Eq. 7.9, we see that d_{obs} depends on the QSO luminosity function that has been determined assuming a FLRW flat universe model with $H_0 = 70$ (km s^{-1} Mpc^{-1}) and $\Omega_m = 0.3$. Thus assuming a FLRW universe model defined by the set of parameters, $U_1 = \{H_{0,1}, \Omega_{m,1}, \Omega_{\Lambda,1}\} = \{70, 0.3, 0.7\}$, the LF $\Phi_1(M_1, z)$ has been determined from a set of observations. M_1 is the absolute magnitude of a source with apparent magnitude m at redshift z (as determined in U_1). M_1 and m are linked through

$$M_1 = m - K(z) - DM_1(z),$$

where K is the K-correction and where DM_1 is the distance modulus associated with the redshift z as calculated for U_1.

Φ_1 has been determined to be consistent with the observed distribution of the sources as a function of the redshift and apparent magnitude. Consequently, if we define $dn(m, z)$ as the number of sources detected with a redshift and an apparent magnitude in the range $[z, z + dz[$ and $[m, m + dm[$, respectively , it comes

$$dn(m, z) = \Phi_1(m - K - DM_1, z)\left(\frac{dV_c}{dz}\right)_{U1}, \tag{7.23}$$

where $\left(\frac{dV_c}{dz}\right)_{U1}$ is the redshift variation of the comoving volume accessible to the survey at redshift z. In a flat universe

$$\left(\frac{dV_c}{dz}\right)_{U1} = \Omega D_C^2 \frac{dD_C}{dz}, \tag{7.24}$$

where D_C is the comoving distance and Ω the solid angle of the survey.

If the determination of the QSO LF were done assuming a universe with characteristics U_2, we would obtain a LF $\Phi_2\left(M_2, z\right)$, with $M_2 = m - K - DM_2$. This second LF would also need to be consistent with the observed (m, z) distribution of the observations. Consequently, relation 7.23 would also be satisfied for Φ_2. This implies

$$\Phi_1\left(m - K - DM_1, z\right)\left(\frac{dV_c}{dz}\right)_{U1} = \Phi_2\left(m - K - DM_2, z\right)\left(\frac{dV_c}{dz}\right)_{U2}.$$

Consequently, Φ_2 is linked to Φ_1 by means of the relation

$$\Phi_2\left(M, z\right) = \Phi_1\left(M - DM_1 + DM_2, z\right)\left(\frac{dV_c}{dz}\right)_{U1}\left(\frac{dV_c}{dz}\right)_{U2}^{-1}. \tag{7.25}$$

When changing the universe model, the QSO LF is changed according to Eq. 7.25.

In Eq. 7.9, we see that $d_{obs}\left(M, z\right)$ depends on the selection function $S\left(M, z\right)$. When considering the universe model U_2 we should consider in the selection function the absolute magnitude M_2 as calculated for this universe model. We have seen that the definition of a QSO is arbitrary and implies to be brighter than a critical absolute magnitude of -22.5 in the i band. To be consistent with the calculation done in Chapter 6, we want to calculate the lensing statistics for a same sample of sources. We thus select the sources that are defined as QSOs in the universe model characterized by U_1.

7.4.2 Comparison between the different distributions

Fig. 7.5 shows the dependence of the mean value of ω_τ (a), ω_{z_d} (b) and ω_{z_s} (c), as a function of Ω_m.

Let us first consider the dependence of the mean optical depth (Fig. 7.5a). The dark curve shows the quantity $\langle\tau\rangle$, calculated using the formulation with $d_{obs}\left(M, z\right)$ (i.e. Eq. 7.10).

As the dependence of the mean optical depth has already been calculated in Chapter 5 (cf. Fig. 6.10) by simulating a catalogue and calculating the lensing probability of all sources, we have plotted the results previously obtained as the black circles. The very good agreement attests the reliability of the new method for the calculation of $\langle\tau\rangle$.

If we now compare the dependence of $\langle\tau\rangle$ with those of $\langle z_d\rangle$ (b) and $\langle z_s\rangle$ (c), the mean optical depth shows the highest relative variation.

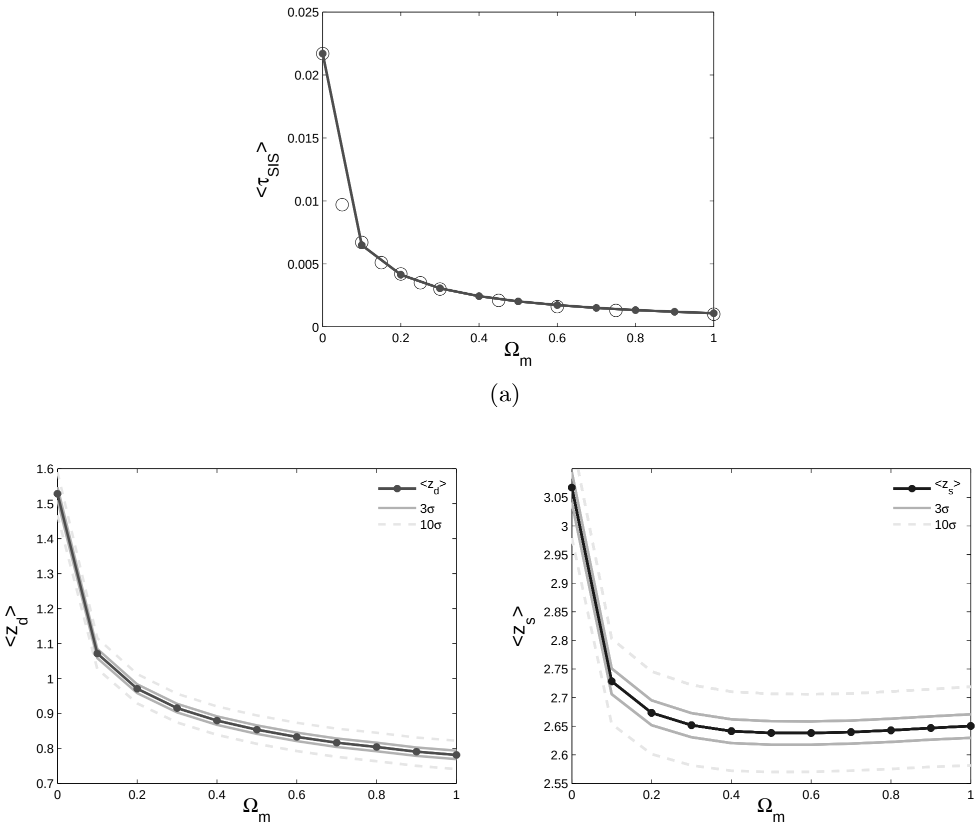

(a)

(b)

(c)

Figure 7.5: (a)Dependence of $\langle\tau\rangle$ as a function of Ω_m. For comparison, the results derived in Chapter 6 are shown as black circles. The bottom figures show the dependence as a function of Ω_m of $\langle z_d\rangle$ (b) and $\langle z_s\rangle$ (c). In both cases, the limits of the area included by 3 and 10 times the standard deviation of the distribution are shown. In figure (a) the 3 σ limit is not larger than the line thickness.

On figures (b) and (c) we have plotted the area defined by 3 and 10 times the standard deviation of the distributions. In figure (a), the area defined by 3 times the standard deviation is smaller than the line thickness.

Thus when comparing the sensitivity of the distributions on the basis of the relative change of the mean value of the distribution (i.e. $\langle\tau\rangle$, $\langle z_d\rangle$ and $\langle z_s\rangle$), ω_τ is clearly the most sensitive to the choice of a universe model, followed by ω_{z_d}.

For what concerns ω_τ, the only thing directly accessible through the observation is its first moment $\langle\tau\rangle$ (i.e. the fraction of lens events in the sample). The distribution itself may be estimated by calculating τ for each source and doing a histogram of the source lensing optical depth. Nevertheless, this estimation of ω_τ is model dependent as we have to calculate τ for each source.

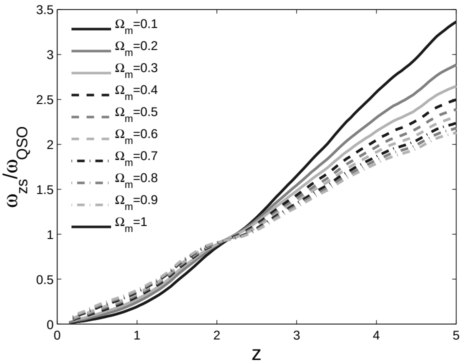

Figure 7.6: Dependence of the ratio $\omega_{z_s}/\omega_{QSO}$ as a function of the source redshift, for different values of Ω_m.

On the other hand, ω_{z_d} and ω_{z_s} are directly observable. Thus the distributions calculated through Eq. 7.18 and Eq. 7.22 can be directly compared to the observed ones in order to constrain the cosmological parameters.

One problem in the use of ω_{z_d} is the possible importance of biases: because the deflectors are faint objects, they are not always detectable, and thus it is not possible to determine the deflector redshifts for all the lenses.

As the redshift of all the lensed sources is measurable (because they are all detected, which is not the case for the deflectors), ω_{z_s} is expected to be determined with a better accuracy than ω_{z_d}.

We have noticed in Section 7.3.3, that ω_{z_s} tends to have an excess with respect to ω_{QSO} at high redshift. In Fig. 7.6 we have plotted the ratio $\omega_{z_s}/\omega_{QSO}$ as a function of the source redshift, for different values of Ω_m. As can be seen in the figure, the redshift dependence of this ratio is significantly modified by the value of Ω_m. Measurement of this excess of the density population of the lensed sources at high redshift could be a way to efficiently constrain the value of Ω_m.

Furthermore, the use of the distributions ω_{z_d} and ω_{z_s} gives access to a probability. Indeed, let us consider the probability $P\left((z_d = Z_d) \cap (z_s = Z_s) \mid GLE\right)$ of having a deflector with a redshift z_d in the range $[Z_d, Z_d + dZ_d[$ and a source at a redshift z_s in the range $[Z_s, Z_s + dZ_s[$, knowing that the source is multiply imaged. It comes

$$
\begin{aligned}
&P\left(\left(z_d=Z_d\right) \cap \left(z_s=Z_s\right) \mid GLE\right) \\
&\qquad = P\left(\left(\left(z_d=Z_d\right) \mid GLE\right) \cap \left(\left(z_s=Z_s\right) \mid GLE\right)\right), \\
&\qquad = P\left(\left(z_d=Z_d\right) \mid GLE\right) \cap \ . \ P\left(\left(z_s=Z_s\right) \mid GLE\right), \\
&\qquad = \omega_{z_d}\left(Z_d\right) \omega_{z_s}\left(Z_s\right) \, dZ_d \, dZ_s,
\end{aligned}
$$

where the last relation is obtained by using the definition of ω_{z_d} and ω_{z_s} (Eq. 7.15 and Eq. 7.20, respectively). This expression can thus be used to calculate the a posteriori probability of having a deflector and a source with a given redshift, knowing that the source is being multiply imaged. In a sample of gravitationally lensed sources, this expression can then be used for all the lensed sources for which the deflector redshift is known. As we are calculating the a posteriori probability of having all of the observables, this should be the most efficient way to constrain the value of Ω_m, using likelihood methods.

Finally, in this work we have considered a simplified model for the deflector population, which is not able to account for the existence of multiply imaged sources with more than 2 lensed images. The definition of the probability densities ω_{z_d} and ω_{z_s} may be adapted by using the SIE mass distribution. We may thus define the probability densities associated with the formation of a given number of sources. The likelihood of an event for a single source will then be constrained by the source and deflector redshift as well as the numbers of lensed images. As we are using, simultaneously, all of the observables in the gravitationally lensed source sample, this is the most efficient way to constrain the value of Ω_m from a sample of lensed sources.

Chapter 8

Conclusions

As the size, complexity and cost of astronomical telescopes keep increasing, leading to constantly more pressure on the available observing time and on the astronomers to extract results from every possible set of data, liquid mirror telescopes offer an alternative allowing the construction of large collectors that, thanks to their low cost, may be entirely dedicated and optimised for specific scientific projects.

A large effort has been invested to make this technology viable for astronomical observations, increasing the mirror optical quality and the field-of-view accessible by a fixed telescope. The technology has now been brought to maturity for scientific applications. One of the key elements leading to the success of liquid mirrors as viable astronomical tools has been the development of CCD cameras working in the TDI mode, allowing zenith pointing telescopes to track objects electronically.

The International Liquid Mirror Telescope (ILMT) project is the first attempt to correct images for the particular distortions induced by TDI imaging, thanks to a dedicated optical corrector. The ILMT should achieve very accurate photometric measurements of all objects passing in its FOV thanks to the combination of such an optical corrector with the ease of TDI data reduction as well as the low air mass at the zenith.

Photometric and astrometric precision essentially rely on the quality of the primary mirror. In the framework of the present thesis, we have developed an innovative technique to determine the quality of liquid mirrors, by detecting and characterising wavelets propagating on the mercury surface and affecting its quality. This technique is based on the use of a laser beam whose reflection on the mercury surface is affected by local slope variations induced by the wavelets.

We have designed and manufactured the necessary equipment (the light source and the detector) and have made preliminary tests on the ILMT primary mirror.

Thanks to the absence of a co-phased oscillation signature along the reflected beam section, our instrument tends to reveal the absence of concentric wavelets, possibly transmitted by the bearing. On the other hand, the presence of spiral wavelets was inferred from peaks at a frequency of $\sim$ 8 Hz in the Fourier transform of the oscillations, which seem to indicate that their apparent frequency is undersampled by the videos. Possible improvement of the measurements (the acquisition of longer videos and/or the use of a faster detector) will allow the measurement of the wavelet amplitude via the reflected beam oscillation amplitude.

We have also put in evidence the impact of vibrations transmitted to the mirror by a nearby fan, inducing a complex frequency pattern of wavelets, leading to the conclusion that sources of vibration should be avoided as much as possible on site.

Besides our contribution to the development of the ILMT, we have considered potential scientific applications of the project, among which the statistics of strong gravitational lensing effects in the QSO population, a research work presented in the second part of the present thesis. Thanks to the Earth rotation, the ILMT will access a strip of sky, centred on a declination equal to the telescope latitude, covering 150 square degrees, among which 70 sq.deg. at a high galactic latitude. As the telescope will image parts of this strip night after night, on one hand, image co-addition will lead to an increased Signal-to-Noise of the images making possible the detection of much fainter objects. On the other hand, subtraction between a reference CCD frame and those recorded each night will enable an unprecedented photometric variability study of all objects detected in the narrow strip, making the ILMT a very suitable tool for the detection and follow up of photometric variable objects such as supernovae and quasars.

In Chapter 5, we have presented an estimate of the expected number of QSOs to be detected with the ILMT, these being selected on the basis of their photometric variability.

We have determined a synthetic quasar luminosity function from the interpolation of LFs constructed from several recent and independent surveys (cf. SDSS-Dr7, SDSS-BOSS III and the MMT survey), allowing to cover the entire redshift and absolute magnitude ranges probed with the ILMT.

As a reliability test of our composite LF, we have succeeded in reproducing the observed magnitude distribution of QSOs from various surveys, achieving a very good agreement with the observations in the redshift range $2.2 < z < 3.2$. For the lower redshift range, although the brighter source distributions are very well reproduced (cf. data from the SDSS-DR3), we seem to underestimate the number of fainter QSOs at low redshift (compared to data from the 2SLAQ and 2QZ/6QZ surveys).

Assuming that the telescope will detect all objects brighter than $i' = 22.5$ at high galactic latitude ($|b| > 30°$), we expect the detection of some $\sim$ 9000 quasars. Furthermore, we have seen that degrading the limiting magnitude to $i' = 22$ would lead to the detection of only $\sim$ 7700 sources, thus reducing by more than 10 % the number of detected sources.

Among these $\sim$ 9000 QSOs to be detected with the ILMT, some are expected to be multiply imaged, due to the presence of a foreground deflecting galaxy near the line-of-sight. In the second part of this thesis, we have tried to answer the following question: among these QSOs, how many sources will be detected as being multiply imaged?

To answer this question, we have used two simple mass distributions to represent the deflectors, the SIS and SIE models, mainly motivated by the success of the isothermal mass profile to reproduce the observed flat rotation curves of galaxies.

In Chapter 4 we have derived some practical expressions for the calculation of the lensing optical depth that a source, with a given redshift and apparent magnitude, is lensed by a SIS or SIE deflector population, accounting for both the increase of the lensing geometrical volume with the source redshift and the bias induced by the amplification effect. Following earlier work done in lensing statistics, we have expressed the amplification bias in terms of the source differential number counts as a function of their magnitude. Furthermore, we have assumed a non-evolving deflector population. The latter has been characterised thanks to the measured local galaxy VDF and, comforted by recent results showing the good correlation between the ellipticity alignments of the total and the luminous mass distributions, we have adopted the same mass ellipticity distribution as the one derived from the luminous isophotes of local galaxies.

In Chapter 5, we have applied the derived optical depth expressions to the estimation of the mean lensing probability of the ILMT QSOs.

First, considering an instrument with a perfect resolution, among the 9000 QSOs to be detected with the ILMT, we should find about 28 multiply imaged sources formed by early type galaxy deflectors. The total lensing expectation is very similar when modelling the deflectors with the SIS or the SIE profiles, although, because of the radial-pseudo caustic flattening with the deflector ellipticity, the SIS tends to give a slightly overestimated value for the optical depth.

Modelling the deflectors with the SIE distribution showed that about $\sim 10\%$ of these lensing events are expected to be formed by more than 2 lensed images. Furthermore, the amplification bias tends to increase the number of lensing events with 3 and 4 lensed images, because of a higher amplification of their lensed images, formed closer to the tangential critical curve.

The number of multiply imaged sources effectively detected is highly dependent on the best angular resolution achievable with the ILMT, because lensed images angularly close to each other may not be resolved. Motivated by the fact that the lensed images close to the tangential critical curve, contributing the most to the cross section thanks to the amplification bias, are the closest from one another and have a similar amplification, we have subsequently assumed a telescope angular resolution independent of the flux ratio between the nearby lensed images.

In the ILMT best case scenario, assuming that we can resolve sources with an angular separation down to 0.5" using multiple PSF fitting techniques, we expect the detection of 22 gravitational lens systems, ~ 3 having more than 2 lensed images. Nevertheless in the resolution range 0.5-1", the average lensing optical depth is very sensitive to the telescope angular resolution and the number of detected lens systems drops dramatically for an angular resolution deteriorated to 1”, with only a few (5-6 gravitational lens systems) detections. The first lensing events to be missed because of the degraded instrumental resolution, are those formed by very distant deflectors as they tend to form lensed images with smaller angular separations.

The impact of the late-type galaxy population has also been studied showing that, although more numerous, they are not very efficient deflectors. Furthermore, as the multiple images tend to be closer to each other, even in the best case scenario for the ILMT angular resolution, we should not detect any lensing event due to a late type galaxy deflector.

Because the number of detected lens systems is highly and critically dependent on the telescope angular resolution, many efforts ought to be made to improve the latter as much as possible.

Since we intend to make use of this sample of lensed sources as a cosmological probe, we have also studied for the case of FLRW universes the impact of the cosmological mass density on the fraction of lensed sources, putting in evidence that the fraction of lens events is highly affected by the value of Ω_m, as it changes by more than an order of magnitude in the range 0 to 1. As the mean optical depth variation is steeper for low values of Ω_m, this observable is a very efficient tool to determine a lower limit on Ω_m.

Finally, in the last chapter, we have introduced theoretical considerations to determine the most efficient way to use the clean statistical sample of multiply imaged QSOs that is to be detected with the ILMT.

When used as a cosmological probe, the sample of multiply imaged sources is used by maximising the likelihood of the fraction of detected lensing events or the observed redshift distribution of the deflectors, for the events where both the source and deflector redshifts may be determined, or the observed redshift distribution of the multiply imaged sources.

To compare the relative sensitivity of these methods on the cosmological model, we have introduced a new formalism, based on the joined probability density of the observed QSOs, allowing to calculate three different probability densities; namely, the lensing optical depth distribution, the average of the deflector redshift and of the lensed source redshift distributions.

The main power of this formalism is that the joined probability density of the QSOs, as well as the redshift distribution of the deflectors and the lensed sources are directly accessible through the observations.

Using this new formalism, we have compared the sensitivity of the three distributions on the universe model parameter Ω_m, by comparing the evolution of their first and centred second moments, and concluded that the most sensitive distribution is that of the fraction of lensing events, followed by that of the lens redshift distribution. We have shown that the lensed source distribution mean value and standard deviation are not very sensitive to variations of Ω_m.

However, we have noticed that the QSO emission lines tend to produce an excess of lensed sources at redshifts where strong emission lines enter the observed spectral band (i' in our case). Furthermore, compared to the redshift distribution of all the detected sources, the lensed ones show an excess at higher redshift. We have proposed to use this excess of lensed sources at high redshift to probe the value of Ω_m.

As a final conclusion, we have shown that the introduction of the distribution ω_{z_d} and ω_{z_s} with our new formalism gives access to a new probability calculation: the probability for a source to be lensed for a given deflector redshift and source redshift. Used in combination with the maximum likelihood method, this quantity constitutes an efficient way to constrain the cosmological parameters, as it makes use of all the accessible observables (i.e. the deflector and source redshifts, QSO i' magnitude), and it may be further combined with the use of the SIE cross section allowing to simultaneously include the observed number of lensed images as a further constraint on the cosmological mass density.

As the ILMT QSOs will form a very clean statistical sample thanks to the absence of observational biases, we expect them to provide a very high quality sample for the application of our new formalism and for constraining the cosmological model, with the hope and belief that, along this path, the Universe has still some surprises to offer.

Bibliography

Alard, C. *Image subtraction using a space-varying kernel. Astronomy and Astrophysics Supplement*, 144:363–370, 2000.

Alard, C. and Lupton, R.H. *A method for optimal image subtraction. Astrophysical Journal*, 503:325, 1998.

Bolton, A.S., Burles, S., Koopmans, L.V.E., Treu, T., Gavazzi, R., Moustakas, L.A., Wayth, R., and Schlegel, D.J. *The Sloan Lens ACS Survey. V. The Full ACS Strong-Lens Sample. The Astrophysical Journal*, 682:964–984, 2008. `0805.1931`.

Borra, E.F. *The liquid-mirror telescope as a viable astronomical tool. Journal of the Royal Astronomical Society of Canada*, 76:245–256, 1982.

Borra, E.F. *On the correction of the aberrations of a liquid-mirror telescope observing at large zenith angles. Astronomy & Astrophysics*, 278:665–668, 1993.

Borra, E.F. *Liquid Mirrors: A Review. ArXiv Astrophysics e-prints*, 1994. `arXiv:astro-ph/9410008`.

Borra, E.F. *The need for a paradigm shift in optical astronomy: A solution given by liquid mirrors and examples of their applications to cosmology. eprint arXiv:astro-ph/9503019*, 1995.

Borra, E.F. *Astronomical research with liquid mirror telescopes. eprint arXiv:astro-ph/9706108*, 1997.

Borra, E.F., Arsenault, R., and Lalande, R. *The Liquid-Mirror Telescope: A Progress Report.* In *Bulletin of the American Astronomical Society*, *Bulletin of the American Astronomical Society*, vol. 14, p. 940. 1982.

Borra, E.F., Content, R., Drinkwater, M.J., and Szapiel, S. *A diffraction-limited f/2 1.5 meter diameter liquid mirror. Astrophysical Journal*, 346:L41–L44, 1989.

Borra, E.F., Content, R., and Girard, L. *Optical shop tests of a f/1.2 2.5 meter diameter liquid mirror. Astrophysical Journal*, 418:943, 1993.

Borra, E.F., Content, R., Girard, L., Szapiel, S., Tremblay, L.M., and Boily, E. *Liquid mirrors - optical shop tests and contributions to the technology. Astrophysical Journal*, 393:829–847, 1992.

Borra, E.F., Moretto, G., and Wang, M. *An optical corrector design that allows a fixed telescope to access a large region of the sky. Astronomy and Astrophysics Suppl.*, 109:563–570, 1995. `arXiv:astro-ph/9410019`.

Branch, D. and Tammann, G.A. *Type IA supernovae as standard candles. Annual review of astronomy and astrophysics*, 30:359–389, 1992.

Cao, S., Pan, Y., Biesiada, M., Godlowski, W., and Zhu, Z.H. *Constraints on cosmological models from strong gravitational lensing systems. Journal of Cosmology and Astroparticle Physics*, 3:016, 2012. `1105.6226`.

Cen, R., Gott, III, J.R., Ostriker, J.P., and Turner, E.L. *Strong gravitational lensing statistics as a test of cosmogonic scenarios. The Astrophysical Journal*, 423:1–11, 1994.

Chae, K.H. *Galaxy evolution from strong-lensing statistics: the differential evolution of the velocity dispersion function in concordance with the* Λ *cold dark matter paradigm. Monthly Notices of the Royal Astronomical Society*, 402:2031–2048, 2010.

Chae, K.H., Biggs, A.D., Blandford, R.D., Browne, I.W., de Bruyn, A.G., Fassnacht, C.D., Helbig, P., Jackson, N.J., King, L.J., Koopmans, L.V., Mao, S., Marlow, D.R., McKean, J.P., Myers, S.T., Norbury, M., Pearson, T.J., Phillips, P.M., Readhead, A.C., Rusin, D., Sykes, C.M., Wilkinson, P.N., Xanthopoulos, E., and York, T. *Constraints on Cosmological Parameters from the Analysis of the Cosmic Lens All Sky Survey Radio-Selected Gravitational Lens Statistics. Physical Review Letters*, 89(15):151301, 2002. `arXiv:astro-ph/0209602`.

Choi, Y.Y., Park, C., and Vogeley, M.S. *Internal and collective properties of galaxies in the Sloan Digital Sky Survey. The Astrophysical Journal*, 658:884–897, 2007.

Claeskens, J.F., Sluse, D., Riaud, P., and Surdej, J. *Multi wavelength study of the gravitational lens system RXS J1131-1231. II. lens model and source reconstruction. Astronomy and Astrophysics*, 451(3):865–879, 2006a.

Claeskens, J.F., Smette, A., Vandenbulcke, L., and Surdej, J. *Identification and redshift determination of quasi-stellar objects with medium-band photometry: application to gaia. Monthly Notices of the Royal Astronomical Society*, 367:879–904, 2006b.

Claeskens, J.F. *Aspects statistiques du phénomène de lentille gravitationnelle dans un échantillon de quasars très lumineux.* Ph.D. thesis, Bulletin de la Société Royale des Sciences de Liège, Volume 68, 1999.

Content, R. *Tests optiques sur un miroir liquide de 1.5 m et développement de la technologie des miroirs liquides.* Ph.D. thesis, Université Laval, 1992.

Croom, S.M., Richards, G.T., Shanks, T., Boyle, B.J., Strauss, M.A., Myers, A.D., Nichol, R.C., Pimbblet, K.A., Ross, N.P., Schneider, D.P., Sharp, R.G., and Wake, D.A. *The 2df-SDSS LRG and QSO survey: the QSO luminosity function at 0.4 $<$ z $<$ 2.6. Monthly Notices of the Royal Astronomical Society*, 399:1755–1772, 2009.

Croom, S.M., Smith, R.J., Boyle, B.J., Shanks, T., Miller, L., Outram, P.J., and Loaring, N.S. *The 2df QSO Redshift Survey - XII. the spectroscopic catalogue and luminosity function. Monthly Notices of the Royal Astronomical Society*, 349(4):1397–1418, 2004.

Denis, S. *Test report - angular velocity stability of ILMT primary mirror with mercury (3mm).* Tech. rep., AMOS, 2011.

Dobke, B.M., King, L.J., Fassnacht, C.D., and Auger, M.W. *Estimating cosmological parameters from future gravitational lens surveys. Monthly Notices of the Royal Astronomical Society*, 397:311–319, 2009.

Duffet-Smith, P. *Astronomy with your Personal Computer.* Cambridge University Press, 1988.

Etherington, I.M.H. *On the definition of distance in general relativity. Phil. Mag.*, 15:761, 1933.

Faure, C., Anguita, T., Alloin, D., Bundy, K., Finoguenov, A., Leauthaud, A., Knobel, C., Kneib, J.P., Jullo, E., Ilbert, O., Koekemoer, A.M., Capak, P., Scoville, N., and Tasca, L.A.M. *On the evolution of environmental and mass properties of strong lens galaxies in COSMOS. Astronomy and Astrophysics*, 529:A72, 2011.

Fontanot, F., Cristiani, S., Monaco, P., Nonino, M., Vanzella, E., Brandt, W.N., Grazian, A., and Mao, J. *The luminosity function of high-redshift quasi-stellar objects. a combined analysis of GOODS and SDSS. Astronomy and Astrophysics*, 467:39–48, 2007.

Fukugita, M., Ichikawa, T., Gunn, J.E., Doi, M., Shimasaku, K., and Schneider, D.P. *The Sloan Digital Sky Survey photometric system. Astronomical Journal*, 111:1748, 1996.

Gibson, B.K. and Hickson, P. *Time-delay integration ccd read-out technique - image deformation. Monthly Notices of the Royal Astronomical Society (ISSN 0035-8711)*, 258(3):543–551, 1992.

Girard, L. and Borra, E.F. *Optical tests of a 2.5-m-diameter liquid mirror: behavior under external perturbations and scattered-light measurements. Applied Optics*, 36,:6278–6288, 1997.

Glikman, E., Djorgovski, S.G., Stern, D., Dey, A., Jannuzi, B.T., and Lee, K.S. *The faint end of the quasar luminosity function at $z \sim 4$: Implications for ionization of the intergalactic medium and cosmic downsizing. The Astrophysical Journal Letters*, Volume 728:5 pp., 2011.

Hickson, P. *Wide-field tracking with zenith-pointing telescopes. Monthly Notices of the Royal Astronomical Society*, 330:540–546, 2002. `arXiv:astro-ph/0106191`.

Hickson, P. *Requirements for the ILMT primary mirror system.* Tech. Rep. R02, The University of British Columbia, 2008a.

Hickson, P., Borra, E.F., Cabanac, R., Content, R., Gibson, B.K., and Walker, G.A.H. *UBC/Laval 2.7 meter liquid mirror telescope. Astrophysical Journal, Part 2 - Letters*, 436:L201–L204, 1994.

Hickson, P. and Racine, R. *Image Quality of Liquid-Mirror Telescopes. The Publications of the Astronomical Society of the Pacific*, 119:456–465, 2007.

Hickson, P. *Analysis and recommendations concerning the ILMT primary mirror, air bearing, interface and air system.* Tech. Rep. R01, The University of British Columbia, 2008b.

Hickson, P., Gibson, B.K., and Hogg, D.W. *Large astronomical liquid mirrors. Astronomical Society of the Pacific,*, 105(687):501–508, 1993.

Hickson, P. and Richardson, E.H. *A curvature-compensated corrector for drift-scan observations. The Publications of the Astronomical Society of the Pacific*, 110(110):1081–1086, 1998.

Hogg, D.W. *Distance measures in cosmology. arXiv:astro-ph/9905116*, -:–, 2000.

Ikeda, H., Nagao, T., Matsuoka, K., Taniguchi, Y., Shioya, Y., Kajisawa, M., Enoki, M., Capak, P., Civano, F., Koekemoer, A.M., Masters, D., Morokuma, T., Salvato, M., Schinnerer, E., and Scoville, N.Z. *Constraints on the faint end of the quasar luminosity function at $z \sim 5$ in the COSMOS field. The Astrophysical Journal*, Volume 756(Issue 2):article id. 160, 2012.

Ikeda, H., Nagao, T., Matsuoka, K., Taniguchi, Y., Shioya, Y., Trump, J.R., Capak, P., Comastri, A., Enoki, M., Ideue, Y., Kakazu, Y., Koekemoer, A.M., Morokuma, T., Murayama, T., Saito, T., Salvato, M., Schinnerer, E., Scoville, N.Z., and Silverman, J.D. *Probing the faint end of the quasar luminosity function at $z\sim 4$ in the COSMOS field. The Astrophysical Journal Letters*, 728(Issue 2):5 pp, 2011.

Johnston, R. *Shedding light on the galaxy luminosity function. The Astronomy and Astrophysics Review*, 19:article id. 41, 2011.

Keeton, C.R. *Rethinking Lensing and Λ. The Astrophysical Journal Letters*, 575:L1–L4, 2002. `arXiv:astro-ph/0206496`.

Keeton, C.R. and Kochanek, C.S. *Gravitational Lensing by Spiral Galaxies. The Astrophysical Journal*, 495:157, 1998. `arXiv:astro-ph/9705194`.

Keeton, C.R., Kochanek, C.S., and Falco, E.E. *The Optical Properties of Gravitational Lens Galaxies as a Probe of Galaxy Structure and Evolution. The Astrophysical Journal*, 509:561–578, 1998. `arXiv:astro-ph/9708161`.

Keeton, II, C.R. *Using Gravitational Lenses to Study Galaxies and Cosmology.* Ph.D. thesis, Harvard University, 1998.

Kim, A., Goobar, A., and Perlmutter, S. *A Generalized K Correction for Type IA Supernovae: Comparing R-band Photometry beyond z=0.2 with B, V, and R-band Nearby Photometry. Publications of the Astronomical Society of the Pacific*, 108:190, 1996. `arXiv:astro-ph/9505024`.

Kochanek, C., Schneider, P., and Wambsganss, J. *Gravitational Lensing: Strong, Weak & Micro.* Lecture Notes of the 33rd Saas-Fee Advanced Course, 2005.

Koopmans, L.V.E., Treu, T., Bolton, A.S., Burles, S., and Moustakas, L.A. *The Sloan Lens ACS Survey. III. The Structure and Formation of Early-Type Galaxies and Their Evolution since z ˜ 1. The Astrophysical Journal*, 649:599–615, 2006. `arXiv:astro-ph/0601628`.

Kormann, R., Schneider, P., and Bartelmann, M. *Isothermal elliptical gravitational lens models. Astronomy and Astrophysics*, 284:285–299, 1994.

Krisciunas, K. *The usefulness of type ia supernovae for cosmology—a personal review. The Journal of the American Association of Variable Star Observers*, 40:334, 2012.

Lane, A.P. *A cautionary note on conversions between galactic and equatorial coordinate systems. Astronomical Society of the Pacific*, 91:405–407, 1979.

Masters, D., Capak, P., Salvato, M., Civano, F., Mobasher, B., Siana, B., Hasinger, G., Impey, C.D., Nagao, T., Trump, J.R., Ikeda, H., Elvis, M., and Scoville, N. *Evolution of the quasar luminosity function over* $3 < z < 5$ *in the COSMOS survey field. The Astrophysical Journal*, Volume 755,(Issue 2):16 pp., 2012.

Matsumoto, A. and Futamase, T. *Validity of strong lensing statistics for constraints on the galaxy evolution model. Monthly Notices of the Royal Astronomical Society*, 384:843–848, 2008.

Mitchell, J.L., Keeton, C.R., Frieman, J.A., and Sheth, R.K. *Improved Cosmological Constraints from Gravitational Lens Statistics. The Astrophysical Journal*, 622:81–98, 2005. `arXiv:astro-ph/0401138`.

Mulrooney, M. *A 3.0 meter liquid mirror telescope.* Ph.D. thesis, RICE UNIVERSITY, 2000.

Ninane, N., Flebus, C., and Kumar, B. *The 3,6 m indo-belgian Devasthal Optical Telescope: general description.* In *Ground-based and Airborne Telescopes IV. Proceedings of the SPIE*. 2012.

Ofek, E.O., Rix, H.W., and Maoz, D. *The redshift distribution of gravitational lenses revisited: constraints on galaxy mass evolution. Monthly Notices of the Royal Astronomical Society*, 343:639–652, 2003. `arXiv:astro-ph/0305201`.

Oke, J.B. and Gunn, J.E. *Secondary standard stars for absolute spectrophotometry. Astrophysical Journal*, vol. 266:p. 713–717., 1983.

Oke, J.B. and Sandage, A. *Energy Distributions, K Corrections, and the Stebbins-Whitford Effect for Giant Elliptical Galaxies. Astrophysical Journal*, 154:21, 1968.

Palanque-Delabrouille, N., Magneville, C., Yeche, C., Eftekharzadeh, S., Myers, A.D., Petitjean, P., Paris, I., Aubourg, E., McGreer, I., Fan, X., Dey, A., Schlegel, D., Bailey, S., Bizayev, D., Bolton, A., Dawson, K., Ebelke, G., Malanushenko, E., Malanushenko, V., Oravetz, D., Pan, K., Ross, N.P., Schneider, D.P., Sheldon, E., Simmons, A., Tinker, J., White, M., and Willmer, C. *Luminosity function from dedicated SDSS-III and MMT data of quasars in $0.7<z<4.0$ selected with a new approach. Astronomy & Astrophysics*, Accepted for publication:eprint arXiv:1209.3968, 2012.

Peebles, P. *Principles of Physical Cosmology*. Princeton University Press, 1993.

Refsdal, S. *On the possibility of determining Hubble's parameter and the masses of galaxies from the gravitational lens effect. Monthly Notices of the Royal Astronomical Society*, 128:307, 1964a.

Refsdal, S. *The gravitational lens effect. Monthly Notices of the Royal Astronomical Society*, 128:295, 1964b.

Refsdal, S. and Surdej, J. *Gravitational lenses. Reports on Progress in Physics*, 57:117, 1994.

Richards, G.T., Strauss, M.A., Fan, X., Hall, P.B., Jester, S., Schneider, D.P., Vanden Berk, D.E., Stoughton, C., Anderson, S.F., Brunner, R.J., Gray, J., Gunn, J.E., Ivezić, Ž., Kirkland, M.K., Knapp, G.R., Loveday, J., Meiksin, A., Pope, A., Szalay, A.S., Thakar, A.R., Yanny, B., York, D.G., Barentine, J.C., Brewington, H.J., Brinkmann, J., Fukugita, M., Harvanek, M., Kent, S.M., Kleinman, S.J., Krzesiński, J., Long, D.C., Lupton, R.H., Nash, T., Neilsen, Jr., E.H., Nitta, A., Schlegel, D.J., and Snedden, S.A. *The sloan digital sky survey quasar survey: Quasar luminosity function from data release 3. The Astronomical Journal, Volume 131, Issue 6, pp. 2766-2787*, Volume 131, Issue 6:2766–2787, 2006.

Ross, N.P., McGreer, I.D., White, M., Richards, G.T., Myers, A.D., Palanque-Delabrouille, N., Strauss, M.A., Anderson, S.F., Shen, Y., Brandt, W.N., Yeche, C., Swanson, M.E.C., Aubourg, E., Bailey, S., Bizyaev, D., Bovy, J., Brewington, H., Brinkmann, J., DeGraf, C., Di Matteo, T., Ebelke, G., Fan, X., Ge, J., Malanushenko, E., Malanushenko, V., Mandelbaum, R., Maraston, C., Muna, D., Oravetz, D., Pan, K., Paris, I., Petitjean, P., Schawinski, K., Schlegel, D.J., Schneider, D.P., Silverman, J.D., Simmons, A., Snedden, S., Streblyanska, A., Suzuki, N., Weinberg, D.H., and York, D. *The SDSS-III Baryon Oscillation Spectroscopic Survey: The Quasar Luminosity Function from Data Release Nine.* *ArXiv e-prints*, 2012. `1210.6389`.

Sagar, R., Kumar, B., Omar, A., and Joshi, Y.C. *New optical telescopes at Devasthal observatory : 1.3-m installed and 3.6-m upcoming.* In *Astronomical Society of India Conference Series*, vol. 4. 2012a.

Sagar, R., Kumar, B., Omar, A., and Pandey, A.K. *New optical telescope projects at Devasthal Observatory.* In *Ground-based and Airborne Telescopes IV. Proceedings of the SPIE.* 2012b.

Sagar, R., Stalin, C.S., Pandey, A.K., Uddin, W., Mohan, V., Sanwal, B.B., Gupta, S.K., Yadav, R.K.S., Durgapal, A.K., Joshi, S., Kumar, B., Gupta, A.C., Joshi, Y.C., Srivastava, J.B., Chaubey, U.S., Singh, M., Pant, P., and Gupta, K.G. *Evaluation of devasthal site for optical astronomical observations.* *Astron. Astrophys. Suppl. Ser.*, 144:349–362, 2000.

Schechter, P. *An analytic expression for the luminosity function for galaxies.* *Astrophysical Journal*, 203:297–306, 1976.

Schneider, P. *The amplification caused by gravitational bending of light.* *Astronomy and Astrophysics*, 140:119–124, 1984.

Schroeder, D.J. *Astronomical Optics.* San Diego, CA, Academic Press, 1987.

Sheth, R.K., Bernardi, M., Schechter, P.L., Burles, S., Eisenstein, D.J., Finkbeiner, D.P., Frieman, J., Lupton, R.H., Schlegel, D.J., Subbarao, M., Shimasaku, K., Bahcall, N.A., Brinkmann, J., and Ivezić, Ž. *The Velocity Dispersion Function of Early-Type Galaxies.* *The Astrophysical Journal*, 594:225–231, 2003. `arXiv:astro-ph/0303092`.

Sluse, D., Chantry, V., Magain, P., Courbin, F., and Meylan, G. *COSMOGRAIL: the COSmological MOnitoring of GRAvItational Lenses. X. Modeling based on high-precision astrometry of a sample of 25 lensed quasars: consequences for ellipticity, shear, and astrometric anomalies.* *Astronomy & Astrophysics*, 538:A99, 2012. `1112.0005`.

Sluse, D., Claeskens, J.F., Altieri, B., Cabanac, R.A., Garcet, O., Hutsemékers, D., Jean, C., Smette, A., and Surdej, J. *Multi-wavelength study of the grav-*

itational lens system RXS J113155.4-123155. I. Multi-epoch optical and near infrared imaging. Astronomy and Astrophysics, 449(2):539–550, 2006.

Sluse, D., Claeskens, J.F., Hutsemékers, D., and Surdej, J. *Multi-wavelength study of the gravitational lens system RXS J1131-1231. III. long slit spectroscopy: micro-lensing probes the QSO structure. Astronomy and Astrophysics*, 468(3):885–901, 2007.

Stalin, C.S., Sagar, R., Pant, P., Mohan, V., Kumar, B., Joshi, Y.C., Yadav, R.K.S., Joshi, S., Chandra, R., Durgapal, A.K., and Uddin, W. *Seeing and microthermal measurements near devasthal top. Bulletin of the Astronomical Society of India*, 29:39–52, 2001.

Surdej, J., Claeskens, J.F., Crampton, D., Filippenko, A.V., Hutsemekers, D., Magain, P., Pirenne, B., Vanderriest, C., and Yee, H.K.C. *Gravitational lensing statistics based on a large sample of highly luminous quasars. Astronomical Journal*, 105:2064–2078, 1993.

Thomas, J., Saglia, R.P., Bender, R., Thomas, D., Gebhardt, K., Magorrian, J., Corsini, E.M., Wegner, G., and Seitz, S. *Dynamical masses of early-type galaxies: a comparison to lensing results and implications for the stellar initial mass function and the distribution of dark matter. Monthly Notices of the Royal Astronomical Society*, 415:545–562, 2011.

Treu, T., Koopmans, L.V., Bolton, A.S., Burles, S., and Moustakas, L.A. *The Sloan Lens ACS Survey. II. Stellar Populations and Internal Structure of Early-Type Lens Galaxies. The Astrophysical Journal,*, 640:662–672, 2006. `arXiv:astro-ph/0512044`.

Turner, E. L.and Ostriker, J.P. and Gott, J. R., I. *The statistics of gravitational lenses - the distributions of image angular separations and lens redshifts. Astrophysical Journal*, 284:1–22, 1984.

Vanden Berk, D.E., Richards, G.T., Bauer, A., Strauss, M.A., Schneider, D.P., Heckman, T.M., York, D.G., Hall, P.B., Fan, X., Knapp, G.R., Anderson, S.F., Annis, J., Bahcall, N.A., Bernardi, M., Briggs, J.W., Brinkmann, J., Brunner, R., Burles, S., Carey, L., Castander, F.J., Connolly, A.J., Crocker, J.H., Csabai, I., Doi, M., Finkbeiner, D., Friedman, S., Frieman, J.A., Fukugita, M., Gunn, J.E., Hennessy, G.S., Ivezić, Ž., Kent, S., Kunszt, P.Z., Lamb, D.Q., Leger, R.F., Long, D.C., Loveday, J., Lupton, R.H., Meiksin, A., Merelli, A., Munn, J.A., Newberg, H.J., Newcomb, M., Nichol, R.C., Owen, R., Pier, J.R., Pope, A., Rockosi, C.M., Schlegel, D.J., Siegmund, W.A., Smee, S., Snir, Y., Stoughton, C., Stubbs, C., SubbaRao, M., Szalay, A.S., Szokoly, G.P., Tremonti, C., Uomoto, A., Waddell, P., Yanny, B., and Zheng, W. *Composite Quasar Spectra from the Sloan Digital Sky Survey. The Astronomical Journal*, Volume 122(Issue 2):pp. 549–564, 2001.

Vangeyte, B., Manfroid, J., and Surdej, J. *Study of CCD mosaic configurations for the ILMT: Astrometry and photometry of point sources in the absence of a TDI corrector. Astronomy and Astrophysics*, 388:712–731, 2002.

Weedman, D.W. *Quasar astronomy.* Cambridge University Press, 1986.

Zaritsky, D., Schectman, S.A., and Bredthauer, G. *The great-circle camera: A new drift-scanning instrument. Publications of the Astronomical Society of the Pacific*, 108:104, 1996.

Appendix A

Detector to lens plane mapping

Determination of the detector characteristics

We here determine precisely the distance between the lens and the CMOS detector, and thus the out of focus distance. We also want to determine the position of the optical axis (the axis of symmetry of the lens) on the detector.

We have taken a calibration image where in front of the detector lens, we introduced a transparent mask where we have drawn vertical lines every 5 mm. These lines act as masks and decrease the apparent flux from the laser. In the image, we can thus detect the points x_d corresponding to the rays that impacted on the vertical lines.

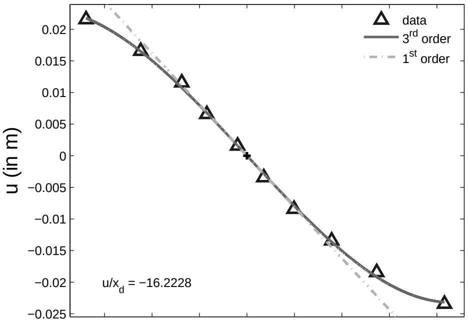

Figure A.1: Experimental determination of the $u\left(x_d\right)$ relation, leading to the precise knowledge of the optical axis position on the detector and the out-of-focus distance of the detector.

In Fig. A.1, we represent the lens impact coordinate u as a function of the CMOS detector impact coordinate x_d, both expressed in meters. The origin of the x_d and u coordinates has been determined by fitting the relation $u\left(x_d\right)$ with a third order polynomial and taking as origin the point where the curvature sign changes.

We clearly see that the mapping between x_d and u is non linear. This non linear mapping is due to both the non linear deflection law (as a function of the impact radius) induced by the lens to the impacting rays, and to the divergence of the impact rays (cfr emitter characteristics).

In order to determine the distance between the lens and the detector, let us consider the paraxial case, i.e. we only consider the rays around the origin. In the paraxial approximation, the relation $u\left(x_d\right)$ is linear, and this relation is given by the linear approximation of the third order fit, around the origin. The linear approximation is shown in Fig. A.1 with a dashed line.

We have seen that we can find a linear relation between the impact coordinates Y and the one on the line u (i.e. $u = SY$, cfr Eq. 2.28). Thus, at the impact point on the lens, the rays seem to arrive from a point-like source at a distance ${d_s}^1$

$$d_s = \frac{(d - X_0))}{\sin\left(\alpha - 2\theta_{X_0}\right)(S - 1)}. \tag{A.1}$$

As an indication, for the impact point at a radius of 1.59 m, $d_s \sim 100$ m.

Thus, defining d_i the distance from the lens to the plane where this point like source is imaged, we have

$$\frac{1}{d_s} + \frac{1}{d_i} = \frac{1}{f} \Rightarrow d_i = \frac{f d_s}{d_s - f}, \tag{A.2}$$

where f is the focal length of the lens.

Finally, defining d_l as the distance between the lens and the detector, the relation between u and x_d is given by

$$x_d = -u\frac{d_l - d_i}{d_i}. \tag{A.3}$$

Consequently, from the experimental measurement of the linear relation $u\left(x_d\right)$ in the paraxial case, we determine the distance between the lens and the detector (and thus, the out-of-focus distance of the detector). From the linear approximation in Fig. A.1, we find $d_l = 0.159485$ (m).

---

[1] This can be shown using the linear relation between u and Y and

$$\frac{d_s}{u} = \frac{d_s - \bar{ID}}{Y},$$

where $\bar{ID}$ is the distance between the impact point on the mirror and the lens. From Fig. 2.7, simple geometrical arguments lead to

$$\bar{ID} = \frac{(d - X_0)}{\sin\left(\alpha - 2\theta_{X_0}\right)}.$$

The mapping $u\left(x_d\right)$ measured in the calibration video results from the deflection applied by the lens on the ray impacting the lens and from the inclination of the incident ray. Let us separate the two contributions.

Let us consider a ray (contained in the lens equatorial plane) impacting at a coordinate u and forming a small angle δ_u with the optical axis. The position x_d where the ray impacts the detector is given by

$$\begin{aligned} x_d &= u - d_l \tan\left(\rho_l\left(u\right) - \delta_u\right), & \text{(A.4)} \\ &\simeq u - d_l \tan\left(\rho_l\left(u\right)\right) + d_l \delta_u, & \text{(A.5)} \end{aligned}$$

where $\rho_l\left(u\right)$ is the deflection angle induced by the lens to a ray impacting at u. The second relation has been derived assuming $\delta_u \ll 1$ and $\tan^2\left(\rho_l\left(u\right)\right) \ll \tan\left(\rho_l\left(u\right)\right) < 1$[2]. Let us now develop $\tan\left(\rho_l\left(u\right)\right)$ to the third order

$$\tan\left(\rho\right) \simeq= c_1 u^3 + c_2 u^2 + c_3 u, \tag{A.6}$$

we consider $c_4 = 0$ because a ray arriving along the optical axis at $u = 0$ is not deflected. Furthermore, using the fact that

$$\delta_u = \frac{u}{d_s}, \tag{A.7}$$

Eq. A.5 becomes

$$\begin{aligned} x_d &= u - d_l\left(c_1 u^3 + c_2 u^2 + c_3 u\right) + d_l \frac{u}{d_s}, \\ &= \left(-d_l c_1\right) u^3 + \left(-d_l c_2\right) u^2 + \left(1 + \frac{d_l}{d_s} - d c_3\right) u. & \text{(A.8)} \end{aligned}$$

As the value of d_l is known, the coefficients of a third order fit of the relation $x_d\left(u\right)$ (i.e. the data from Fig. A.1) allows to retrieve the parameters c_1, c_2 and c_3 characterising the lens deflection

$$\begin{aligned} c_1 &= 357.9113, \\ c_2 &= -0.9559993, \\ c_3 &= 6.619645. \end{aligned}$$

Mapping relation

Let us now assume that a light ray is impacting at a point (u, v) on the lens, where the coordinates u and v are in the sagittal and meridional planes, respectively.

---

[2] In our case, the maximum value $\tan\rho_{l,max}$ of $\tan\left(\rho_l\left(u\right)\right)$ is of the order

$$\tan\rho_{l,max} \sim \frac{u_{max}}{f} = \frac{2\,.10^{-2}}{1.5\,.10^{-1}}.$$

Let us assume that the ray is impacting with an angle δ_u (and δ_v, respectively) relatively to the optical axis, as measured in the sagittal (meridional, respectively) plane. These two angles are given by

$$\begin{pmatrix} \delta_u \\ \delta_v \end{pmatrix} = \begin{pmatrix} 1/d_s & 0 \\ 0 & 1/d_v \end{pmatrix} \begin{pmatrix} u \\ v \end{pmatrix}, \tag{A.9}$$

where d_s has been previously defined and where

$$d_v = \frac{d - X_0}{\sin\left(\alpha - 2\theta_{X_0}\right)} \tag{A.10}$$

is the distance between the impact point on the mirror and the lens, as measured along the lens optical axis.

In two dimensions, adapting Eq. A.8, the coordinates (x_d, y_d) on the detector are given by

$$\begin{aligned} \begin{pmatrix} x_d \\ y_d \end{pmatrix} &= \begin{pmatrix} u \\ v \end{pmatrix} - \frac{d_l}{r_l}\left(c_1 r_l^3 + c_2 r_l^2 + c_3 r_l\right) \begin{pmatrix} u \\ v \end{pmatrix} \\ &+ d_l \begin{pmatrix} 1/d_s & 0 \\ 0 & 1/d_v \end{pmatrix} \begin{pmatrix} u \\ v \end{pmatrix}, \end{aligned} \tag{A.11}$$

where $r_l = \sqrt{u^2 + v^2}$ is the impact parameter in the lens plane. This relationship is used to map the coordinates of the ray impacts on the detector to the lens plane. For inverting the relation, we proceed by generating a grid in the (u, v) plane, for which we calculate the image through the mapping. The (u, v) coordinates corresponding to a given measured position on the detector is then obtained by interpolating the original grid.